2009

Development of a Storm Surge Model using a High-Resolution Unstructured Grid Over a Large Domain

Tao Shen
College of William and Mary - Virginia Institute of Marine Science

Development of a Storm Surge Model Using a High-Resolution Unstructured Grid over a Large Domain

---

A Thesis

Presented to

The Faculty of the School of Marine Science

The College of William and Mary in Virginia

In Partial Fulfillment

Of the Requirements for the Degree of

Master of Science

---

by Tao Shen

2009

APPROVAL SHEET

This thesis is submitted in partial fulfillment of

the requirements for the degree of

Master of Science

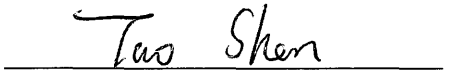

Tao Shen

Approved by the committee, May 2009

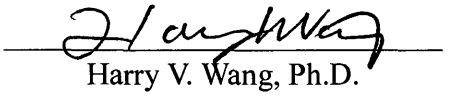

Harry V. Wang, Ph.D.
Advisor

Carl H. Hershner, Ph.D.

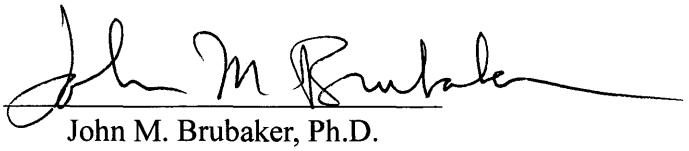

John M. Brubaker, Ph.D.

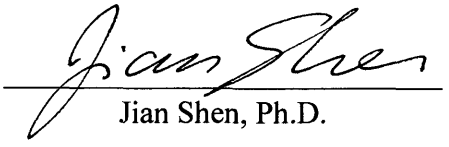

Jian Shen, Ph.D.

TABLE OF CONTENTS

Page

ACKNOWLEDGEMENTS

I would like to thank my advisor, Harry Wang for his guidance and direction during my graduate study and in this research. I would also like to thank my other committee members: Jian Shen, John Brubaker and Carl Hershner who gladly offered help and suggestion to me. I would like to thank Dr. Leonidas Linardakis for his assistance in this study and Mr. Mac Sisson for his proofreading of this thesis. I would also like to thank the whole three-dimensional modeling group and my Chinese friends at VIMS for their help during the last three years.

Finally I would like to thank my parents, my elder sister and my wife for their encouragement and support throughout my studies.

LIST OF TABLES

LIST OF FIGURES

ABSTRACT

A quasi-3D storm surge modeling system was developed for forecasting the storm surge and inundation in the Chesapeake Bay. The system was constructed with one large unstructured grid covering the Atlantic Coast from Nova Scotia to Florida and a smaller, limited domain unstructured grid covering the Chesapeake Bay, Virginia Beach, Hampton Roads and the adjacent continental shelf regions. It was demonstrated that, with the large domain grid, the model could simulate the hurricane induced storm surge reasonably well using astronomical tide at the open boundary condition and in turn, provide boundary condition for the limited domain model. Since the difficulty of specifying the open boundary condition in the limited domain was solved using this dual-grid methodology, the model achieved the predictive capability for forecasting storm surge as long as accurate atmospheric wind is provided. The high resolution, limited domain grids could, at the same time, be used to map inundation features in details inside the Chesapeake Bay..

The storm surge modeling system has been linked with different atmospheric models. The simulations with different winds proved that the storm surge simulation is highly dependent on the quality of the winds generated by atmospheric models and ensemble technology is necessary for the forecasting purpose and the uncertainty associate with it. Procedures of ensemble simulations were developed in this study so that the modeling system could be used for forecasting storm surge with ensemble winds. Realistic simulations conducted in this study demonstrated that the high-resolution unstructured grid, which is able to resolve complex bathymetry, topography, and coastline structure, could generate accurate storm surge and inundation results if LiDAR data are incorporated. The high-resolution grid and accurate LiDAR topographic data are essential for generating accurate inundation maps. One of the significant findings in this study is that the coastal Ekman dynamics does play an important role in water exchanges between continetial shelf and the Chesapeake Bay. In this context, it is, thereofer, necessary to use a quasi-3D model, rather than 2D model, in order to resolve vertical varying Ekman transport, which significantly improve the storm surge prediction.

Development of a Storm Surge Model Using a High-Resolution Unstructured Grid over a Large Domain

Chapter 1. Introduction

1.1 Literature review

Storm surge is an abnormal rise in sea level accompanying a hurricane or other intense storm, and whose height is the difference between the observed level of the sea surface and the level that would have occurred in the absence of the cyclone (National Hurricane Center, NWS, 2009). In the past several decades, there are many storm surge studies conducted in the Chesapeake Bay (Bretschneider, 1959; Harris, 1963; Pore, 1965; Valle-Levinson et al., 2002; Wang et al., 2005; Li et al., 2006; Shen et al., 2006a, 2006b, 2008). Harris (1956) is the first one who started systematic studies on the storm surges due to hurricanes on the East Coast of the United States. In his paper 'characteristics of the hurricane storm surge', Harris (1963) summarized five distinct processes that can alter the water level in tidal water regions during a storm surge: (a) the pressure effect, (b) the direct wind effect, (c) the effect of the earth's rotation, (d) the effect of waves, and (e) the rainfall effect. Pore (1965) included two more factors involved in the generation and modification of storm surges in the Chesapeake Bay: (1) the height of the tide in the Atlantic Ocean near the entrance of Chesapeake Bay and (2) modifying effects of coastline configuration and bathymetry.

Numerical model studies of hurricane-induced storm surge began in the early 1970s. Jelesnianski (1972) developed the Special Program to List Amplitude of Surges from Hurricanes (SPLASH) in 1972. After that, Sea, Lake, and Overland Surges from Hurricanes (SLOSH) was developed and widely used by NOAA for coastal flooding and inundation forecasts along the Gulf Coast and Eastern Seaboard of the United States (Jelesnianski et al., 1984; Jelesnianski et al.,1992). Despite its popularity, the SLOSH model has several disadvantages that need to be improved. First, because its' use of structured grid, the SLOSH model has a limitation in resolving complicated coastlines and thus severely restricts its capability for accurate simulation of inundation. Second, the advection terms in the momentum equations are neglected in this model, which will influence the accuracy of the simulation. In recent decades, many other models using different numerical schemes have been developed for the simulation of storm surges in different areas (Lynch, 1983; Blumberg and Mellor, 1987; Flather et al., 1991; Luettich et al., 1992; Westerink et al., 1992; Hubbert and McInnes, 1999). One of these models is the ADCIRC model, which employs the unstructured grid and is able to resolve the complex coastline and the bathymetry of shallow water quite well.

In recent years, due to the potential increase in the strength and frequency of hurricanes and their associated storm surges related to global warming, there is a renewed interest for improving storm surge and inundation models along the Gulf Coast and the Eastern Coast of the USA (Valle-Levinson et al,. 2002; Wang et al., 2005; Bernier and Thompson, 2006; Kohut et al., 2006; Li et al., 2006; Weisberg and Zheng, 2006; Shen et al., 2006a, 2006b, 2008). However, up to date, there is no forecasting model developed in the Chesapeake Bay. This study aims at developing a storm surge and inundation forecasting system for the Chesapeake Bay. The

forecasting system adopted the unstructured grid strategy and made model calculation over a large domain with a very high grid resolution near the coast and inside the Chesapeake Bay. This approach will allow us to set up an early warning system before Hurricane makes landing and ease to specify open boundary for forecasting. At the same time, the high-resolution unstructured grid, aided by incorporation of LiDAR data, will greatly enhance the accuracy of inundation simulation in the Chesapeake Bay.

1.2 Science context of this study

The storm surge and associated inundation can cause severe loss of life and immense damage to the property in coastal areas, which is usually due to lack of warning and insufficient preparedness. Hurricane Katrina of the 2005 Atlantic hurricane season, which is the most recent example showing the severe hazard of storm surges, caused at least 1,836 people to lose their lives in the Gulf of Mexico area and the storm is estimated to have been responsible for $81.2 billion (2005 USD, wikipedia.org) in damage, making it the costliest tropical cyclone in U.S. history. Much of this loss was due to the storm surge (wikipedia.org). The Chesapeake Bay area is also a large, low-lying coastal area that is vulnerable to inundation during a storm surge caused by either a hurricane or nor' easter. Hurricane Isabel of the 2003 Atlantic hurricane season caused about 17 deaths, damage to 4000 homes along the Chesapeake Bay area, and total damage of about $3.6 billion (2003 USD, wikipedia.org). The lower Chesapeake Bay, including the Hampton Roads and Virginia Beach areas, was the most damaged area during Hurricane Isabel. According to U.S. Census data, more than 16 million people live in the Chesapeake Bay watershed and this population continues to grow. Factoring in the anticipated sea-level rise, continuing coastal development, and potential increases in the frequency and severity of storms

possibly related to global warming, the people of the Chesapeake Bay region and their property are facing ever increasing risks. To reduce the economic and environmental impacts of future storms on the Chesapeake Bay area, a sufficient accurate storm surge and inundation prediction model is highly desirable. However, such a model is still lacking due to following reasons: (1) insufficient resolution and accuracies in the meteorological forecasting fields; (2) inadequate resolution and accuracy of the topographic and bathymetric data; (3) difficulties in obtaining the open boundary condition during the storm condition; (4) insufficient computational power for setting up a high resolution grid over a large domain simultaneously. These problems are expected to be partially solved by the employment of the following developments in this study:

(1) A powerful computing system was employed in the storm surge simulation. Thanks to the advance of the computer technology, a heterogeneous cluster computing system named SciClone at College of William and Mary has been used in this study. Specifically, a subcluster named Typhoon, which has 72 dual-processors, dual-core servers, was employed. It has supplied enough computational power for calibrating and running the storm surge model. At the same time, a computationally efficient numerical model named Eulerian-Lagrangian Circulation (ELCIRC) is employed to set up the storm surge model in order to get the best computational speed for prediction purposes. Previous study (Wang et al., 2005) has proved the capability of this model for simulating the storm surge. In the future, the parallel computing technology will be employed as well for more powerful computing capability.

(2) Model grid resolution is vital in a numerical model to predict surge and inundation accurately in low-lying coastal areas (Shen et al., 2006c). The structured grid that has been widely used in the previous studies is not able to resolve the complex coastline and low-lying coastal areas at a high resolution while still covering a large domain, since it cannot freely change spatial

resolution in a given grid. In contrast to the structured grid, the unstructured grid could have a high resolution in coastal areas and relatively low resolution in the open ocean at the same time. Some unstructured grid models using a finite difference scheme have been developed previously, but the problem with those models is that they are usually restricted by the CFL condition when increasing the grid resolution. In this study, the ELCIRC model, with the employment of the semi-implicit and Eulerian-Lagrangian schemes, is less restricted by the stability condition, which means that a large time step can be used. Thus, a high-resolution grid can be employed without much decrease in computational speed compared to other unstructured grid models.

(3) Without accurate topographic data, a high-resolution grid is not quite useful to predict the inundation accurately. Fortunately, the high-resolution Light Detection and Ranging (LiDAR) topographic data is now available. This LiDAR technology is a state-of-the-art technology that can measure the land topography at a horizontal resolution of 1 meter. With the employment of LiDAR topographic data in the Hampton Roads and Virginia Beach areas, our high-resolution grid can generate an accurate inundation prediction. Despite the use of powerful computer resource and an efficient numerical model, questions as to whether the model could run with such a high-resolution grid quickly and stably enough and how much the LiDAR data could help improve the prediction quality of inundation in the lower Bay area were uncertain before this study. This study proved that the model could be set up with the high-resolution grid and could simulate storm surge and inundation efficiently and that the LiDAR data is quite necessary for the inundation simulation.

(4) To solve the problem of specifying the open boundary condition for the model, a large domain grid covering an area much larger than the size of the storm system is used. With this large domain, the open boundary condition of our model would be negligibly impacted by storm

systems like the hurricane or nor' easter, so it could be simply specified as the tide boundary only. However, it is not proper to only specify the tide boundary condition for the limited domain high-resolution grid for the lower Bay when using the model for predicting the inundation, since the boundary is influenced by the storm systems. Thus the limited domain grid and the large domain grid are coupled together. After the large domain execution completes, the output of this large domain model is used for specifying the open boundary condition of the limited domain. The question about how large is large enough for a domain, and if it is possible to simulate hydrodynamic process accurately with such a large domain is an open question. It was not answered until the model was set up and several test runs were conducted. Compromise was also made with an acceptable computational speed. Instead of using only one grid with both the large domain and high resolution in the lower Bay, two grids, namely a very large domain grid and a limited domain grid, were used in conjunction with a coupling process. In fact, there are several considerations about it. They are: (a) If the two grids were combined together, the size of the new grid would be too large and the computational speed would diminish. Since this model is set up for prediction purposes in the future, the computational speed is a key issue. To get better speed, the grids are separately generated. (b) The expansibility of this prediction model system is considered for the future research. Now the inundation prediction is only set up for the lower bay area, but in the future, other areas will be included as well, like the low lying areas in the middle and upper Bay and possibly even the areas along the Atlantic coastline. If now only one grid is used, then every time a new area needs to be included, the grid needs to be regenerated and calibrated again. That is not an efficient way since the expansibility is awkward. Instead of using this way, the large domain grid will be kept unchanged, but every time a new small domain grid will be generated to cover the new area of interest with high-resolution and LiDAR topographic

data input. Hence, in the future, the prediction model system would be set up with one large domain grid and several small domain grids with high resolution for different areas coupled together. With the power of parallel computing, the model could run with these grids at the same time. Each small domain grid could get its own boundary condition from the same large domain grid as soon as the large domain model output becomes available. With this approach, the computing speed will not be decreased much while more high-resolution areas are included.
(5) To solve the problem of the uncertainty of meteorological modeling, the ensemble technology was employed in this study. Our hydrodynamic model was coupled with different atmospheric models to run the ensemble simulations in order to get a range of the predicted water elevation. Each type of wind from different atmospheric models was compared with the observations. The most reliable wind we found is the WRF-GFS wind. It is proved that the observed water elevation fell into the envelope of water elevation generated with different winds. This thesis will discuss all the details of processes and approaches that have been used to set up the model and solve the existing problems.

During the setting up of the large domain model, it was found that the Ekman transport plays a very important role in the exchange of flux across the Chesapeake Bay mouth during storm surge events. Taking Hurricane Isabel as an example, without the Coriolis force, the water elevation in the Bay was underestimated before the storm surge peak. In fact, during this period, north and northeast wind was blowing over the continental shelf near the Chesapeake Bay. Since the Ekman transport in the Northern Hemisphere is perpendicular to the wind direction and to the right-hand side, under normal conditions, the wind will transport the water into the Bay. Thus, without the Coriolis force, not enough water was transported into the Bay and the water elevation

before the storm surge peak was underestimated. Similarly, the water elevation was overestimated after the peak without the Coriolis force since the southeast and south wind was blowing. This thesis will discuss the importance of Ekman transport in modeling storm surge and the necessity of setting up a 3-dimensional model.

1.3 Objectives and outline

The primary goal of this study is to develop a storm surge and inundation forecast model system by employing a coupled large domain, high-resolution grid, and linking with atmospheric models in the Chesapeake Bay area. The specific objectives of the proposed project are:

1. To create a large domain orthogonal unstructured grid that covers the Atlantic Coast from Nova Scotia to Florida.
2. To generate a high-resolution grid covering the Virginia Beach and Hampton Roads area with interpolation of LiDAR data for simulating the inundation.
3. To set up this model system by nesting the two grids with the computationally efficient model ELCIRC and to calibrate it by adjusting parameters.
4. To employ wind data from different atomspheric models, to simulate two cases of storm surge, including the storm surges caused by (1) Hurricane Isabel and (2) Tropical Storm Ernesto, and to compare with observation data to examine the prediction capability of the atmospheric model and our hydrodynamic large domain model.
5. To simulate and visualize the inundation for the Virginia Beach and Hampton Roads areas with the high-resolution grid using the output from the large domain model as the boundary condition.

The outline of this thesis is as follows:

In Chapter 2, the atmospheric models generating the wind and pressure fields are described. A detailed description of the hydrodynamic model ELCIRC, including the governing equations, treatment of bottom and surface boundary conditions, and the parameterization of eddy viscosity, Coriolis force, and tidal potential, is given. The model set up, including grid generation and tide calibration, are described in this chapter as well.

In Chapter 3, the storm surge and inundation simulation for two scenarios, Hurricane Isabel and Tropical Storm Ernesto, are discussed. Description for each storm, wind and pressure comparison, storm surge, and inundation results are introduced in this chapter.

In Chapter 4, discussions about the uncertainty of the ensemble runs are given. Several numerical experiments were carried out to examine the influence of Ekman transport, the open boundary condition of the limited domain model and accuracy of the topographic data on the storm surge and inundation simulations.

The conclusions and discussions of this whole study are given in Chapter 5.

Appendix A gives the definition of statistic measures

Appendix B gives the category of the hurricane strength

Chapter 2. Description of atmospheric model products and storm surge hydrodynamic model

2.1 Description of atmospheric models

The wind and pressure fields are key elements for simulating the storm surge but are difficult to predict in coastal areas. Because the Chesapeake Bay topography is complex and large contrasts in wind speeds are observed between land and water surfaces, the currently operational model from the NOAA National Centers for Environmental Prediction (NCEP), which has a horizontal resolution of 12 km, is inadequate for resolving detailed wind fields over the Chesapeake Bay and its tributaries. Therefore, a high-resolution atmospheric model is required to provide detailed surface winds. In this project, two high-resolution atmospheric models, Weather Research and Forecasting (WRF) Model and Regional Atmospheric Modeling System (RAMS), are employed.

The NWS at Wakefield, VA (AKQ) operates a high-resolution WRF model, which is a complete numerical weather prediction system tailored for a workstation for a specified local modeling domain. The Weather Research and Forecasting (WRF) Model is a next-generation mesoscale numerical weather prediction system designed to serve both operational forecasting and atmospheric research needs. It features multiple dynamical cores, a 3-dimensional variational (3DVAR) data assimilation system, and a software architecture allowing for computational parallelism and system extensibility. WRF is suitable for a broad spectrum of applications across

spatial scales ranging from meters to thousands of kilometers. AKQ has configured this model to run at approximately a 4-km horizontal resolution, using either the NCEP non-hydrostatic mesoscale model core (NMM) or the advance weather research core (ARW) developed by the National Center for Atmospheric Research. This model is state-of-the-art with configurable parameters and the resolution to provide the best forecast for the Chesapeake Bay. The local WRF will use the NMM core at 4-km resolution. This grid allows the model to run with explicit convection. Consequently, the model is able to produce detailed banding structures in tropical systems and wind field changes at fine scales.

The RAMS is a high-resolution numerical model that has been run operationally at Weatherflow for over 3 years and is a well-established, mesoscale model. RAMS was developed at Colorado State University and uses a different numerical core and physics package from WRF. In this study, RAMS is run using 3 grids and the highest one is at 2-km resolution (versus 4-km resolution for WRF), so this grid may resolve additional mesoscale features of the winds in the Chesapeake Bay region.

Ensemble forecasting of weather, including winds, has been shown to improve forecasts and provides a means of conveying uncertainty. Therefore, a multi-model (WRF and RAMS), multi-boundary conditions approach will be used to obtain a series of wind fields with increasing resolution. The tandem use of WRF and RAMS will provide a range of potential wind fields. An ensemble forecast is a collection of two or more forecasts predicting at the same time. For the wind part, NWS will run WRF within a 6-hr forecast cycle for a 7-to-14-day period for each case. The WRF model will use the Global Forecast System (GFS) and North American Mesoscale

model (NAM) as initial and boundary conditions. In addition, the NAM (12-km) and GFS (~32-km) also will provide two more independent wind fields (in coarse grid). Thus, NWS will generate four wind fields, including GFS, NAM, WRF-GFS and WRF-NAM. At the same time the Weatherflow Inc will run RAMS using three grids with different domain size and resolution (Grid1, Grid2 and Grid3). Grid1 has the lowest resolution (~24-km) and largest domain size (66.062° W to 94.787° W and 23.940° N to 45.754° N) ; Grid2 has the medium resolution (8-km) and domain size (68.740° W to 75.580° W and 34.466° N to 40.802° N); Grid3 has the highest resolution (2-km) and smallest domain size (74.948° W to 77.504° W and 36.436° N to 39.586° N). So a total ensemble of seven surface wind and pressure (atmospheric) fields are created. This ensemble approach frequently is used in meteorological forecasts and has been shown to produce more accurate forecasts than individual model runs. The seven-field atmospheric ensemble will drive our storm surge model, creating a 6-hr 7-ensemble forecast of storm surge in the Chesapeake Bay and its tidal tributaries.

2.2 Description of ELCIRC model

In order to simulate storm surge in a large modeling domain with high-resolution grids in the nearshore, a computationally efficient numerical model is required. For this reason, ELCIRC, which has the advantage of allowing large time step without severely restricted by CFL condition, is used to simulate the storm surge and inundation in the Chesapeake Bay. The numerical model ELCIRC, originally developed by Zhang et al. (2004), uses an orthogonal, unstructured grid with mixed triangular and quadrilateral grids in the horizontal and the z-coordinate in the vertical. The model is capable of simulating both two-dimensional and three-dimensional hydrodynamics and transport processes. When using one vertical layer, the formulation of the model automatically

reduces to the 2D depth-integrated version. The governing equations were discretized according to a semi-implicit scheme. The barotropic pressure gradient in the momentum equation and the flux term in the continuity equation are treated semi-implicitly, with implicitness factor $0.5 \le \theta \le 1$; the vertical viscosity term and the bottom boundary condition for the momentum equations are treated fully implicitly; and all other terms are treated explicitly. This ensures both stability (Casulli and Cattani, 1994) and computational efficiency. Different from the traditional treatment of advection terms using explicit schemes, this model employs the Eulerian-Lagrangian scheme to treat the advection terms so that it will not be severely restricted by the CFL condition. In fact, with the use of the semi-implicit and Eulerian Lagrangian schemes, this model can simulate storm surge using a high-resolution grid over a large domain while still maintaining a relatively large time step. This model also employed a robust wetting-and-drying algorithm so that the inundation process can be well simulated. The ELCIRC model has been successfully used for simulation of hurricane-induced storm surge in a previous study (Wang et al., 2005).

2.2.1 Governing equations

The ELCIRC model solves for the free surface elevation, 3D water velocity, salinity, and temperature, with its formulation from a set of six hydrostatic equations based on the Boussinesq approximation, which represent mass conservation (in both 3D and depth-integrated forms), momentum conservation, and conservation of salt and heat:

$$\frac{\partial u}{\partial x}+\frac{\partial v}{\partial y}+\frac{\partial w}{\partial z}=0$$

$$\frac{\partial \eta}{\partial t} + \frac{\partial}{\partial x}\int_{H_R-h}^{H_R+\eta} u dz + \frac{\partial}{\partial y}\int_{H_R-h}^{H_R+\eta} v dz = 0$$

$$\frac{Du}{Dt} = fv - \frac{\partial}{\partial x}\left\{ g(\eta - \alpha\hat{\psi}) + \frac{P_a}{\rho_0} \right\} - \frac{g}{\rho_0}\int_z^{H_R+\eta} \frac{\partial \rho}{\partial x} dz + \frac{\partial}{\partial z}\left(K_{mv} \frac{\partial u}{\partial z} \right) + F_{mx}$$

$$\frac{Dv}{Dt} = -fu - \frac{\partial}{\partial y}\left\{ g(\eta - \alpha\hat{\psi}) + \frac{P_a}{\rho_0} \right\} - \frac{g}{\rho_0}\int_z^{H_R+\eta} \frac{\partial \rho}{\partial y} dz + \frac{\partial}{\partial z}\left(K_{mv} \frac{\partial u}{\partial z} \right) + F_{my}$$

$$\frac{DS}{Dt} = \frac{\partial}{\partial z}\left(K_{sv} \frac{\partial S}{\partial z} \right) + F_s$$

$$\frac{DT}{Dt} = \frac{\partial}{\partial z}\left(K_{hv} \frac{\partial T}{\partial z} \right) + \frac{Q}{\rho_0 C_p} + F_h$$

where

(x, y)	horizontal Cartesian coordinates, (m)
(ϕ, λ)	latitude and longitude
z	vertical coordinate, positive upward, (m)
t	time, (s)
H_R	z-coordinate at reference level (geoid or mean sea level (MSL))
$\eta(x, y, t)$	free-surface elevation, (m)
$h(x, y)$	bathymetric depth, (m)
$\vec{u}(\vec{x}, t)$	water velocity at $\vec{x}=(x, y, z)$, with Cartesian components (u, v, w), (ms^{-1})
f	Coriolis factor, (s^{-1})
g	acceleration of gravity, (ms^{-2})
$\psi(\phi, \lambda)$	tidal potential, (m)

α effective Earth elasticity factor (≈ 0.69)

$\rho(\vec{x},t)$ water density; by default, reference value ρ_0 is set as 1025 kgm^{-3}

$P_a(x,y,t)$ atmospheric pressure at the free surface,(Nm^{-2})

S, T salinity and temperature of the water, (practical salinity units (psu), $^{\circ}C$)

K_{mv} vertical eddy viscosity, ($m^2 s^{-1}$)

K_{sv}, K_{hv} vertical eddy diffusivity, for salt and heat, ($m^2 s^{-1}$)

$F_{mx}, F_{my}; F_s; F_h$ horizontal diffusion for momentum and transport equations

$Q(\phi,\lambda,z,t)$ rate of absorption of solar radiation(Wm^{-2})

C_p specific heat of water ($Jkg^{-1}K^{-1}$)

Our storm surge model is set up as a barotropic model, so the last two equations for the conservation of salinity and temperature are not solved. In fact, the salinity and temperature are set as constant values. From scale analysis, it is found that the horizontal diffusion F_{mx} and F_{my} in the momentum equations are much smaller than the vertical diffusion. In practice, horizontal diffusion is negligible for storm surge simulation, so F_{mx} and F_{my} are set to 0 in our model. The formula for calculating Coriolis factors and tidal potential $\psi(\phi,\lambda)$ were given in Section 2.2.5. It is not only the ocean that responds to tidal forcing; the solid Earth does as well. Since the Earth under the tidal forcing also deforms, the tidal potential need to be adjusted in order to consider the influence of Earth deformation. The effective Earth elasticity factor α is widely used in numerical modeling of ocean tide for adjusting the tidal potential and it is set to 0.69 in our model.

To make these equations attain closure, an equation of state is also used in the model:

$$\rho(S,T,p) = \frac{\rho(S,T,0)}{[1-10^5 p / K(S,T,p)}$$

where $\rho(S,T,p)$ (kg/m^3) is the density at one standard atmosphere, and K(S,T,p) is the secant bulk modulus. In this research, the baroclinic effect has not been taken into account, so the density ρ is set as a constant value.

2.2.2 Vertical boundary conditions

At the sea surface, this model enforces the balance between the internal Reynolds stress and the applied shear stress, i.e.

$$\rho_0 K_{mv}\left(\frac{\partial u}{\partial z}, \frac{\partial v}{\partial z}\right) = (\tau_{Wx}, \tau_{Wy}) \text{ at } z = H_R + \eta$$

In our model the surface stresses is calculated as:

$$(\tau_{Wx}, \tau_{Wy}) = \rho_a C_{Ds} \left|\vec{W}\right| (W_x, W_y)$$

where, ρ_a is the air density (kg/m^3) , C_{Ds} is the wind drag coefficient, $\vec{W}(x,y,t)$ is the wind velocity at 10 m above the sea surface, with magnitude $\left|\vec{W}\right|$ and components in east-west W_x and north-south W_y (m/s) .

Wind drag coefficient C_{Ds} is calculated using Large and Pond's (1981) formulation, which is:

$$C_{Ds} = 10^{-3}\left(0.49 + 0.065\left|\vec{W}\right|\right) \qquad \text{if } 4\text{m/s} \le \left|\vec{W}\right| \le 33\text{m/s}$$

$$C_{Ds} = 0.75 \times 10^{-3} \qquad \text{if } \left|\vec{W}\right| \le 4m/s$$

$$C_{Ds} = 2.64 \times 10^{-3} \qquad \text{if } \left|\vec{W}\right| \ge 33m/s$$

C_{Ds} hold constant outside the range. The lower limit of the formula, 4 m/s, is based on Donelan (2004); the upper limit of the formula, 33 m/s, is based on Powell (2003) using real measurements during the hurricane. For moderately strong winds, this formula allows the efficiency of the air–ocean transfer of momentum to increase with increasing wind speed.

As is customary, this model enforces at the sea bottom the balance between the internal Reynolds stress and the bottom frictional stress, i.e.

$$\rho_0 K_{mv}\left(\frac{\partial u}{\partial z}, \frac{\partial v}{\partial z}\right)_b = (\tau_{bx}, \tau_{by}) \text{ at } z = H_R - h$$

where the bottom stress is defined as:

$$(\tau_{bx}, \tau_{by}) = \rho_a C_{Db} \sqrt{u_b^2 + v_b^2}\,(u_b, v_b)$$

The bottom drag coefficient C_{Db} is typically variable in space, and might also vary at various temporal scales (e.g., through current–wave interactions or long-term changes in bottom texture). Site-specific calibration is often required.

In our model the C_{Db} is calculated based on the modified Manning's formula, which is:

$$C_{Db} = \frac{gn^2}{\Delta z^{1/3}} - \beta U_b$$

$$0.001 < C_{Db} < 0.003$$

where g is the gravity acceleration (m/s^2), n is the Manning coefficient, Δz is the thickness of bottom layer, β is a coefficient for correcting the current effect on bottom friction, U_b is the magnitude of bottom current velocity. The Manning's formula in its original form does not depend on bottom current velocity. The modification we made taking current effect into account is based on Spitz and Klinck (1998). Future modification of Manning coefficient during inundation may be needed due to different characteristics of surface roughness, such as the effect of submerged aquatic vegetable, permeable versus impermeable. However, these effects have not been taken into account. The Manning coefficient used now is a constant value throughout the entire domain, but in the future variable values will be used for different areas.

2.2.3 Wetting and drying scheme

ELCIRC uses the approach of Casulli and Cheng (1992) and of Casulli and Zanolli (1998) for the wetting-and-drying simulation. The scheme is a natural and robust handling of the wetting-and-drying formulation with primarily careful bookkeeping of indices. After all unknowns have been found for time step n+1, the free-surface indices are updated with the newly computed elevations. Elements are dried if $h_t + \eta < h_0$ (a small positive number h_0 is used in the code in lieu of zero in order to avoid underflow), otherwise the elements are wet.

2.2.4 Parameterization of turbulent vertical mixing

Since the storm surge model is developed as a quasi-3D model, the vertical eddy viscosity at each layer needs to be specified properly. However, parameterization of turbulent vertical mixing is still an open question in coastal modeling. There are multiple options in the use of the ELCIRC Model, including a zero-equation model and multiple two-and-a-half equation models. The two-and-a half equation turbulence closure schemes, like Mellor &Yamada, kinetic energy and mixing length, have been tested in this study but no satisfactory results were obtained. A possible explanation of this is that the resolution of our vertical grid is not high enough to get accurate results with these closure schemes. In fact, our model is using a z-grid and the vertical grid resolution in the Bay and coastal area is only 5 meters in the surface layers, so some shallow areas have only 1 to 2 layers, which is insufficient to obtain accurate eddy viscosity using turbulence closure schemes. To use these schemes, more vertical layers need to be included. This will decrease the computational speed and thus is not a good option for a prediction model. At the same time, these schemes are highly dependent on the baroclinic mode, which means the model needs to simulate the salinity and temperature in order to get the correct density distribution. This will make this model more complicated and it is beyond the scope of this study. Generally, without enough measurement data, it is hard to set up the initial conditions of temperature and salinity for the entire large domain and the open boundary conditions for every time step. The baroclinic mode will slow down the computational speed significantly. Considering the difficulty of specifying the boundary condition and computational speed, a baroclinic model was not used. Therefore, rather than using the two-and-a-half equation turbulent scheme, a semi-empirical formulation combining current dependent eddy viscosity with wind wave-dependent eddy viscosity, (Davies, 1997), was shown to generate reasonable

results. The formulation of wind wave-dependent eddy viscosity was based on Dobroklonsky, (1947) and Ichiye (1967).

The formulae are shown here:

$$K_z = K_0 + 0.0025h|U| + 0.028\frac{H^2}{T}e^{-2\pi\frac{z}{L}} \qquad \text{h} \le 200\text{m}$$

$$K_z = K_0 + 0.0025|U|^2 + 2.84\times10^{-5}\times\frac{|W|^3}{g}e^{-2\pi\frac{z}{L}} \qquad \text{h}>200\text{m}$$

where K_z is the eddy viscosity at vertical layer z with units m^2/s. K_0 is a background eddy viscosity that is set to $0.0005\,m^2/s$, h is the water depth in meter, $|U|$ is the mean current in m/s for the whole layer; H is the significant wave height in meters, T is the average wave period in seconds, z is the depth of the layer in meters, and L is the wave length in meter; $|W|$ is the wind magnitude in m/s; Here the formulae for shallow water areas (depths less than 200 m) and deep ocean areas (depths more than 200 m) are different. For the shallow water areas, $0.0025h|U|$ is the eddy viscosity generated by current and $0.028\frac{H^2}{T}e^{-2\pi\frac{z}{L}}$ is the wave-generated eddy viscosity. For the deep ocean areas, $0.0025|U|^2$ is the eddy viscosity generated by current and $2.84\times10^{-5}\times\frac{|W|^3}{g}e^{-2\pi\frac{z}{L}}$ is the wave generated eddy viscosity. For the current generated eddy viscosity, $0.0025h|U|$ has been widely used in shallow water modeling, so it was employed in our model when water depth is less than 200 m. However, the eddy viscosity calculated by $0.0025h|U|$ is too large when water depth increases. In terms of Davies (1997)'s paper,

$0.0025|U|^2$ was employed in our model when water depth is larger than 200 m and reasonable eddy viscosity was obtained. For the wave generated eddy viscosity, $2.84\times10^{-5}\times\frac{|W|^3}{g}e^{-2\pi\frac{z}{L}}$ has been widely used in open ocean areas, but in the shallow water area, especially in the Bay, $0.028\frac{H^2}{T}e^{-2\pi\frac{z}{L}}$ was employed in order to get better results.

Generally, H is calculated by:

$$H = 2.12\times10^{-2}\times|W|^2$$

T is calculated by:

$$T = 0.81\frac{2\pi|W|}{g}$$

However, in the Bay the wave height is not only dependent on the wind speed, but also dependent on the direction. Based on the statistics of NWS, (http://www.erh.noaa.gov/lwx/marine/wind_waves.html), the wave height is calculated in 8 directions separately:

North wind: $H = 0.0928\times|W|+0.2608$ (Figure 2.1)

Northeast wind: $H = 0.0889\times|W|+0.0339$ (Figure 2.2)

East wind: $H = 0.0731\times|W|+0.0914$ (Figure 2.3)

Southeast wind: $H = 0.0889 \times |W| + 0.0339$ (Figure 2.4)

South wind: $H = 0.0928 \times |W| + 0.2608$ (Figure 2.5)

Southwest wind: $H = 0.0889 \times |W| + 0.0339$ (Figure 2.6)

West wind: $H = 0.0731 \times |W| + 0.0914$ (Figure 2.7)

Northwest wind: $H = 0.0691 \times |W| + 0.1693$ (Figure 2.8)

Based on the regression of the wind and wave observation during Hurricane Isabel, the wave period is calculated by:

T =3.28(s) W<15m/s

and

T=$0.1315|W|+1.2713$ (s) (Figure 2.9) $W \geq 15$ m/s

L is calculated by :

$$L = \frac{gT^2}{2\pi}\sqrt{\tanh\left(\frac{4\pi^2}{T^2}\frac{h}{g}\right)}$$

2.2.5 Coriolis force and tidal potential

For the large domain, the Coriolis factor is set as variable and it varies with the latitude. The Coriolis factor, f, is a well-known function of latitude, ϕ:

$f(\phi) = 2\Omega \sin\phi$

where $\Omega = 7.29 \times 10^{-5} rads^{-1}$ is the angular velocity of rotation of the earth.

The tidal potential used for simulating the large-scale tide, is defined as:

$$\hat{\psi}(\phi,\lambda,t) = \sum_{n,j} C_{jn} f_{jn}(t_0) L_j(\phi) \cos\left[\frac{2\pi(t-t_0)}{T_{jn}} + j\lambda + v_{jn}(t_0)\right]$$

where

C_{jn} constants characterizing the amplitude of tidal constituent n of species j (j=0, declinational; j=1, diurnal;j=2, semi-diurnal), (m)

t_0 reference time

$f_{jn}(t_0)$ nodal factors

$v_{jn}(t_0)$ astronomical arguments, (r)

$L_j(\phi)$ species-specific coefficients ($L_0 = \sin^2\phi; L_1 = \sin(2\phi); L_2 = \cos^2\phi$)

T_{jn} period of constituent n of species j

For the small model domain, the f plane approximation was used and the Coriolis factor, f, is assumed to be locally constant centered at latitude 37° N.

2.3 Grid generation

2.3.1 Grid generation and LiDAR data

In this study, two separate grids have been generated. One is the large domain grid for the storm surge prediction purpose covering the Atlantic Ocean from Nova Scotia to Florida; the other is the small, limited domain grid covering the land parts in the Hampton Roads and Virginia Beach areas for the inundation prediction purpose. Adequacy of the grid resolution is one of the key issues for accurately predicting nearshore storm surge and inundation along the coast and inside the Bay. Numerical studies show that storm surge modeling requires a much higher grid resolution than normal tide simulation due to the spatially varying wind forcing function that interacts with the geometric complexities of land boundaries and near coastal bathymetry (Westerink et al., 1992). Thus, both of the grids are generated with high resolution in the nearshore area and the small domain one has even higher resolution, as high as 50 meters in shallow water areas and for low-lying land. The domain size of a model is also an important issue for storm surge simulation since hurricanes and northeasters are large-scale phenomena. Blain et al. (1994) found that a small domain is inadequate for storm surge simulation because cross-shelf boundary conditions are in the regions of significant storm surge generation. As such, a large domain (with an area extending beyond the scale of the storm) is needed in order to specify the proper open boundary condition and more realistically capture the physics associated with storm surge generation and propagation. That is why the large domain grid is generated. Because it is very difficult for a structured or curvilinear grid to have a very fine grid nearshore and also to cover a large modeling domain, an unstructured grid was used to resolve the complex coastline of the Chesapeake Bay and cover the large domain Atlantic Coast from Nova Scotia to Florida. In our model, coarser grid cells are used in the deep ocean while significant refinement is performed near the coastline and inside the Bay. The large domain grid used is shown in Figure 2.11. The large domain grid has a total of 165,015 cells and 92,212 nodes. As discussed

by Casulli and Zanolli (1998), orthogonality is, in a strict sense, a requirement for calculation of finite difference approximations of spatial gradients in unstructured grids. This requirement might in practice be relaxed, but the accuracy of solutions suffers from deviations from orthogonality. While second-order accuracy can be achieved with uniform structured or unstructured orthogonal grids, only first-order accuracy is attainable with non-uniform orthogonal grids. For general non-orthogonal grids, the line connecting the two element centroids is not perpendicular to the common side, which is an additional source of errors. To ensure the accuracy of model calculations, the orthogonality of our grids are checked in JANET (an acronym for JAva NET generator) software before the model is executed.

The small, limited domain grid for the Chesapeake Bay area with especially high resolution in the lower Bay area was generated for the simulation of inundation (Figure 2.10 and Figure 2.12). The small, limited domain grid has 218,553 cells and 116,504 nodes. The high- resolution grid needs a high-resolution bathymetric and topographic data set. To ensure that the model domain in the lower Bay has correct and accurate prediction capability for inundation for Virginia Beach, a high-resolution bathymetric and topographic data set from LiDAR data is employed. LiDAR is a technology that uses laser pulses to determine the distance to an object or surface. In fact, the distance to an object is determined by measuring the time delay between transmission of a pulse and detection of the reflected signal. This could be applied to the measurement of topography on land with a one-meter-by-one-meter horizontaal resolution. The LiDAR data we used was remapped to 10m-by-10m because the database for 1 m-by-1 m data was too large and the resolution of our grid, which is in 50 m to 100 m, does not require 1 m-by-1 m bathymetric data. LiDAR data has been mapped into the high-resolution Hampton Roads and Virginia Beach grid

in the lower Bay. With the combination of the high-resolution unstructured grid and LiDAR data for representing inter-tidal zone, the model is capable of simulating the inundation process that occurs near the low-lying shoreline during hurricane and northeaster events.

In order to generate the grid, the coastline is obtained from the coastline extractor website: http://rimmer.ngdc.noaa.gov/. The coastline data is then transformed to shape file format by a script, which is from the NOAA website as well. The grids are then generated by the commercial program JANET, using the shapefile of the coastline. This grid generator is designed to generate ELCIRC conforming grids by Delaunay triangulation. JANET provides a number of powerful tools that help in generating an orthogonal grid. For example, JANET permits the modeler to redistribute the nodes on the boundary polygons to control the element sizes. It allows restriction of maximum permissible inside angles, which help generate triangles with acute angles. It allows isolating certain areas within the grid for which separate refinement or coarsening criteria can be applied. If the grid is too big, JANET also permits splitting the grid into several submeshes and dealing with these submeshes separately and then merging them together. This property of the grid generator allows the modeler to efficiently generate the grid with the desired quality. Another important property of JANET is that it can check and optimize the orthogonality of the grid automatically, which is very useful in maintaining the orthogonality.

After the grid is generated, the bathymetric and topographic data is mapped into the grid using a bilinear interpolation scheme. The dataset we are using is shown in Table 2.1. For the open ocean, the Global Relief Model (ETOPO2) in 2-arc-min (about 3.6-km) resolution is employed; for the coastal area and the Bay, the Coastal Relief Model in 3-arc-sec (about 90-m) horizontal

resolution and 0.1 m vertical resolution is used; and for the land part of the lower Bay, the high resolution LiDAR data in 10-meter resolution is used. It is well-known that the change in water level depends on the change in volume and the volume is the product of cross section and depth. Considering the cross section usually has the uncertainty on the order of tens of meters but the error of the bathymetry (depth) is usually on the scale of meter, we can learn that the error of the volume is mostly from the uncertainty of the cross section other than depth. Therefore, the water level will not very sensitive to the uncertainty of the bathymetry (depth).

2.3.2 Large domain projection

The longitude/latitude coordinate system is a spherical coordinate system since our earth is a sphere, but the governing equation of ELCIRC model mentioned earlier is in Cartesian coordinates. To do the calculation in the ELCIRC model, either the governing equation need to be modified from the Cartesian coordinate system to a spherical coordinate system, or the grids need to be generated in the Cartesian coordinate system instead of longitude/latitude. The latter method is chosen since it is more straightforward, but first a Cartesian coordinate system that could accurately represent the locations over our entire domain need to be selected. The Universal Transverse Mercator (UTM) coordinate system is employed in this study. The UTM coordinate system is a grid-based method of specifying locations on the surface of the Earth. The UTM system divides the surface of the Earth between 80° S latitude and 84° N latitude into 60 zones, each 6° of longitude in width and centered over a meridian of longitude. Zones are numbered from 1 to 60. Zone 1 is bounded by longitude 180° to 174° W and is centered on the 177th West meridian. Zone numbering increases in an easterly direction. Each of the 60 longitude zones in the UTM system is based on a transverse Mercator projection, which is

capable of mapping a region of large north-south extent with a low amount of distortion. Our grid covered the area from 23° to 46°N and from -82° to -60° W. The distortion with this projection is small, about 7.5m/km in the south and 16m/km in the north, which is much smaller than the grid resolution (~ 2000 m) in these areas. When the grid is generated, the shoreline in longitude/latitude is first projected to the UTM coordinate system and then the grid is generated in the UTM system. After the grid is generated, wind and pressure forces from the atmospheric model using other projections could be projected to our UTM system as well, so that the wind could be interpolated into our grid.

2.4 Tidal calibration

Storm tide is a combination of the astronomical tide and the surge caused by the strong wind during the storm. To make the model simulate the storm tide correctly, the tide needs to be calibrated beforehand. To calibrate the tide, the open boundary of our model is specified using harmonic constituents. The water elevation at each node of the open boundary is calculated by the following formula:

$$h(t) = MSL + \sum_j f_j H_j \cos \sigma_j t + (V_0 + u)_j - g_j)$$

where h(t) = height of the tide at the time t

MSL = mean sea level

f_j = nodal factor for constituent j

H_j = amplitude to constituent j

σ_j = frequency for constituent j

$(V_0 + u)_j$ = phase by time t = 0

g_j = phase lag of the equilibrium tide at Greenwich

The model is executed without wind forcing for 35 days. The first 5 days of running is to spin-up the model and then the tidal results of the following 30 days are analyzed by harmonic analysis, so that the harmonic constituents at each tide gauge station are calculated. The observed harmonic constituents at each station could be directly obtained from the NOAA current and tide website (http://co-ops.nos.noaa.gov/). For the large domain model, 19 tidal gage stations (Figures 2.13 and 2.14) are selected along the Atlantic Coast and in the Chesapeake Bay for the tide calibration. For the small domain model, 11 stations (Figure 2.13) are selected in the Chesapeake Bay. The tidal amplitude of each harmonic constituent from both NOAA observations and our model simulation are compared.

The large domain model was set up in a quasi-3-dimensional mode without salinity and surface wind forcing. It was driven by 13 harmonic constituents at the open boundary, which are M_2, S_2, N_2, K_1, K_2, O_1, Q_1, L_2, MU_2, NU_2, P_1, T_2, and $2N_2$ derived from the U.S Army East Coast 2001 database of tidal constituents (Mukai et al., 2002).

For the large domain, 19 tidal stations are included in this calibration, including 11 stations (Figure 2.13) in the Bay and 8 stations (Figure 2.14) along the Atlantic coastline. The amplitude of the harmonic constituents of the modeled results is calculated by least-squares harmonic analysis. The amplitude of the harmonic constituents of the observed tide at each tidal station

was obtained from http://co-ops.nos.noaa.gov/ directly. Comparison of amplitudes between the model results and NOAA data are shown in Table 2.2 for the tidal stations along the Atlantic coastline and Table 2.3 for the tidal stations in the Chesapeake Bay, respectively. Here only the major tidal constituents of M_2, S_2, N_2, K_1, O_1 and Q_1 are compared. As it can be seen in Table 2.2, the model simulates the dominant tidal constituent (M_2 tide) along the Atlantic Coast quite well. For the M_2 tide, the difference between the modeled tide and NOAA value at most of the stations is less than 10 cm except at St. Simons Island, GA. The mean difference is 0.05 m and the standard deviation of the difference is 0.05 m, which is 7.8% of the mean observed tidal amplitude. The discrepancy mainly comes from the stations far away from the Chesapeake Bay, where the grid resolution is not very high. Since the grid may not resolve the complex bathymetries of these stations very well, a relatively large difference can be expected. Generally, the M_2 tidal results with errors within 10 cm are acceptable for the stations along the Atlantic Coast. For the constituent of S_2, the mean difference is -0.01 m and the standard deviation of the difference is 0.01 m, which is about 9.1% of the mean observed S_2 tidal amplitude. For the constituent N_2, the mean difference is 0.01 m and the standard deviation of the difference is 0.01 m, which is about 6.7% of the mean observed S_2 tidal amplitude. For K_1, the mean difference is 0 m and the standard deviation of the difference is 0.01 m, which is about 10% of the mean observed K_1 tidal amplitude. For O_1, the mean difference is -0.01 m and the standard deviation of the difference is 0.01 m, which is about 14.3% of the mean observed O_1 tidal amplitude. For Q_1, both of the mean difference and standard deviation are 0. As can be seen in Table 2.3, for the M_2 tide, the difference for the phase between the modeled tide and NOAA observations at all the stations is less than 10 degrees; for the S_2, the difference is less than 20 degrees; for the N_2 tide, the difference is less than 10 degrees. It is demonstrated that the amplitude and phase of the

modeled tide is quite reasonable when compared to the observations along the Atlantic coast. Overall, the large domain model is capable of tide simulation along the Atlantic Coastline.

As can be seen in Table 2.4, for Chesapeake Bay stations where the high-resolution grid is ensured, the model results agree with the observations even better. For the M_2 tide, the differences for most of the stations in the Bay are within 2 cm, except Stations Yorktown, Sewells Pt. and Cambridge, which have 5 cm, 4 cm, and 4 cm differences, respectively. All these three stations are located in the tributaries at locations with more detailed bathymetry that might not be resolved very well by our grid, but the tide simulations in other stations along the main Bay are very good. The mean amplitude difference of the dominant tidal constituent M_2 tide is -0.02 m and the standard deviation of the difference is 0.02 m, which is about 8% of the mean observed M_2 amplitude. For S_2, N_2, K_1, O_1, and Q_1, the mean differences of tidal amplitude are all 0 m, and the standard deviation of the differences are within 0.01 m. As can be seen in Table 2.5, for the M_2 tide, the difference for the phase between the modeled tide and NOAA observations at all the stations is less than 15 degrees; for the S_2 tide, the difference is less than 20 degrees; for the N_2 tide, the difference is less than 20 degrees. It is demonstrated that the amplitude and phase of the modeled tide is reasonable when compared to the observations in the Chesapeake Bay. Overall, with higher resolution in the Bay, the large domain model simulated the tide very satisfactorily in the Bay.

Overall, the large domain model was demonstrated to be able to simulate the tide along the Atlantic Coastline and in the Chesapeake Bay reasonably well. After the large domain model was calibrated, it could be used for generating the open boundary condition for the small domain. When the grids were generated, each of the open boundary nodes of the small domain grid has an

exact corresponding node in the large domain grid. Thus, the water elevations of these nodes at each time step were saved when the large domain model was running. After the simulation of the large domain model was completed, a water elevation history file was generated and it could be read into the small domain model to specify the water elevation at each open boundary node at each time step. That is the coupling process of the two models.

The small, limited domain model is also set up on a quasi-3D mode with the same vertical grid as the large domain model. In order to verify the coupling process, the open boundary is specified as the water elevation output of the large domain model. Table 2.6 shows comparisons of the harmonic analysis results of the modeled tide and the observations. It can be seen that the model predicted tidal amplitudes compare reasonably well to the observations. This comparison indicates that this small domain model could simulate the tide very well. The mean difference of M_2 amplitude between model results and observations is -0.01 m and the standard deviation of the difference is 0.03 m, which is about 12% of the mean M_2 amplitude. For the S_2 tide, the mean difference is -0.02 and the standard deviation is 0.01, which is 25% of the mean observed S_2 amplitude. For N_2, K_1, O_1 and Q_1, the mean differences are within 0.01 m and the standard deviations of the differences are with in 0.01 m as well. Overall, the small domain grid model has proven to simulate the tide in the Chesapeake Bay very well. It demonstrated that this small domain model could be used for the simulation of both storm surge and inundation and the coupling process for the two grids was successful.

Chapter 3. Storm surge and inundation simulation

In this chapter, the storm surge and inundation simulation results for two scenarios, Hurricane Isabel and Tropical Storm Ernesto, are shown and discussed. The large domain model is forced by the tidal constituents at the open boundary. A 5-min time step was used and a total of 30 layers were used in the vertical grid. The thickness of layers varied in the vertical as follows: (a) A 5-m resolution was used for the top 50 m. (b) Resolutions of 10-m and 20-m were used between depths of 50 and 150 m. (c) Layer thicknesses of 50 m, 100 m, and 500 m were used gradually until attaining the depth of 2500 m. (d) A 1000-m depth interval was used between depths of 3000 and 6000 m. To simulate the storm surge, a 5-day simulation without atmospheric forcing was conducted initially to spin-up the tide. Then the wind and pressure data for two storm surge cases from the different atmospheric models were input to force the large domain hydrodynamic model. For each wind and pressure field, the wind speeds, directions, and pressures were compared with the observations from NOAA separately to check the quality of each wind. The root-mean-square (RMS) error values of wind speeds, directions, and pressures were calculated to compare the capability of different atmospheric models. Through the procedure, the WRF-GFS wind was found to be the most reliable wind. For each run with different atmospheric winds, water-level predictions from our storm surge model were compared against the observed water levels at 9 tidal-gage stations located throughout the Chesapeake Bay

region. RMS, relative errors, correlation coefficients and the skill score were calculated to assess our model's predictive capability. Appendix A gives the mathematical definitions of these statistical measures. Using the boundary condition output from the large domain model, the small domain model predicted the inundation and the results were presented via visualization. In this study, the inundation simulation is only using the WRF-GFS wind since it is the most reliable wind.

3.1 Hurricane Isabel

3.1.1 General description

Hurricane Isabel was the costliest and deadliest hurricane in the 2003 Atlantic hurricane season. The ninth named storm, fifth hurricane, and second major hurricane of the season, Isabel formed from a tropical wave on September 6 in the tropical Atlantic Ocean. It moved northwestward and, within an environment of light wind shear and warm waters, it steadily strengthened to reach peak winds of 165 mph (265 km/h) on September 11. After fluctuating in intensity for four days, Isabel gradually weakened and made landfall on the Outer Banks of North Carolina with winds of about 105 mph (165 km/h) on September 18. It quickly weakened over land and became extratropical over western Pennsylvania the next day.

The track of Hurricane Isabel is shown in Figure 3.1. Here is a detailed description of the track of Isabel: Isabel became the ninth named storm of the 2003 Atlantic basin tropical cyclone season about 625 miles west of the Cape Verde Islands on Saturday morning, September 6. Isabel began as a strong tropical wave off the West African Coast about three days before, and was upgraded to a hurricane at 11 a.m. EDT Sunday, September 7. Isabel intensified rapidly Monday,

September 8, going through Categories 2 and 3 of the Saffir-Simpson Hurricane Scale (Appendix B) and reaching Category 4 intensity by 11 p.m. EDT that day. Isabel remained a strong Category 4 hurricane until reaching the rare Category 5 status, the highest category of hurricane strength on the Saffir-Simpson Scale, Thursday, September 11 at 5 p.m. EDT. Isabel was moving slowly west and had reached a location about 500 miles east northeast of the northern Leeward Islands. Isabel remained at or near Category 5 intensity until Sunday, September 14, when it weakened to a Category 4 storm. Isabel weakened to a Category 3 late Monday, September 15. Weakening continued through Tuesday, decreasing to a Category 2 at 11 a.m. EDT Tuesday, September 16. Hurricane watches were issued by the Tropical Prediction Center (TPC) for parts of the North Carolina, Virginia, Maryland, Delaware, and New Jersey coasts at 11 a.m. EDT Tuesday. Hurricane warnings were issued by the TPC at 11 p.m. EDT Tuesday, and extended northward at 5 a.m. EDT Wednesday, September 17. Isabel made landfall near Drum Inlet, Carteret County, North Carolina, around 1 p.m. EDT Thursday, September 18. Isabel moved northwest to Roanoke Rapids, NC, by 5 p.m. EDT Thursday, and accelerated to northeast West Virginia by 5 a.m. Friday, September 19 as a tropical storm. By 11 a.m. EDT Friday, the center of the storm was losing tropical characteristics and was near Cleveland, Ohio, moving northward into Canada (Johnson, 2004).

3.1.2 Wind and pressure comparison

For Hurricane Isabel, there are seven types of winds generated by different atmospheric models, including four from NWS (GFS, NAM, WRF-GFS, WRF-NAM), three from RAMS model of Weatherflow, Inc. (Grid1, Grid2 and Grid3). The winds from the RAMS model are generated with three grids. From Grid1 to Grid3, the grid resolution increases and Grid3 has the highest

resolution at 2-km. All the winds were provided from 9/16/2003 to 9/19/2003. For the wind from NWS, four winds are given every day, starting at 0:00, 6:00, 12:00 and 18:00 UTC separately and each wind lasts 30 hours. So there are total of 64 winds ((4 different types) × (4 days) ×(4 winds of each day)). For the wind from Weaterflow, Inc, two winds are given every day, starting at 0:00 and 12:00 UTC separately and each wind lasts 24 hours. So there are a total of 24 winds ((3 different types) × (4 days) × (2 winds of each day)). These winds are generated for ensemble runs. But before the ensemble runs, for each kind of wind, a run with continuous wind from 9/16/2003 1:00 UTC to 9/19/2003 22:00 UTC is initially conducted in order to check the accuracy of each type of wind. For this reason, for each of the 4 kinds of wind from NWS, a continuous wind is generated by piecing the 4 (days) ×4 (winds of each day) = 16 winds together and for each of the 3 kinds of wind from Weatherflow, Inc., a continuous wind is generated by piecing the 4 (days) ×2 (winds of each day) = 8 winds together. To piece them together, for each 30-hour length (24-hour length) wind, 6-hour length wind (12-hour length wind) is selected. Combining the 16 (8) winds, a continuous wind with a 96-hour length is generated for each type of wind. The reason that the 6 hour (12 hour) wind is selected from the second hour to seventh (second to thirteenth) hour is because these hours are the most accurate prediction of each 30-hour length (24-hour length) wind and the accurary is decreasing as the time increases. At the beginning, 6-hour (12-hour) wind is selected from first hour to sixth (first hour to twelfth) hour, but the continuous wind with this kind of selection is not very smooth because the first hour wind of the atmospheric model is adjusted by new initial conditions so it is not consistent with the previous predictions. After the continous wind is generated for each kind of wind, the wind speed directions and pressures from them are compared to the observations. Totally, six wind stations in the Bay are selected. All the plots are based on UTC time.

For the GFS wind, as can be seen in Figure 3.2, at Stations CBBT, Sewells Point, Cambridge, the wind speeds compare well with the observations except they slightly overestimate after the peak. At Station Lewisetta, the wind speeds are overestimated a little bit before the peak and underestimated a little bit during the peak. The wind speeds are underestimated at Station Thomas Point and overestimated at station Tolchester Beach. It can be seen in Figure 3.3 that GFS modeled wind directions compare very well with observed wind directions from hour 24 to hour 96 at stations CBBT, Lewisetta, Thomas Point, and Tolchester Beach. However, the modeled wind directions have a small shift from the observed directions at stations Cambridge and Sewells Point. The comparison of modeled and observed pressures are shown in Figure 3.4. The GFS modeled pressures are generally underestimated before the depression, but match the depression quite well. Statistically, the RMS calculated using the observed and modeled wind and pressure data for each station are shown in Table 3.1. The mean RMS values of six stations are 2.95 m/s for the wind speed; 34.68 degrees for the wind direction; and 192.96 Pa for the pressure.

For the NAM wind, the wind speeds, wind directions, and pressures comparisons are shown in Figure 3.5, Figure 3.6, and Figure 3.7, respectively. At Stations CBBT, Sewells Point, and Thomas Point, the modeled wind speeds are underestimated compared with the observations. At Station Lewisetta, the wind speeds are overestimated a little bit before the peak and underestimated a little bit during the peak, which is quite similar to the GFS wind. Cambridge is the only station where the wind speeds matched the observations quite well. At Station Tolchester Beach, the wind speeds are overestimated. NAM modeled wind directions did not

compare as well as GFS modeled directions with observations from Hour 24 to Hour 96. At Stations CBBT, Lewisetta, Cambridge, and Tolchester Beach, the modeled wind directions have a small shift from the observed directions. For the pressure comparison, the NAM modeled pressure are generally overestimated during the depression and underestimated a little after the depression. As can be seen in Table 3.1, the mean RMS error values of six stations for the wind speed is 3.14 m/s; for the wind direction, RMS is 35.50 degrees; for the pressure, RMS is 201.31 Pa. These statistical measures demonstrated that the NAM modeled wind and pressure have more error than the GFS modeled wind and pressure.

For the WRF-GFS wind, as can be seen in Figure 3.8, at Stations CBBT, Sewells Point, Lewisetta, Cambridge, the wind speeds compared well with the observations except they slightly overestimated after the peak. At Station Lewisetta, the wind speeds are overestimated a little before the peak as well. The wind speeds at Station Thomas Point are underestimated before and after the peak, but matched the peak. At Station Tolchester Beach, the wind speeds are overestimated more than the NAM and GFS winds. In Figure 3.9, the WRF-GFS modeled wind directions compared very well with observed wind directions from Hour 24 to Hour 96 at Stations CBBT, Lewisetta, Thomas Point, and Tolchester Beach. The modeled wind directions have a small shift from the observed at Stations Cambridge and Sewells Point. For the pressure comparison in Figure 3.10, the WRF-GFS modeled pressure are generally underestimated a little after the depression, but match the depression quite well. Overall, as can be seen in Figure 3.8, Figure 3.9, and Figure 3.10, the WRF-GFS wind is better than the GFS and NAM winds. The scatter plots of the modeled wind against the observed wind are shown in Figures 3.11, 3.12, 3.13, 3.14, 3.15, 3.16, 3.17, 3.18, 3.19. Three stations are selected to represent the wind in the

lower Bay (CBBT), the middle Bay (Lewisetta) and the upper Bay (Thomas point). For each station, the wind speed, wind direction and pressure are plotted seperately. As can be seen in Figure 3.11, 3.12 and 3.13, the RMS error of the modeled wind speed at CBBT is 2.55 m/s, the RMS error of the wind direction is 8.54 degree and the RMS error of the pressure is 164.04 Pa. As shown in Figure 3.14, 3.15 and 3.16, the RMS error of the modeled wind speed at Lewisetta is 3.40 m/s, the RMS error of the wind direction is 18.67 degree and the RMS error of the pressure is 126 Pa. In Figure 3.17, 3.18 and 3.19, the RMS error of the modeled wind speed at Thomas Point is 2.81 m/s, the RMS error of the wind direction is 16.03 degree and the RMS error of the pressure is 151.54 Pa. For other stations, the statistical measures are shown in Table 3.1. The mean RMS error values of the WRF-GFS wind for the wind speed is 3.59 m/s; for the wind direction is 26.45 degrees; and for the pressure is 152.62 Pa. The increase in mean RMS of wind speed is mainly due to station Tolchester Beach, which has a RMS of 6.62 m/s. If the mean RMS is calculated without Station Tolchester, it is 2.98 m/s, which is better than the GFS and NAM winds. The mean RMS of wind direction and pressure for WRF-GFS wind are also better than those for GFS and NAM. Thus, the higher-resolution WRF model did generate better wind and pressure fields than the lower-resolution GFS and NAM models.

For the WRF-NAM wind, the wind speeds comparison is shown in Figure 3.20. For all the stations except Tolchester Beach, the wind speeds compared well with the observations. Specifically, the wind speeds are overestimated a little after the peak at Station Cambridge. At Station Tolchester Beach, the wind speeds are overestimated as winds generated by other atmospheric models from NWS. Overall the wind speeds simulated by the WRF-NAM model matched even better than those generated by the WRF-GFS wind, but the problem of the WRF-

NAM wind is that it has more fluctuations, so the wind speeds are not as smooth as the WRF-GFS wind. For the wind directions, as shown in Figure 3.21, the WRF-NAM modeled wind directions compared well with observed wind directions from Hour 24 to Hour 96 at Stations CBBT, Lewisetta, Thomas Point, and Tolchester Beach. Quite similar to the other three winds generated by NWS, the modeled wind directions have a small shift from the observed at stations Cambridge and Sewells Point. However, the WRF-NAM simulated wind directions also have several small fluctuations. The WRF-NAM modeled pressures (Figure 3.22) are generally overestimated during the depression and have several fluctuations. The statistical measures for WRF-NAM could be found in Table 3.1, the mean RMS of six stations for the wind speed is 3.20 m/s; for the wind direction, the RMS is 25.84 degrees; for the pressure, the RMS is 238.29 Pa. Similar to the WRF-GFS wind, the increase in mean RMS of wind speed is mainly due to station Tolchester Beach, which has a RMS of 6.21 m/s. If the mean RMS is calculated without Station Tolchester Beach, it is 2.60 m/s, which is even better than the WRF-GFS wind (2.98 m/s). It is consistent with our observation based on the plots, but the fluctuations prevent the WRF-NAM wind from being the best choice. At the same time, the mean RMS of pressure for WRF-NAM wind (238.29Pa) is worse than that for WRF-GFS (152.62). Thus, WRF-GFS wind is overall better than WRF-NAM wind.

For RAMS grid1 wind, it can be seen in Figure 3.23 that the wind speeds are generally underestimated at all stations except Tolchester Beach, At Tolchester Beach, the wind speeds are overestimated like other winds. In Figure 3.24, RAMS grid1 modeled wind directions are compared very well with observed wind directions from Hour 24 to Hour 96 at stations CBBT, Lewisetta, Thomas Point, and Tolchester Beach. Similar to the atmospheric models from NWS,

the RAMS wind directions have a small shift from the observed at Stations Cambridge and Sewells Point as well. As shown in Figure 3.25, the RAMS grid1 modeled pressures have a big underestimation during the depression, especially in the stations located in the lower Bay. In Table 3.1, the mean RMS of six stations for the wind speed is 3.94 m/s; for the wind direction, the mean RMS is 31.31 degrees; for the pressure, the mean RMS is 378.95 Pa. The mean RMS of wind speed, direction and pressure for the RAMS Grid1 wind are worse than those for the WRF-GFS wind, especially the pressure.

For the RAMS Grid2 wind, as shown in Figure 3.26, Figure 3.27, and Figure 3.28, the wind speeds, wind directions, and pressures at all the stations are quite similar to the pattern of the RAMS Grid1 wind, but the wind speeds of the RAMS Grid2 wind are slightly increased and the pressures are slightly decreased. For the statistical measures in Table 3.1, the mean RMS error value of six stations for the wind speed is 3.41 m/s; for the wind direction, the mean RMS is 30.35 degree; for the pressure, the mean RMS is 382.07 Pa. The RMS of wind speeds and directions are getting better compared with the RAMS Grid1 wind, but the RMS of pressures are getting worse.

For the RAMS Grid3 wind, the wind speeds compared well with the observations (Figure 3.29) at Stations CBBT, Sewells Point, Lewisetta, Cambridge, and Thomas Point. For the other two stations, the wind speeds are underestimated a little during the peak at Station Lewisetta and overestimated at Station Tolchester Beach. In Figure 3.30, RAMS grid3 modeled wind directions compared well with observed wind directions from Hour 24 to Hour 96 at Stations CBBT, Lewisetta, Thomas Point, and Tolchester Beach. Similar to all the other models, the modeled

wind directions have a small shift from the observed at Stations Cambridge and Sewells Point. In Figure 3.31, the RAMS grid3 modeled pressures have a big underestimation during the depression, especially in the stations located in the lower Bay. As can be seen in Table 3.1, the mean RMS of six stations for the wind speed is 2.86 m/s; for the wind direction, the mean RMS is 30.57 degree; for the pressure, the mean RMS is 409.99 Pa. This indicates that the wind speeds simulated by the RAMS Grid3 model are better than those simulated by the RAMS Grid1 and RAMS Grid2, but the pressures are worse.

Overall, for all stations except Cambridge and Sewells Point, the modeled wind directions from different models are simulated quite well. The cause of the shift of wind directions at Stations Cambridge and Sewells Point is unknown. It might be because all the wind models did not resolve the local features at these two stations during Hurricane Isabel. For the wind speeds, different wind models have different accuracies. Generally, the high-resolution WRF model has better simulations than the low-resolution GFS and NAM models and the GFS model generates better wind fields than the NAM model. The RAMS model from Weather Flow, Inc. did not generate very good wind, especially with low-resolution Grid1 and Grid2. Both the wind speeds from Grid1 and Grid2 are understimated. The wind from Grid3 is the best for the RAMS model since it has the highest resolution of 2-km. For the pressure field, the RAMS model generated a very bad simulation. The higher the grid resolution, the worse the pressure field generated. The RAMS model with Grid3 generates the worst pressure field. For this reason, the RAMS-Grid3 wind was not selected as the best wind, even though it had the highest resolution. Out of all the atmospheric models, the WRF-GFS model had the best pressure simulation. It should be noted that the modeled wind speeds are overestimated for all of the wind models at Station Tolchester

Beach.This is consistent for all the 7 different modeled winds. In looking at the sighting of the instrument there are some trees to the north and east of the instrument which might cause some sheltering. Thus, the observations might be lower than the real wind. Also since we are dealing with a 4 km grid it is possible that most of that grid is over the water so that when a value is calculated it might be more representative over the water which would have the higher winds. (Billet, 2009). In summary, the best wind obtained was by using the WRF-GFS wind for the Bay area and the GFS wind for other areas outside of the WRF model domaindoes not cover.

3.1.3 Water elevation comparison

In the last section, the 7 different winds generated by different atmospheric models are compared with the observations so that the quality of these winds is known. In this section, storm tide simulations during Hurricane Isabel with 7 different winds are compared with the observations to see if the prediction skill of our hydrodynamic model is consistent with the quality of these winds.

For the water elevation results with the GFS wind, it can be seen in Figure 3.32 that the modeled water elevations at the 9 stations in the Bay compared well with the observations overall. However, the water elevations generated with the GFS wind are overestimated at the lower Bay Stations (CBBT, Kiptopeke, and Sewells Point) and underestimated in the upper Bay Stations (Annapolis, Baltimore, and Tolchester Beach). From the previous analysis of wind, it is known that the GFS-modeled winds are overestimated a little during the peak in the lower Bay and underestimated in the upper Bay (Thomas Point). This might explain the water elevation simulation results. Statistical measures are shown in Table 3.2. For the water elevations

generated with the GFS wind, the RMS is within 0.22 m in the lower Bay and is within 0.18 m in the upper Bay. The mean RMS is 0.15 m. The mean relative error is 4.72%, the mean correlation coefficient is 0.98, and the mean skill score is 0.98.

For the water elevation results with the NAM wind, it can be seen in Figure 3.33 that the modeled water elevations at the 4 stations of CBBT, Kiptopeke, Sewells Point, and Cambridge are not smooth but with fluctuations. In the upper Bay, the modeled water elevations are a little bit underestimated before the peak but matched the peak. In fact, based on the wind comparisons, it is known that the NAM wind and pressure have several fluctuations that would generate the fluctuations of water elevations. As shown in Table 3.3, for the water elevations generated with the NAM wind, the RMS is within 0.17 m in the lower Bay and is within 0.21 m in the upper Bay. The mean RMS is 0.18 m. The mean relative error is 6.09%, the mean correlation coefficient is 0.96, and the mean skill score is 0.97. So the water elevations generated with the NAM wind are worse than those generated with the GFS wind, which is consistent with the idea that the quality of the NAM wind is worse than that of the GFS wind.

The water elevations generated with the WRF-GFS wind matched the observations very well (Figure 3.34), just slightly underestimated in the upper Bay. The scatterplots of modeled water elevations against observed storm surges are shown in Figure 3.35, Figure 3.36 and Figure 3.37. Three staions are selected to represent the upper Bay (Baltimore), middle Bay (Lewisetta) and lower Bay (CBBT). As shown in Figure 3.35, the water elevations are underpredicted at station Baltimore. The RMS error of the water elevations is 0.19 m, the relative error E is 3.80 %, the correlation coefficient r is 0.99 and the skill score is 0.98. In Figure 3.36, the modeled water

elevations are compared well with the observations at station Lewisetta. The RMS error of the water elevations is 0.12 m, the relative error E is 3.73 %, the correlation coefficient r is 0.98 and the skill score is 0.98. In Figure 3.37, the modeled water elevations are compared very well with the observations at station CBBT. The RMS error of the water elevations is 0.12 m, the relative error E is 3.82 %, the correlation coefficient r is 0.97 and the skill score is 0.98. For the statistical measures at other stations, as can be seen in Table 3.4, the RMS is within 0.13 m in the lower Bay and is within 0.19 m in the upper Bay. The mean RMS is 0.15 m. The mean relative error is 4.11%, the mean correlation coefficient is 0.98, and the mean skill score is 0.98. These statistical measures proved that the WRF-GFS wind generated better water elevation simulations than did either the GFS wind or the NAM wind.

For the water elevations generated with the WRF-NAM wind, it can be seen in Figure 3.38 that the water elevations are underestimated both in the lower and upper Bay. In fact, the analysis of winds and pressures in the last section showed that the pressures generated with WRF-NAM are higher than the observations during the depression. The difference between the modeled pressures and observations in the lower Bay is about 400 to 600 Pa. In terms of the inverted barometer effect, roughly a drop of 100 Pa could generate a 0.01-m increase in water elevation. Here the pressures are 400 to 600 Pa higher than the observations, which could generate a 4-cm to 6-cm underestimation of water elevation in the lower Bay. Statistically, the RMS of water elevation generated with the WRF-NAM wind (Table 3.5) is within 0.18 m in the lower Bay, which is higher than that of water elevation generated with the WRF-GFS wind (0.13m). The difference is 0.06 m, which is consistent with the inverted barometer effect. The mean RMS is 0.16 m. The mean relative error is 5.97%, the mean correlation coefficient is 0.97 and the mean

skill score is 0.97. Overall, the water elevations generated by the WRF-NAM wind are worse than those generated with WRF-GFS in terms of these statistical measures.

For the water elevations generated with the RAMS Grid1 wind (Figure 3.39), the water elevations are overestimated in the lower Bay and underestimated in the upper Bay during the peak. Based on the analysis of the wind field, it is shown that the wind speeds are underestimated in both of the lower and upper portions of the Bay, but here the water elevations are overestimated in the lower Bay, which seems unreasonable. However, this can be explained if the the pressure field is considered. In fact, the modeled pressures during the depression are significantly lower than the observations. The difference of the modeled and observed pressures in the lower Bay is about 2000 Pa and in the upper Bay is about 500 Pa. In terms of the inverted barometer effect, this can cause a 0.05-m to 0.20-m increase in water elevation. Thus, even though the wind speeds are underestimated, the water elevations are still overestimated in the lower Bay. Statistically, as can be seen in Table 3.6, the RMS is within 0.19 m in the lower Bay and is within 0.19 m in the upper Bay. The mean RMS is 0.16 m. The mean relative error is 5.32%, the mean correlation coefficient is 0.96 and the mean skill score is 0.97. Based on these statistical measures, the water elevations generated with the RAMS Grid1 wind are worse than those generated by the WRF-GFS wind.

The water elevations generated with the RAMS Grid2 winds (Figure 3.40) are overestimated in the lower Bay during the peak. The overestimation in the lower Bay is also due to the incorrect pressure field. In fact, the pressures generated with the RAMS Grid2 are even lower than those generated by the RAMS Grid1, so more overestimation is expected. At the same time, the wind

speeds generated by the RAMS Grid2 also increased compared to that generated by the RAMS Grid1. Combining the decrease in pressure and increase in wind speeds, the water elevations are overestimated more in the lower Bay and are no longer underestimated in the upper Bay. As shown in Table 3.7, the RMS is within 0.21 m in the lower Bay and is within 0.13 m in the upper Bay. It proved that the water elevations are getting worse in the lower Bay and getting better in the upper Bay. The mean RMS is 0.15 m. The mean relative error is 4.86%, the mean correlation coefficient is 0.97, and the skill score is 0.97. Overall, these are still worse than the water elevations generated with the WRF-GFS wind.

The water elevations generated with the RAMS Grid3 wind (Figure 3.41) are overestimated in the lower Bay during the peak and overestimated a little bit in the upper Bay during the peak. This could be expected since the pressures generated by the RAMS Grid3 is even lower than those generated by the RAMS Grid2 and the wind speeds generated by the RAMS Grid3 are higher than those generated by the RAMS Grid2. As can be seen in Table 3.8, the RMS is within 0.23 m in the lower Bay and is within 0.16m in the upper Bay. The mean RMS is 0.17m. The mean relative error is 5.51%, the mean correlation coefficient is 0.97, and the mean skill score is 0.97. These proved that water elevations generated with the RAMS Grid3 wind are worse than those generated with the WRF-GFS wind as well.

Overall, the water elevations simulated with the WRF-GFS wind and pressure fields during Hurricane Isabel are the best overall of the simulations with the 7 different types of winds. Water elevations simulated by the GFS wind are better than those simulated by the NAM wind. The water elevations generated with WRF-NAM, RAMS (Grid1, Grid2, Grid3) are not very good due

to the poor quality of pressure and wind fields. The quality of the water elevation simulations is consistent with the quality of wind and pressure fields. That means that our hydrodynamic model could generate accurate water elevations with accurate wind and pressure fields.

3.1.4 Inundation simulation

Inundation simulation is using the high-resolution small domain grid with the outputs of the large domain model as the open boundary condition. The inundation simulation is only using WRF-GFS wind since it is the best wind available. This simulation is focusing on the lower Bay, so here only the modeled water elevations of the stations in the lower Bay are compared with the observations. It can be seen in Figure 3.42 that the model is shown to reproduce the peak flood levels to a high degree of accuracy.

It is hard to find the exact inundation map for the lower Bay during Hurricane Isabel, but the storm surge inundation maps under different categories of hurricanes can be found at www.vaemergence.com, which is the website of Virginia Department of Emergency Management (VDEM). The maps are created using SLOSH model and MEOW (Maximum Envelope of Water) and MOM (Maximum of Maximum) analysis, as follows:

1. Select hypothetical storms appropriate to those found from historical record: storm directions, forward speeds, (Saffir-Simpson) intensities, sizes (radius of maximum winds, or RMW), and landfall sites sufficiently close together (typically 15 miles or less) to adequately map the surge flood plain.
2. Generate the set of hypothetical storms. Typically there will be about 10 directions, 4 forward speeds, 5 intensities and 10 to 20 landfall points, resulting in 2000 to 4000 individual storms.

3. Create MEOW maps of SLOSH modeled storm surge, for each combination of storm direction, speed, Saffir-Simpson intensity and initial datum. In the example NO.2 above, (10 directions, 4 speeds and 5 Saffir-Simpson Categories), there would be 200 MEOWs. Simply put, the MEOW analysis represents the highest water due to a "family" of parallel tracks with the same direction, speed and intensity. The analysis is done for varying storm direction, speed of movement and category.

4. Consolidate MEOW results into maps of MEOWS Of MEOWS or MOMs. Typically, MOM depicts surge flooding for each of intensity only, regardless of storm direction or speed.

The inundation map above from VDEM is the MOM map which represents the worst scenario of inundation for each category hurricane, thus, the coverage of inundated area will be larger than that generated by our model with the same category hurricane. Figure 3.43 shows the southside storm surge inundation map covering the Virginia Beach, Norfolk, and Hampton Roads areas. It shows that the area around the Back Bay is vulnerable to inundation. Figure 3.44 shows the Peninsula Storm Surge Inundation Map covering Hampton, Newport News, Poquoson, Yorktown, and Gloucester. It shows that Poquoson, the eastern part of Yorktown, and Gloucester are vulnerable to inundation during a storm surge. Figure 3.45 shows the Eastern Shore Storm Surge Inundation Map. It shows that the areas near the Atlantic Ocean are vulnerable to storm surge inundation. Figure 3.46 shows the modeled inundation map at the beginning of the Hurricane Isabel at 0:30 UTC 9/18/2003. It can be seen that not many areas are inundated at this time, since the water elevations in the lower Bay are still low. Figure 3.47 shows the modeled inundation map at the peak of Hurricane Isabel at 21:00 UTC 9/18/2003. It can be seen that the Eastern Shore, Poquoson, and the eastern part of Yorktown are inundated at that time. Since

Isabel was a Category 2 hurricane, the modeled inundation map is quite consistent with the storm surge inundation map generated by the VA Department of Emergency Management, but our modeled inundated area is smaller than that from VDEM. Figure 3.48 shows the modeled inundation map in the aftermath of Hurricane Isabel at 20:00 UTC 9/19/2003. It can be seen that the inundation has disappeared for most of the inundated area by this time since the water elevations in the lower Bay had dropped substantially. Overall, our high-resolution inundation model can generate a reasonable inundation map from the beginning to the end of Hurricane Isabel. It is capable of generating a reasonable inundation prediction in the future for forecasting purposes.

3.2 Tropical Storm Ernesto

3.2.1 General description

Hurricane Ernesto was the costliest tropical cyclone of the 2006 Atlantic hurricane season. The sixth tropical storm and first hurricane of the season, Ernesto developed from a tropical wave on August 24 in the Eastern Caribbean Sea. Ernesto first affected the Northern Caribbean, reaching minimal hurricane status near Haiti before weakening and moving across Eastern Cuba as a tropical storm. Despite initial predictions for it to track through the Eastern Gulf of Mexico as a major hurricane, Ernesto moved across Eastern Florida as a weak tropical storm. After turning to the northeast, it re-intensified and made landfall on August 31 on the North Carolina Coast just below hurricane status. The remnants spread moisture across the Northeastern United States before dissipating over Eastern Canada on September 14.

The track of Ernesto is shown in Figure 3.49. Ernesto made landfall at Plantation Key, Florida, in the upper Florida Keys, around 0300 UTC 30 August. A short time later, around 0500 UTC, a second Florida landfall occurred on the Florida mainland in southwestern Miami-Dade County. At both landfalls Ernesto had maximum sustained winds of 40 knot and a minimum central pressure of 1003 mb. Thereafter, Ernesto weakened only slightly, and it remained a tropical storm with maximum sustained winds of 35 knot throughout the remainder of its path over Florida. The storm moved northward along the center of the Florida Peninsula and within a weakness in the mid-level ridge, and the cyclone passed over Lake Okeechobee around 1800 UTC 30 August. Ernesto gradually turned north-northeastward, and its center emerged over the Atlantic Ocean near Cape Canaveral, Florida very early on 31 August. Fueled by the warm waters of the Atlantic, convection increased over the center of the cyclone, and Ernesto intensified to a strong tropical storm as it continued north-northeastward ahead of a deep layer trough approaching from the west. It reached an intensity of 60 knot by 1800 UTC 31 August while centered about 150 nautical miles south-southwest of Wilmington, North Carolina. The central pressure continued to gradually fall and an eye was becoming discernible in satellite imagery as the storm center approached the coast. The center came ashore at 0340 UTC 1 September on Oak Island, North Carolina, a few miles south-southwest of Wilmington and just west of Cape Fear. At the time of final landfall, Ernesto was very near the threshold between tropical storm and hurricane status, with an intensity of 60 knot and a minimum pressure of 985 mb. Thereafter, Ernesto weakened as it moved across eastern North Carolina where it became a tropical depression by 1200 UTC 1 September. Even before Ernesto made final landfall, however, it combined with a high pressure system centered over Southeastern Canada to indirectly produce gale-force winds near the Coasts of Virginia, Maryland, Delaware, and New

Jersey. Ernesto reached the North Carolina/Virginia border at about 1800 UTC 1 September, although by that time it had transformed into an extratropical cyclone, as it interacted with a pre-existing frontal zone that extended eastward from Virginia. The intensity of Ernesto as an extratropical cyclone as it moved slowly northward over Virginia and Maryland on 2 September is estimated at 40 knot. By 1800 UTC that day, extratropical Ernesto was centered very near Washington, D.C., and after that time the system began to weaken. On 3 September, it was no longer producing gale-force winds as it accelerated across Pennsylvania and New York into Southeastern Canada, and it was absorbed into a larger extratropical low pressure system the next day (Knabb et al., 2006).

3.2.2 Wind and pressure comparison

For Tropical storm Ernesto, there are 3 types of wind available, including the GFS wind, the NAM wind, and the WRF-GFS wind. All the winds were provided from 8/27/2006 to 9/5/2006. For each type of wind, two winds are given every day, starting at 0:00, 12:00 UTC separately and each wind lasts 30 hours. So there are total 3 (different kinds)$\times$10 (days) $\times$2 (winds of each day) = 60 winds. Similar to the procedure for simulating Isabel, a run with continuous wind from 0:00 UTC 8/27/2006 to 23:00 UTC 9/5/2006 is carried out first in order to check the accuracy of each kind of wind. For this reason, for each of the 3 kind of winds, a continuous wind is generated by piecing 20 winds together ((10 days) $\times$2 winds of each day)). To piece them together, for each 30-hour-length wind, 12 hour-length wind (from second to thirteenth hour) is selected. Combining the 20 winds, a continuous wind with 12 (hour) $\times$20 (winds)=240 hour-length is generated for each type of wind. After the continous wind is generated for each type of wind, the wind magnitude and directions from them are compared to the observations.

The GFS modeled speeds (Figure 3.50) are underestimated at Stations CBBT, Rappahanock, Lewisetta, and Thomas Point. At Station Cambridge, the modeled wind speeds matched the observation quite well, but just underestimated a little during the peak. The modeled wind speeds are overestimated at Station Tolchester Beach. The modeled directions (Figure 3.51) matched the observations quite well. The modeled pressures (Figure 3.52) have several small fluctuations, but overall, the modeled pressures are good. Statistical measures are shown in Table 3.9. For wind speed, the mean RMS is 2.98 m/s. For all 6 stations, the largeest RMS for wind speed is 4.07 m/s at Tolchester Beach and the smallest RMS is 1.65 m/s at Cambridge, which is consistant with the time series plots. For wind directions, the mean RMS is 41.12; for pressure, the mean RMS is 120.23 Pa.

The NAM modeled speeds (Figure 3.53) are underestimated during the peak and overestimated after the peak at Stations CBBT, Rappahanock, Lewisetta, Cambridge, and Thomas Point. At Station Tolchester Beach, the modeled wind speeds are overestimated. The modeled directions (Figure 3.54) matched the observations quite well. The modeled pressures (Figure 3.55) have several fluctuations and the modeled pressures are higher than the observations during the depression, especially in the lower Bay. The statistical measures in Table 3.9 show that, for wind speed, the mean RMS is 2.74 m/s. Of all 6 stations, the largest RMS for wind speed is 4.95 m/s at Tolchester Beach and the smallest RMS is 1.82 m/s at Cambridge, which is consistant with the plots. For wind directions, the mean RMS is 41.85; for pressure, the mean RMS is 155.99 Pa.

The WRF-GFS modeled speeds (Figure 3.56) compared with the observations very well at Stations CBBT, Rappahanock, Cambridge and Thomas Point. At Station Lewisetta, the modeled wind speeds matched the observation quite well except for a fluctuation during the peak. At Station Tolchester Beach, the modeled wind speeds are overestimated more than GFS and NAM winds. In Figure 3.57, the modeled directions matched the observations well. In Figure 3.58, the modeled pressures in the middle and upper portions of the Bay have a spike during the depression, but in the lower Bay the modeled pressures are good. The scatter plots of the modeled wind against the observed wind are shown in Figures 3.59, 3.60, 3.61, 3.62, 3.63, 3.64, 3.65, 3.66, 3.67. Three stations are selected to represent the wind in the lower Bay (CBBT), the middle Bay (Lewisetta) and the upper Bay (Thomas point). For each station, the wind speed, wind direction and pressure are plotted seperately. As shown in Figure 3.59, 3.60 and 3.61, the RMS error of the modeled wind speed at CBBT is 2.08 m/s, the RMS error of the wind direction is 38.88 degree and the RMS error of the pressure is 113.41 Pa. In Figure 3.62, 3.63 and 3.64, the RMS error of the modeled wind speed at Lewisetta is 2.71 m/s, the RMS error of the wind direction is 46.63 degree and the RMS error of the pressure is 146.75 Pa. In Figure 3.65, 3.66 and 3.67, the RMS error of the modeled wind speed at Thomas Point is 1.87 m/s, the RMS error of the wind direction is 33.17 degree and the RMS error of the pressure is 172.09 Pa. The wind direction at the three stations are worse than that during Hurricane Isabel. For other stations, the statistical measures are shown in Table 3.9. As can be seen in Table 3.9, for wind speed, the mean RMS is 2.77 m/s. Comparing all 6 stations, the largest RMS for wind speed is 5.55 m/s at Tolchester Beach and the smallest RMS is 1.85 m/s at Cambridge, which is consistant with the plots. For wind directions, the mean RMS is 43.93; for pressure, the mean RMS is 148.98 Pa.

Overall, the modeled wind directions from different models have the similar accuracy, but they are worse than the wind directions for Hurricane Isabel. At the same time, the modeled wind speeds for Ernesto were not as good as those for Isabel. Wind speeds generated by the GFS and NAM models are generally underestimated. The wind speeds generated by the WRF-GFS model are better, but have fluctuations. The modeled wind speeds are overestimated at Tolchester Beach for all of the models, as discussed in the section Hurricane Isabel. If the mean RMS is calculated without Tolchester Beach, for the GFS wind the RMS for wind speed is 2.76 m/s; for the NAM wind the RMS for wind speed is 2.30 m/s; for the WRF-GFS wind, the RMS for wind speed is 2.22 m/s. The RMS errors also indicated that wind speeds generated by WRF-GFS are the best. The pressures generated by the three models also are not very good, because there are fluctuations existing in the pressures generated by all three models. The pressure gradients generated by the WRF-GFS model are smoother than those generated by GFS and NAM. In summary, the best wind obtained was by using the WRF-GFS wind for the Bay area and the GFS wind for the other areas that the WRF model does not cover, but the quality of the wind is worse than that for Isabel.

3.2.3 Water elevation comparison

For the water elevation results with the GFS wind, it can be seen in Figure 3.68 that the water elevations at the lower Bay Stations (CBBT, Kiptopeke and Sewells Point) are underestimated on 8/30/2006 and 8/31/2006 as well as during the peak (15:00 to 23:00 UTC on 9/1/2006). The water elevations at the middle Bay Stations (Windmill Point, Lewisetta, and Cambridge) are underestimated from 8/30/2006 to 9/2/2006. The water elevations in the upper Bay Stations (Annapolis, Baltimore, and Tolchester Beach) are underestimated on 8/30/2006 and 8/31/2006,

then overestimated at the beginning of 9/2/2006 and underestimated from 10:00 to 23:00 UTC on 9/2/2006. The statistical measures are shown in Table 3.10. The RMS in the lower Bay is around 0.15 m and in the upper Bay it is around 0.19 m. The mean RMS is 0.18 m. The mean relative error is 23.13%. In the lower Bay the relative error is from 10.85% to 12.15%, but in the upper Bay the relative error is especially high, more than 30%. The highest relative error is 37.77% at Tolchester Beach. The average mean correlation coefficient is 0.88. In the lower Bay the mean correlation coefficient is not very bad, from 0.96 to 0.97, but in the upper Bay the mean correlation coefficient is less than 0.9 and the worst correlation is 0.68 at Tolchester Beach. The mean skill score is 0.87. It is higher in the lower Bay (around 0.94) and lower in the upper Bay (around 0.80). All these statistical measures proved that the GFS wind did not generate good water elevations, especially in the upper Bay.

For the water elevation results with the NAM wind (Figure 3.69), the water elevations in the lower Bay compared well with the observations. The water elevations in the middle Bay are underestimated from 8/30/2006 to 9/2/2006, especially during the peak. The water elevations in the upper Bay are underestimated from 8/30/2006 to 9/2/2006 and then overestimated at the beginning of 9/3/2006. As shown in Table 3.11, the RMS in the lower Bay is around 0.12 m and in the upper Bay is around 0.26 m. The mean RMS is 0.19 m. The mean relative error is 30.62%, even worse than results with the GFS wind. In the lower Bay the relative error is from 5.99% to 7.55%, but in the upper Bay the relative error is especially high, which is more than 40%. The highest relative error is 57.11% at Annapolis. The average mean correlation coefficient is 0.83. In the lower Bay the correlation coefficient is not very bad, from 0.94 to 0.96, but in the upper Bay the correlation coefficient is less than 0.8 and the worst correlation is 0.66 at Baltimore. The

mean skill score is 0.82. It is higher in the lower Bay (around 0.97) and lower in the upper Bay (from 0.65 to 0.75). These statistical measures proved that the NAM wind generated even worse water elevation than the GFS wind.

For the water elevation results with the WRF-GFS wind (Figure 3.70), the water elevations in the lower Bay compared well with the observations except that they slightly underestimated on 8/30/2006. The water elevations in the middle Bay are underestimated from 8/30/2006 to 9/1/2006, but generally matched the peak. The water elevations in the upper Bay are underestimated from 8/30/2006 to 9/1/2006, but matched the peak very well. The scatterplots of modeled water elevations against observed storm surges are shown in Figure 3.71, Figure 3.72 and Figure 3.73. Three staions are selected to represent the upper Bay (Baltimore), middle Bay (Lewisetta) and lower Bay (CBBT). In Figure 3.71, the water elevations are underpredicted before the peak at station Baltimore. The RMS error of the water elevations is 0.18 m, the relative error E is 28.0 %, the correlation coefficient r is 0.90 and the skill score is 0.84. In Figure 3.72, the modeled water elevations are underpredicted before the peak at station Lewisetta. The RMS error of the water elevations is 0.18 m, the relative error E is 12.94 %, the correlation coefficient r is 0.97 and the skill score is 0.93. In Figure 3.73, the modeled water elevations are compared very well with the observations at station CBBT. The RMS error of the water elevations is 0.14 m, the relative error E is 8.96 %, the correlation coefficient r is 0.96 and the skill score is 0.95. The statistical measures for all the stations in the Bay are shown in Table 3.12. The RMS in the lower Bay is around 0.14 m and in the upper Bay is around 0.18 m. The mean RMS is 0.17m, which is better than those obtained by using the GFS and NAM winds. The mean relative error is 19.13. In the lower Bay the relative error is from 8.00% to 8.96%, but in the

upper Bay, the relative error is higher, which is more than 20%. The highest relative error is 33.07% in Annapolis. The average correlation coefficient is 0.93. In the lower Bay the correlation coefficient is not very bad, from 0.95 to 0.96 and in the upper Bay the correlation coefficient is around 0.91. The mean skill score is 0.89. It is higher in lower Bay (around 0.95) and lower in upper Bay (less than 0.90). These statistical measures proved that the WRF-GFS wind generates the best water elevations of all the wind models.

Overall, all the winds did not generate very good water elevations compared to the scenario for Isabel. There are several possible reasons that the water elevations during Tropical Storm Ernesto are not simulated very well. First, the scenario TS Ernesto is not as organized as Hurricane Isabel. It is known that Hurricane Isabel was a strong hurricane whose wind structure was clearly defined, so that the wind and pressure field is easier to be simulated. As a result, the storm surge simulation results fro Hurricane Isabel are very good. In contrast, Tropical Storm Ernesto was not well organized and wind and pressure field during this period is more complicated. In fact, the wind and pressure field is formed by the combination of the Tropical Storm and the strong northeast wind in the continetal shelf area. Since the atmopheric models might not be able to simulate this complicated condition very well, the modeled wind during TS Ernesto are not as good. Consequently, the water elevation results are not simulated very well. Second, there might be some processes already going on before Tropical Storm Ernesto. It is possible that before this period, some processes that drive the water into the bay were already going on, but our model did not catch it since our simulation is not last long enough. In fact, from the plots of pressures, it seems like there is a low pressure before the TS Ernesto came. This low pressure might cause a small surge in the Bay which is not simulated by our model and thus

the underestimation appeared from 8/30/2006 to 9/1/2006. These are only the possible reasons. Additional studies need to be done in order to determine the exact cause of the underestimation.

3.2.4 Inundation simulation

The inundation simulation for TS Ernesto is only using the WRF-GFS wind as well since it is the best wind available. Only the modeled water elevations of the stations in the lower Bay are compared with the observations. As can be seen in Figure 3.74, the model is shown to reproduce the peak flood levels to a high degree of accuracy.

It is hard to find the exact inundation map for the lower Bay during Tropical Storm Ernesto, so the storm surge inundation map from www.vaemergence.com is still used for the comparison. Figure 3.75 shows the modeled inundation map at the beginning of the TS Ernesto at 0:30 UTC 8/31/2006. It can be seen that not many areas are inundated at this time while the water elevations are still low. Figure 3.76 shows the modeled inundation map at the peak of Ernesto at 15:30 UTC 9/1/2006. It can be seen that parts of the Eastern Shore, Poquoson, and Yorktown are inundated at that time, but not as seriously as during Hurricane Isabel. Since Tropical Storm Ernesto was even weaker than a Category 1 hurricane, the modeled inundation map is generally consistent with but the inundated area is less than the storm surge inundation map generated by VDEM. Figure 3.77 shows the modeled inundation map after Tropical Storm Ernesto vacated by 18:00 UTC 9/3/2006. It can be seen that the inundation has disappeared for most of the inundated area at this time. Overall, our high-resolution inundation model can generate a reasonable inundation map during Tropical Storm Ernesto.

3.3 Conclusions

The storm surge model with a large domain grid was able to generate reasonable water elevation results during Hurricane Isabel using only a tidal boundary condition at the open boundary. Since the difficulty of specifying the open boundary condition in the limited domain was solved using the dual-grid methodology, the model achieved the predictive capability for forecasting storm surge and inundation as long as acurate atmospheric wind is provided. The water elevations results are highly dependent on the quality of the wind and pressure fields. In this study, 7 types of wind are given and the WRF-GFS wind has proven to be the best wind. The high-resolution inundation model using the water elevations output from the large domain model as the open boundary condition could generate a reasonable inundation map. It is proved that this model framework could be used for the inundation simulation. The atmospheric models used in this study simulate the hurricane winds reasonably well, but could not generate the required quality of winds for an weak tropical storm like Ernesto. As a result, the storm surge results generated during Ernesto were not as good statistically as that of Hurricane Isabel. This demonstrated that the accuracy of the atmospheric forecasting wind field matters and it requires a major improvement for the wind field before the storm surge and inundation forecasting can become a reality.

Chapter 4. Model sensitivity analysis

Sensitivity analysis in this chapter is to study how different sources of variation in the model input, setup, and parameters can affect the output of the model. Specifically, three issues in connection with storm surge and inundation modeling are investigated. They are: (1) ensemble forecasting (2) influence of continental shelf dynamics and (3) accuracy of topographic data on storm surge and inundation simulation.

4.1 Ensemble forecasting

The ensemble forecast is usually evaluated in terms of the ensemble mean and the ensemble spread of a forecast variable, which represents the degree of agreement between various forecasts in the ensemble system, known as ensemble members. Use of ensemble forecasts helps to define the forecast uncertainty and extend weather forecasting farther into the future than would otherwise be possible. In the last Chapter, it was reported that the water elevations are simulated with 7 different members of winds provided by NWS Wakefield office and Weatherflow Inc. . For each member of wind, one continuous simulation was conducted and lasted for the period of storm from the beginning to the end as a benchmark. These continuous winds are generated by piecing together the 30-hour-length (or 24-hour-length in the case of RAMS) forecasting winds together. The simulation with continuous winds is a useful exercise only for the hindcast mode in exploring the capability of either atmospheric or storm surge models. In the forecasting mode,

there is no continuous wind lasting from the beginning to the end of a storm. Instead, the wind we could get is the 30-hour-length (or 24-hour-length) forecasting wind which is updating every 6 or 12 hour. Since our model is developed for forecasting purpose, the ensemble runs with the different kinds of 30-hour-length forecasting wind are simulated and discussed in this section. For a continuous wind, one run with one submission is sufficient. However, for the simulation with forecasting winds, 7 runs with different kinds of wind but the same initial condition are needed. Since the winds are updated every 6 hour (or 12 hour), the initial condition for the hydrodynamic model need to be updated every 6 hour (or 12 hour) as well. Thus, Every time the new update is available, a new 7-run will be submitted. A Linux script file has been developed and executed in a Linux cluster machine. The ensemble results discussed here is for the Hurricane Isabel only (the tropical storm wind field for Ernesto is yet to be assembled and verified). For Hurricane Isabel, the surface elevation results of ensemble runs have been generated with 30 hour (when using winds from NWS) or 24 hour (when using winds from RAMS) lengths. Among 55 outputs, 40 used the 4 members of wind from NWS (WRF-GFS, WRF-NAM, GFS, NAM), so for each member of wind model there are 10 outputs starting at 9/17/2003 0:00 UTC, 9/17/2003 6:00 UTC, 9/17/2003 12:00 UTC, 9/17/2003 18:00 UTC, 9/18/2003 0:00 UTC, 9/18/2003 6:00 UTC, 9/18/2003 12:00 UTC, 9/18/2003 18:00 UTC, 9/19/2003 0:00 UTC and 9/19/2003 6:00 UTC in separate runs. There are 15 outputs used 3 winds from Weatherflow Inc (RAMS Grid 1, Grid 2 and Grid 3). In the case of RAMS wind there are 5 outputs starting at 9/17/2003 0:00 UTC, 9/17/2003 12:00 UTC, 9/18/2003 0:00 UTC, 9/18/2003 12:00 UTC and 9/19/2003 0:00 UTC in separate runs. In the following, discussions about the ensemble results starting at 9/18/2003 12:00 UTC are given.

In Figure 4.1, plots of 30 hour-length water elevations at station CBBT were generated with different forecasting winds. It is obvious that the water elevations generated with different winds do have differences. The water elevations generated with WRF-GFS winds matched the observations the best. The water elevations generated with NAM and WRF-NAM winds were underestimated during the peak and overestimated after the peak. The water elevations generated with RAMS winds (Grid1, Grid2, and Grid3) were overestimated during the peak and underestimated after the peak. Figure 4.2 shows the difference between the modeled and observed water elevations at station CBBT. It can be seen that the water elevations generated with WRF-NAM and NAM were underestimated as low as approximately 0.5 m during the peak period and overestimated more than 0.5 m after the peak. The water elevations generated with RAMS Grid1 wind were overestimated 0.7 m during the peak and underestimated 0.3 m after the peak. The difference between the modeled water elevations generated by WRF-GFS wind and the observations is generally within 0.2 m. For Station Kiptopeke in the lower Bay, it can be seen in Figure 4.3 that the pattern of the time series plot of water elevations generated with different winds is quite similar to that at Station CBBT. Figure 4.4 shows the difference between the modeled and observed water elevations at Station Kiptopeke. It can be seen that the water elevations generated with WRF-NAM and NAM were underestimated as low as about 0.4 m during the peak period and overestimated about 0.5 m after the peak. The water elevations generated with RAMS Grid1 wind are overestimated 0.5 m over the peak and underestimated 0.3 m after the peak. The difference of the modeled water elevations by WRF-GFS wind and observations is generally within 0.2m. For Station Sewells Point in the lower Bay, it can be seen in Figure 4.5 that the water elevations generated with different winds have an even larger deviation than those at Stations CBBT and Kiptopeke. Figure 4.6 shows the difference between

the modeled and observed water elevations at Station Sewells Point. It can be seen that the water elevations generated with WRF-NAM and NAM were underestimated as low as 0.5 m during the peak period and overestimated more than 0.5 m after the peak. The water elevations generated with RAMS Grid1 wind were overestimated about 0.9 m during the peak and underestimated 0.4 m after the peak. The difference of the modeled water elevations by WRF-GFS wind and observations is generally within 0.3m. It can be seen at the three stations in the lower Bay (CBBT, Kiptopeke and Sewells Point), the patterns of the water elevation plots with different winds are very similar. The observations are generally in the envelope generated by the ensemble water elevations. The deviation increases from the Bay mouth to the inner lower Bay.

As can be seen in Figure 4.7, at Station Lewisetta the deviation of the water elevations generated with different winds decreased compared with that at Station Sewells Point. The water elevations generated with WRF-GFS and GFS winds were overestimated after the peak. The water elevations generated with NAM and WRF-NAM winds were underestimated during the peak and overestimated after the peak. The water elevations generated with RAMS winds (Grid1, Grid2, and Grid3) compare well with the observations. Figure 4.8 shows the difference between the modeled and observed water elevations at Station Lewisetta. It can be seen that the difference between the water elevations generated with WRF-NAM and NAM is larger than that in the lower Bay. The water elevations generated with WRF-NAM winds were underestimated by about 0.3 m during the peak period, but the water elevations generated with NAM winds were underestimated by about 0.5 m during the peak. The water elevations generated with WRF-GFS winds are overestimated 0.3 m after the peak. The difference of the modeled water elevations by RAMS winds and observations is generally within 0.3 m.

For Station Cambridge, it can be seen in Figure 4.9 that the deviation of the water elevations generated with different winds increased. The water elevations generated with NAM and WRF-NAM winds are underestimated over the peak. The water elevations generated with other winds are not so bad. Figure 4.10 shows the difference between the modeled and observed water elevations at Station Cambridge. It can be seen that the water elevations generated with WRF-NAM and NAM are overestimated about 0.4 m and 0.2 m separately before the peak and underestimated 0.7 m and 0.9 m separately during the peak period. The water elevations generated with WRF-GFS winds are overestimated 0.3 m after the peak. The difference of the modeled water elevations by RAMS wind and observations is generally within 0.4 m.

For the three stations in the upper Bay (Annapolis, Baltimore and Tolchester Beach), as can be seen in Figure 4.11, Figure 4.13 and Figure 4.15, respectively, the deviation of the water elevations generated with different winds increases while moving to the upper Bay. The deviation is mainly from WRF-NAM and NAM winds. At these stations, the water elevations generated with NAM and WRF-NAM winds are underestimated during the peak and overestimated before the peak. Figure 4.12, Figure 4.14, and Figure 4.16 show the difference between the modeled and observed water elevations at Stations Annapolis, Baltimore, and Tolchester Beach. It can be seen that the water elevations generated with WRF-NAM are underestimated 1.0 m at Annapolis, 1.2 m at Baltimore, and 1.3 m at Tolchester Beach during the peak and are overestimated 0.2 m at Annapolis, 0.2 m at Baltimore, and 0.4 m at Tolchester Beach after the peak. The water elevations generated with NAM are underestimated 1.2 m at Annapolis, 1.4 m at Baltimore, and 1.5 m at Tolchester Beach during the peak.

As can be seen in the figures of ensemble results, the observed water elevations generally fell in the range of the water elevations generated with different winds. So our storm surge model could generate a range of the modeled storm surge and give the best and worst conditions that would occur. From the comparisons, it can be seen that the WRF-GFS and GFS winds are generally more reliable than other winds for most of the stations in the Bay and the WRF-NAM and NAM winds are the two most unreliable winds. The WRF-NAM and NAM winds could generate more than 1 meter error in water elevation simulations, so when the NAM and WRF-NAM winds are included in the ensemble runs, one should be careful utilizing the results. A possible way is to exclude the NAM and WRF-NAM winds while forecasting. This study only generated the range of possible water elevations with different winds during Hurricane Isabel, but did not generate water elevation predictions by averaging all the water elevations simulated with different winds because the simple average was unable to yield good water elevations. More studies should be done in order to utilize the ensemble techniques.

4.2 Influence of continental shelf dynamics on storm surge in the Bay

4.2.1Ekman transport

Ekman dynamics is important when the friction effect is modified by the earth rotation such as that frequently occurred in the continental shelf and in the open ocean. Mathematically, Ekman dynamics within a free surface could be expressed as the balance between the Coriolis force and viscous force in the boundary layer:

$$-fv = K_v \frac{d^2u}{dz^2}$$

$$fu = K_v \frac{d^2 v}{dz^2}$$

The equations can be solved with the boundary condition at the free surface. The solution of the horizontal velocity at different depths form a spiral, called the Ekman spiral. The vertical integration of the velocity shows that the net transport is to the right of the surface wind stress (in the northern hemisphere) which is called Ekman transport. It is a known fact that the Ekman transport plays a role in the water exchange between the Chesapeake Bay and the continental shelf. The questions of whether a vertically averaged 2D model can model the storm surge without resolving Ekman dynamics is an open question.

Initially, we set up the storm surge model in two-dimensional mode. It was found that the water elevation in the lower bay is overestimated after the peak water level during Hurricane Isabel (Figure 4.17). Several attempts had been tried in solving this problem. Eventually, it was discovered that the overestimation only occurred when the wind blew from the south toward the north. Given the only one vertical layer of 2D model, Ekman transport may not be accurately simulated. In this situation, without enough Ekman transport to drive the water out of the Bay, the model simulation inside the Bay is overestimated. In other words, this overestimation could be due to the artifact of formulation in 2D model which is unable to resolve the vertical structure of Ekman layer. In the continental shelf, the water column has a minimum of a surface Ekman layer, an interior layer, and a bottom Ekman layer, which a one-layer 2D model cannot resolve. Ideally, the best way to test the hypothesis is to set up a full blown three-dimensional model with fine resolution in the vertical everywhere. As has been discussed in Chapter 2, section 2.2.4, it is not practical and overkill to develop a full 3D model with all baroclinic effects included for

storm surge prediction. As a compromise, a quasi-3D model was set up, in which baroclinic effect is neglected, and the resolution in the vertical grid given is relatively coarse. The detail assignment of the vertical grid was described in page 34, Chapter 3. One of the issues associated with setting up the quasi-3D model is how to specify vertical eddy viscosity. Traditionally, two-and-a-half-equation turbulent closures were used in the 3D model, but since our model is only a quasi-3D model, these methods were not used. Instead, a semi-empirical formulation from Davies (1997), as discussed the in Chapter 2, section 2.2.4, was employed in our model. The same parameters used in the 2D model for the bottom drag coefficient were used in the 3D model. As can be seen in Figure 4.18, with the quasi-3D model, much improved results were obtained and the previous problem of overestimation (after the storm peak) no longer exists. In addition, the current velocity and eddy viscosity profiles for the 3D and the 2D model were investigated. The location chosen was at node 25165 in the continental shelf (Figure 4.19). The current profiles are plotted during the south wind at speed 13.60 m/s after the Hurricane Isabel made landfall. Figure 4.20 showed the current profiles from the results of 3D model while Figure 4.21 showed the current profiles from the results of 2D model. It can seen in Figure 4.20 and Figure 4.21 that during south wind, the current direction veers toward the right hand side of the wind direction. The current profiles from 3D model showed that the velocity vectors at different layer are different in direction to form a spiral, but the current profiles from 2D model only have one direction. The conresponding eddy viscosity profiles are shown on the right hand side panel of Figure 4.20 and 4.21. Based on our comparison, the 3D model resolve the Ekman layer more accurately and can simulate the current more realisticly than the 2D model.

A further experiment was conducted to test the effect of Ekman transport with and without Coriolis force. It can be seen in Figure 4.22 that with Coriolis force, the modeled water elevation

matches the observations very well, but without the Coriolis force, the water level before the peak is underestimated and after the peak is overestimated. This could be explained as follows: Without Coriolis force, the Ekman effect was missing. As a consequence, when the north to northeast wind was blowing (From 9/17/2003 0:00 UTC to 9/18/2003 12:00 UTC), there is not enough water driven into the Bay (right hand side of the wind direction). In contrast, after the storm peak, when the southeast and south wind is blowing (9/19/2003 0:00 UTC to 9/19/2003 22:00 UTC), without the Ekman transport, the water in the Bay mouth area was overestimated because water was not driven offshore quickly enough. This experiment validated the hypothesis that the Ekman dynamics is an important process that drives the water exchanged between the bay and the continental shelf. It also demonstrated that a quasi-three dimensional model can improve the simulation if the Ekman layer structure in the vertical is incorporated.

It is worth noting that turning off the Coriolis force will not only influence the simulation of Ekman dynamics but also other geophysical processes, such as, Kelvin wave (a wave in the ocean that balances the Earth's Coriolis force against a topographic boundary), geostrophic current (a balance between the Coriolis effect and the pressure gradient force in the continental shelf), and so on. These processes will not be simulated correctly when the Coriolis force is turned off. During the strong wind, however, the Ekman dynamics are the most dominant process that involves the Coriolis force; thus our experiment manifests the importance of the Coriolis force associated with Ekman dynamics.

4.2.2 Specification of limited domain boundary condition

During the hurricane, the water elevation in the continental shelf is dynamically very different from the water elevations in a normal tide condition. The rapid changes of water elevations in the

continental shelf must also have dramatic influence on the water elevations in the Bay. Thus, for an accurate inundation simulation, it is necessary to specify a proper open boundary condition using the water elevation outputs from the large domain model for the high-resolution limited domain model. To test the importance of the open boundary condition for the small limited domain, two simulations – one with tide boundary condition and the other with outputs from the large domain model - were run using exact the same inputs and parameters. The results are shown in Figure 4.23, Figure 4.24 and Figure 4.25 for the lower Bay, middle Bay and upper Bay, respectively. It can be seen in Figure 4.23 that for the simulation with the outputs from the large domain as the boundary conditions (red line), the modeled water elevations matched the observations in the lower Bay very well. For the simulation with tide as the boundary conditions (black line), the water elevations at the three stations in the lower Bay are simulated quite well before the peak and during the peak, but the water elevations drop quickly after the peak and are underestimated about 0.5 m after 9/19 3:00 UTC. As can be seen in Figure 4.24, the water elevations at the three stations in the middle Bay from the simulation using the tide as the boundary condition are underestimated about 0.3 m during the peak and are underestimated about 0.5 m after the peak. For the three stations in the upper Bay, the water elevations from the simulation using the tide as the boundary condition are underestimated before and during the peak (Figure 4.25). The underestimation is around 0.3 m to 0.5 m. This experiment demonstrated that it is necessary for the limited domain model inundation model to use the outputs from the large domain model as the open boundary condition. Otherwise, it will cause 30 to 50 cm underestimation of the water elevation during a hurricane. This in turn will cause the model to generate an incorrect inundation map.

4.3 Effect of the accuracy of topographic data on inundation simulation

The accurate simulation of the inundation highly depends on the resolution of the grid covering the land area. It might be adequate to use a relatively low-resolution grid for an area where the topography does not significantly change, but it is not proper to use a low-resolution grid for an area with different kinds of topographic features. For example, if there is a sand bar or sea wall along a low-lying coastal area, this area may not be inundated with the protection of these features. The simulation will be correct when a high-resolution grid is used and these features are well-represented. However, a low-resolution grid may generate the results that this area is inundated during a hurricane, which is totally wrong. That is why the high-resolution grid was generated for the Virginia Beach and Hampton Roads area. However, the high-resolution grid can not guarantee the correct inundation results without accurate topographic data. Here an experiment is conducted to examine the influence of the high-resolution grid with and without accurate LiDAR data on the inundation. Two simulations are conducted with the same setup and using the water elevation outputs from the large domain model as the open boundary condition. The only difference for the two simulations is that one horizontal grid is with accurate LiDAR data as the topography but the other not. Figure 4.26 shows the inundation map at 9/18/2003 21:00 UTC generated by the simulation using the LiDAR data and Figure 4.27 shows the inundation map at the same time but generated by the simulation using the grid without LiDAR data. In fact, there are several obvious differences. 3 areas are selected for the comparison and each area is labeled with a number. For area 1, the simulation with LiDAR data shows no inundation occurred in this area near the Back Bay in Virginia Beach, but the simulation without LiDAR data shows a large area is inundated. It might be due to that the sea wall along the Virginia Beach protecting these low-lying areas from inundation, but the simulation without

LiDAR data did not resolve the sea wall. For area 2, the simulation with LiDAR data shows that the western part of Craney Island is not inundated during Hurricane Isabel, but the simulation without LiDAR data shows that the western part of Craney Island is inundated. The simulation with the LiDAR data should be correct because it is known that there are walls protecting Craney Island. For area 3, the simulation with LiDAR data shows that the Poquoson area is inundated seriously and the eastern part of the Hampton is inundated as well, but the simulation without LiDAR data shows that the southern part of the Poquoson area is not inundated, the northern part of the Poquoson area is not inundated as seriously as the simulation with LiDAR data and the Hampton area is not significantly inundated. When compared to the inundation map (Figure 3.32) from the Virginia Department of Emergency Management, it can be seen that the inundation generated by the grid with LiDAR data is more realistic. Overall, the grid using high quality topographic LiDAR data did produce more accurate inundation predictions.

Chapter 5. Discussion and conclusion

A large domain grid covering the Atlantic Ocean from Nova Scotia to Florida was generated for the storm surge simulation. With this grid, a 3-dimensional storm surge using ELCIRC model for forecasting purpose was developed. The model uses an unstructured grid, with mixed triangular and quadrilateral cells, allowing boundary fitting and local grid refinements to meet the needs of resolving small topographic and bathymetric features. The combination of the Eulerian-Lagrangian scheme with a semi-implicit finite difference method allows the model to run over a very high resolution grid with a relative large time step. The storm surge simulations proved that this 3D model is a very efficient, stable and accurate model. A large time step (5 minutes) is used for the storm surge simulation, so even though our large domain grid size is huge (165015 cells), it only requires 1.5 hours of execution for a 1-day simulation of water elevation. With only the tide as the open boundary condition, this model can generate reasonable storm surge results, so this model could be used for forecasting purpose. The storm surge caused by Hurricane Isabel is simulated with 7 members of wind. Of all the winds, WRF-GFS is the best one. The water elevations simulated with WRF-GFS wind are also the best modeled water elevations. The storm surge simulations are highly dependent on the quality of the wind and pressure field. Thus the storm surge caused by Tropical Storm Ernesto was not simulated very well.

For the inundation simulation, a limited domain high-resolution grid covering the Virginia Beach and Hampton Roads area mapped with LiDAR data was generated and coupled with the large domain grid. The open boundary was specified using the outputs from the large domain model. The inundation map generated with the high-resolution model is consistent with the inundation map from the Virginia Department of Emergency Management. It demonstrated that a high-resolution model grid is essential to simulate storm surge and inundation accurately.

Several sensitivity tests were performed. Our storm surge model has been set up for forecasting purpose with ensemble methods. The model can forecast a range of water elevations during a hurricane so that the worst and best storm surge and inundation condition can be known. An important finding of this study is that it is necessary to use a quasi-3D model in order to simulate the Ekman dynamics and storm surge accurately. A 2D model is generally unable to resolve the three-layer vertical strucutre (surface Ekman layer, interior layer and bottom Ekman layer) and thus unable to simulate the Ekman dynamics correctly. The simulations with and without Coriolis force proved that the Ekman transport play an important role in the storm tide simulation. Therefore, a quasi-3D model is the preferred choice for a storm surge model. The open boundary condition is quite important for simulating the storm surge and inundation when using the limited small domain grid. Our experiments proved that the coupling of the large domain and limited domain grids is important and that it is necessary to use the water elevation outputs from the large domain model as the open boundary condition. The experiments running the small domain model with and without LiDAR data demonstrated that the grid with LiDAR data could generate more accurate inundation map and that LiDAR data is necessary for the inundation simulation.

Future works

There are still several studies that should be done in the future. First, even though our storm surge and inundation could simulate the Hurricane Isabel very well, more tests with other storm surge cases still need to be performed to validate the capability of our model. Second, for forecasting purpose, the parallel computing technique needs to be employed to improve computational speed. Third, this model needs to be coupled with a wave model in order to improve the simulation. Fourth, to simulate the inundation in other areas in the Bay, the high-resolution grids covering these areas need to be generated and mapped with LiDAR topographic data. Last but not least important, more study of the ensemble method is also needed for forecasting purpose.

APPENDIX

Appendix A. Definitions of statistical quantities for error analysis

To quantify the capability of the atmospheric models and our storm surge model, the following statistical measures are calculated:

The root-mean-square (RMS) error is calculated for wind speeds, wind directions, pressures and water elevations, if they are represented by x, then:

$$RMS = \left\{ \frac{1}{N} \sum_{i=1}^{N} (x_{\mathrm{mod}} - x_{obs})^2 \right\}^{1/2},$$

The relative error (E), the correlation coefficient and skill score are calculated for water elevations, if water elevation is represented by η, then:

The relative error $$E = 100\% \frac{\sum_{i=1}^{N} (\eta_{\mathrm{mod}} - \eta_{obs})^2}{\sum_{i=1}^{N} ((\eta_{\mathrm{mod}} - \overline{\eta}_{obs})^2 + (\eta_{obs} - \overline{\eta}_{obs})^2)}$$

The correlation coefficient $$r = \frac{\sum_{i=1}^{N} (\eta_{\mathrm{mod}} - \overline{\eta}_{\mathrm{mod}})(\eta_{obs} - \overline{\eta}_{obs})}{\left[\sum_{i=1}^{N} (\eta_{\mathrm{mod}} - \overline{\eta}_{\mathrm{mod}})^2 \sum_{i=1}^{N} (\eta_{obs} - \overline{\eta}_{obs})^2 \right]^{1/2}}$$

and the skill score $$skill = 1 - \frac{\sum_{i=1}^{N} (\eta_{\mathrm{mod}} - \eta_{obs})^2}{\sum_{i=1}^{N} \left(|\eta_{\mathrm{mod}} - \overline{\eta}_{obs}| + |\eta_{obs} - \overline{\eta}_{obs}| \right)^2}$$

Appendix B. The Saffir-Simpson Hurricane Sacle

The Saffir-Simpson Hurricane Scale is a 1-5 rating based on the hurricane's present intensity. This is used to give an estimate of the potential property damage and flooding expected along the coast from a hurricane landfall. Wind speed is the determining factor in the scale, as storm surge values are highly dependent on the slope of the continental shelf in the landfall region. Note that all winds are using the U.S. 1-minute average.

Category	Sustained Winds in mph	Barometric Pressure in minibars	Storm Surge in feet above normal	Damage
1	74-95	>980	4-5	Minimal
2	96-110	965-979	6-8	Moderate
3	111-130	945-964	9-12	Extensive
4	131-155	920-944	13-18	Extreme
5	>155	<920	>18	Catastrophic

LITERATURE CITED

Bernier, N. B., and Thompson, K. R. (2006). Predicting the frequency of storm surges and extreme sea levels in the northwest Atlantic. *J. Geophys. Res.,* 111, C10009.

Billet, J. (2009). Personal communication with senior meteorologist in National Weather Service, Wakefield office.

Blain, C.A., Westerink, J.J., and R.A. Luettich. (1994). The influence of domain size on the response characteristics of a hurricane storm surge model. *Journal of Geophysical Research*, 99, 18467-18479.

Blumberg, A.F., and Mellor, G.L. (1987). A description of a three dimensional coastal ocean circulation model. In N. Heaps (ed.), Three Dimensional Coastal Ocean Circulation Models, American Geophysical Union, Washington, D.C., 4:1-16.

Bretschneider, C.L. (1959). Hurricane surge predictors for Chesapeake Bay, Corps of Engineers, Washington, DC, Sept., Technical report, AD699408, 51p.

Casulli, V., and Cattani, E. (1994). Stability, accuracy and efficiency of a semi-implicit method for 3D shallow water flow. *Computers & Mathematics with Applications*, 27, 99 - 112.

Casulli, V., and Cheng, R.T. (1992). Semi-implicit finite difference methods for three-dimensional shallow water flow. *International Journal of Numerical Methods in Fluids*, 15, 629 - 648.

Casulli, V., and Zanolli, P. (1998). A three-dimensional semi-implicit algorithm for environmental flows on unstructured grids. Institute for Computational Fluid Dynamics. Conference on Numerical Methods for Fluid Dynamics VI.

Chuang, W., and Boicourt, W.C. (1989). Resonant seiche motion in the Chesapeake Bay. *J. Geophys. Res.*, 94, C2, 2105-2111.

Davies, A.M., Kwong, S.C.M., and Flather, R.A. (1997). Formulation of a variable-function three-dimensional model, with applications to the M2 and M4 tide on the North-West European continental Shelf. *Continental Shelf Research*, Vol. 17, No. 2, pp. 165-204.

Dobroklonsky, S.V. (1947). Turbulent viscosity in sea surface layer and wind waves, *Reports of the Academy of Sciences of the USSR*, vol.68, No.7.

Donelan, M.A., Haus, B.K., Reul, N., Plant, W.J., Stiassnie, M., Graber, H.C., Brown, O.B., and Saltzman, E.S. (2004). On the limiting aerodynamic roughness of the ocean in very strong winds, *Geophysical research letters*, Vol. 31, L18306.

Flather, R.A., Proctor, R., and Wolf, J. (1991). Oceanographic forecast models. *Computer Modeling in the Environmental Sciences*. D.G. Famer and M.J. Rycroft (Eds.), Oxford. U.K., 15-30.

Harris, D.L. (1956). Some Problems Involved in the Study of Storm Surges. *NHRP Report No. 4*, U.S. Weather Bureau.

Harris, D.L. (1963). Characteristics of the Hurricane storm surge. *Technical Paper No. 48*, U.S.Weather Bureau.

Hubbert, G.D., and McInnes, K.L. (1999). A storm surge inundation model for coastal planning and impact studies. *Journal of Coastal Research* ,15 (1),168-185

Ichiye, T. (1967). Upper ocean boundary-layer flow determined by dye diffusion. *The physics of fluids supplement*. S270-S277

Jelesnianski, C. P. (1972). SLASH (Special Program to List Amplitudes of Surges from Hurricanes) I: Landfall storms. *NOAA Technical Memorandum NWS TDL-46*, U.S. Department of Commerce, NOAA, NWS, Silver Springs, MD., 52 pp.

Jelesnianski, C. P. (1974). SLASH (Special Program to List Amplitudes of Surges from Hurricanes) II: General track and variant storm conditions. *NOAA Technical Memorandum NWS TDL-52*, U.S.Department of Commerce, NOAA, NWS, Silver Springs, MD., 55 pp.

Jelesnianski, C.P., Chen, J. and Shaffer, W.A. (1992). SLOSH: sea, lake, and overland surges from hurricane. National Weather Service, Silver Springs, MD.

Johnson, D.L. (2004). Hurricane Isabel service assessment report. National Weather Service, Silver Springs, MD.

Knabb, R. D., and Mainelli, M. (2006). Tropical cyclone report: Hurricane Ernesto. National Hurricane Center.

Kohut, J. T., Glenn, S. M., and Paduan, J. D. (2006). Inner shelf response to Tropical Storm Floyd. *J. Geophys. Res.*, 111, C09S91.

Large, W.G. and Pond, S., 1981. Open ocean flux measurements in moderate to storng winds. *Journal of Physical Oceanography*, Vol .11, 324-336.

Li, M., Zhong, Li, Boicourt, W.C., Zhang, S., and Zhang, D. L. (2006). Hurricane-induced storm surges, currents and destratification in a semi-enclosed Bay. *Geophysical Research Letter*, 33, L02604.

Luettich, R.A.,Westerink, J.J., and Scheffner, N.W. (1992). ADCIRC: An Advanced Three-Dimensional Circulation Model for Shelves, Coasts, and Estuaries, Report I, Theory and Methodology of ADCIRC-2DDI and ADCIRC-3DL. US Army Corps of Engineers. Technical Report DRP-92-6.

Lynch, D.R. (1983). Progress in hydrodynamic modeling, review of U.S.contributions, 1979-1982. *Reviews of Geophysics and Space Physics* 21 (30), 741-754.

Mukai, A.Y., Westreink, J.J., and Luettich, R.A. (2002). Guidelines for Using East-coast 2001 Database of Tidal Constituents within Western North Atlantic Ocean, Gulf of Mexico and Caribbean. US Army Corps of Engineers, ERDC/CHL CHETN-IV-40, 20 pp.

National Hurricane Center, National Weather Service, NOAA (2009). http://www.nhc.noaa.gov/aboutgloss.shtml

Paraso, M. C., and Valle-Levinson, A. (1996). Meteorological influences on sea level and water temperature in the lower Chesapeake Bay: 1992. *Estuaries,* 19 (3), 548-561.

Pore, N. A. (1965). Chesapeake Bay extratropical storm surges. *Chesapeake Science*, 6(3), 172-182.

Pore, N. A. and Barrientos, C. S. (1976). Storm Surge, MESA New York Bight Atlas Monograph 6.

Powell, M.D., Vickery, P.J., and Reinhold, T.A. (2003). Reduced drag coefficient for high wind speeds in tropical cyclones. Nature,422, March 20 pp.279-283

Shen, J., Wang, H. V., Sisson, M., and Gong W. (2006a). Storm tide simulation in the Chesapeake Bay using an unstructured grid model. *Estuarine, Coastal and Shelf Science*, Vol. 68, pp.1-16.

Shen, J., Gong, W., and Wang, H. V. (2006b). Water level response to 1999 hurricane Floyd in the Chesapeake Bay. *Continental Shelf Research*, 26, 2484-2502.

Shen, J., Zhang, K., Xiao, C. and Gong, W. (2006c) Improved prediction of storm surge inundation with a high-resolution unstructured grid model. *Journal of Coastal Research*, 22, 6, 1309-1319.

Shen, J., and Gong, W. (2008). Influence of model domain size, wind directions and Ekman transport on storm surge development inside the Chesapeake Bay: A case study of extratropical cyclone Ernesto, 2006. *Journal of Marine Systems,* 75, 198-215.

Spitz, Y.H. and Klinck, J.M. (1998). Estimate of bottom and surface stress during a spring-neap tide cycle by dynamical assimilation of tide gauge observations in the Chesapeake Bay, *J. Geophys. Res.*, 103 (C6), 12761-12782.

Valle-Levinson, A., Wong, K.-C., and Bosley, T. (2002). Response of the lower Chesapeake Bay to forcing from Hurricane Floyd. *Continental Shelf Research,* 22, 1715 - 1729.

Wang, H. V, Cho, J., Shen, J., and Wang Y. (2005). What has been learned about storm surge dynamics from Hurricane Isabel model simulations? Hurricane Isabel in Perspective Conference, Baltimore, MD., Proceeding of a Conference, Chesapeake Bay Consortium, pp. 117-125.

Weisberg, R. H. and Zheng, L. (2006). Hurricane storm surge simulations for Tampa Bay. *Estuaries and Coasts*, 29(6A), 899-913.

Westerink, J.J., Luettich, R.A., Baptista, A.M., Scheffner, N.W., and Farrar, P. (1992). Tide and storm surge predictions using a finite element model. *Journal of Hydraulic Engineering*, 118, 1373-1390.

Zhang, Y., Baptista, A. M. and Meyers, E. P. (2004). A cross-scale model for 3D baroclinic circulation in estuary-plume-shelf system: I. Formulation and skill assessment. *Cont. Shelf Res.*, Vol. 24, pp. 2187-2214.

Table 2.1 Bathymetric and topographic data for interpolation

	Dataset	Resolution	Area
Water Portion	Global Relief Model (ETOPO2)	2 min	Ocean
	Coastal Relief Model	3 sec	Coastal area and Bay
	DEM for the lower Bay	1/3 sec	Lower Bay
Land Portion	LiDAR Data	10 m	Hampton Roads and Virginia Beach

Table 2.2 Comparison of harmonic constituents of field observations and modeled tide from large domain model along the Atlantic coastline (tidal amplitude in m)

Stations	Model	NOAA	Diff	Model	NOAA	Diff	Model	NOAA	Diff
	M2			S2			N2		
Newport, RI	0.58	0.50	0.08	0.10	0.10	0.00	0.14	0.12	0.02
Sandy Hook, NY	0.79	0.69	0.10	0.12	0.13	-0.01	0.18	0.16	0.02
Atlantic City, NJ	0.62	0.60	0.02	0.10	0.11	-0.01	0.15	0.14	0.01
Lewes, DE	0.60	0.61	-0.01	0.09	0.10	-0.01	0.14	0.13	0.01
Duck, NC	0.50	0.49	0.01	0.08	0.09	-0.01	0.12	0.11	0.01
Springmaid Pier, SC	0.80	0.74	0.06	0.11	0.12	-0.01	0.19	0.18	0.01
St.Simons Island, GA	1.12	0.98	0.14	0.13	0.16	-0.03	0.25	0.23	0.02
Trident Pier, FL	0.53	0.51	0.02	0.07	0.08	-0.01	0.13	0.12	0.01
Mean	**0.69**	**0.64**	**0.05**	**0.10**	**0.11**	**-0.01**	**0.16**	**0.15**	**0.01**
Standard Deviation	**0.20**	**0.16**	**0.05**	**0.02**	**0.03**	**0.01**	**0.04**	**0.04**	**0.01**
	K1			O1			Q1		
Newport, RI	0.08	0.06	0.02	0.05	0.05	0.00	0.01	0.01	0.00
Sandy Hook, NY	0.09	0.10	-0.01	0.05	0.05	0.00	0.01	0.01	0.00
Atlantic City, NJ	0.09	0.11	-0.02	0.05	0.07	-0.02	0.01	0.01	0.00
Lewes, DE	0.10	0.10	0.00	0.06	0.08	-0.02	0.01	0.01	0.00
Duck, NC	0.09	0.09	0.00	0.06	0.06	0.00	0.01	0.01	0.00
Springmaid Pier, SC	0.11	0.10	0.01	0.07	0.07	0.00	0.01	0.02	-0.01
St.Simons Island, GA	0.13	0.11	0.02	0.08	0.08	0.00	0.02	0.02	0.00
Trident Pier, FL	0.11	0.10	0.01	0.07	0.07	0.00	0.01	0.02	-0.01
Mean	**0.10**	**0.10**	**0.00**	**0.06**	**0.07**	**-0.01**	**0.01**	**0.01**	**0.00**
Standard Deviation	**0.02**	**0.02**	**0.01**	**0.01**	**0.01**	**0.01**	**0.00**	**0.01**	**0.00**

Table 2.3 Comparison of harmonic constituents of field observations and modeled tide from large domain model along the Atlantic coastline (phase in degrees)

Stations	Model	NOAA	Diff	Model	NOAA	Diff	Model	NOAA	Diff
	M2			S2			N2		
Newport, RI	158.94	151.04	7.90	44.09	28.43	15.66	179.61	176.15	3.46
Sandy Hook, NY	164.38	154.97	9.41	60.33	45.44	14.89	185.44	177.11	8.33
Atlantic City, NJ	149.45	144.39	5.06	38.41	32.35	6.06	167.9	164.65	3.25
Lewes, DE	185.26	180.08	5.18	78.40	70.70	7.70	202.22	200.85	1.37
Duck, NC	149.86	147.03	2.83	37.54	32.26	5.28	168.75	167.11	1.64
Springmaid Pier, SC	140.90	146.62	-5.72	39.01	34.24	4.77	169.03	167.05	1.98
St.simons Island, GA	170.51	172.33	-1.82	65.03	67.01	-1.98	188.81	196.44	-7.63
Trident Pier, FL	161.03	156.31	4.72	50.46	42.41	8.05	179.34	174.87	4.47
Mean	**160.04**	**156.60**	**3.45**	**51.66**	**44.11**	**7.55**	**180.14**	**178.03**	**2.11**
Standard Deviation	**13.88**	**12.94**	**5.00**	**14.94**	**16.29**	**5.68**	**11.92**	**13.59**	**4.52**

Table 2.4 Comparison of harmonic constituents of field observations and modeled tide from large domain model in the Chesapeake Bay (tidal amplitude in m)

Stations	Model	NOAA	Diff	Model	NOAA	Diff	Model	NOAA	Diff
	M2			S2			N2		
CBBT, VA	0.36	0.38	-0.02	0.07	0.10	-0.03	0.09	0.09	0.00
Kiptopeke, VA	0.37	0.39	-0.02	0.08	0.07	0.01	0.09	0.09	0.00
Sewells Pt., VA	0.32	0.36	-0.04	0.08	0.06	0.02	0.08	0.08	0.00
Yorktown, VA	0.28	0.33	-0.05	0.06	0.07	-0.01	0.06	0.07	-0.01
Windmill Pt., VA	0.18	0.18	0.00	0.04	0.03	0.01	0.04	0.04	0.00
Lewisetta, VA	0.19	0.18	0.01	0.04	0.03	0.01	0.04	0.04	0.00
Solomons Island, MD	0.16	0.17	-0.01	0.03	0.03	0.00	0.04	0.04	0.00
Cambridge, MD	0.20	0.24	-0.04	0.04	0.04	0.00	0.04	0.05	-0.01
Annapolis, MD	0.12	0.14	-0.02	0.02	0.02	0.00	0.03	0.03	0.00
Baltimore, MD	0.16	0.16	0.00	0.03	0.02	0.01	0.04	0.03	0.01
Tolchester, MD	0.16	0.17	-0.01	0.03	0.02	0.01	0.04	0.04	0.00
Mean	**0.23**	**0.25**	**-0.02**	**0.05**	**0.04**	**0.00**	**0.05**	**0.05**	**0.00**
Standard Deviation	**0.09**	**0.10**	**0.02**	**0.02**	**0.03**	**0.01**	**0.02**	**0.02**	**0.01**
	K1			O1			Q1		
CBBT, VA	0.06	0.06	0.00	0.03	0.04	-0.01	0.01	0.01	0.00
Kiptopeke, VA	0.06	0.06	0.00	0.04	0.04	0.00	0.01	0.01	0.00
Sewells Pt., VA	0.05	0.05	0.00	0.04	0.04	0.00	0.01	0.01	0.00
Yorktown, VA	0.05	0.05	0.00	0.03	0.03	0.00	0.01	0.01	0.00
Windmill Pt., VA	0.04	0.03	0.01	0.03	0.02	0.01	0.00	0.00	0.00
Lewisetta, VA	0.04	0.02	0.02	0.03	0.02	0.01	0.00	0.00	0.00
Solomons Island, MD	0.04	0.03	0.01	0.03	0.02	0.01	0.00	0.01	-0.01
Cambridge, MD	0.05	0.05	0.00	0.04	0.04	0.00	0.01	0.01	0.00
Annapolis, MD	0.05	0.06	-0.01	0.04	0.05	-0.01	0.01	0.01	0.00
Baltimore, MD	0.06	0.07	-0.01	0.05	0.06	-0.01	0.01	0.01	0.00
Tolchester, MD	0.06	0.07	-0.01	0.05	0.06	-0.01	0.01	0.01	0.00
Mean	**0.05**	**0.05**	**0.00**	**0.04**	**0.04**	**0.00**	**0.01**	**0.01**	**0.00**
Standard Deviation	**0.01**	**0.02**	**0.01**	**0.01**	**0.01**	**0.01**	**0.00**	**0.00**	**0.00**

Table 2.5 Comparison of harmonic constituents of field observations and modeled tide from large domain model in the Chesapeake Bay (phase in degrees)

Stations	Model	NOAA	Diff	Model	NOAA	Diff	Model	NOAA	Diff
	M2			S2			N2		
CBBT, VA	171.43	170.02	1.41	63.00	61.21	1.79	189.77	190.25	-0.48
Kiptopeke, VA	185.42	181.48	3.94	80.56	75.18	5.38	203.47	201.92	1.55
Sewells Pt., VA	198.81	195.63	3.18	93.02	88.42	4.60	216.91	217.58	-0.67
Yorktown, VA	207.68	202.49	5.19	101.74	96.17	5.57	225.53	224.66	0.87
Lewisetta, VA	329.52	325.32	4.20	224.95	227.52	-2.57	343.18	342.27	0.91
Solomons Island, MD	351.83	347.74	4.09	246.91	256.42	-9.51	4.91	3.61	1.30
Cambridge, MD	43.23	51.99	-8.76	303.38	318.34	-14.96	56.39	71.86	-15.47
Annapolis, MD	80.99	80.40	0.59	341.83	347.54	-5.71	94.72	100.48	-5.76
Baltimore, MD	117.37	125.86	-8.49	19.38	29.80	-10.42	130.39	144.29	-13.90
Tolchester, MD	124.04	135.44	-11.40	26.32	41.38	-15.06	136.7	151.76	-15.06
Mean	**181.03**	**181.64**	**-0.61**	**150.11**	**154.20**	**-4.09**	**160.20**	**164.87**	**-4.67**
Standard Deviation	**99.25**	**95.05**	**6.36**	**118.16**	**120.62**	**8.21**	**96.80**	**93.83**	**7.31**

Table 2.6 Comparison of harmonic constituents of field observations and modeled tide from small domain model in the Chesapeake Bay (tidal amplitude in m)

Stations	Model	NOAA	Diff	Model	NOAA	Diff	Model	NOAA	Diff
	M2			S2			N2		
CBBT, VA	0.38	0.38	0.00	0.05	0.10	-0.05	0.09	0.09	0.00
Kiptopeke, VA	0.40	0.39	0.01	0.05	0.07	-0.02	0.09	0.09	0.00
Sewells Pt., VA	0.33	0.36	-0.03	0.04	0.06	-0.02	0.07	0.08	-0.01
Yorktown, VA	0.29	0.33	-0.04	0.04	0.07	-0.03	0.06	0.07	-0.01
Windmill Pt., VA	0.17	0.18	-0.01	0.02	0.03	-0.01	0.04	0.04	0.00
Lewisetta, VA	0.18	0.18	0.00	0.02	0.03	-0.01	0.04	0.04	0.00
Solomons Island, MD	0.16	0.17	-0.01	0.02	0.03	-0.01	0.04	0.04	0.00
Cambridge, MD	0.19	0.24	-0.05	0.02	0.04	-0.02	0.04	0.05	-0.01
Annapolis, MD	0.10	0.14	-0.04	0.01	0.02	-0.01	0.04	0.03	0.01
Baltimore, MD	0.13	0.16	-0.03	0.01	0.02	-0.01	0.02	0.03	-0.01
Tolchester, MD	0.15	0.17	-0.02	0.01	0.02	-0.01	0.03	0.04	-0.01
Mean	**0.23**	**0.25**	**-0.02**	**0.03**	**0.04**	**-0.02**	**0.05**	**0.05**	**0.00**
Standard Deviation	**0.12**	**0.10**	**0.03**	**0.02**	**0.03**	**0.01**	**0.02**	**0.02**	**0.01**
	K1			O1			Q1		
CBBT, VA	0.06	0.06	0.00	0.05	0.04	0.01	0.01	0.01	0.00
Kiptopeke, VA	0.07	0.06	0.01	0.05	0.04	0.01	0.01	0.01	0.00
Sewells Pt., VA	0.06	0.05	0.01	0.04	0.04	0.00	0.01	0.01	0.00
Yorktown, VA	0.05	0.05	0.00	0.04	0.03	0.01	0.01	0.01	0.00
Windmill Pt., VA	0.04	0.03	0.01	0.03	0.02	0.01	0.00	0.00	0.00
Lewisetta, VA	0.04	0.02	0.02	0.03	0.02	0.01	0.00	0.00	0.00
Solomons Island, MD	0.04	0.03	0.01	0.03	0.02	0.01	0.00	0.01	-0.01
Cambridge, MD	0.05	0.05	0.00	0.04	0.04	0.00	0.01	0.01	0.00
Annapolis, MD	0.05	0.06	-0.01	0.04	0.05	-0.01	0.01	0.01	0.00
Baltimore, MD	0.06	0.07	-0.01	0.05	0.06	-0.01	0.01	0.01	0.00
Tolchester, MD	0.06	0.07	-0.01	0.05	0.06	-0.01	0.01	0.01	0.00
Mean	**0.05**	**0.05**	**0.00**	**0.04**	**0.04**	**0.00**	**0.01**	**0.01**	**0.00**
Standard Deviation	**0.01**	**0.02**	**0.01**	**0.01**	**0.01**	**0.01**	**0.00**	**0.00**	**0.00**

Table 3.1 RMS errors of different winds at 6 sations in the Bay during Hurricane Isabel

	Stations	CBBT	Sewells Pt.	Lewisetta	Cambridge	Thomas Pt.	Tolchester	**Mean**
GFS	Wind speed (m/s)	3.24	1.80	2.51	2.27	4.47	3.39	**2.95**
	direction (degrees)	17.36	33.47	18.51	71.91	26.50	40.33	**34.68**
	Pressure (Pa)	221.06	277.99	140.25	194.19	172.97	151.30	**192.96**
NAM	Wind speed (m/s)	3.89	3.36	2.33	1.47	3.47	4.33	**3.14**
	Direction (degrees)	15.77	46.46	23.79	53.24	23.94	49.82	**35.50**
	Pressure (Pa)	241.68	210.17	213.47	173.98	211.40	157.18	**201.31**
WRF-GFS	Wind speed (m/s)	2.55	2.83	3.40	3.32	2.81	6.62	**3.59**
	Direction (degrees)	8.54	36.46	18.67	43.55	16.03	35.42	**26.45**
	Pressure (Pa)	164.04	182.52	126.00	155.86	151.54	135.77	**152.62**
WRF-NAM	Wind speed (m/s)	2.99	2.05	2.85	2.96	2.17	6.21	**3.20**
	Direction (degrees)	11.55	33.85	17.76	42.37	16.03	33.50	**25.84**
	Pressure (Pa)	330.04	289.35	263.30	180.38	201.91	164.77	**238.29**
RAMS Grid1	Wind speed (m/s)	4.00	4.25	3.16	3.44	4.56	4.21	**3.94**
	Direction (degrees)	12.20	38.27	22.07	50.98	23.31	41.01	**31.31**
	Pressure (Pa)	522.10	611.54	307.54	303.02	267.58	261.90	**378.95**
RAMS Grid2	Wind speed (m/s)	3.14	3.44	2.81	3.27	3.22	4.60	**3.41**
	Direction (degrees)	11.45	36.65	21.00	50.71	26.25	36.05	**30.35**
	Pressure (Pa)	528.21	619.23	307.17	305.63	268.30	263.90	**382.07**
RAMS Grid3	Wind speed (m/s)	3.07	3.22	2.87	2.57	1.80	3.61	**2.86**
	Direction (degrees)	11.23	37.21	21.87	50.28	26.23	36.59	**30.57**
	Pressure (Pa)	532.16	634.69	391.60	320.42	298.85	282.24	**409.99**

Table 3.2 Statistical measures for estimating the errors of water elevations generated with GFS during Hurricane Isabel

station	RMS (m)	relative error	correlation	skill
Tolchester	0.16	3.06%	0.99	0.98
Baltimore	0.18	3.66%	0.99	0.98
Annapolis	0.13	2.52%	0.99	0.99
Cambridge	0.08	1.12%	0.99	0.99
Lewisetta	0.11	3.15%	0.98	0.98
Sewells Pt.	0.22	8.16%	0.96	0.96
Kiptopeke	0.16	7.65%	0.96	0.96
CBBT	0.19	8.42%	0.95	0.96
mean	**0.15**	**4.72%**	**0.98**	**0.98**

Table 3.3 Statistical measures for estimating the errors of water elevations generated with NAM during Hurricane Isabel

station	RMS (m)	relative error	correlation	skill
Tolchester	0.18	3.24%	0.98	0.98
Baltimore	0.21	4.55%	0.98	0.98
Annapolis	0.18	4.06%	0.98	0.98
Cambridge	0.19	6.46%	0.95	0.97
Lewisetta	0.16	6.73%	0.95	0.97
Sewells Pt.	0.17	6.23%	0.95	0.97
Kiptopeke	0.16	9.21%	0.91	0.97
CBBT	0.17	8.21%	0.93	0.96
mean	**0.18**	**6.09%**	**0.96**	**0.97**

Table 3.4 Statistical measures for estimating the errors of water elevations generated with WRF-GFS during Hurricane Isabel

station	RMS (m)	relative error	correlation	skill
Tolchester	0.18	3.50%	0.99	0.98
Baltimore	0.19	3.80%	0.99	0.98
Annapolis	0.17	3.92%	0.99	0.98
Cambridge	0.17	5.76%	0.97	0.97
Lewisetta	0.12	3.73%	0.98	0.98
Sewells Pt.	0.13	3.51%	0.97	0.98
Kiptopeke	0.12	4.84%	0.95	0.98
CBBT	0.12	3.82%	0.97	0.98
mean	**0.15**	**4.11%**	**0.98**	**0.98**

Table 3.5 Statistical measures for estimating the errors of water elevations generated with WRF-NAM during Hurricane Isabel

station	RMS (m)	relative error	correlation	skill
Tolchester	0.18	3.53%	0.99	0.98
Baltimore	0.19	3.96%	0.99	0.98
Annapolis	0.17	3.75%	0.99	0.98
Cambridge	0.13	3.37%	0.99	0.98
Lewisetta	0.14	5.41%	0.97	0.97
Sewells Pt.	0.17	7.55%	0.95	0.96
Kiptopeke	0.15	9.71%	0.92	0.95
CBBT	0.18	10.45%	0.93	0.95
mean	**0.16**	**5.97%**	**0.97**	**0.97**

Table 3.6 Statistical measures for estimating the errors of water elevations generated with RAMS grid1 during Hurricane Isabel

station	RMS (m)	relative error	correlation	skill
Tolchester	0.19	4.34%	0.97	0.98
Baltimore	0.18	3.66%	0.98	0.98
Annapolis	0.14	2.69%	0.98	0.99
Cambridge	0.15	4.07%	0.96	0.98
Lewisetta	0.11	3.10%	0.97	0.98
Sewells Pt.	0.17	5.85%	0.95	0.97
Kiptopeke	0.18	10.14%	0.92	0.95
CBBT	0.19	8.74%	0.93	0.95
mean	**0.16**	**5.32%**	**0.96**	**0.97**

Table 3.7 Statistical measures for estimating the errors of water elevations generated with RAMS grid2 during Hurricane Isabel

station	RMS (m)	relative error	correlation	skill
Tolchester	0.13	1.62%	0.98	0.99
Baltimore	0.13	1.78%	0.98	0.99
Annapolis	0.12	1.75%	0.99	0.99
Cambridge	0.12	2.32%	0.98	0.99
Lewisetta	0.14	4.41%	0.97	0.98
Sewells Pt.	0.2	7.16%	0.96	0.96
Kiptopeke	0.19	10.60%	0.93	0.94
CBBT	0.21	9.22%	0.94	0.95
mean	**0.15**	**4.86%**	**0.97**	**0.97**

Table 3.8 Statistical measures for estimating the errors of water elevations generated with RAMS grid3 during Hurricane Isabel

station	RMS (m)	relative error	correlation	skill
Tolchester	0.16	2.37%	0.98	0.99
Baltimore	0.15	2.12%	0.98	0.99
Annapolis	0.15	2.58%	0.98	0.99
Cambridge	0.14	3.20%	0.98	0.98
Lewisetta	0.15	5.08%	0.97	0.97
Sewells Pt.	0.23	8.52%	0.96	0.96
Kiptopeke	0.19	10.55%	0.93	0.94
CBBT	0.21	9.62%	0.95	0.95
mean	**0.17**	**5.51%**	**0.97**	**0.97**

Table 3.9 RMS errors of different winds at 6 sations in the Bay during Tropical Storm Ernesto

	Station	CBBT	Rappahannock	Lewisetta	Cambridge	Thomas Pt.	Tolchester	**mean**
GFS	Wind speed (m/s)	2.36	3.14	3.25	1.65	3.4	4.07	**2.98**
	Direction (degree)	36.85	39.62	43.64	59.09	23.62	43.91	**41.12**
	Pressure (Pa)	92.65	140.87	107.13	124.94	136.34	119.48	**120.23**
NAM	Wind speed (m/s)	2.77	2.45	2.39	1.82	2.08	4.95	**2.74**
	Direction (degree)	40.15	47.4	44.12	51.06	29.88	38.47	**41.85**
	Pressure (Pa)	153.15	181.75	150.38	149.77	163.5	137.39	**155.99**
WRF-GFS	Wind speed (m/s)	2.08	2.58	2.71	1.85	1.87	5.55	**2.77**
	Direction (degree)	38.88	37.85	46.63	60.47	33.17	46.58	**43.93**
	Pressure (Pa)	113.41	125.28	146.75	166.44	172.09	169.62	**148.93**

Table 3.10 Statistical measures for estimating the errors of water elevations generated with GFS during Tropical Storm Ernesto

station	RMS (m)	relative error	correlation	skill
Tolchester	0.19	37.77%	0.68	0.79
Baltimore	0.19	31.93%	0.81	0.82
Annapolis	0.20	33.90%	0.86	0.80
Cambridge	0.17	26.10%	0.85	0.86
Lewisetta	0.22	21.40%	0.97	0.88
Sewells Pt.	0.16	10.93%	0.97	0.94
Kiptopeke	0.14	10.85%	0.96	0.94
CBBT	0.15	12.15%	0.97	0.94
mean	**0.18**	**23.13%**	**0.88**	**0.87**

Table 3.11 Statistical measures for estimating the errors of water elevations generated with NAM during Tropical Storm Ernesto

station	RMS (m)	relative error	correlation	skill
Tolchester	0.23	44.06%	0.75	0.75
Baltimore	0.26	54.51%	0.66	0.68
Annapolis	0.26	57.11%	0.70	0.65
Cambridge	0.22	42.11%	0.77	0.76
Lewisetta	0.24	27.13%	0.89	0.85
Sewells Pt.	0.12	5.99%	0.96	0.97
Kiptopeke	0.12	7.55%	0.94	0.96
CBBT	0.11	6.48%	0.96	0.97
mean	**0.19**	**30.62%**	**0.83**	**0.82**

Table 3.12 Statistical measures for estimating the errors of water elevations generated with WRF-GFS during Tropical Storm Ernesto

station	RMS (m)	relative error	correlation	skill
Tolchester	0.18	26.43%	0.91	0.85
Baltimore	0.18	28.00%	0.90	0.84
Annapolis	0.20	33.07%	0.91	0.81
Cambridge	0.18	26.83%	0.91	0.85
Lewisetta	0.18	12.94%	0.97	0.93
Sewells Pt.	0.15	8.00%	0.96	0.96
Kiptopeke	0.13	8.83%	0.95	0.95
CBBT	0.14	8.96%	0.96	0.95
mean	**0.17**	**19.13%**	**0.93**	**0.89**

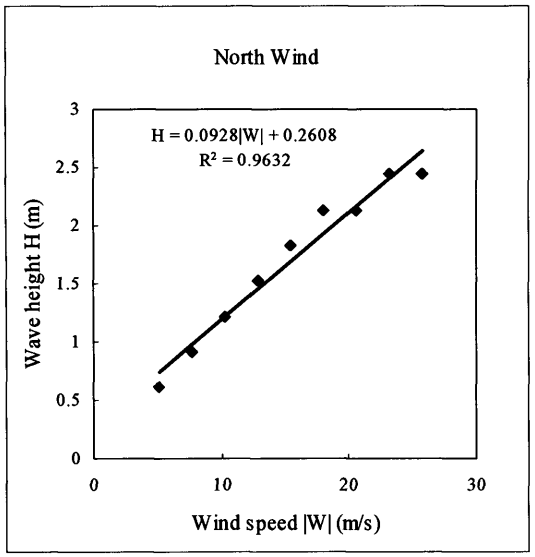

Figure 2.1 Relationship between wave height and wind speed in the Bay during North wind

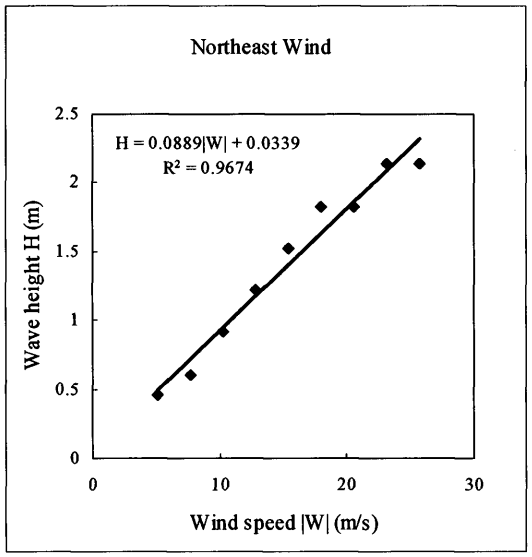

Figure 2.2 Relationship between wave height and wind speed in the Bay during Northeast wind

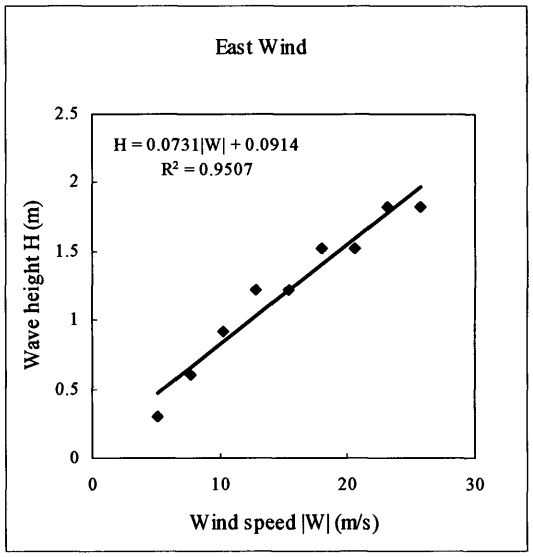

Figure 2.3 Relationship between wave height and wind speed in the Bay during East wind

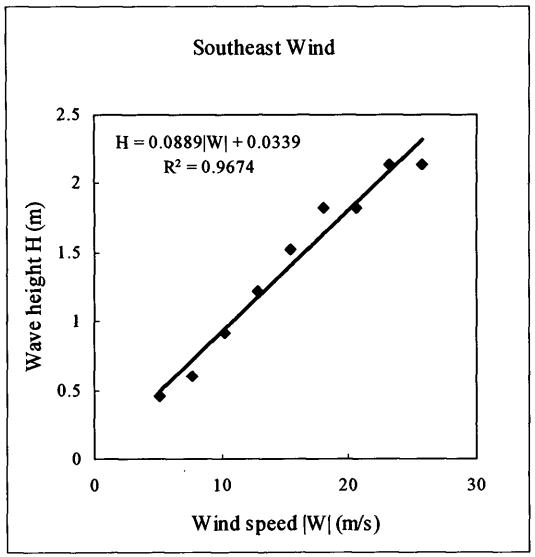

Figure 2.4 Relationship between wave height and wind speed in the Bay during Southeast wind

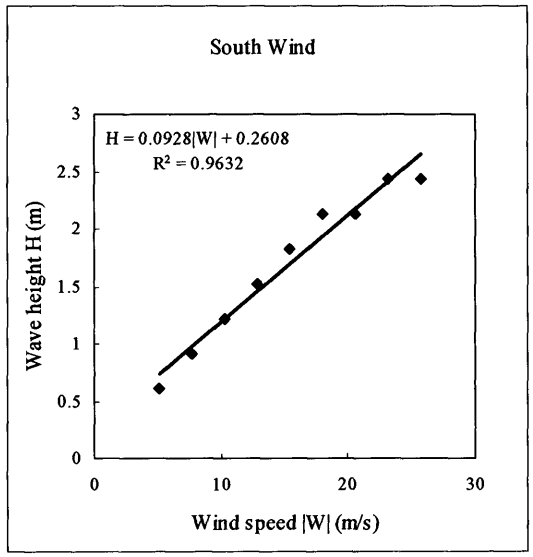

Figure 2.5 Relationship between wave height and wind speed in the Bay during South wind

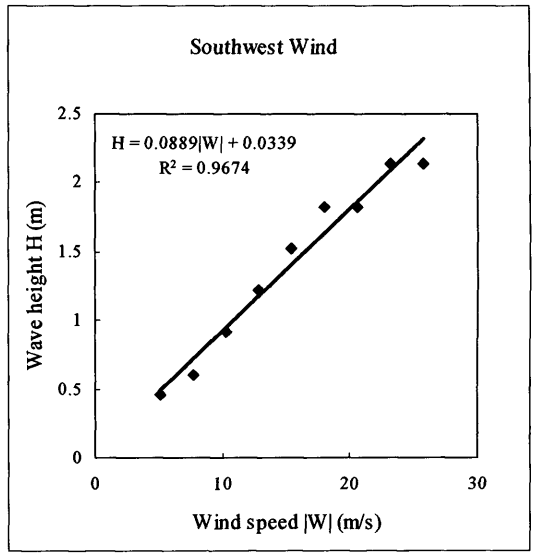

Figure 2.6 Relationship between wave height and wind speed in the Bay during Southwest wind

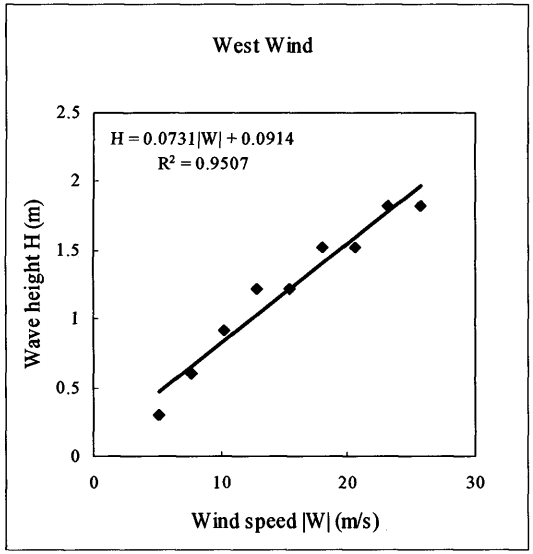

Figure 2.7 Relationship between wave height and wind speed in the Bay during West wind

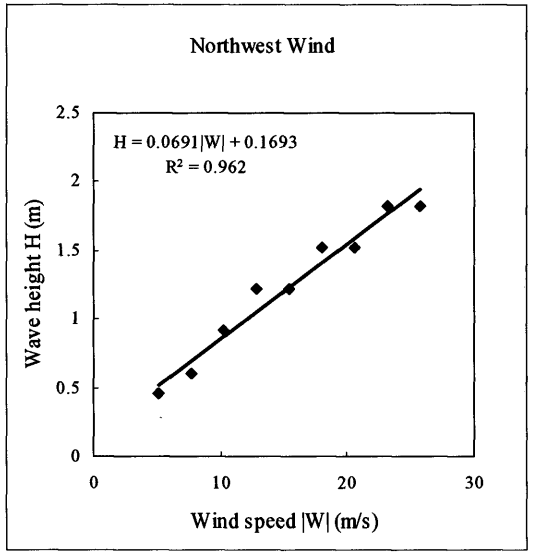

Figure 2.8 Relationship between wave height and wind speed in the Bay during Northwest wind

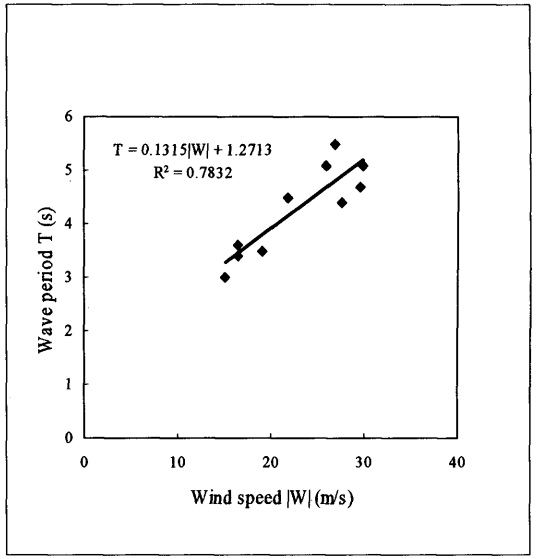

Figure 2.9 Relationship between wave period and wind speed in the Bay during Hurricane Isabel

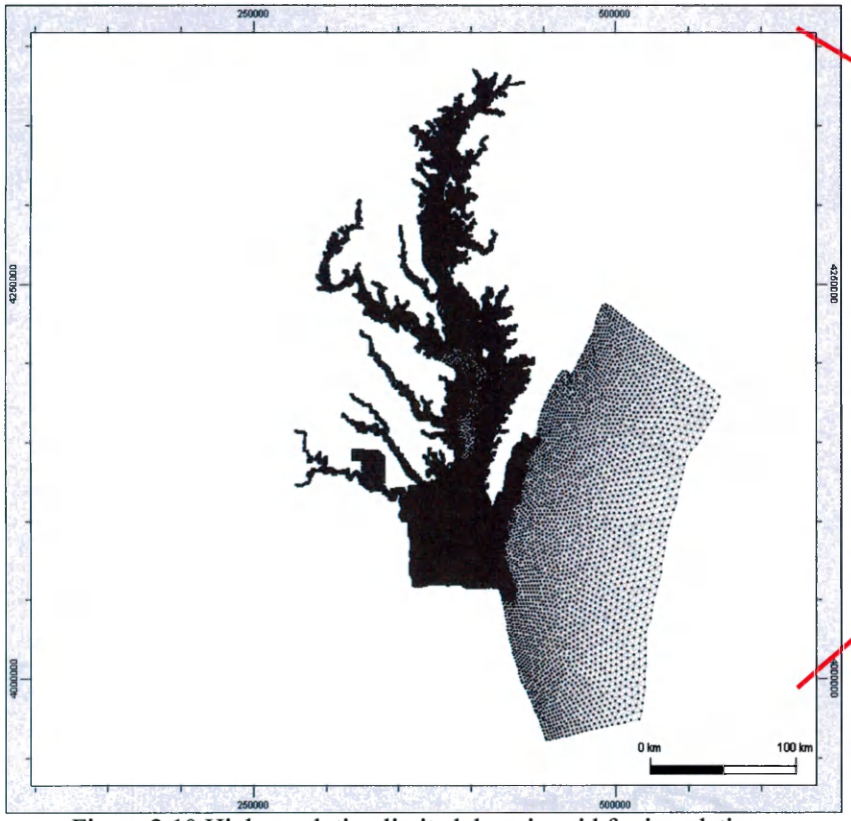

Figure 2.10 High-resolution limited domain grid for inundation simulation

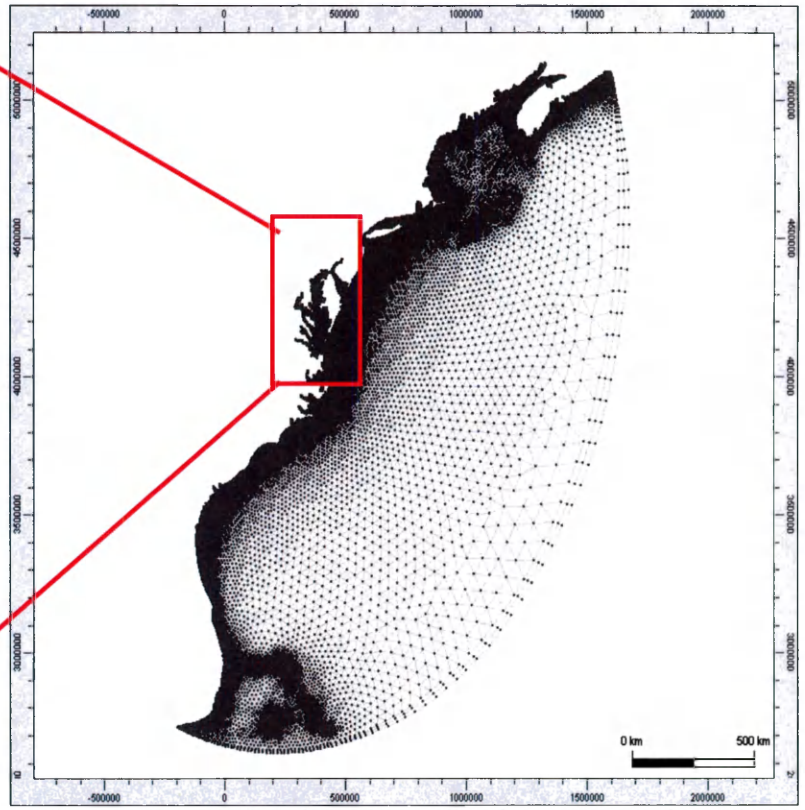

Figure 2.11 Large domain grid extending from Nova Scotia to Florida

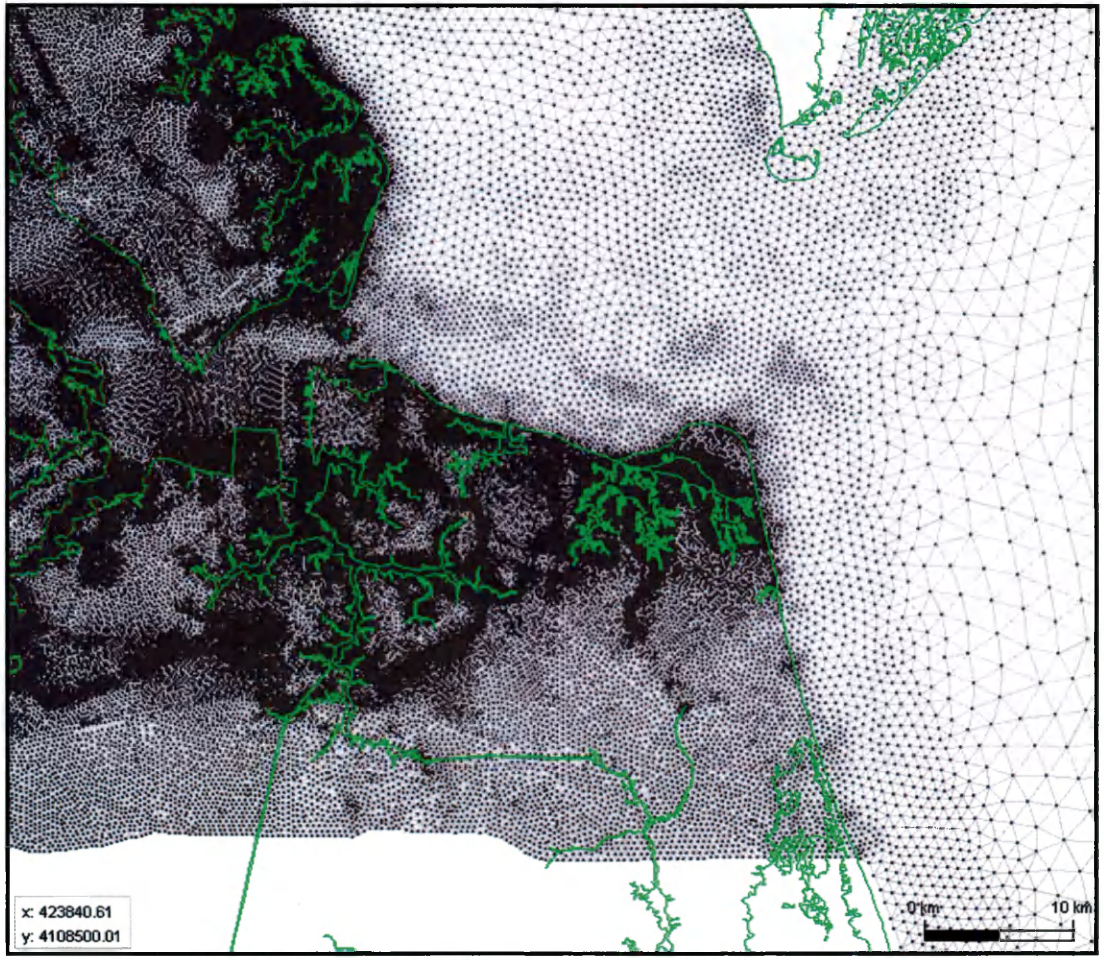

Figure 2.12 High-resolution grid in Hampton Roads

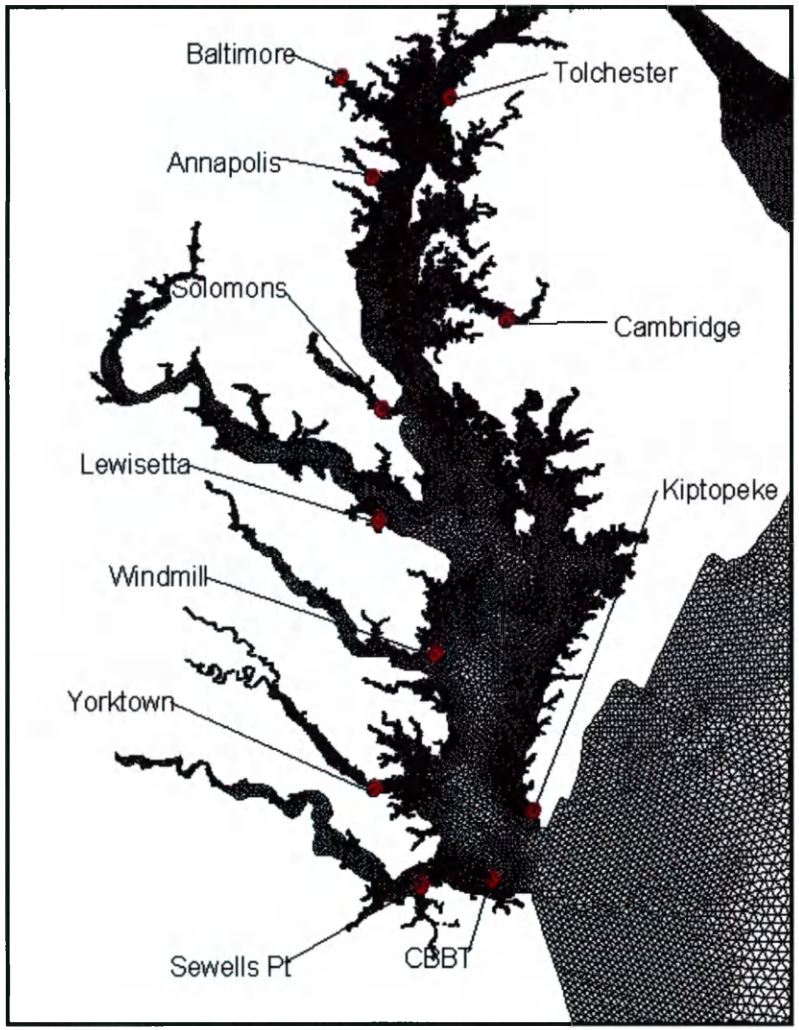

Figure 2.13 Tidal gauge stations in the Chesapeake Bay

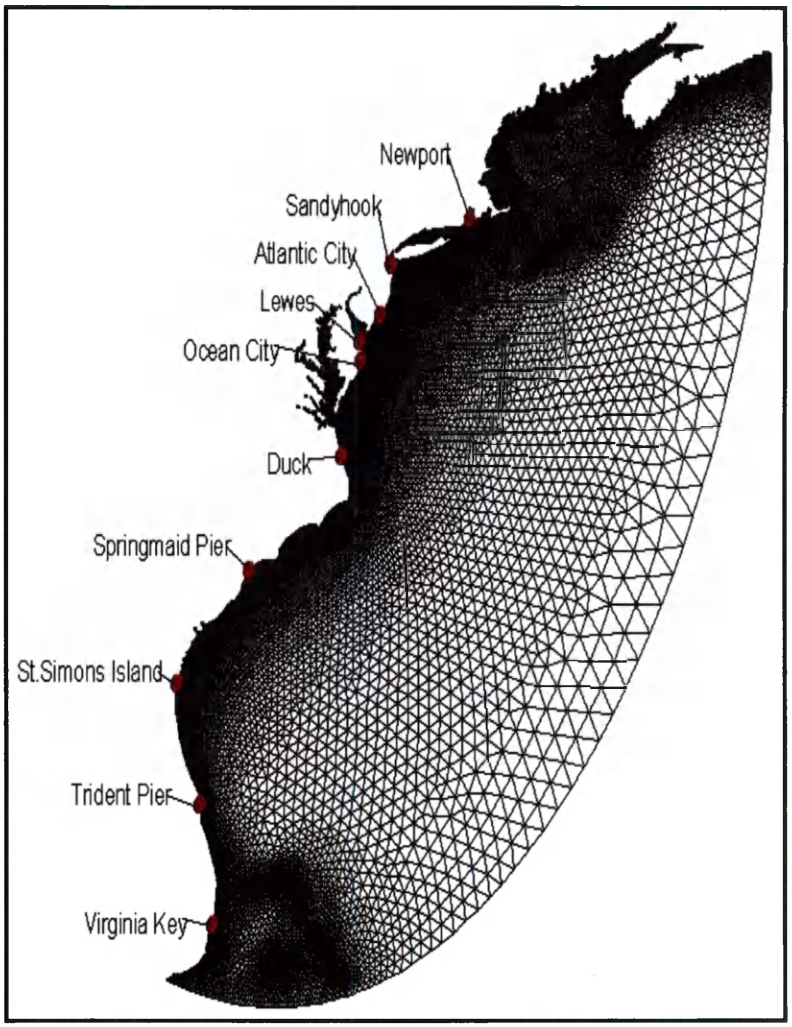

Figure 2.14 Tidal gauge stations along the Atlantic coastline

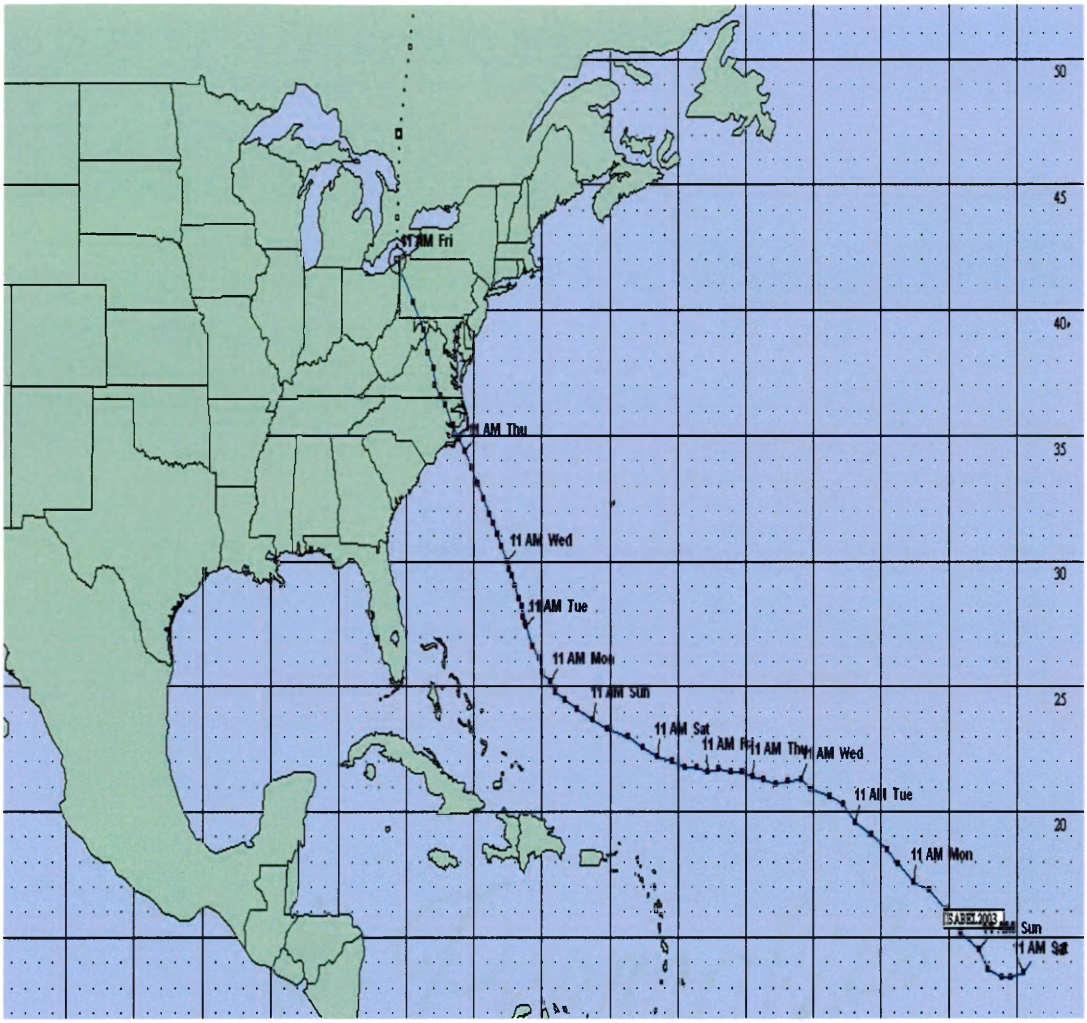

Figure 3.1 Track of Hurricane Isabel (from www.erh.noaa.gov)

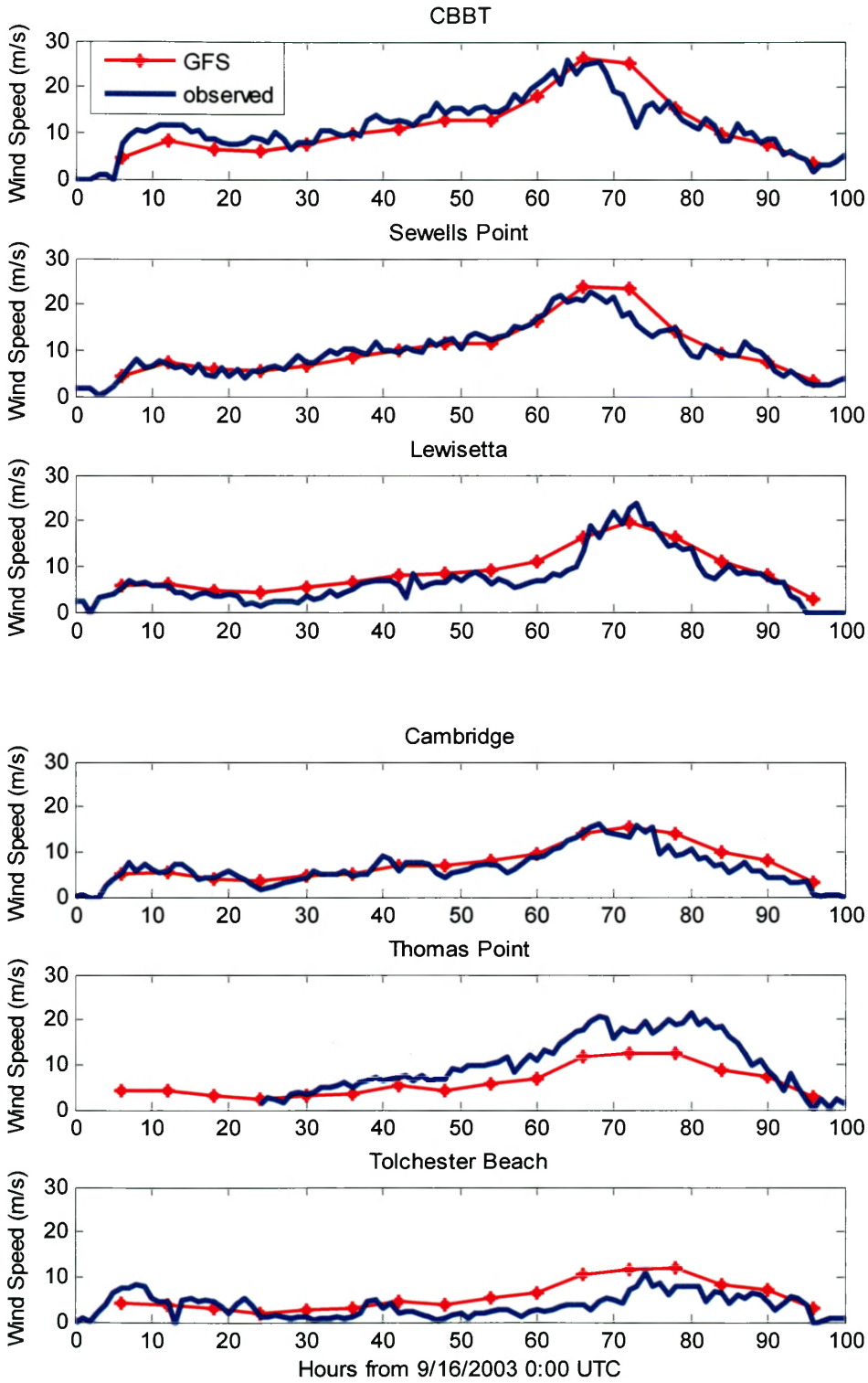

Figure 3.2 Comparison of wind speeds between GFS modeled wind and observation in the Bay

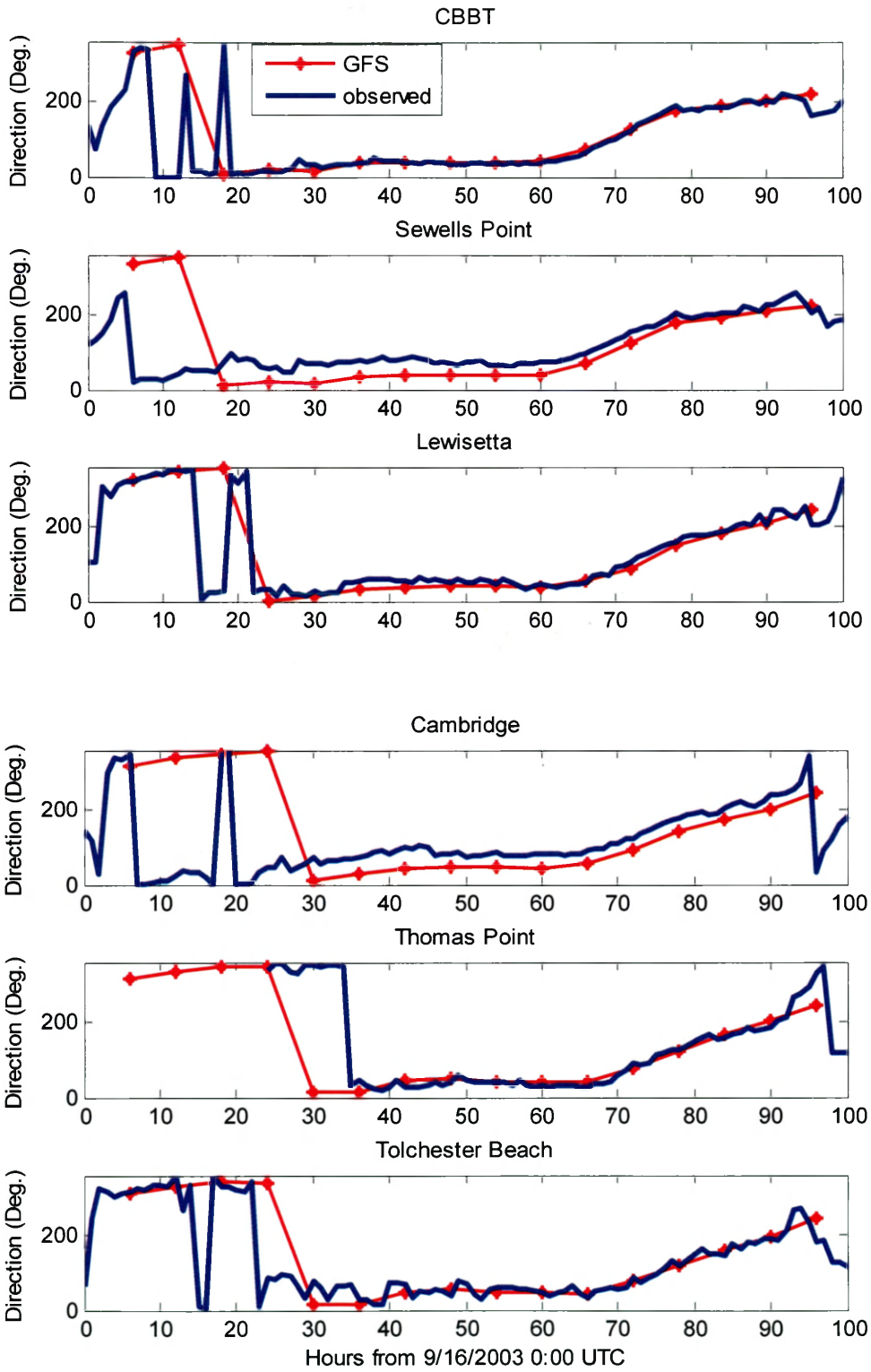

Figure 3.3 Comparison of wind directions between GFS modeled wind and observation in the Bay

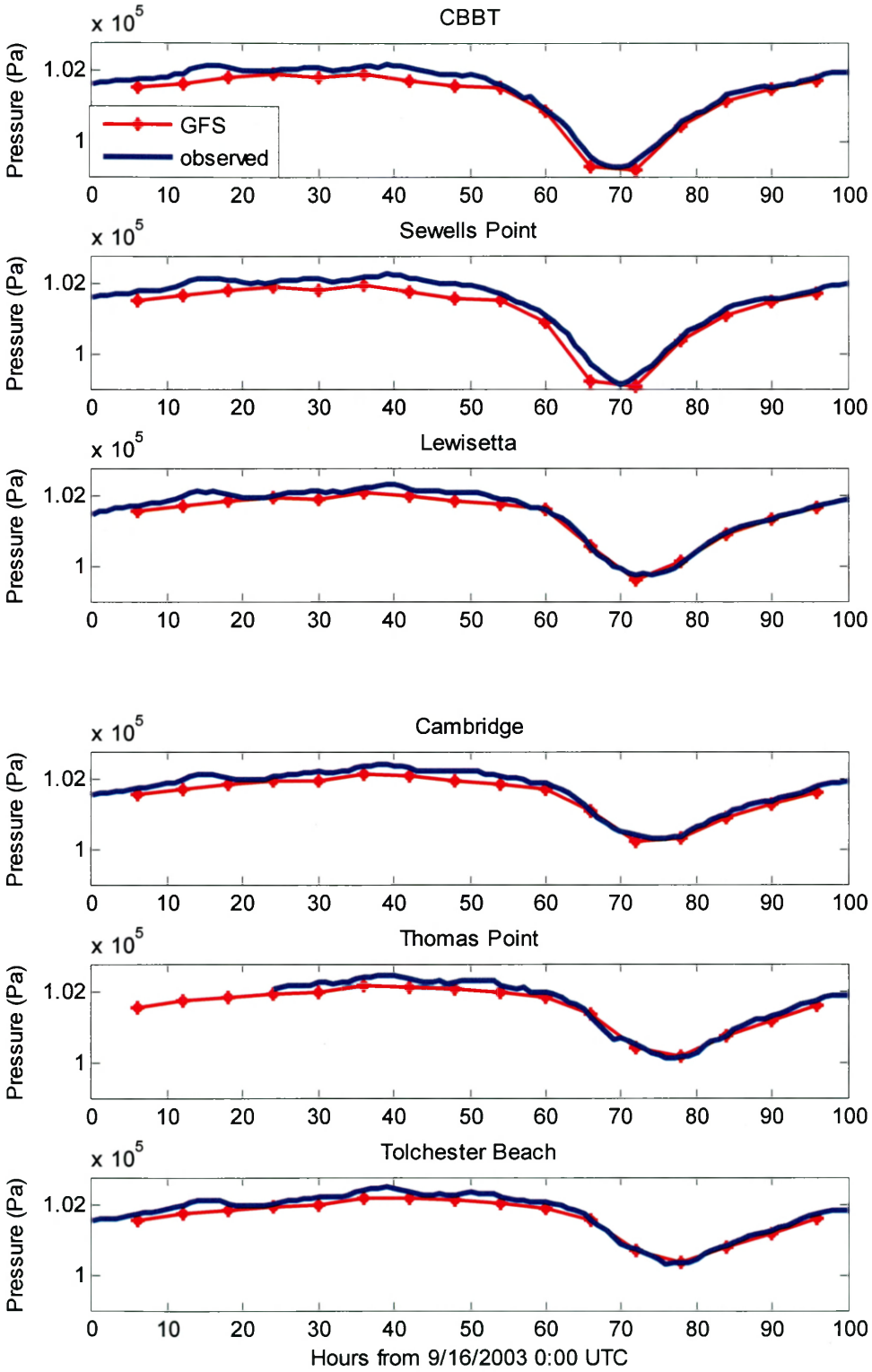

Figure 3.4 Comparison of pressures between GFS modeled pressure and observation in the Bay

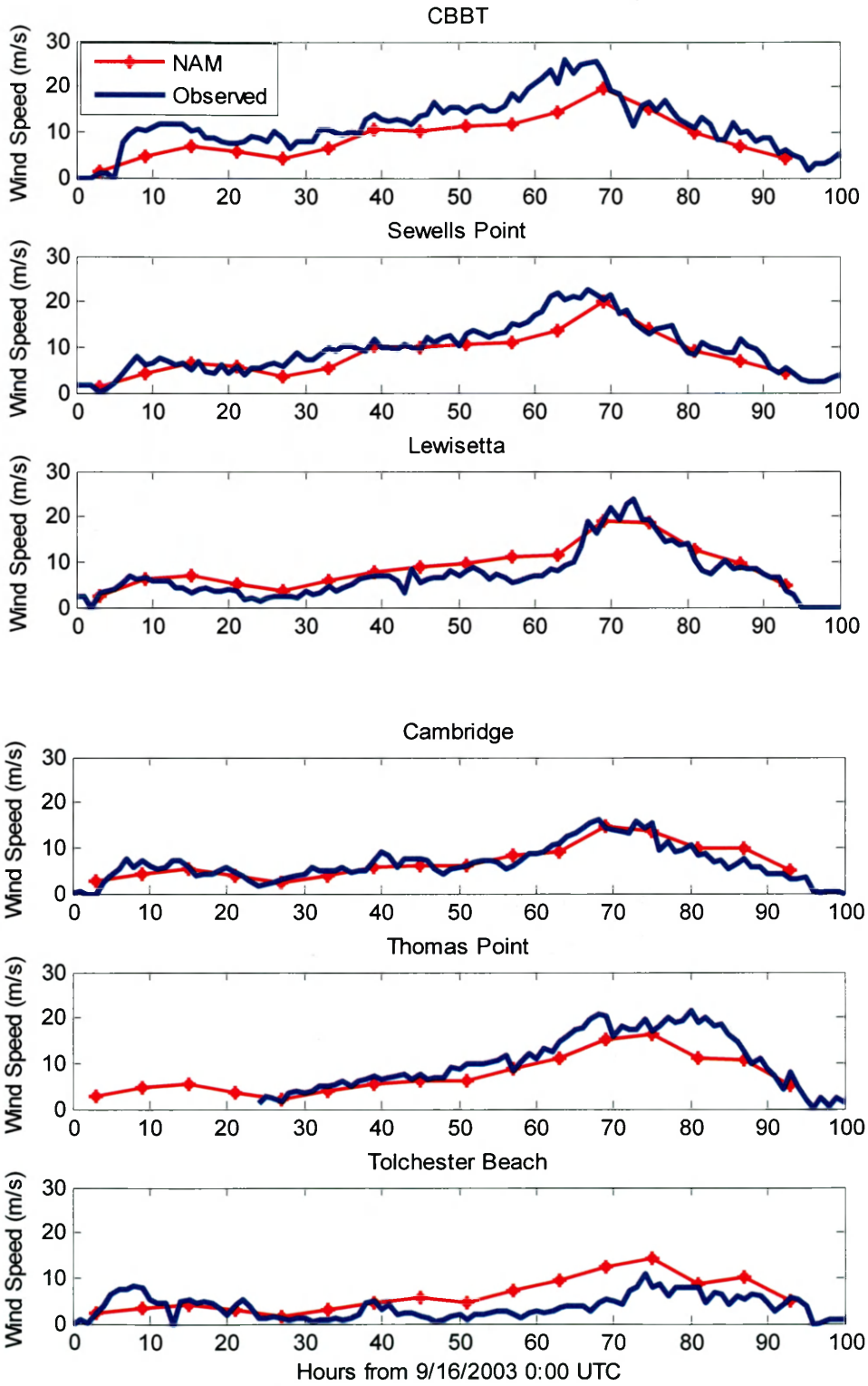

Figure 3.5 Comparison of wind speeds between NAM modeled wind and observation in the Bay

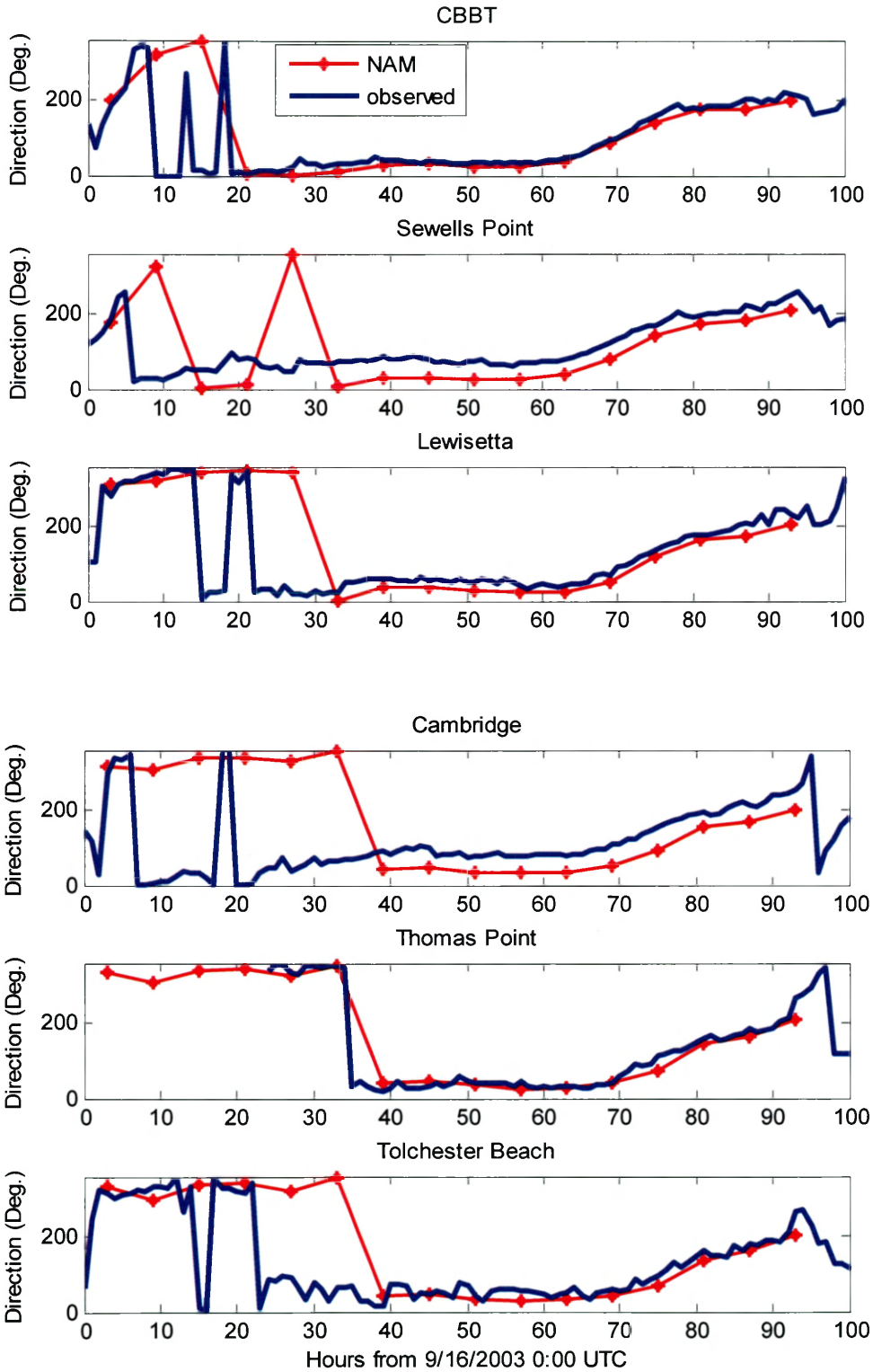

Figure 3.6 Comparison of wind directiosn between NAM modeled wind and observation in the Bay

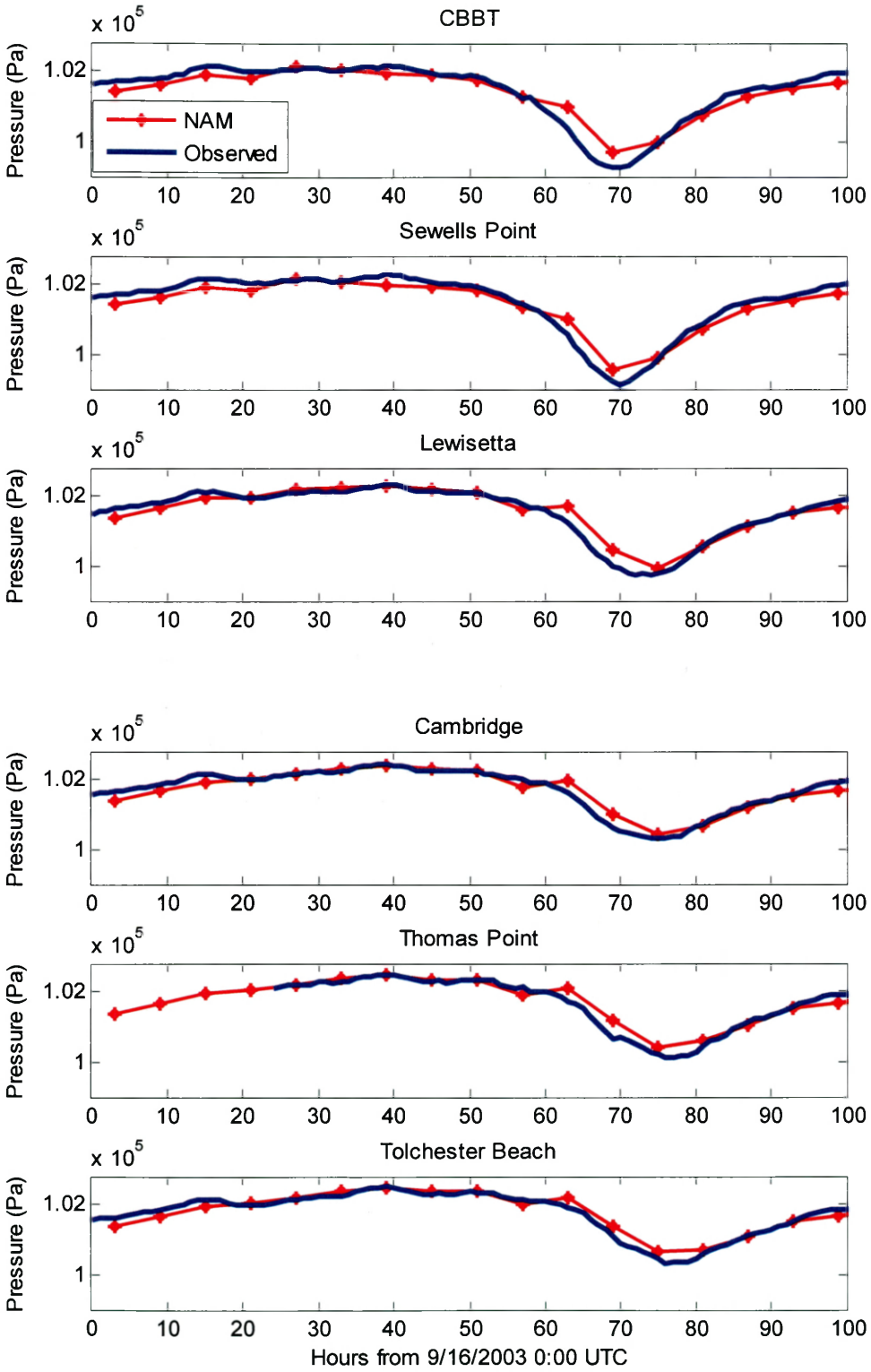

Figure 3.7 Comparison of pressures between NAM modeled pressure and observation in the Bay

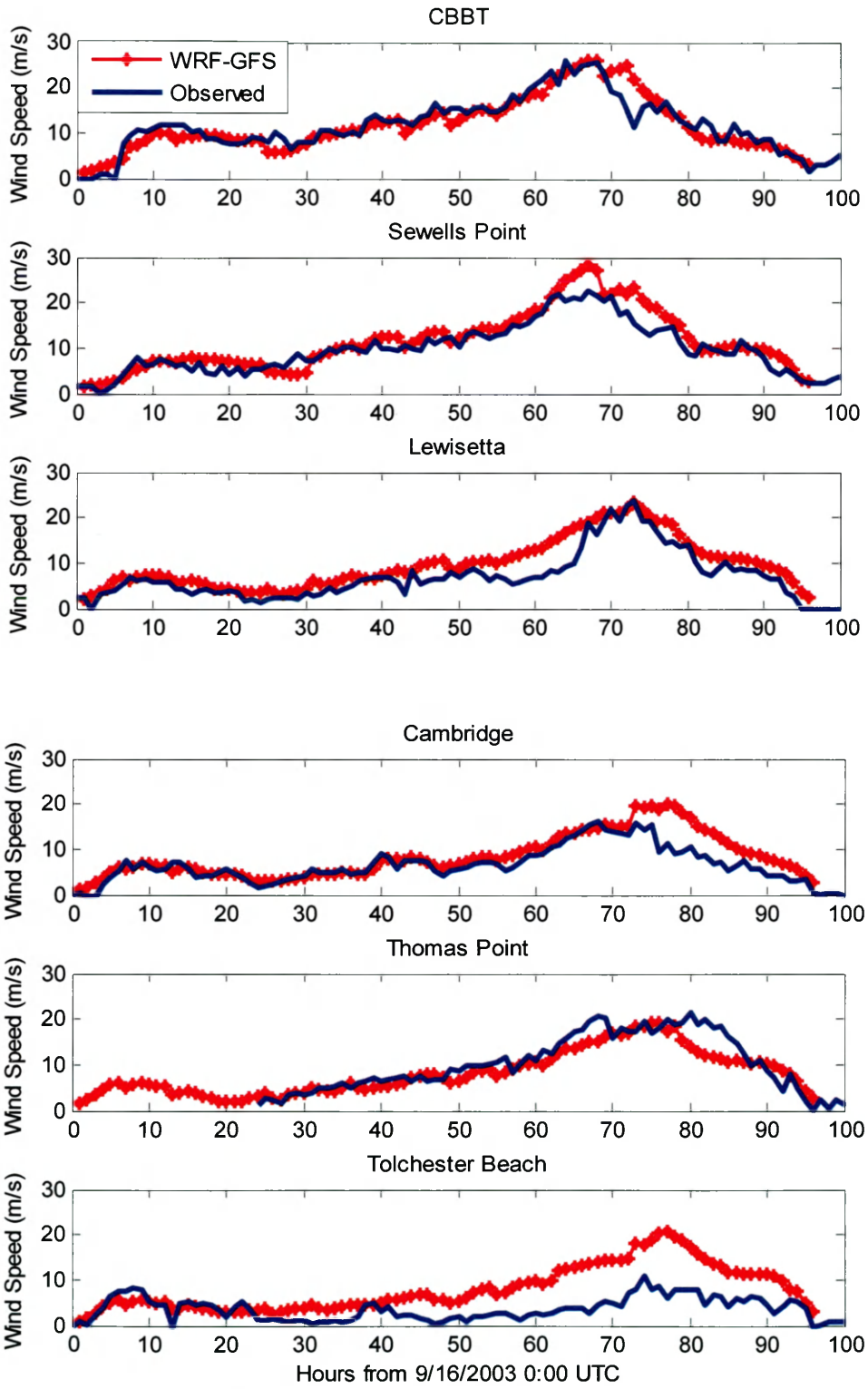

Figure 3.8 Comparison of wind speeds between WRF-GFS modeled wind and observation in the Bay

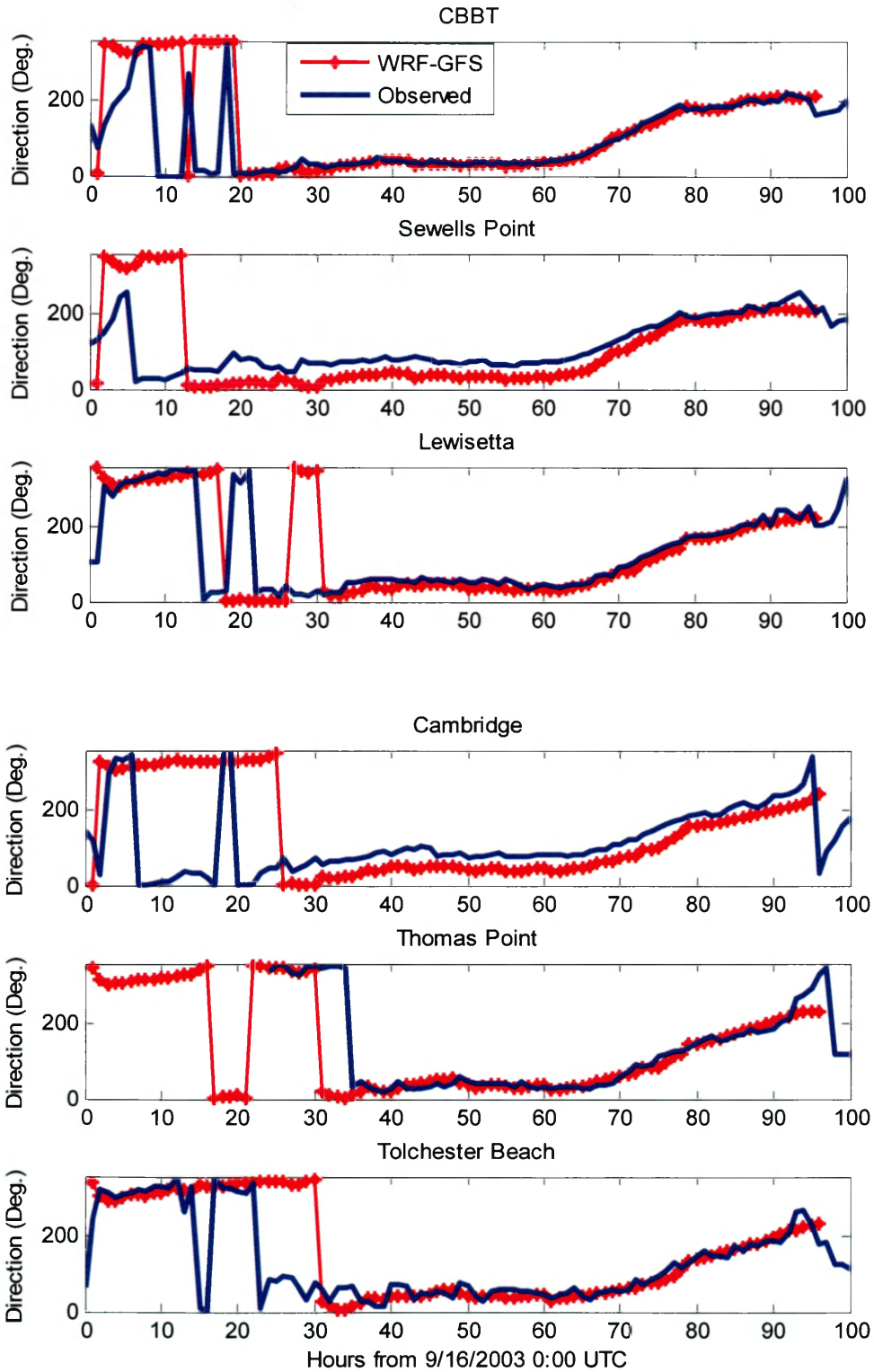

Figure 3.9 Comparison of wind directions between WRF-GFS modeled wind and observation in the Bay

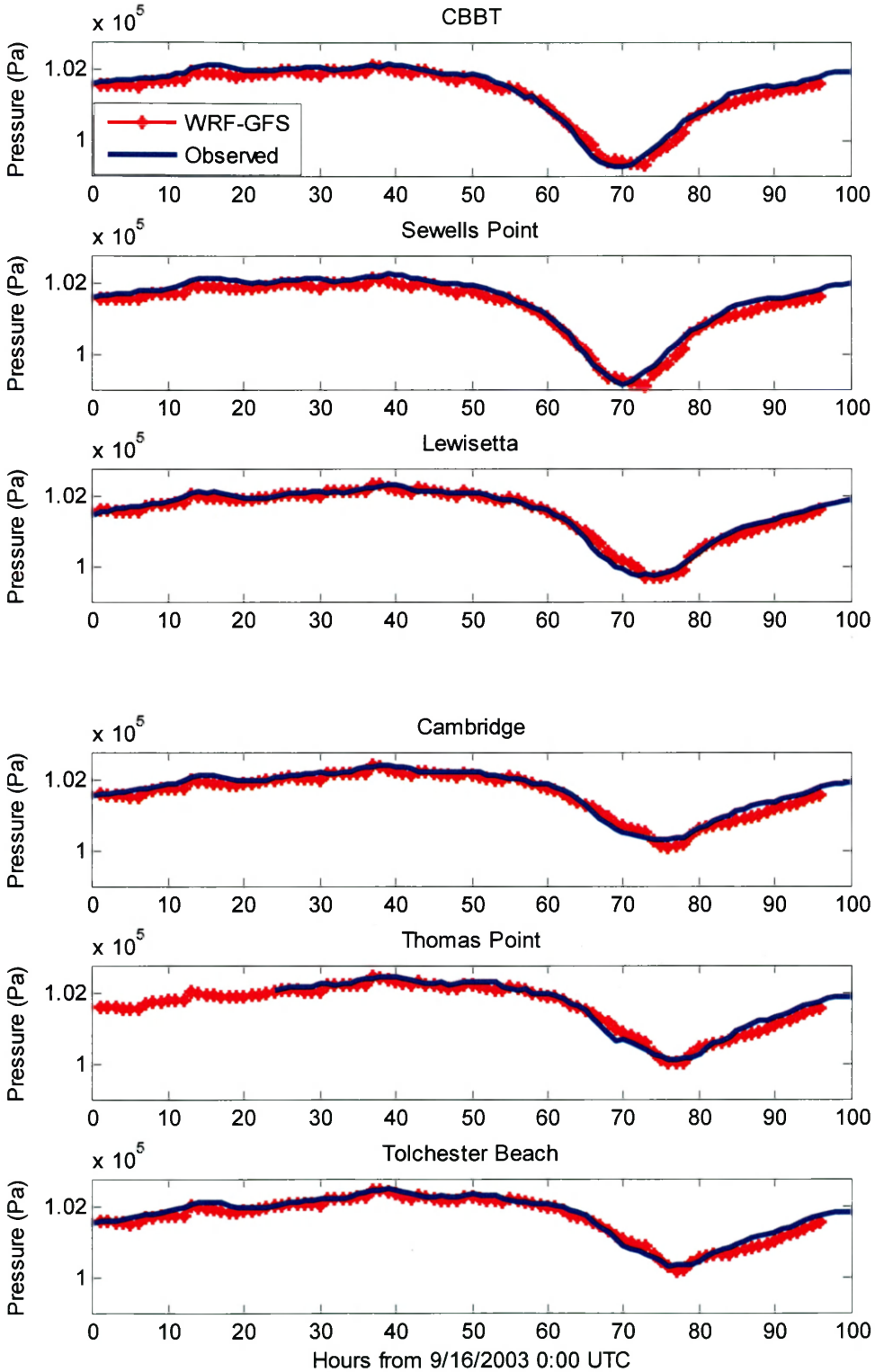

Figure 3.10 Comparison of pressures between WRF-GFS modeled pressure and observation in the Bay

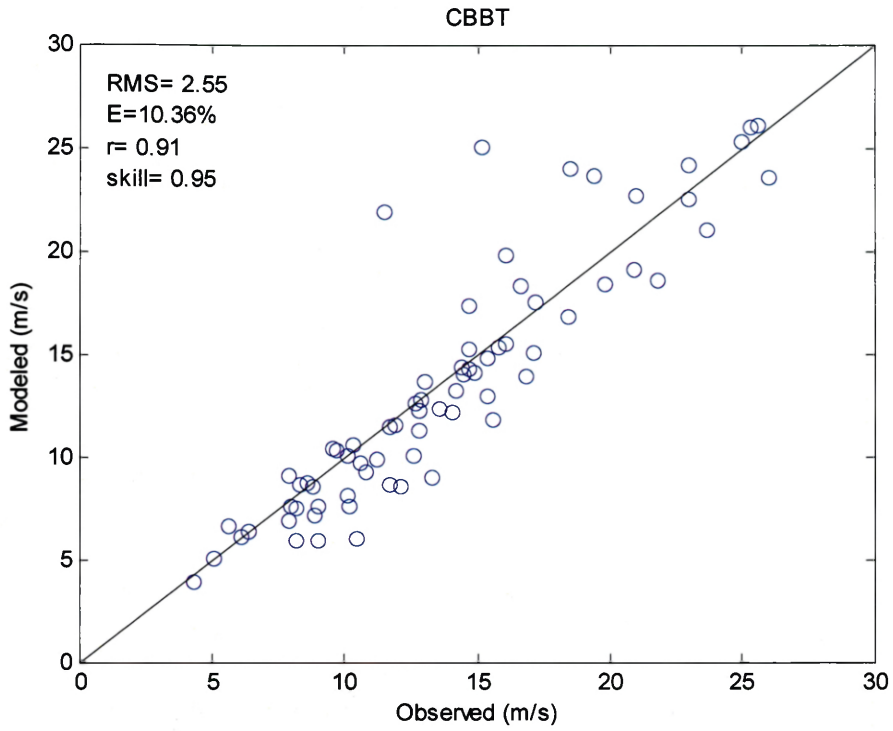

Figure 3.11 WRF-GFS modeled wind speed against observed wind speed at CBBT

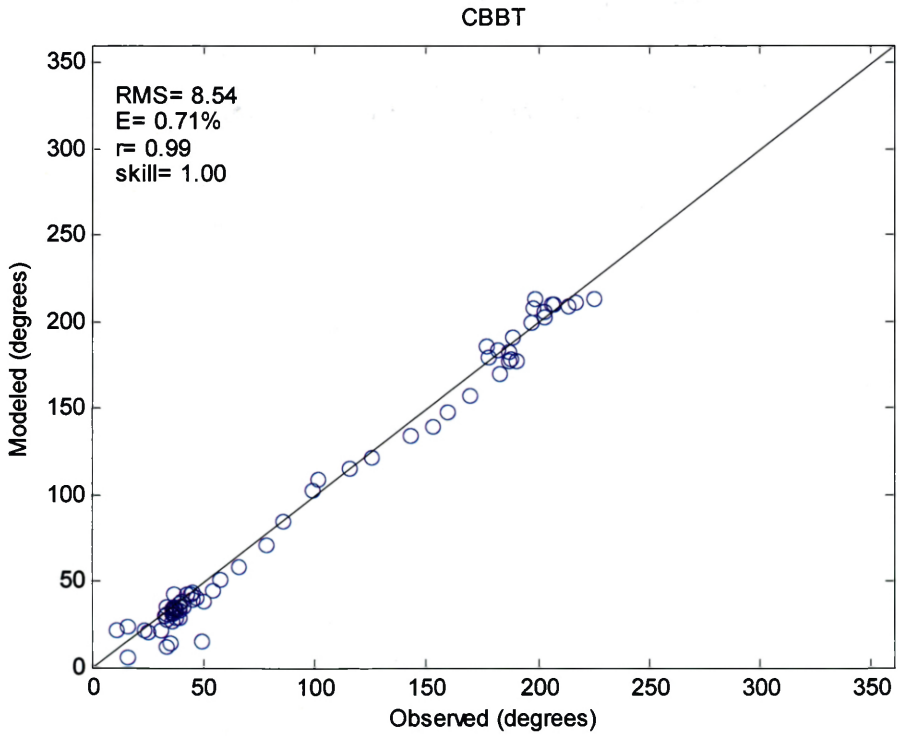

Figure 3.12 WRF-GFS modeled wind direction against observed wind direction at CBBT

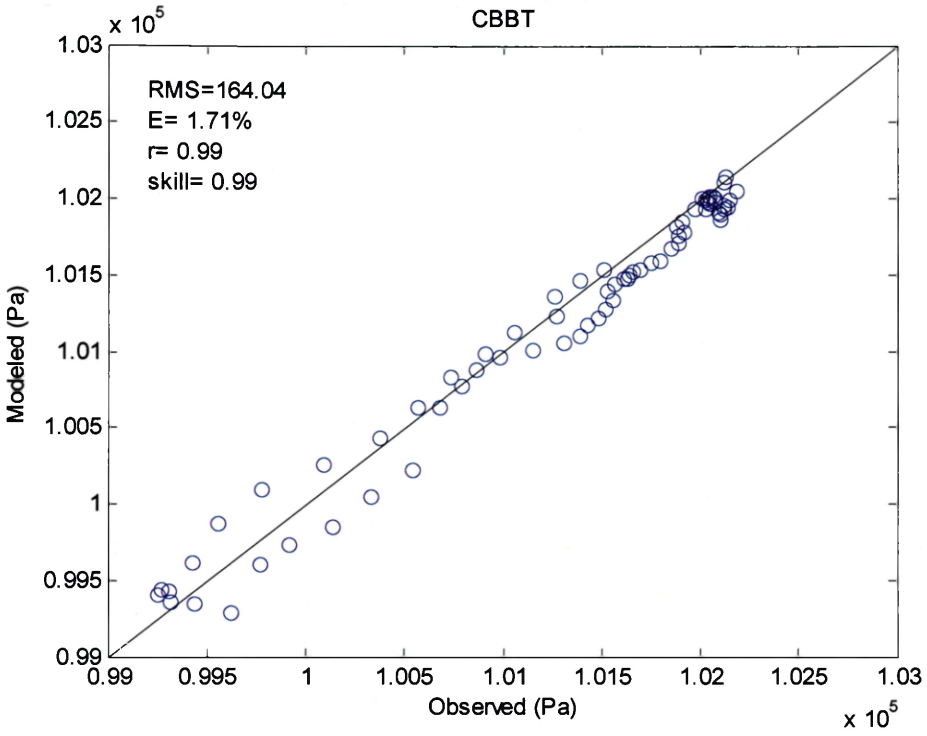

Figure 3.13 WRF-GFS modeled pressure against observed pressure at CBBT

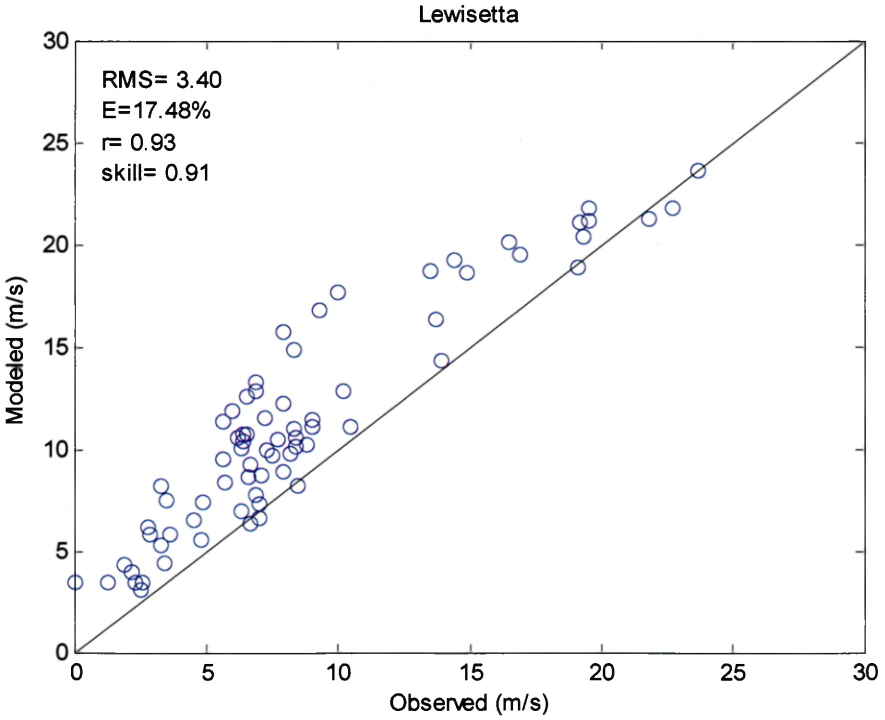

Figure 3.14 WRF-GFS modeled wind speed against observed wind speed at Lewisetta

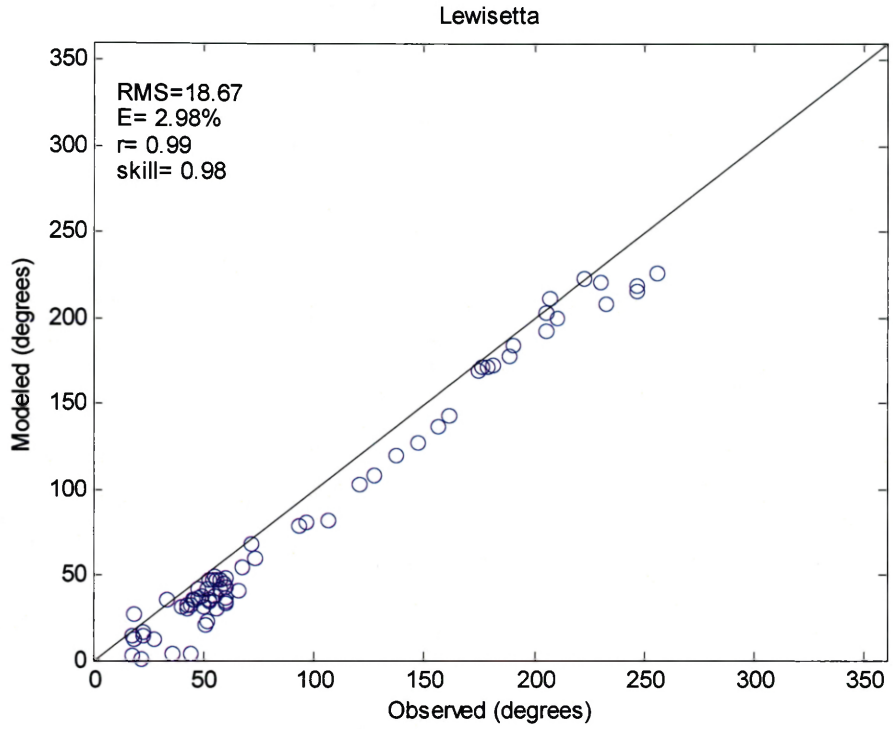

Figure 3.15 WRF-GFS modeled wind direction against observed wind direction at Lewisetta

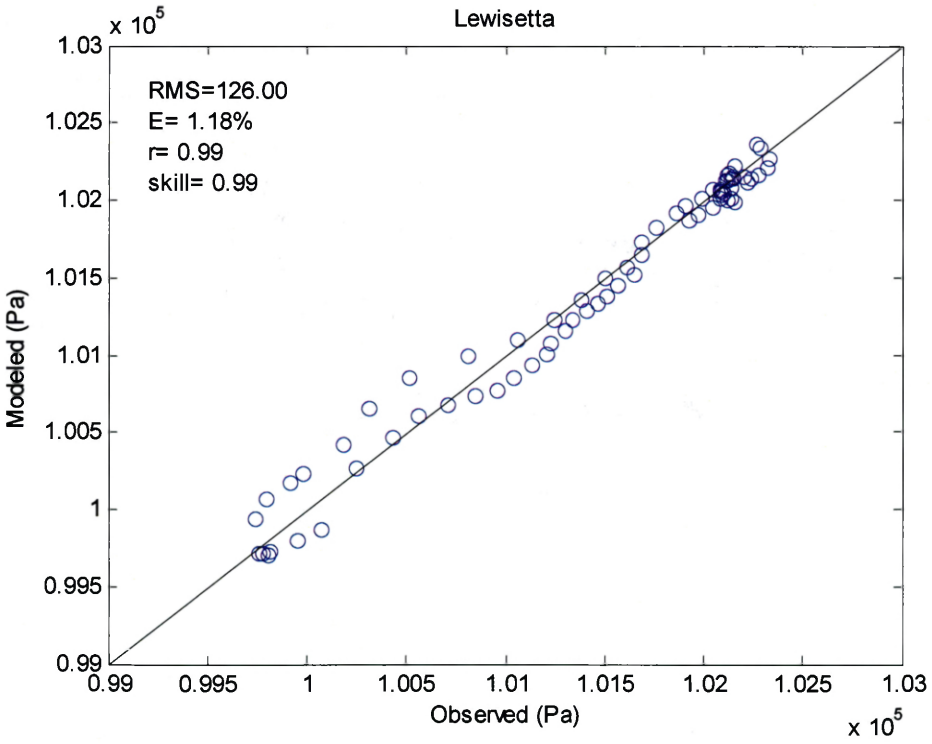

Figure 3.16 WRF-GFS modeled pressure against observed pressure at Lewisetta

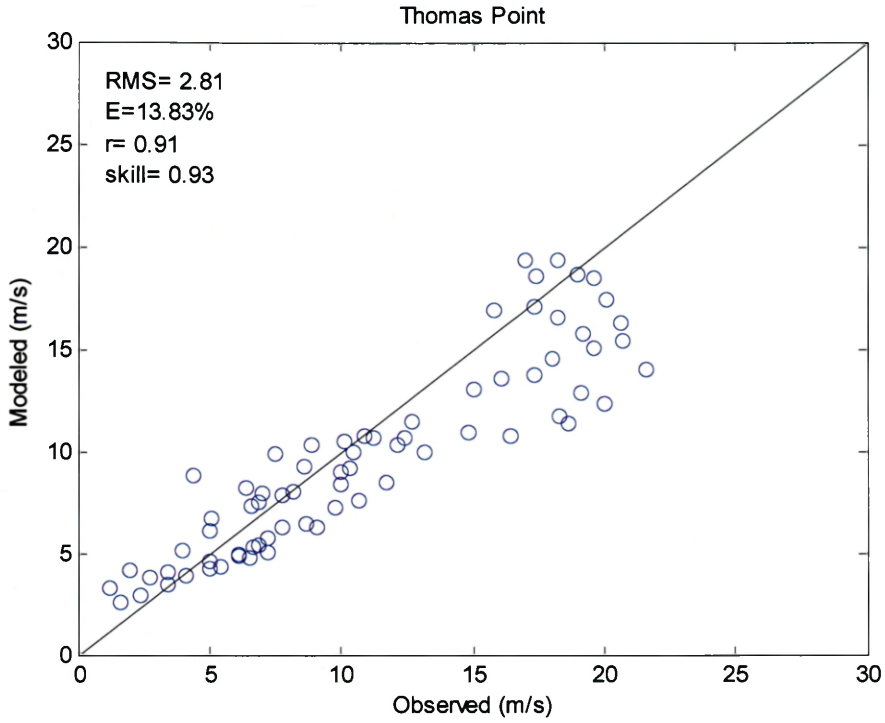

Figure 3.17 WRF-GFS modeled wind speed against observed wind speed at Thomas Point

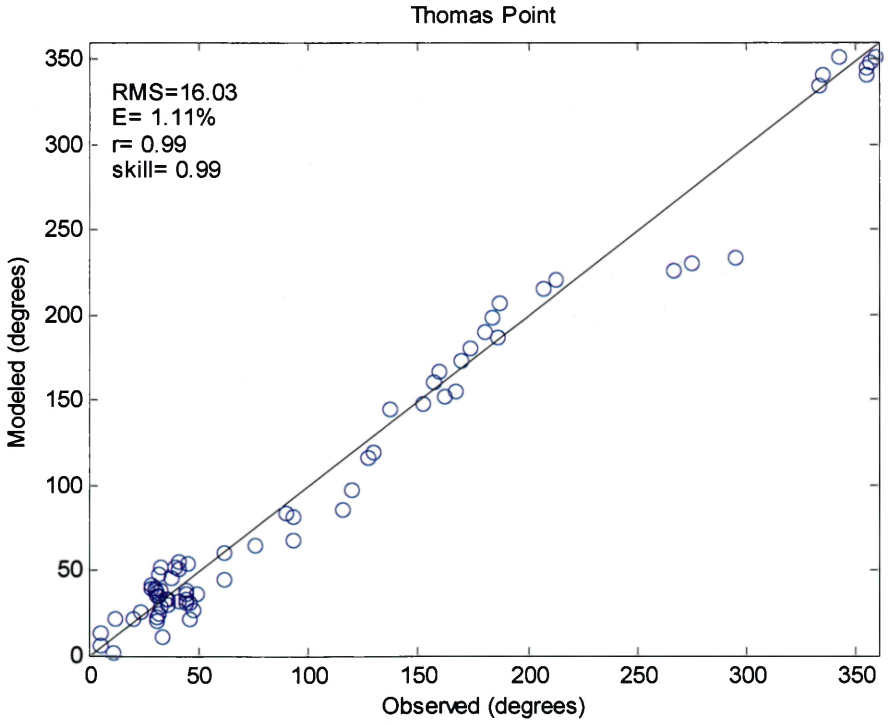

Figure 3.18 WRF-GFS modeled wind direction against observed wind direction at Thomas Point

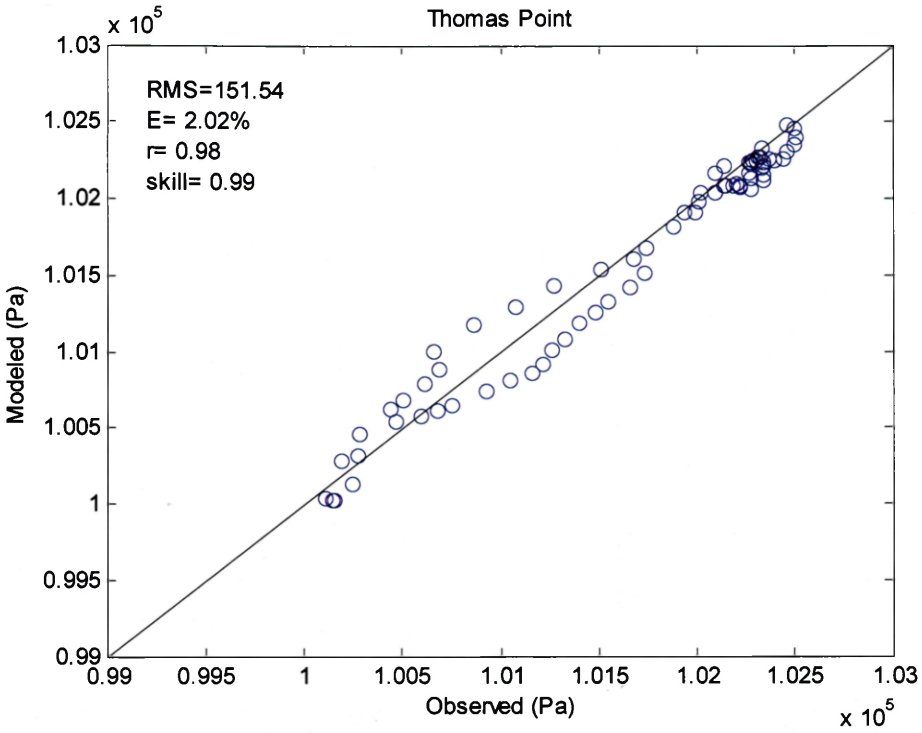

Figure 3.19 WRF-GFS modeled pressure against observed pressure at Thomas Point

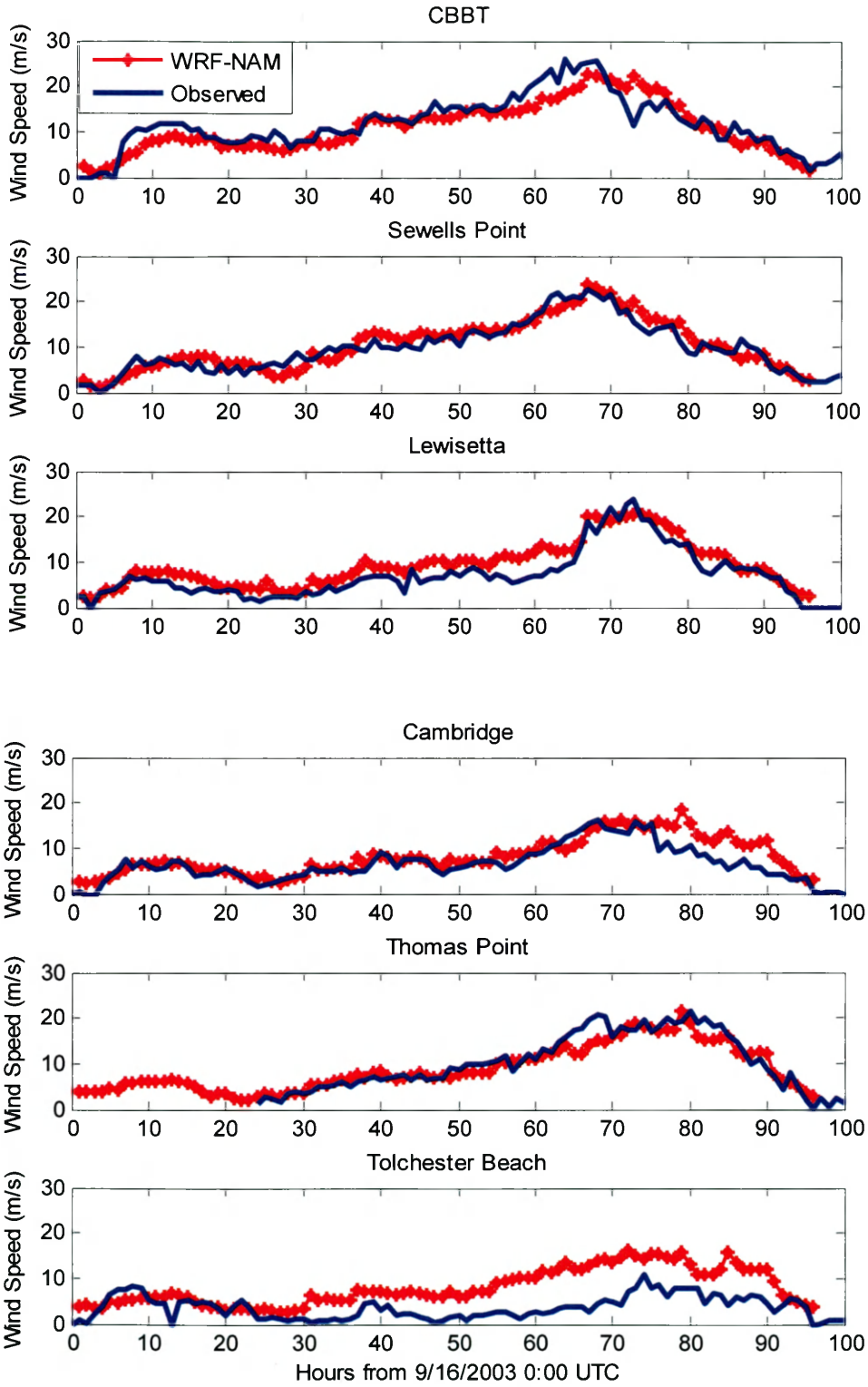

Figure 3.20 Comparison of wind speeds between WRF-NAM modeled wind and observation in the Bay

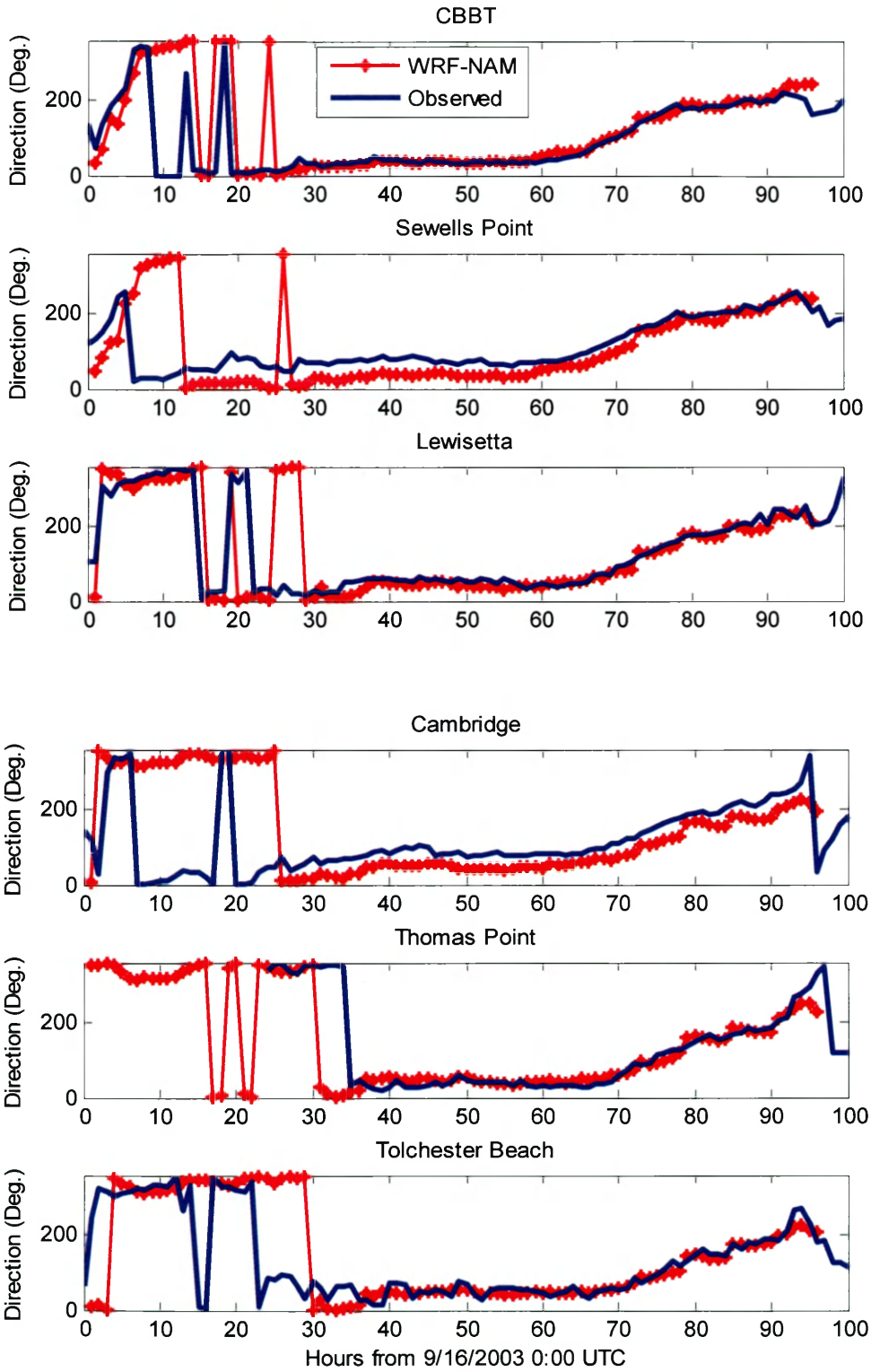

Figure 3.21 Comparison of wind directions between WRF-NAM modeled wind and observation in the Bay

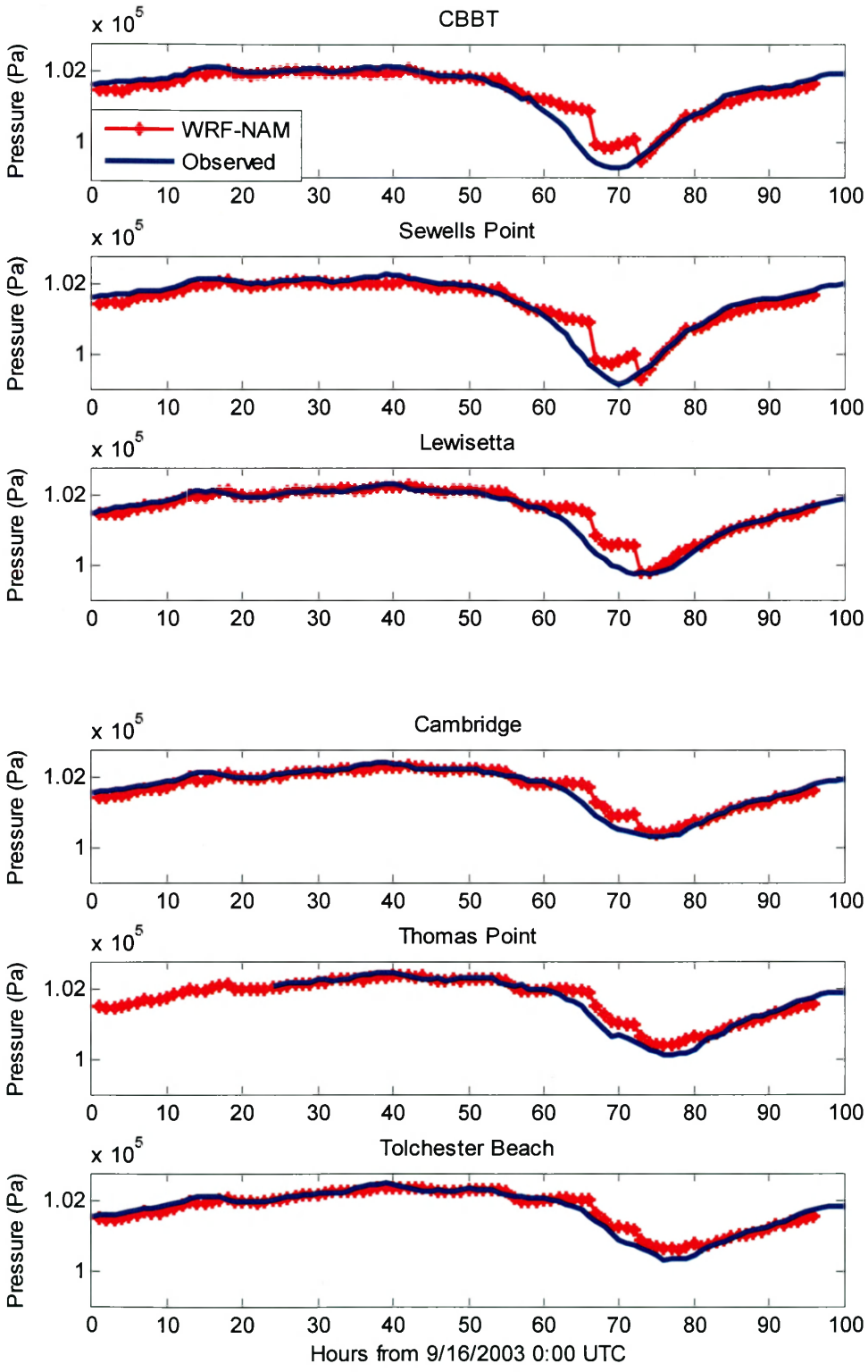

Figure 3.22 Comparison of pressures between WRF-NAM modeled pressure and observation in the Bay

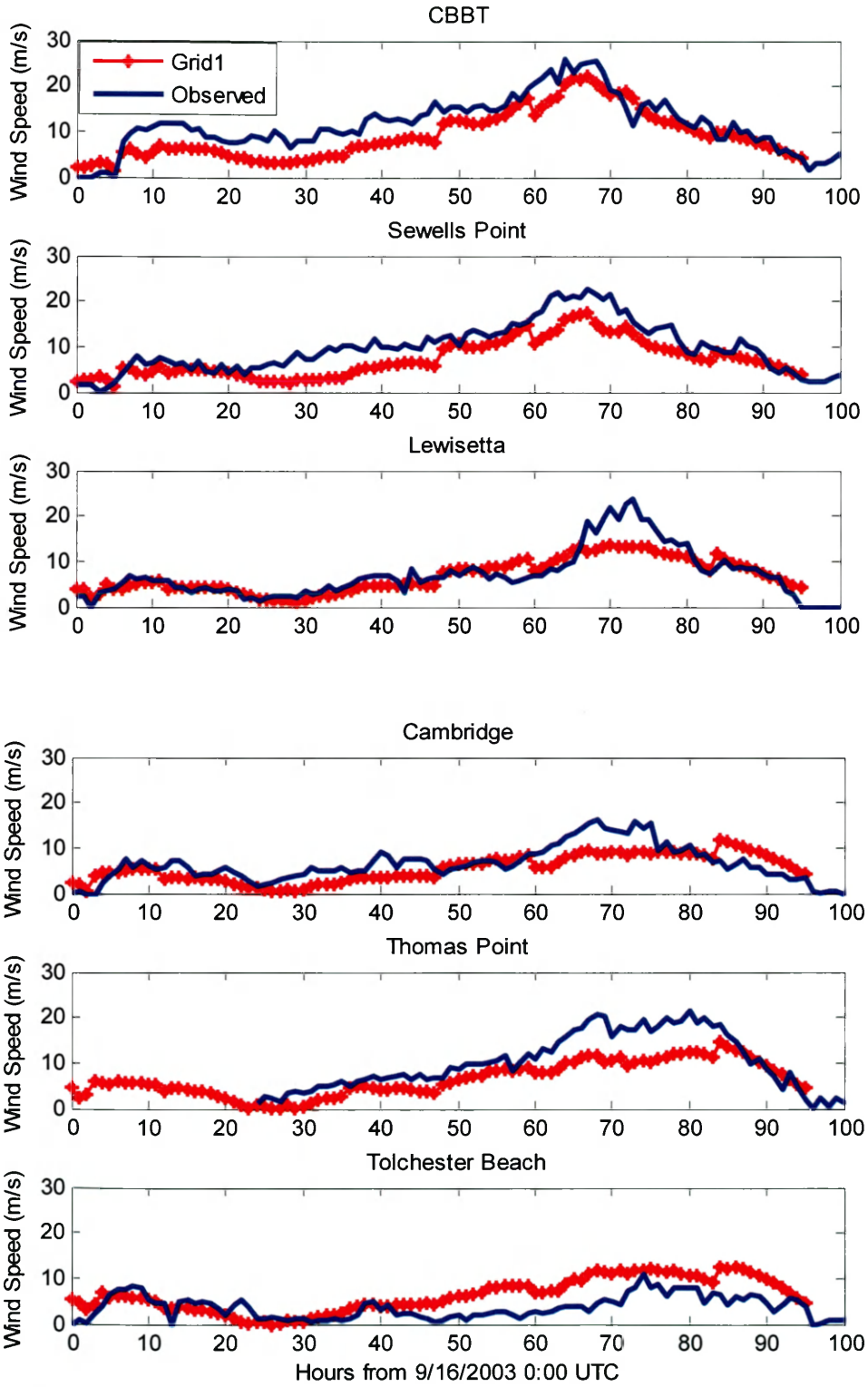

Figure 3.23 Comparison of wind speeds between RAMS (grid1) modeled wind and observation in the Bay

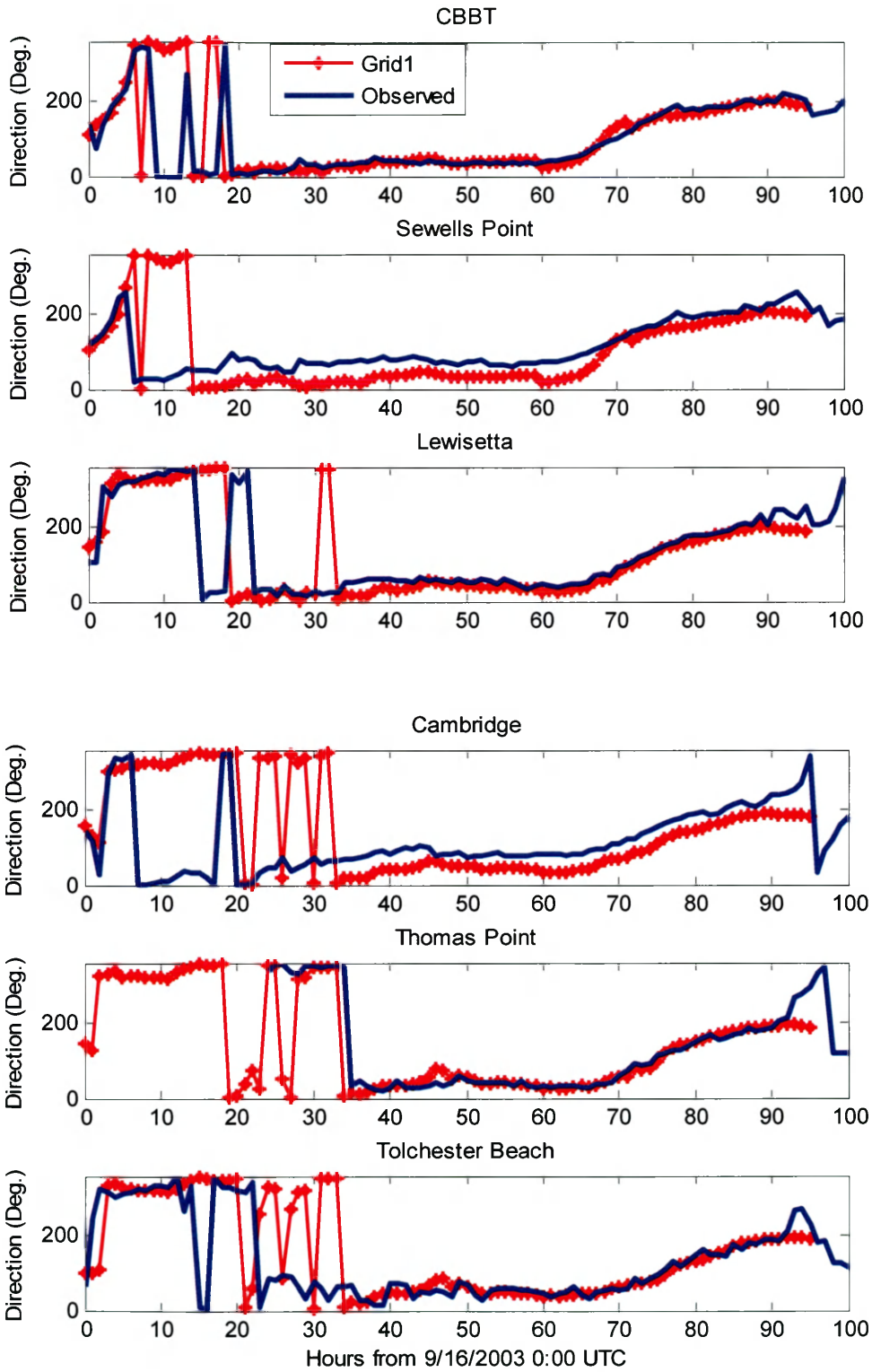

Figure 3.24 Comparison of wind directions between RAMS (grid1) modeled wind and observation in the Bay

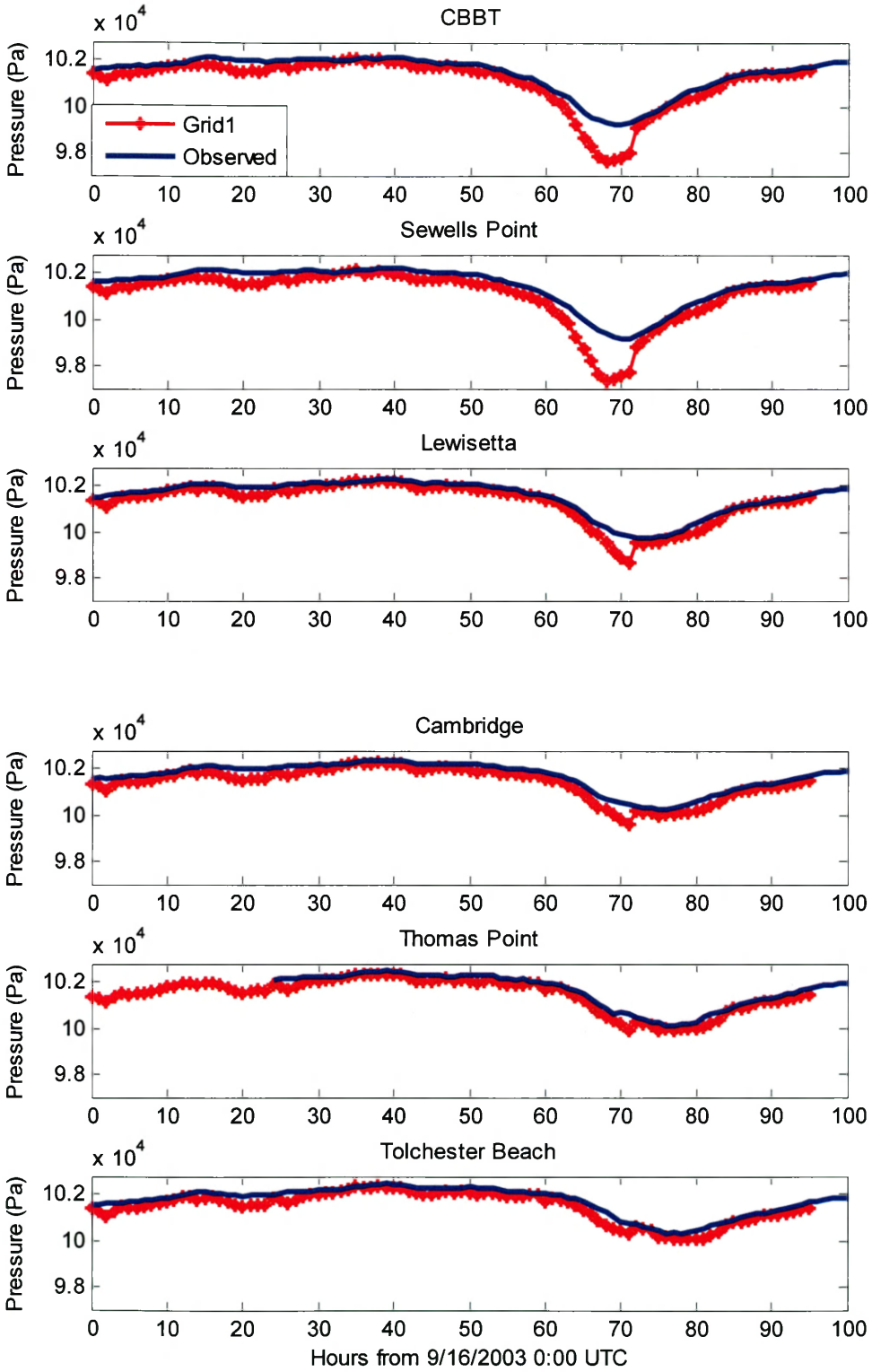

Figure 3.25 Comparison of pressures between RAMS (grid1) modeled pressure and observation in the Bay

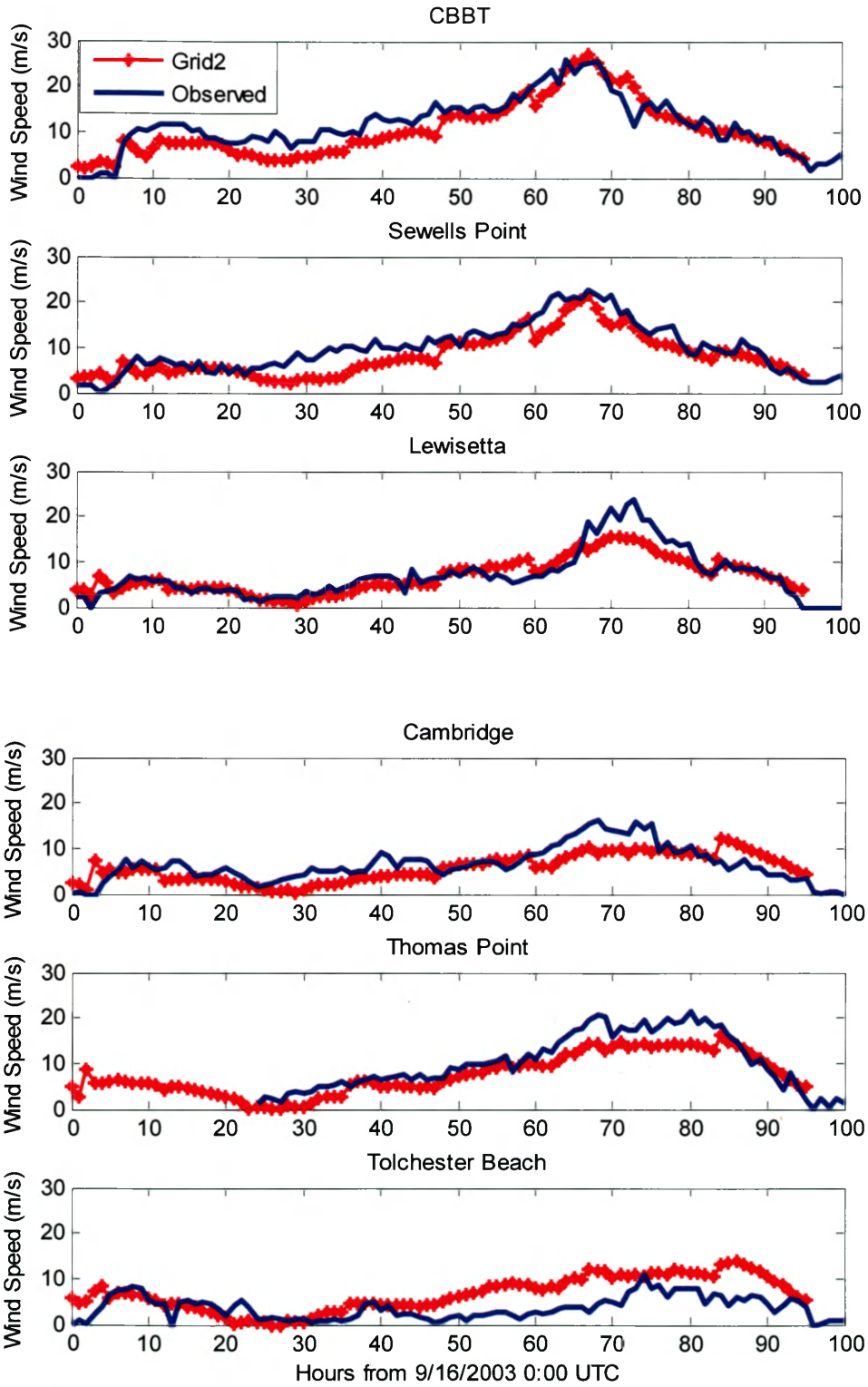

Figure 3.26 Comparison of wind speeds between RAMS (grid2) modeled wind and observation in the Bay

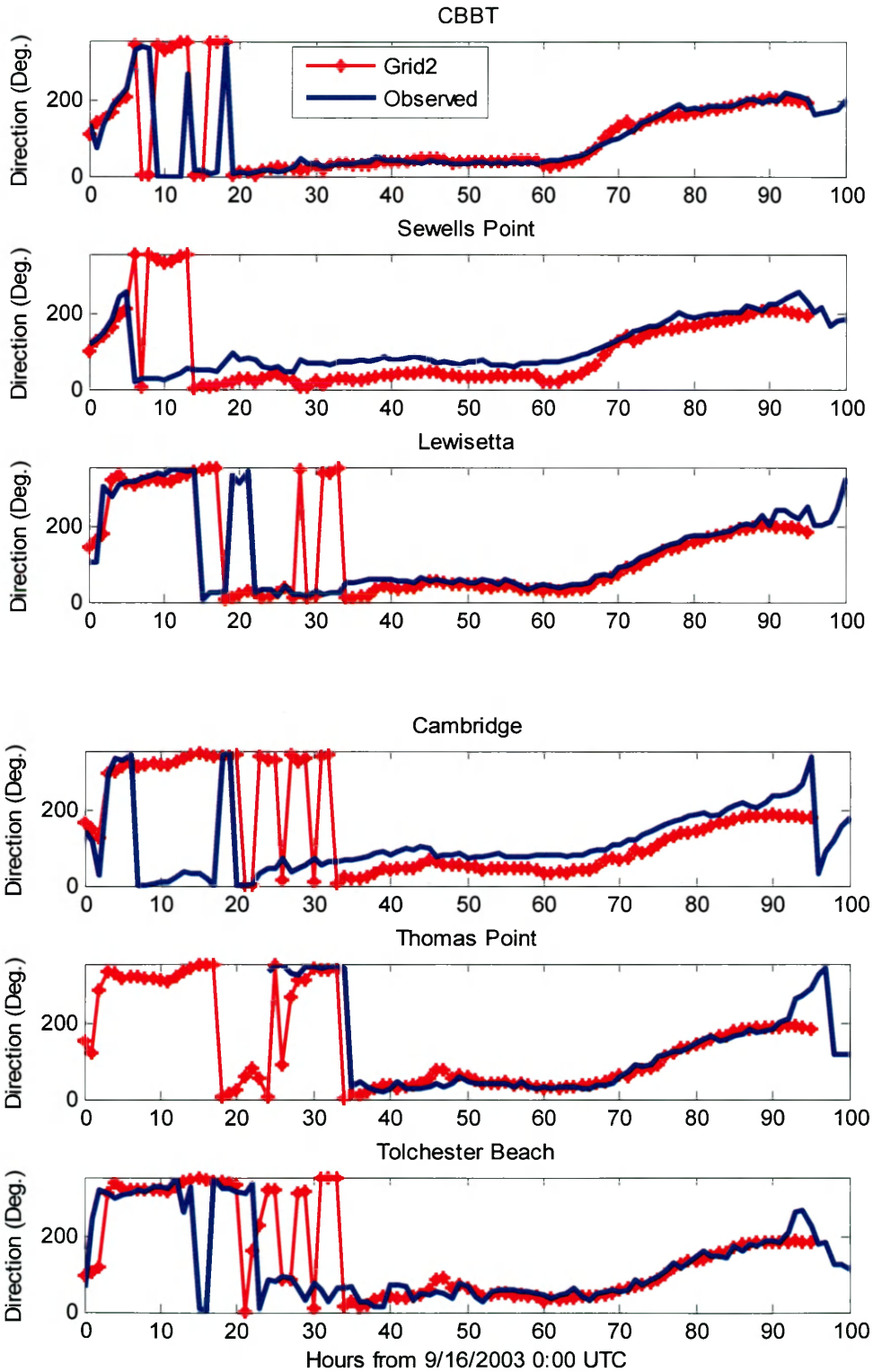

Figure 3.27 Comparison of wind directions between RAMS (grid2) modeled wind and observation in the Bay

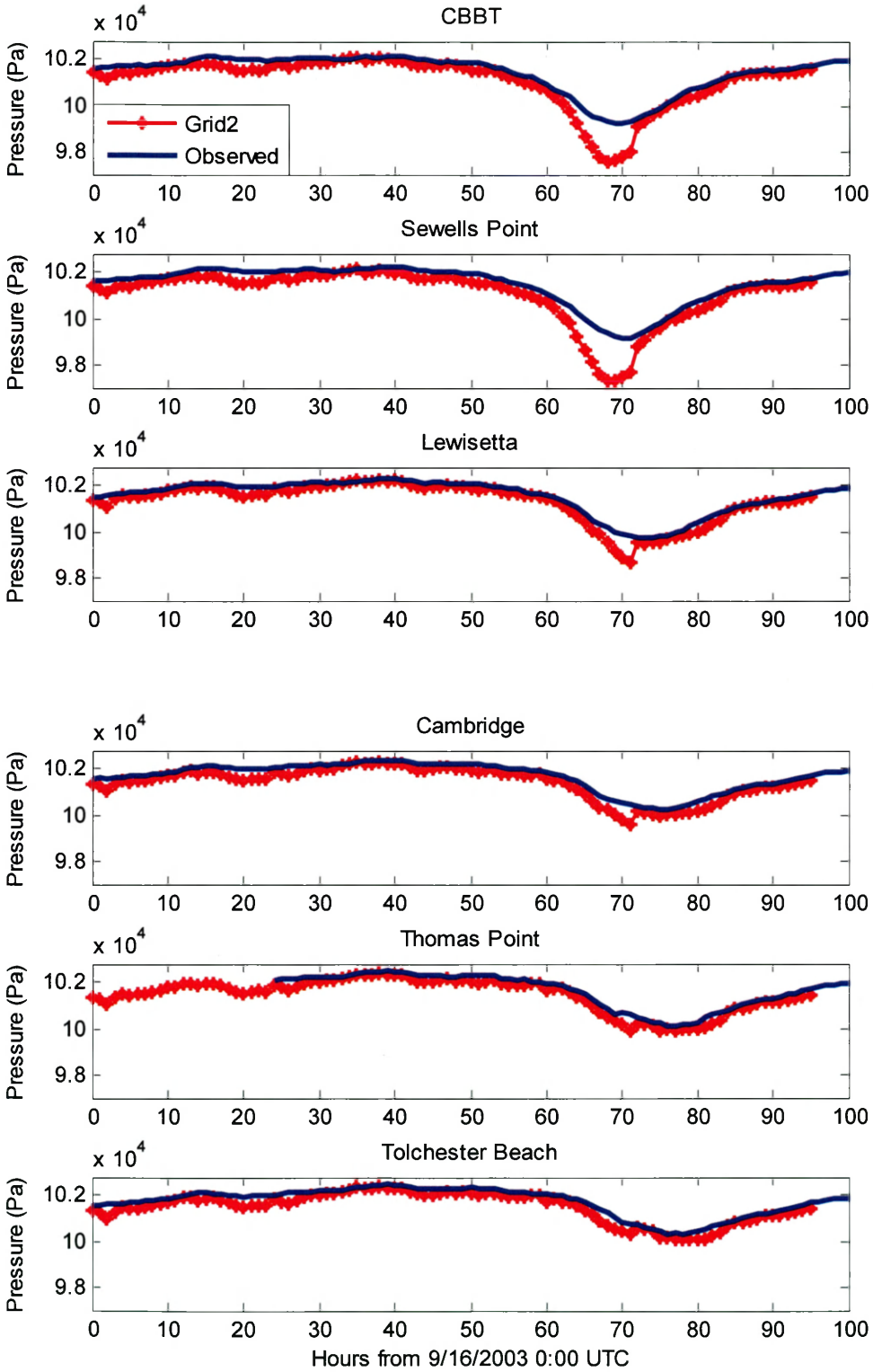

Figure 3.28 Comparison of pressures between RAMS (grid2) modeled pressure and observation in the Bay

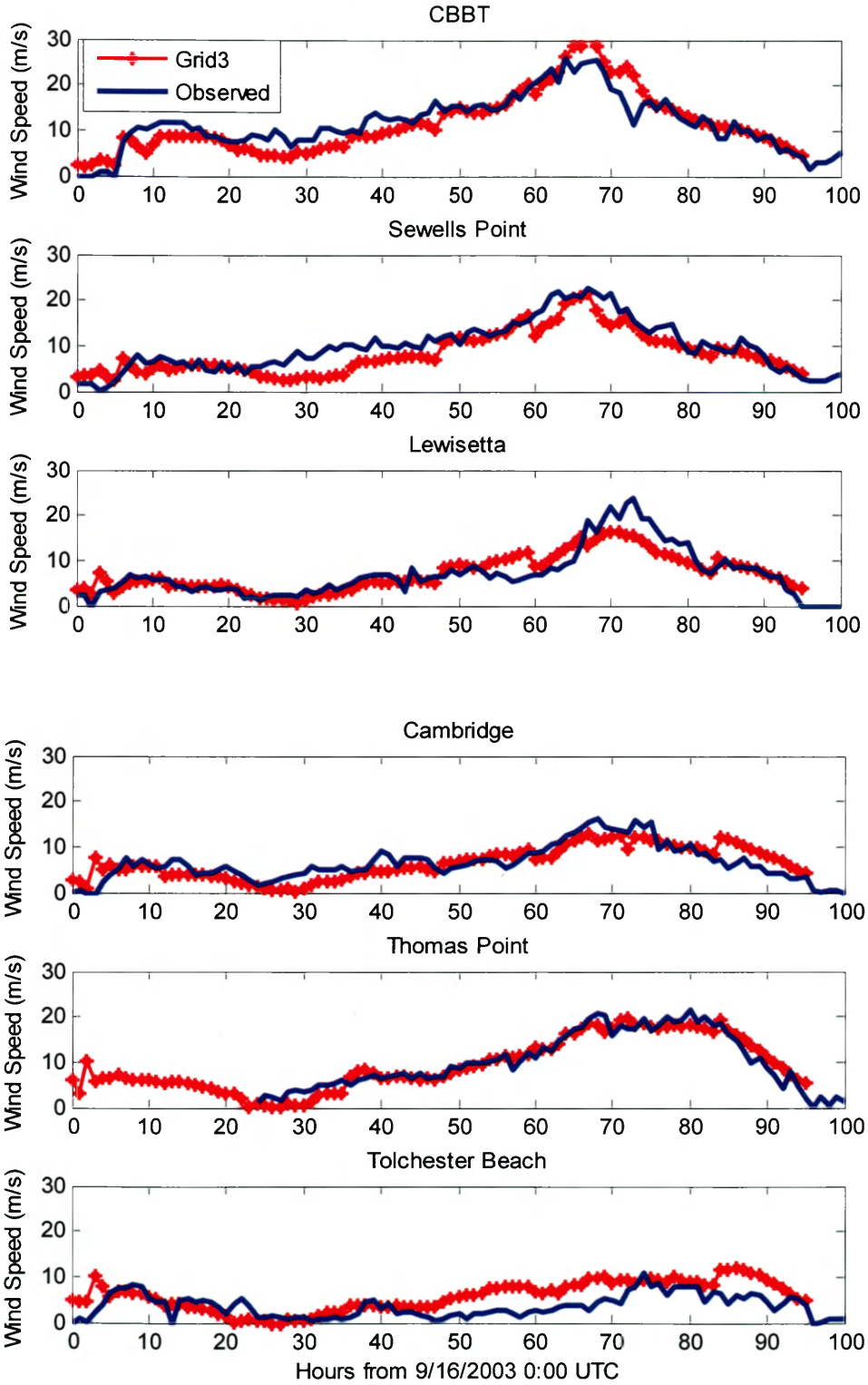

Figure 3.29 Comparison of wind speeds between RAMS (grid3) modeled wind and observation in the Bay

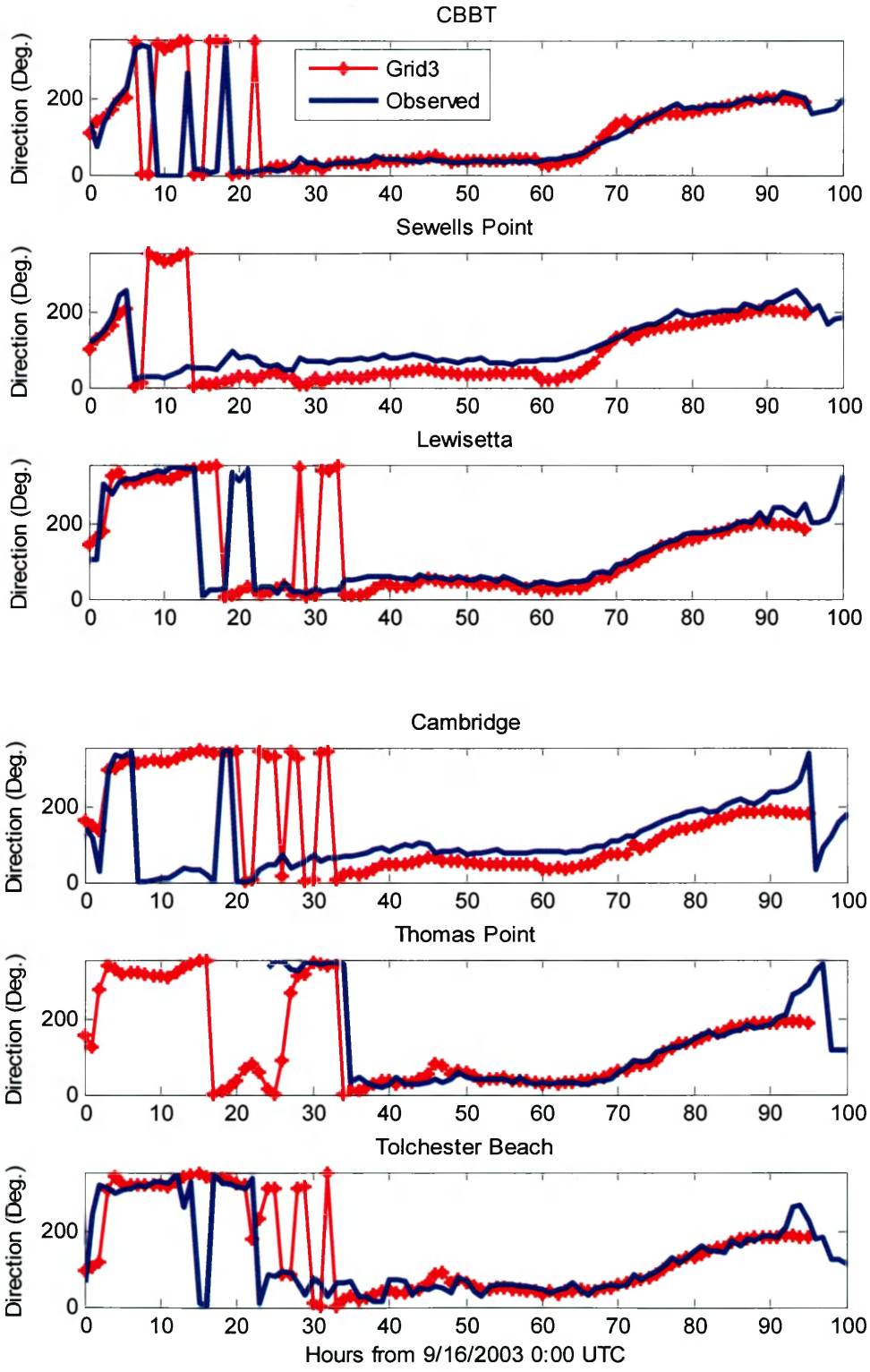

Figure 3.30 Comparison of wind directions between RAMS (grid3) modeled wind and observation in the Bay

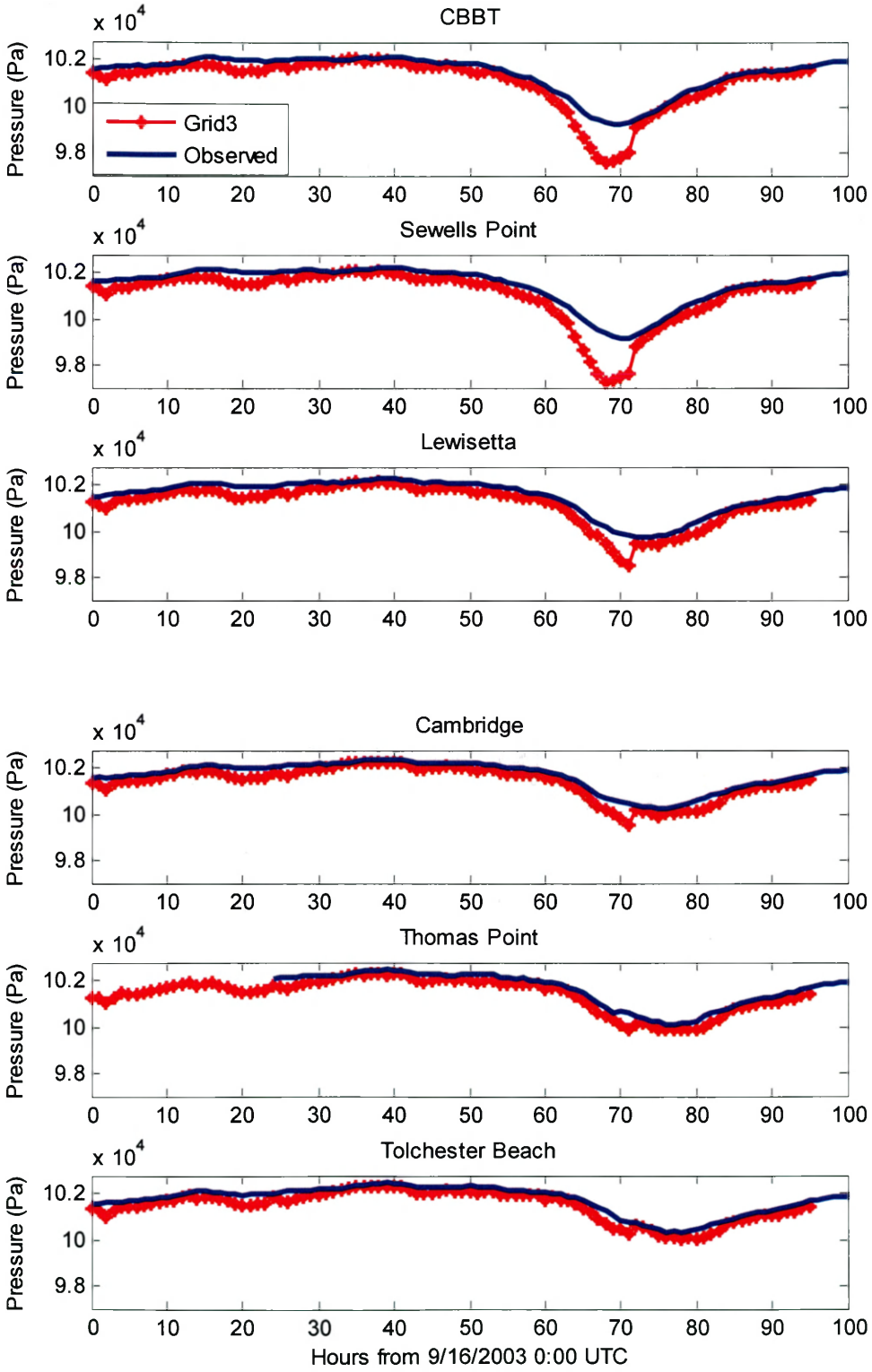

Figure 3.31 Comparison of pressures between RAMS (grid3) modeled pressure and observation in the Bay

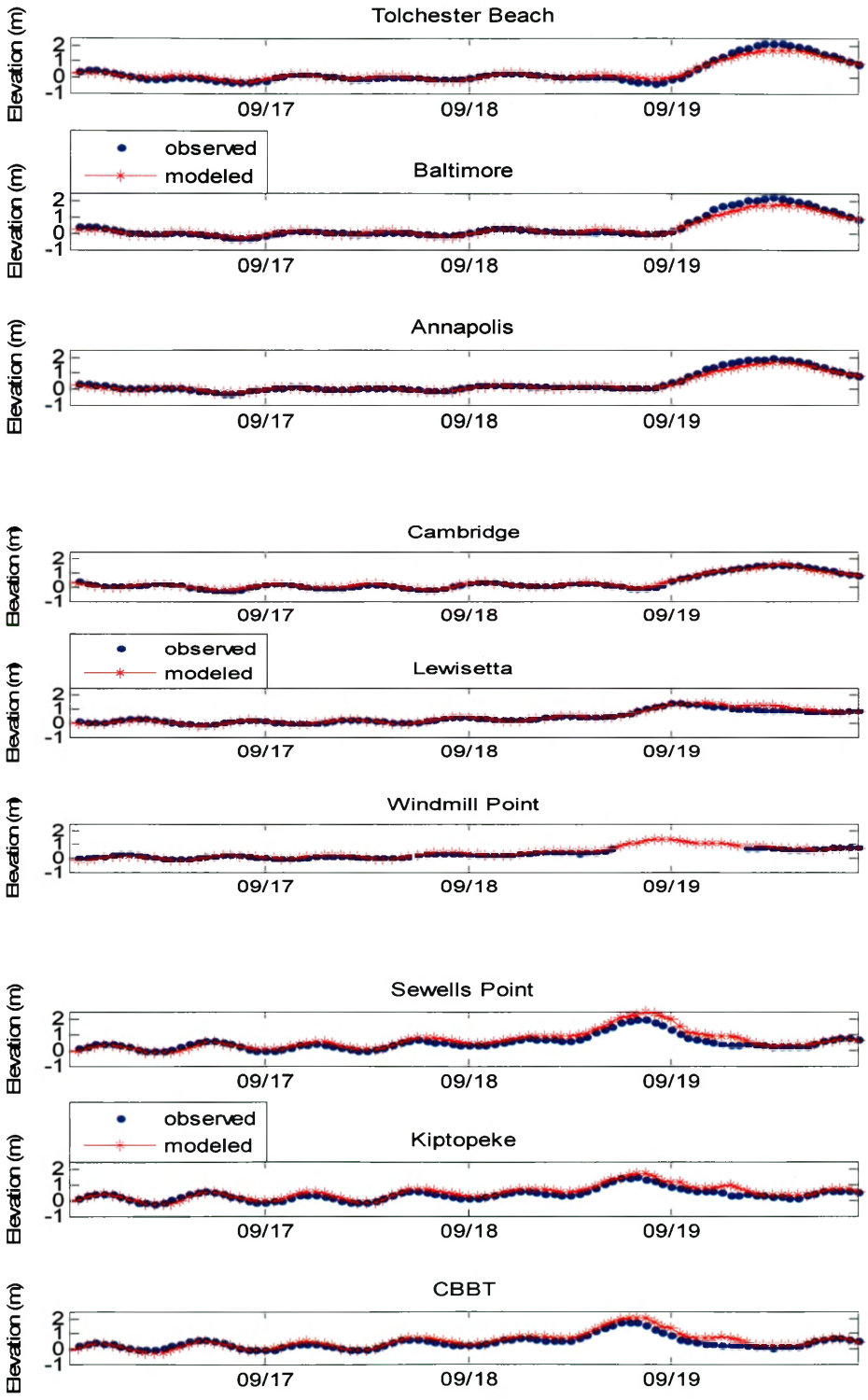

Figure 3.32 Comparison between modeled surface elevation using GFS wind and observation

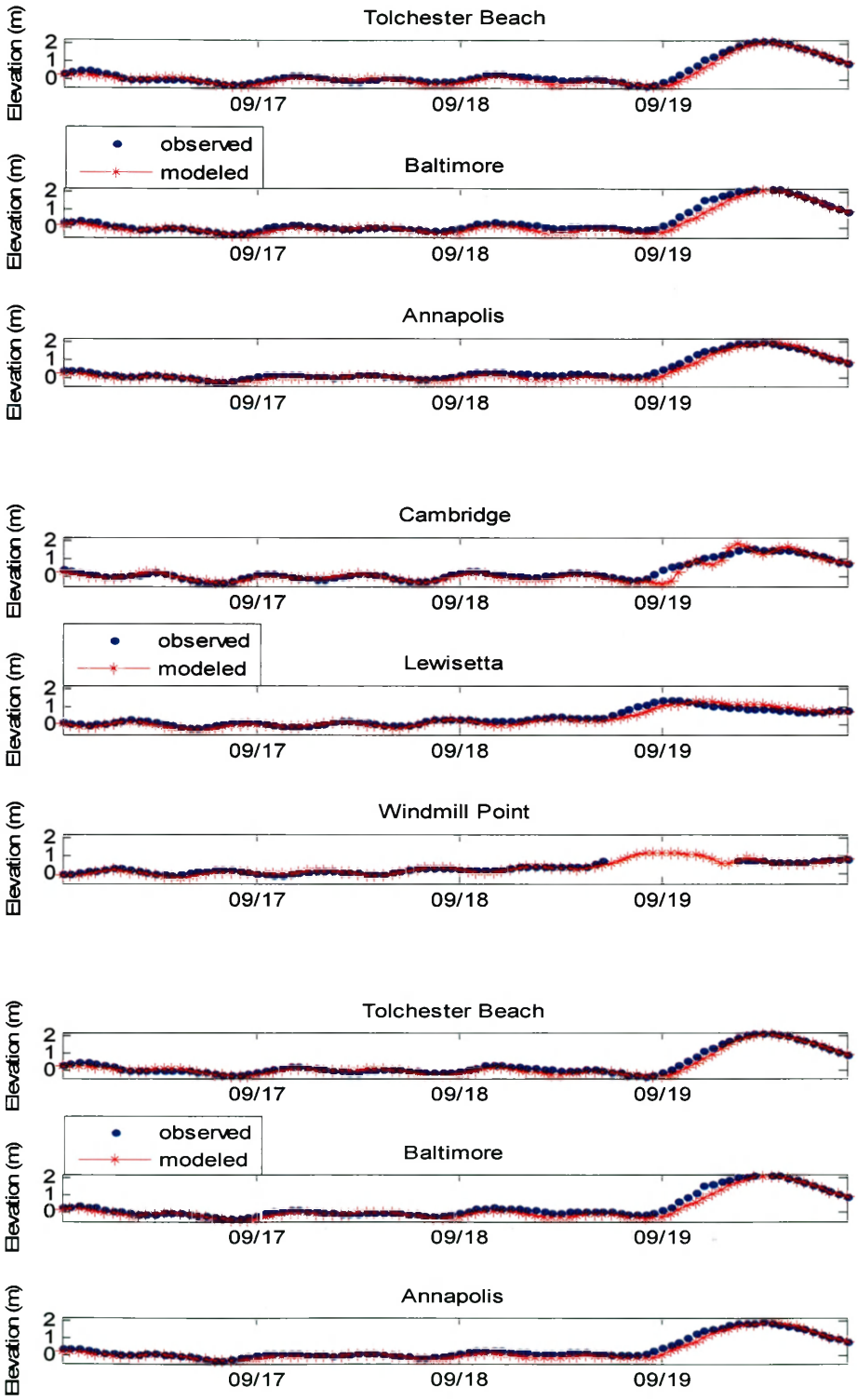

Figure 3.33 Comparison between modeled surface elevation using NAM wind and observation

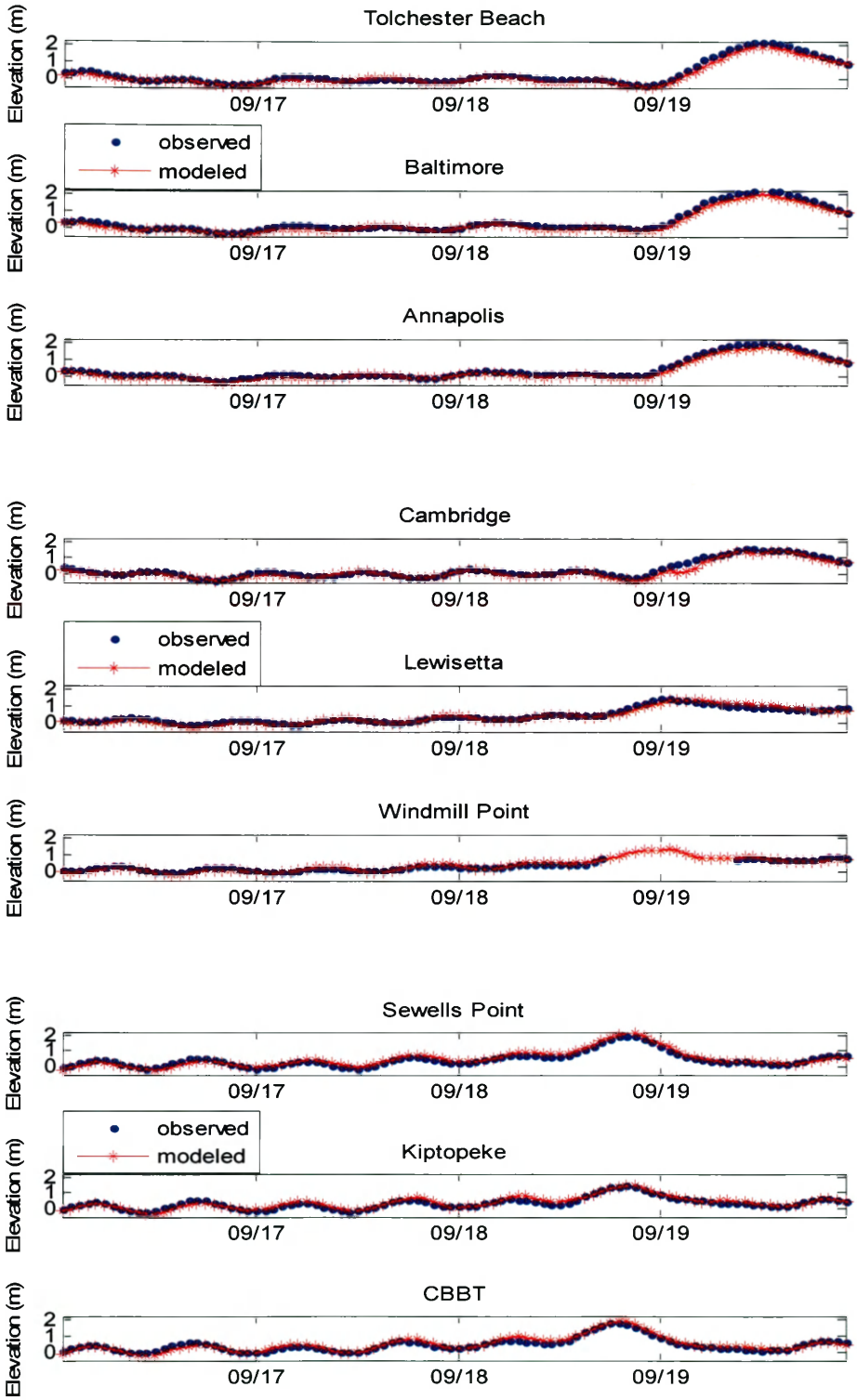

Figure 3.34 Comparison between modeled surface elevation using WRF-GFS wind and observation

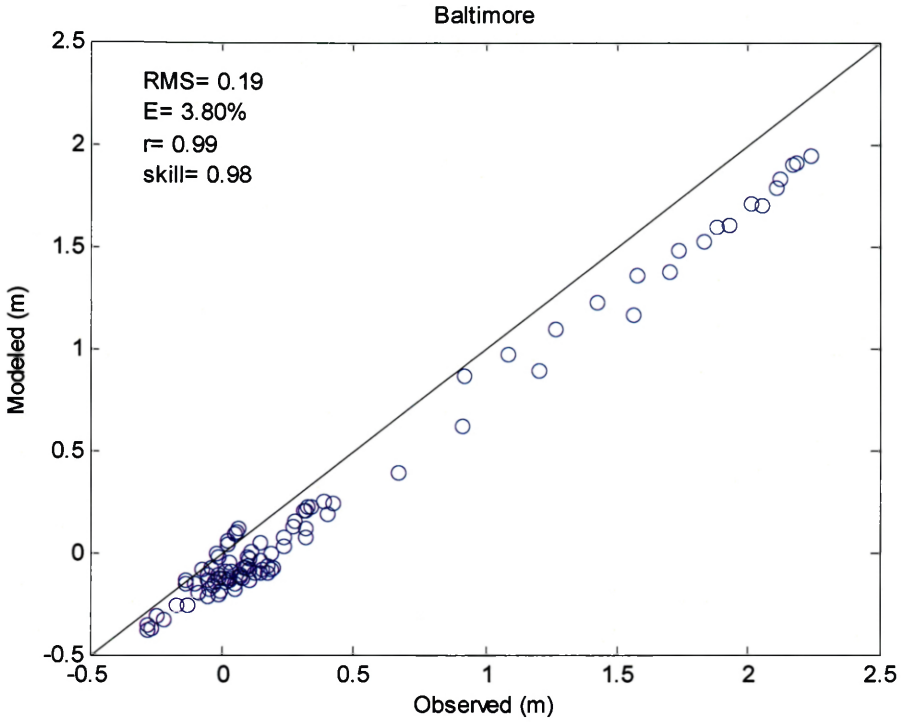

Figure 3.35 Modeled surface elevation against observed storm surge at Baltimore

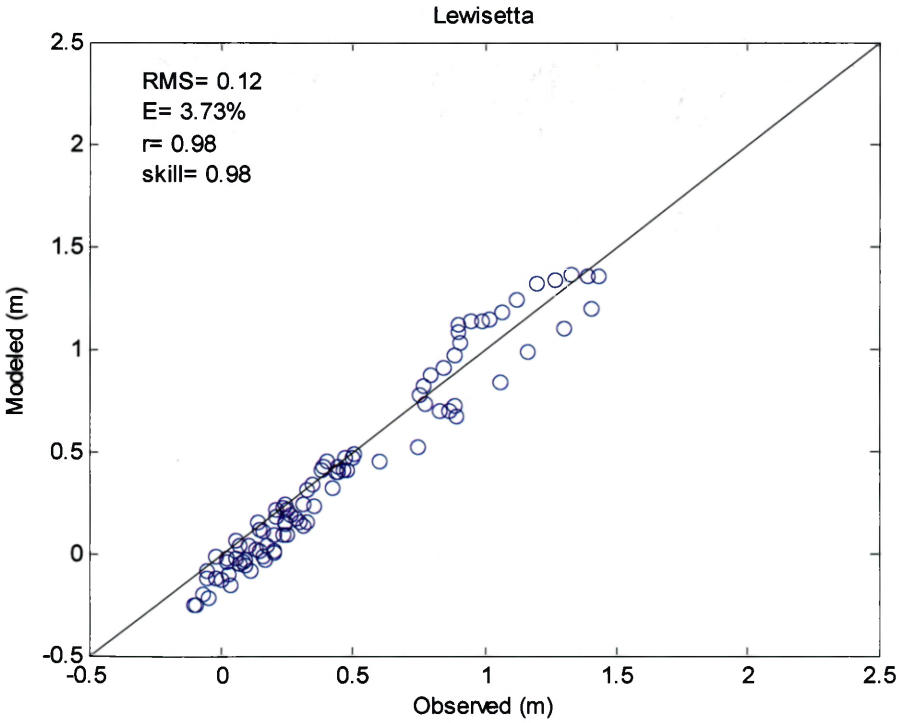

Figure 3.36 Modeled surface elevation against observed storm surge at Lewisetta

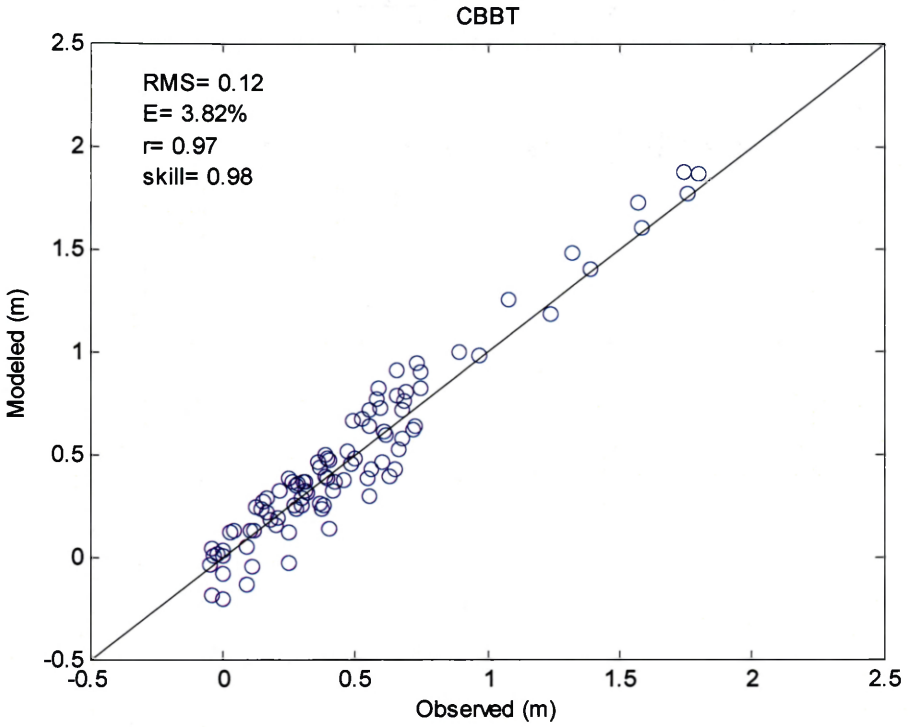

Figure 3.37 Modeled surface elevation against observed storm surge at CBBT

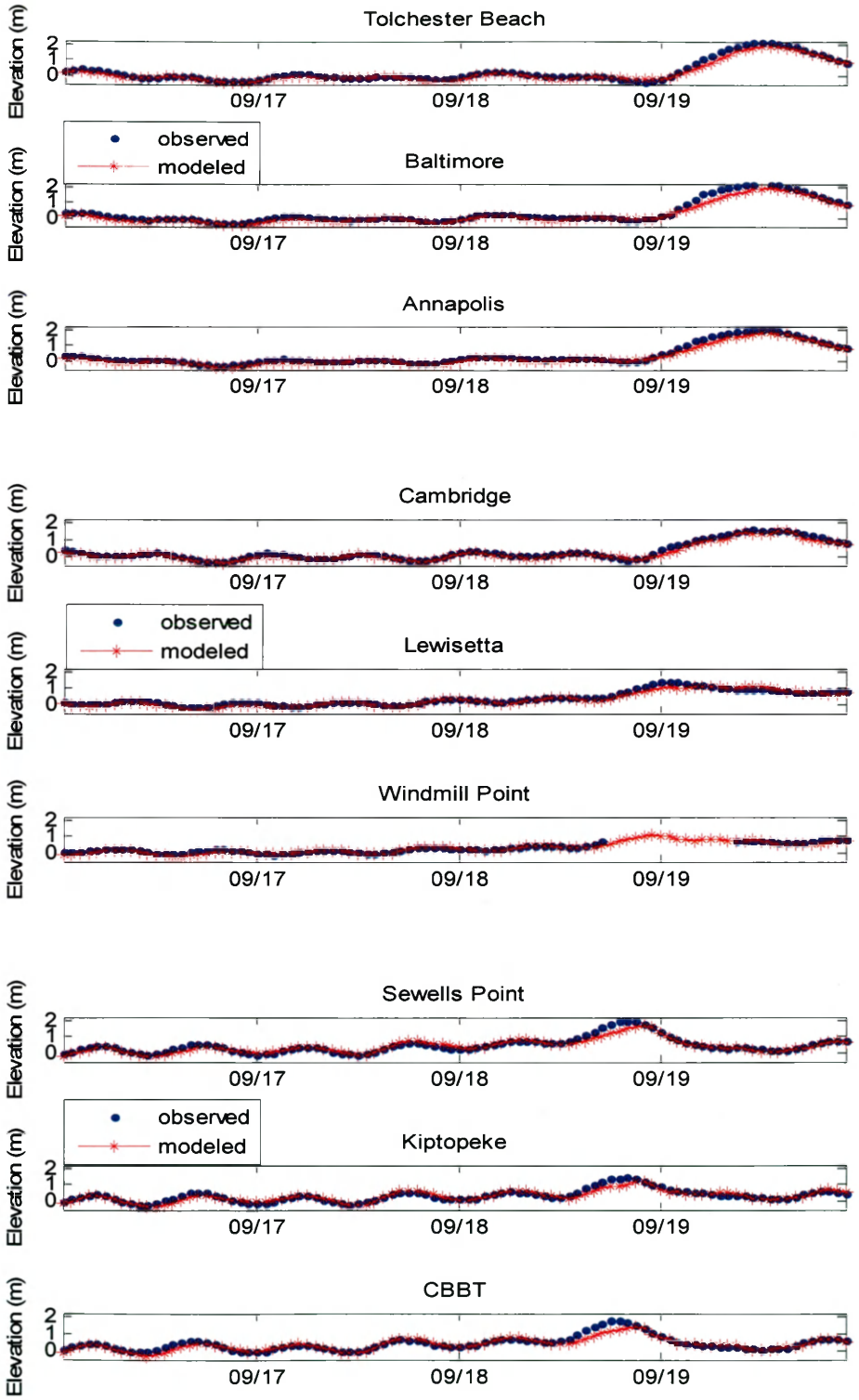

Figure 3.38 Comparison between modeled surface elevation using WRF-NAM wind and observation

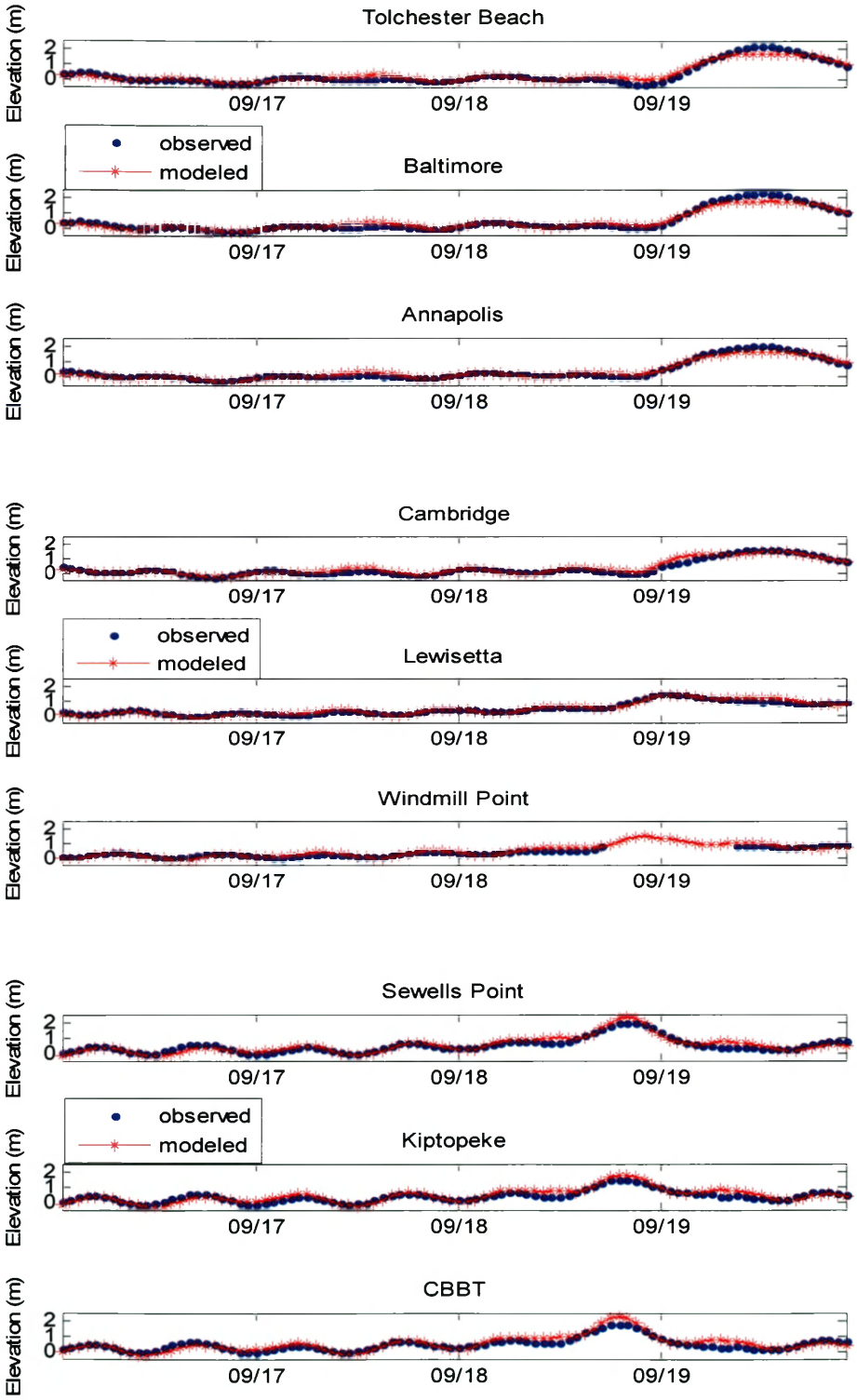

Figure 3.39 Comparison between modeled surface elevation using RAMS (grid1) wind and observation

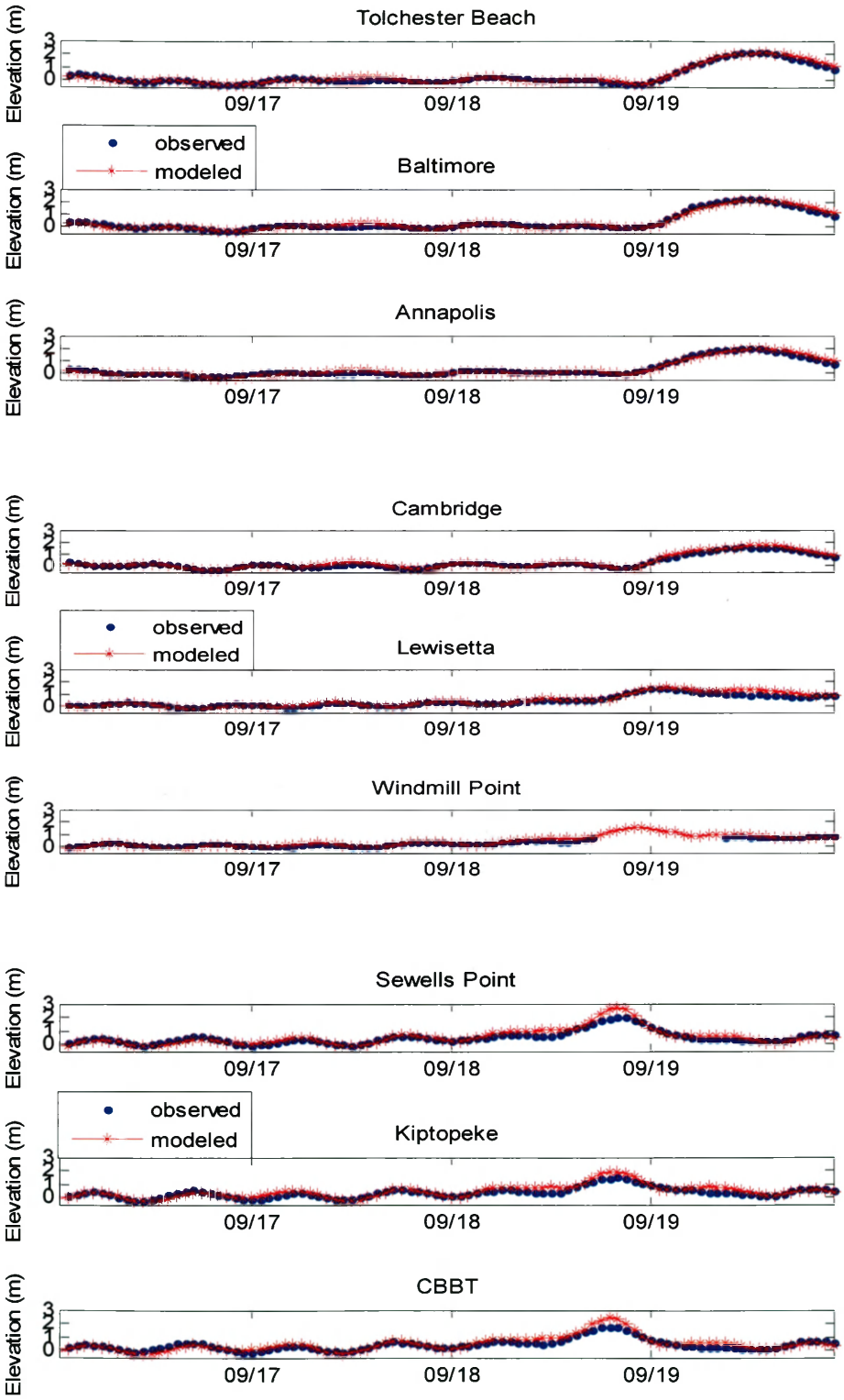

Figure 3.40 Comparison between modeled surface elevation using RAMS (grid2) wind and observation

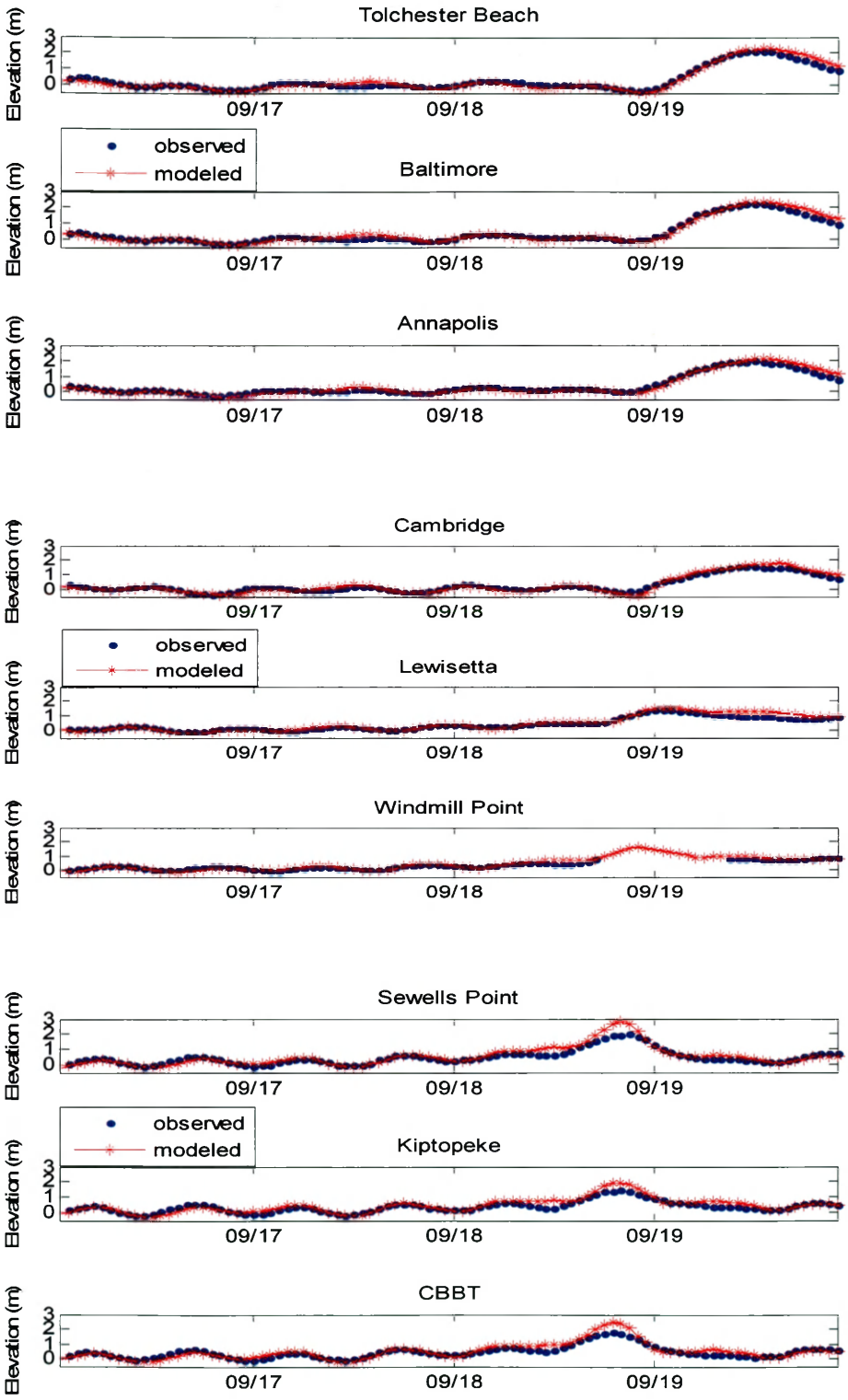

Figure 3.41 Comparison between modeled surface elevation using RAMS (grid3) wind and observation

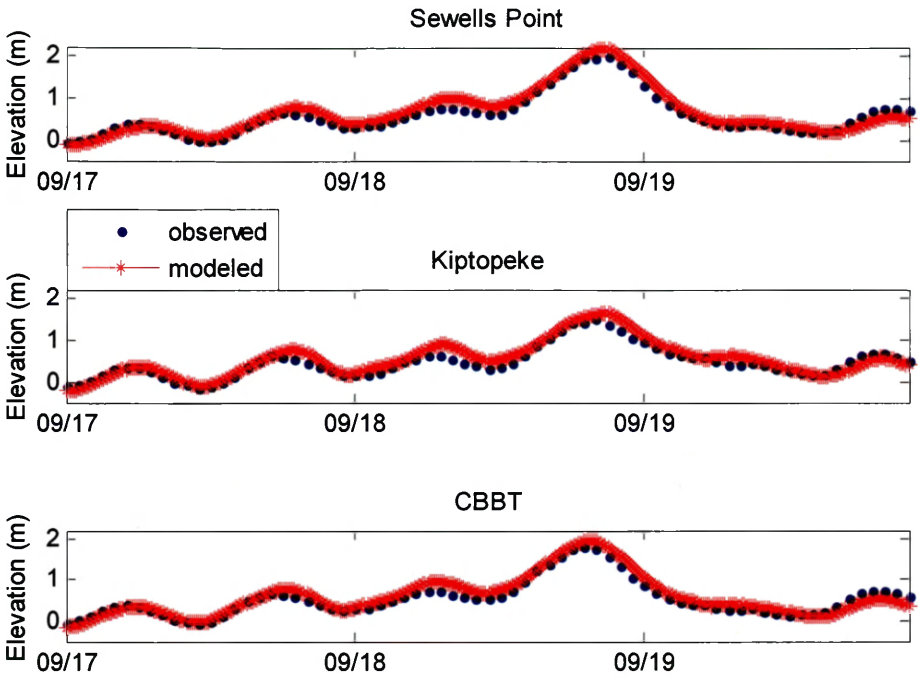

Figure 3.42 Comparison between modeled surface elevation and observation during Hurricane Isabel using small domain grid

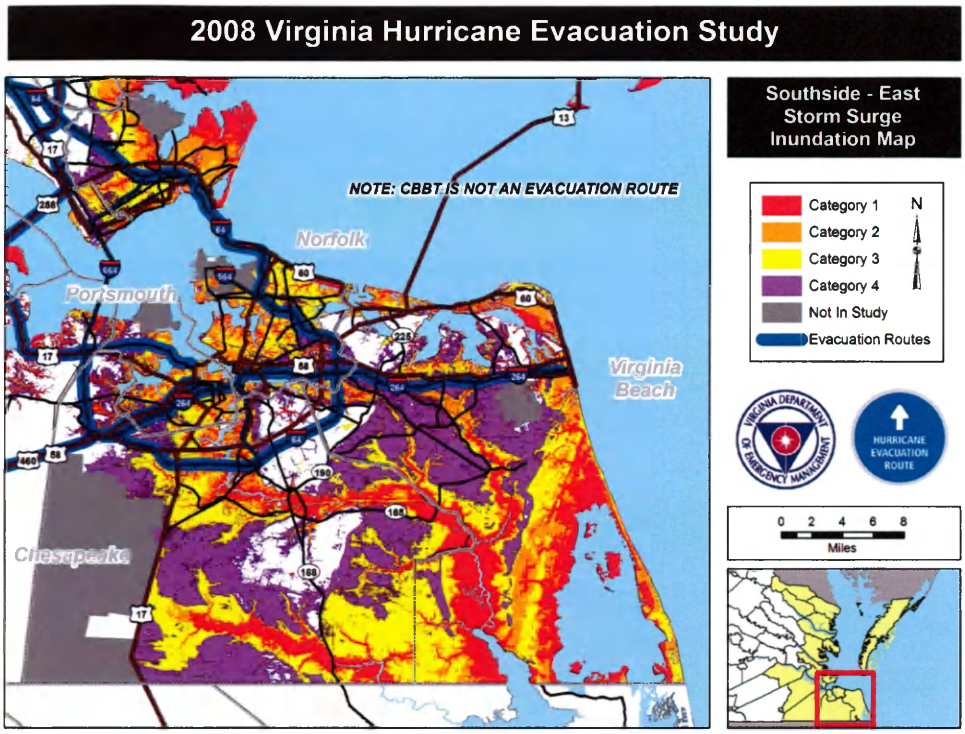

Figure 3.43 Southside-East Storm Surge Inundation Map (From www.vaemergency.com)

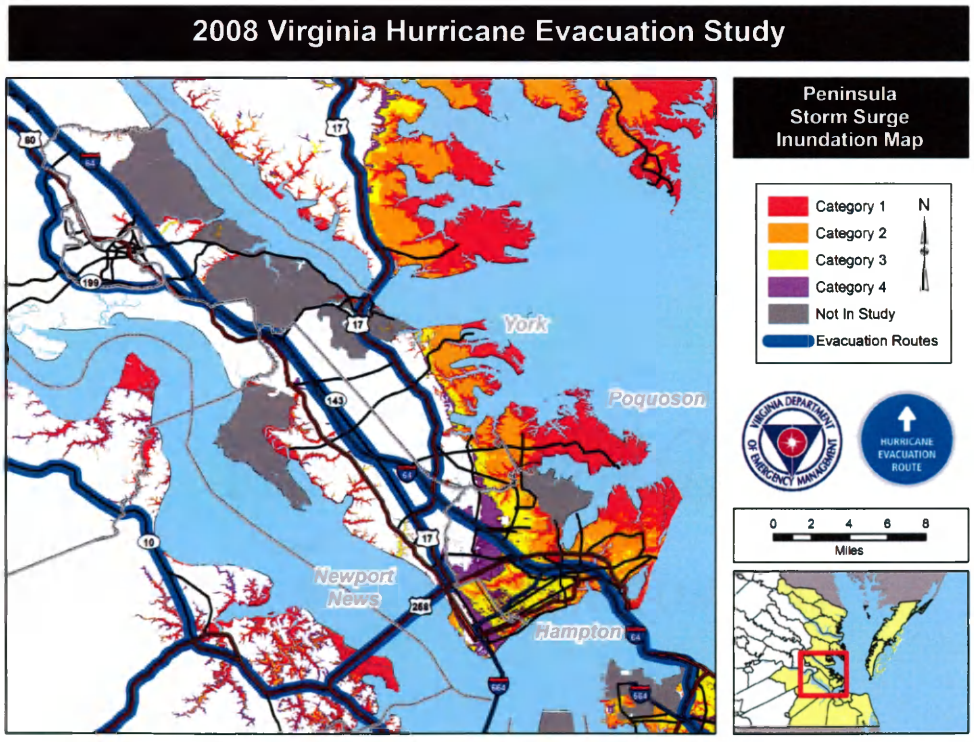

Figure 3.44 Penisula Storm Surge Inundation Map in Virginia

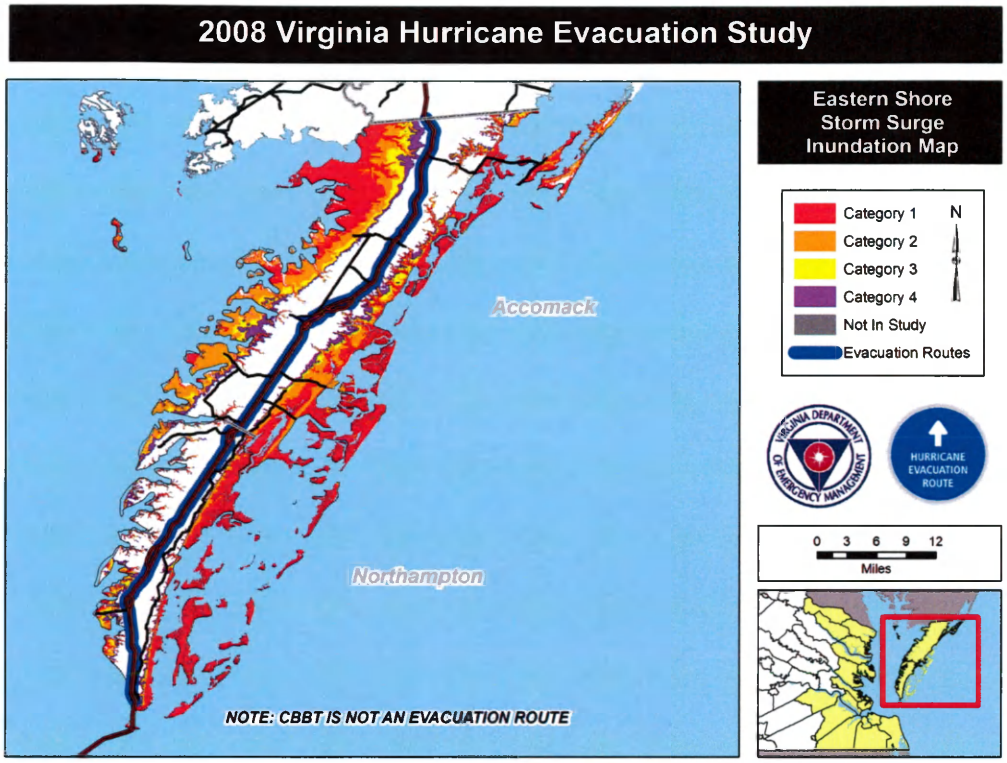

Figure 3.45 Eastern Shore Storm surge Inundation Map

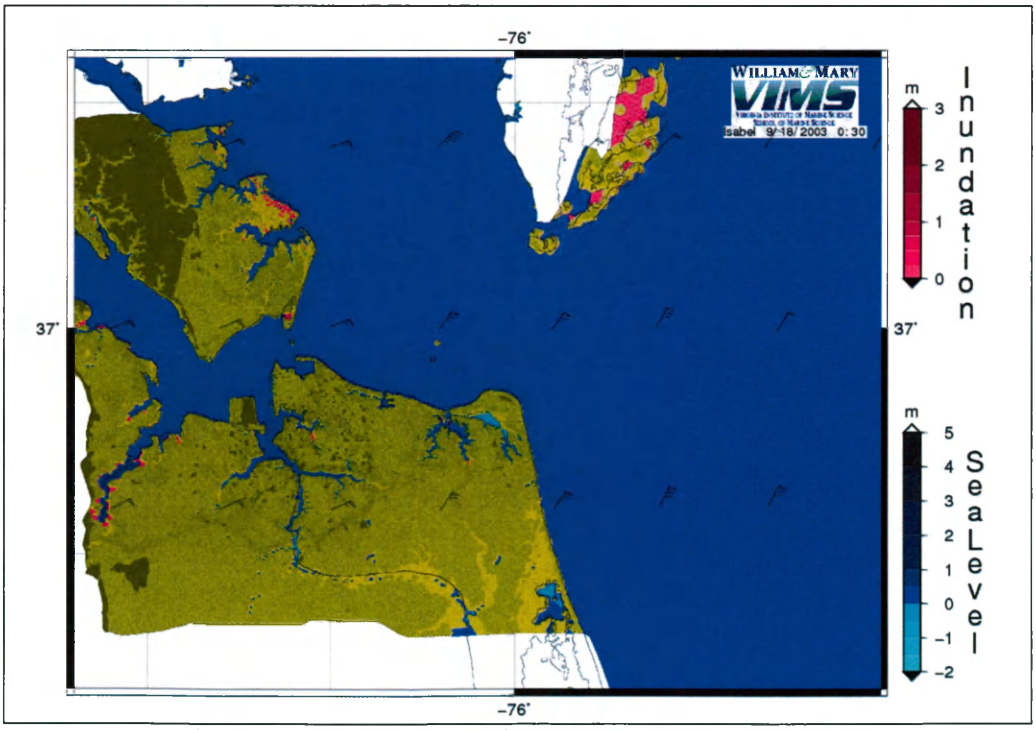

Figure 3.46 Modeled Inundation Map at 0:30 UTC 9/18/2003

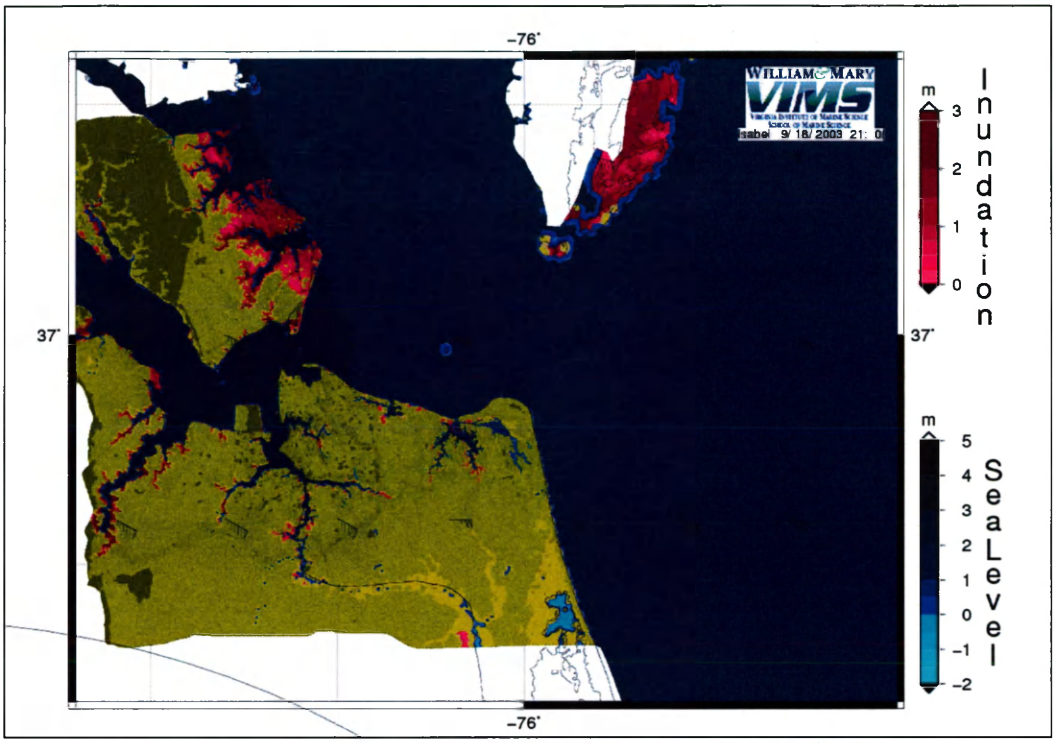

Figure 3.47 Modeled Inundation Map at 21:00 UTC 9/18/2003

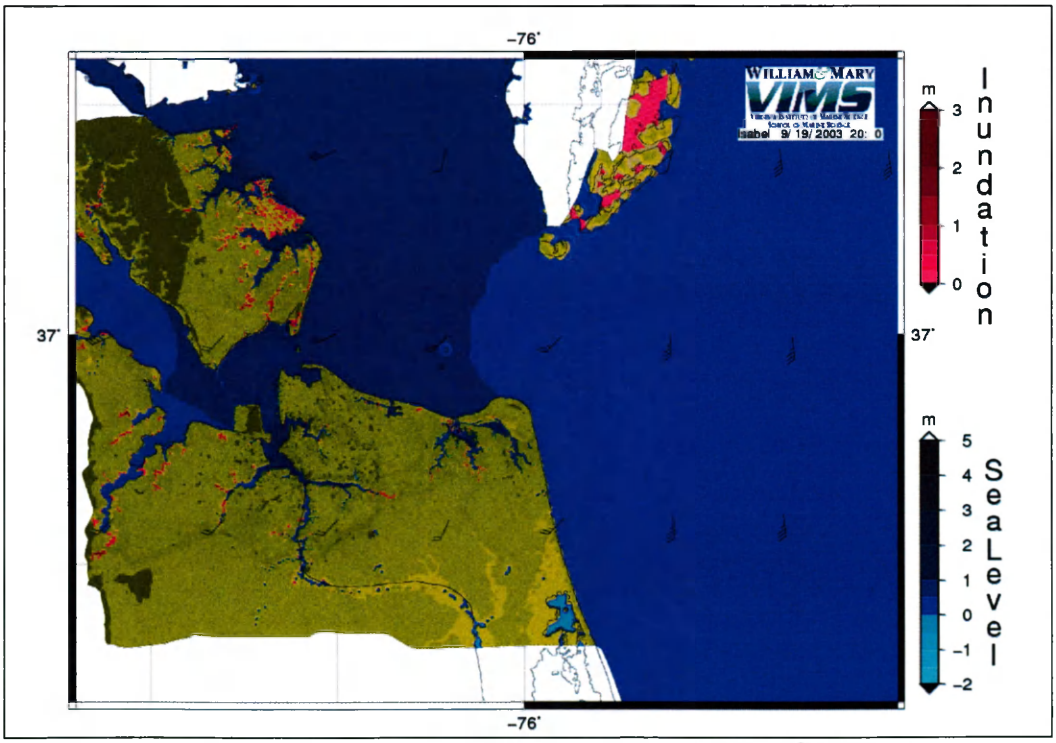

Figure 3.48 Modeled Inundation Map at 20:00 UTC 9/19/2003

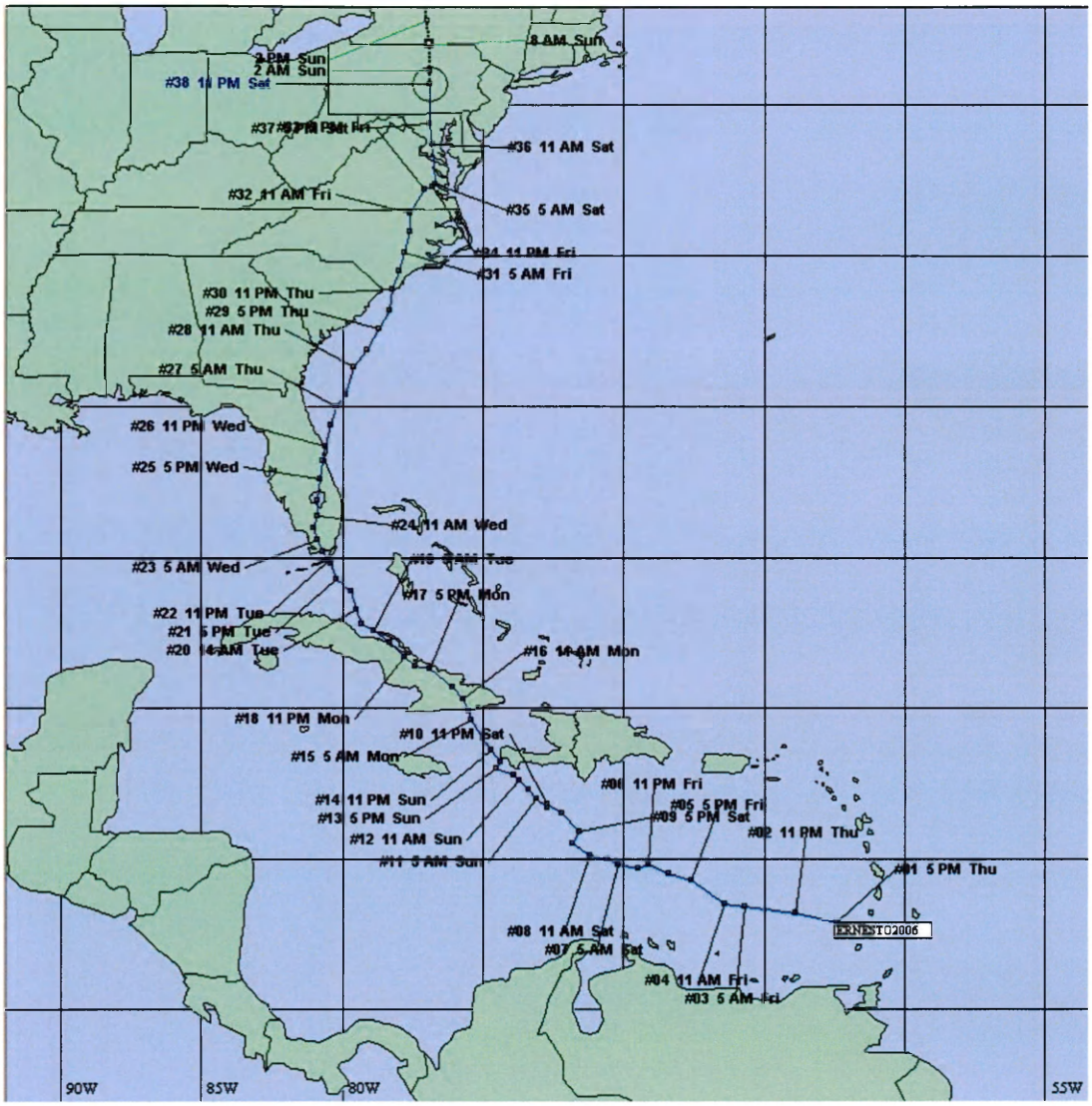

Figure 3.49 Track of Tropical Storm Ernesto

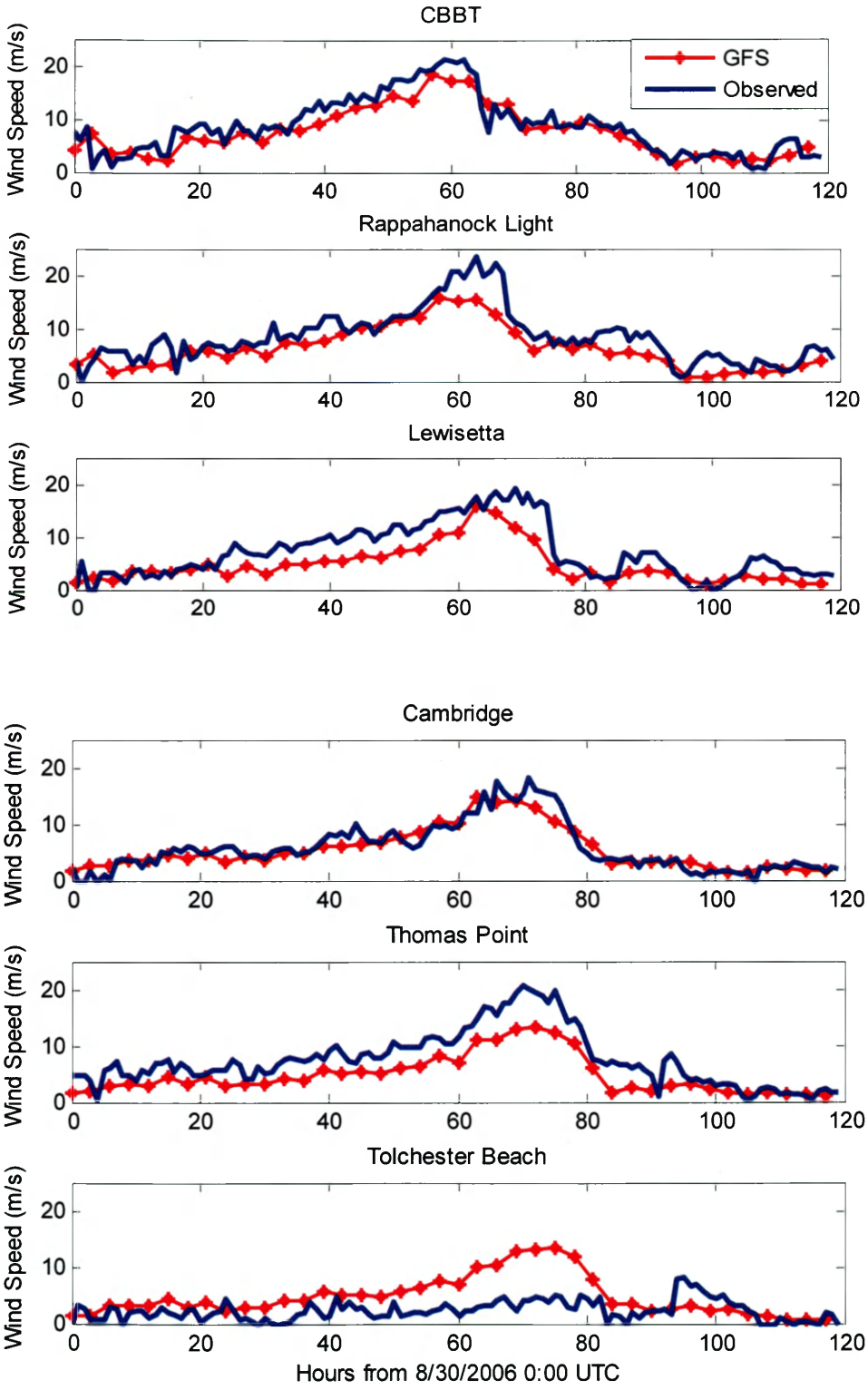

Figure 3.50 Comparison of wind speeds between GFS modeled wind and observation in the Bay

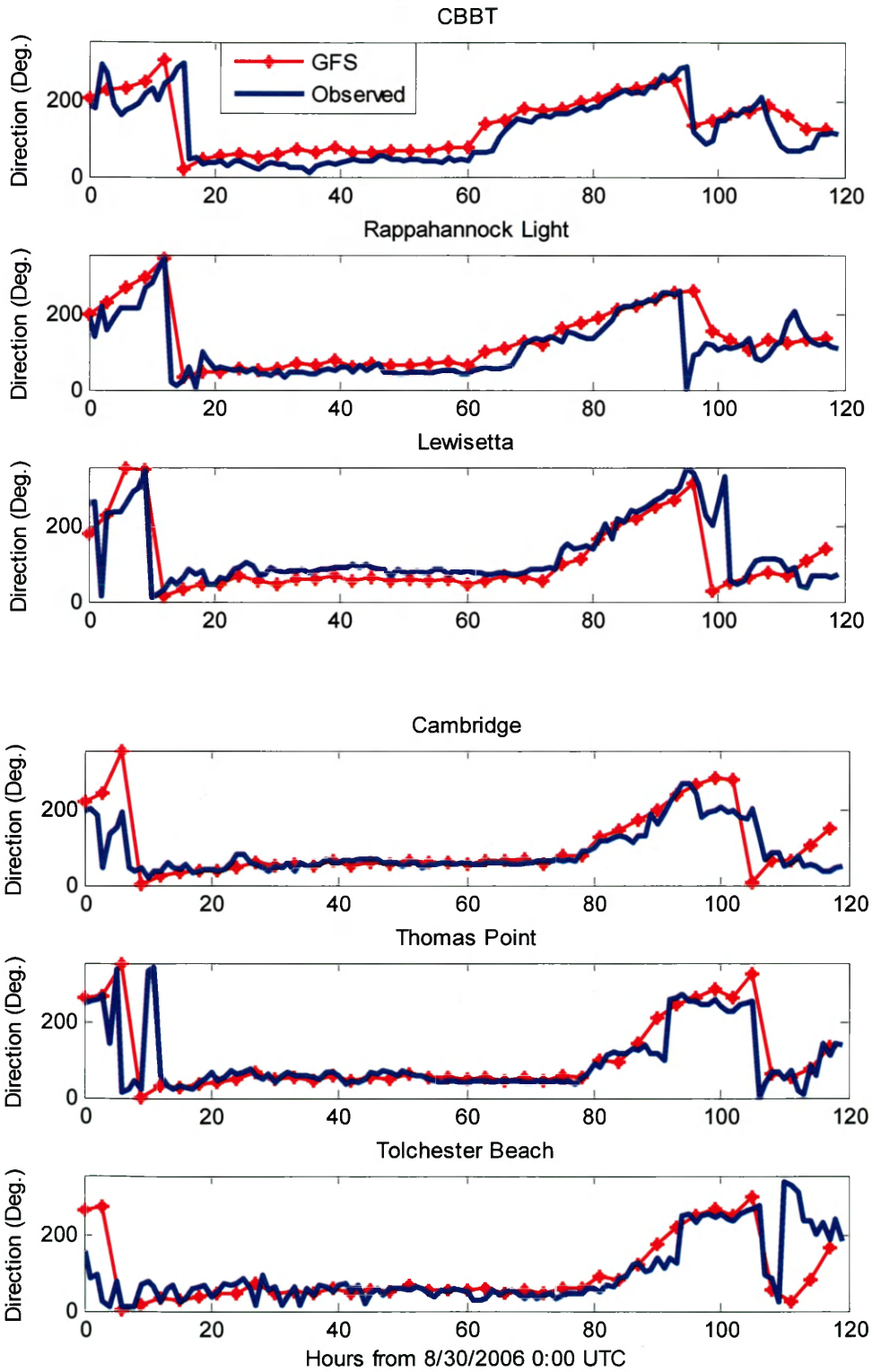

Figure 3.51 Comparison of wind directions between GFS modeled wind and observation in the Bay

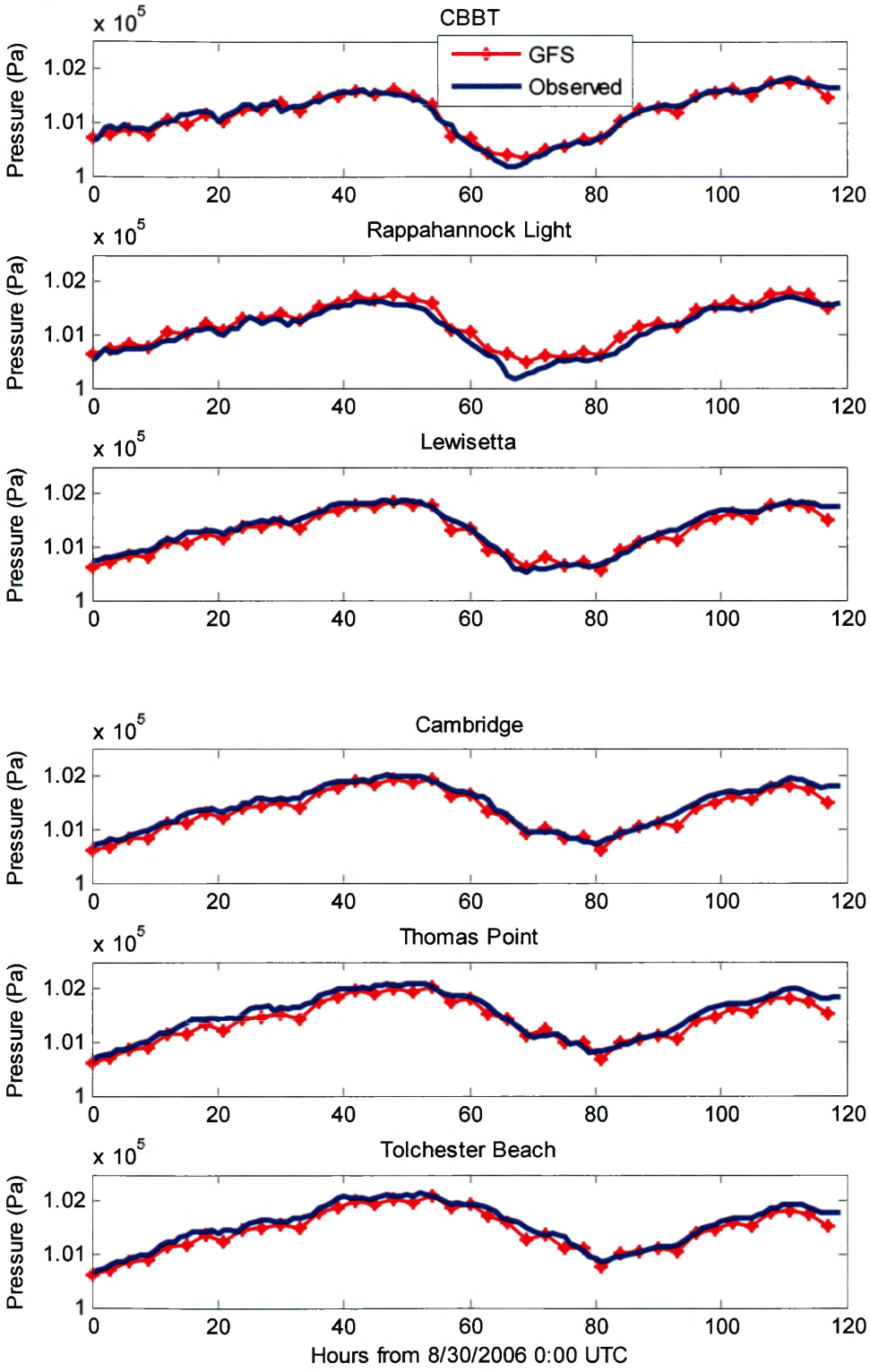

Figure 3.52 Comparison of pressure between GFS modeled pressure and observation in the Bay

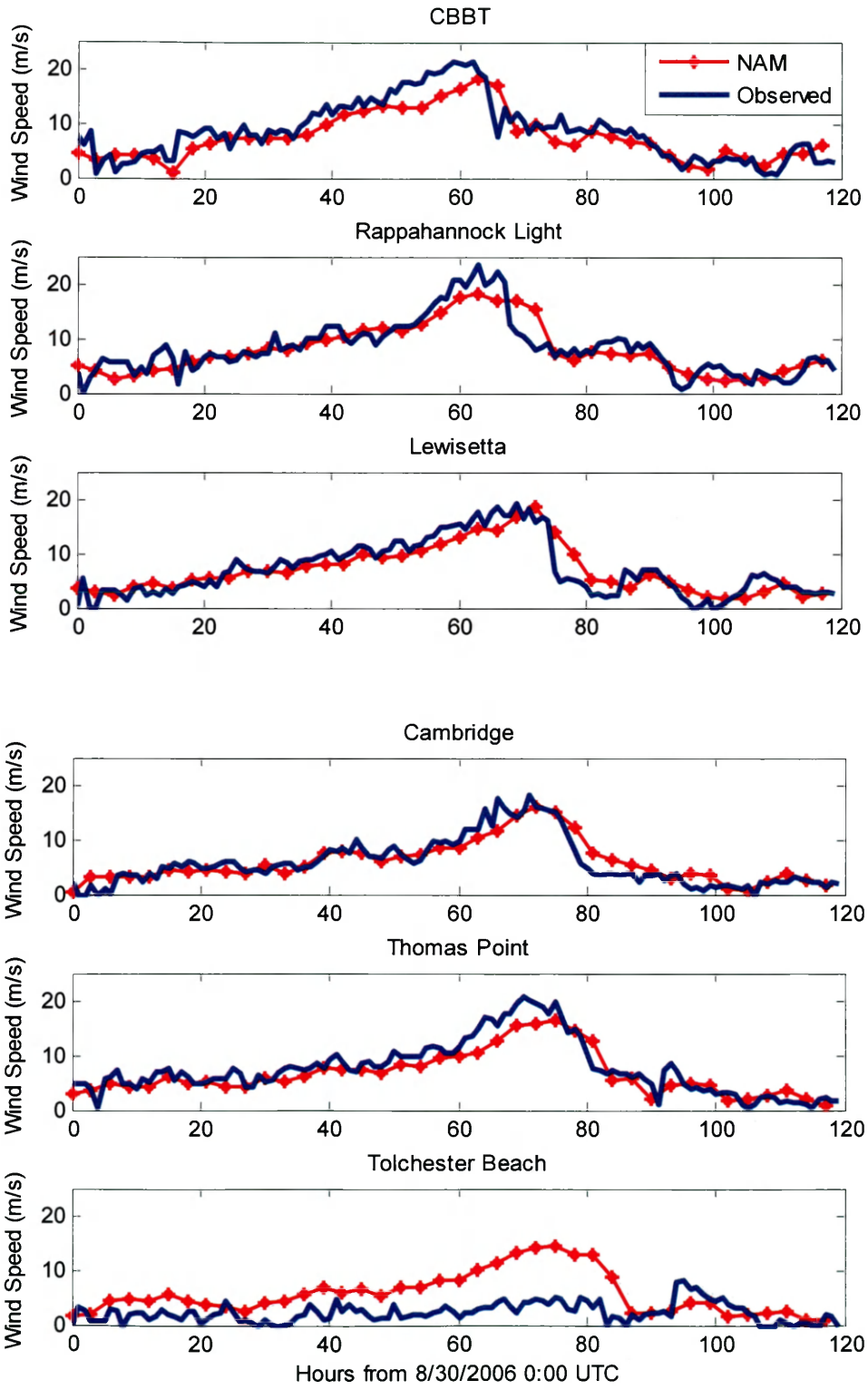

Figure 3.53 Comparison of wind speeds between NAM modeled wind and observation in the Bay

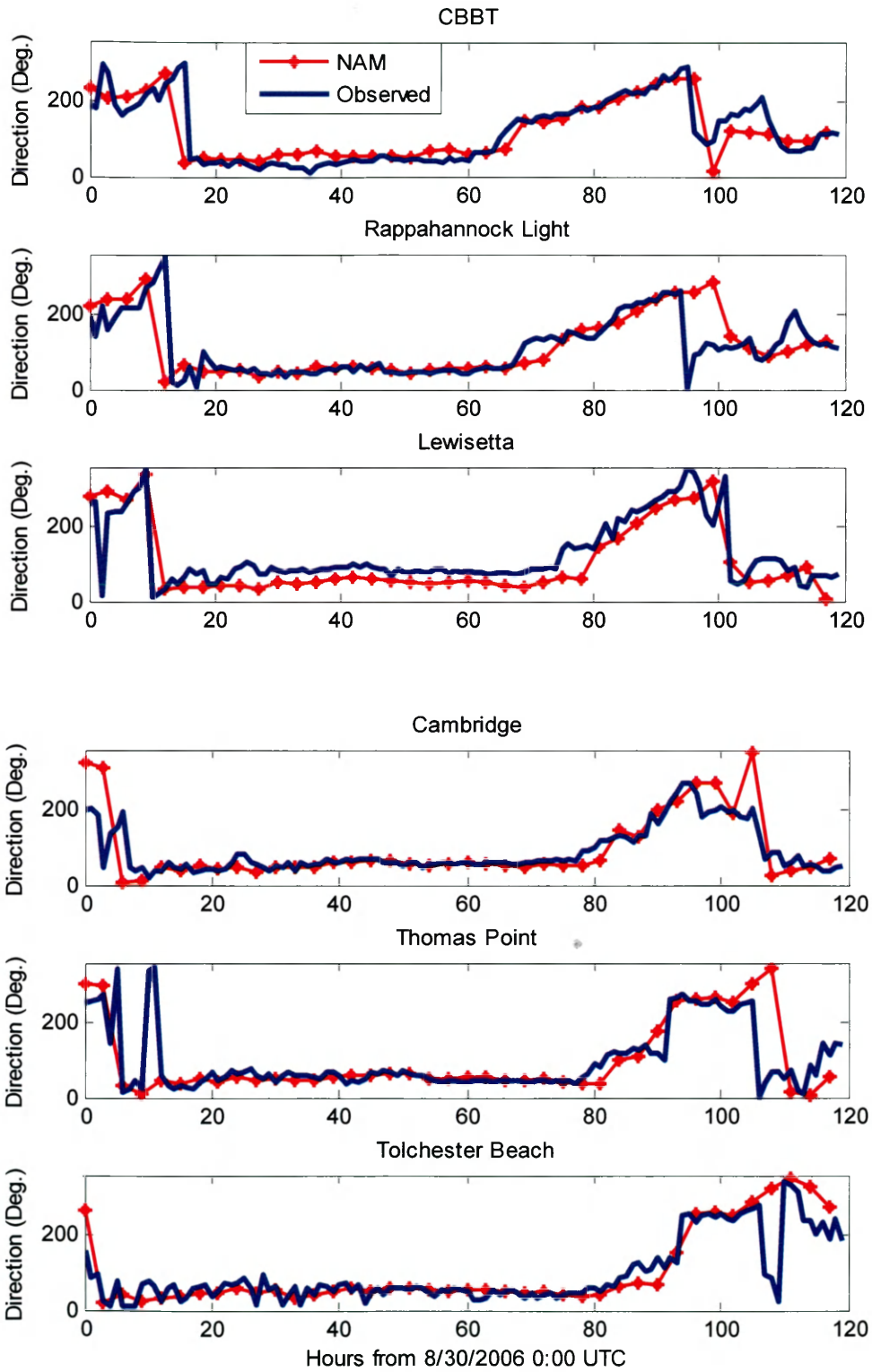

Figure 3.54 Comparison of wind directions between NAM modeled wind and observation in the Bay

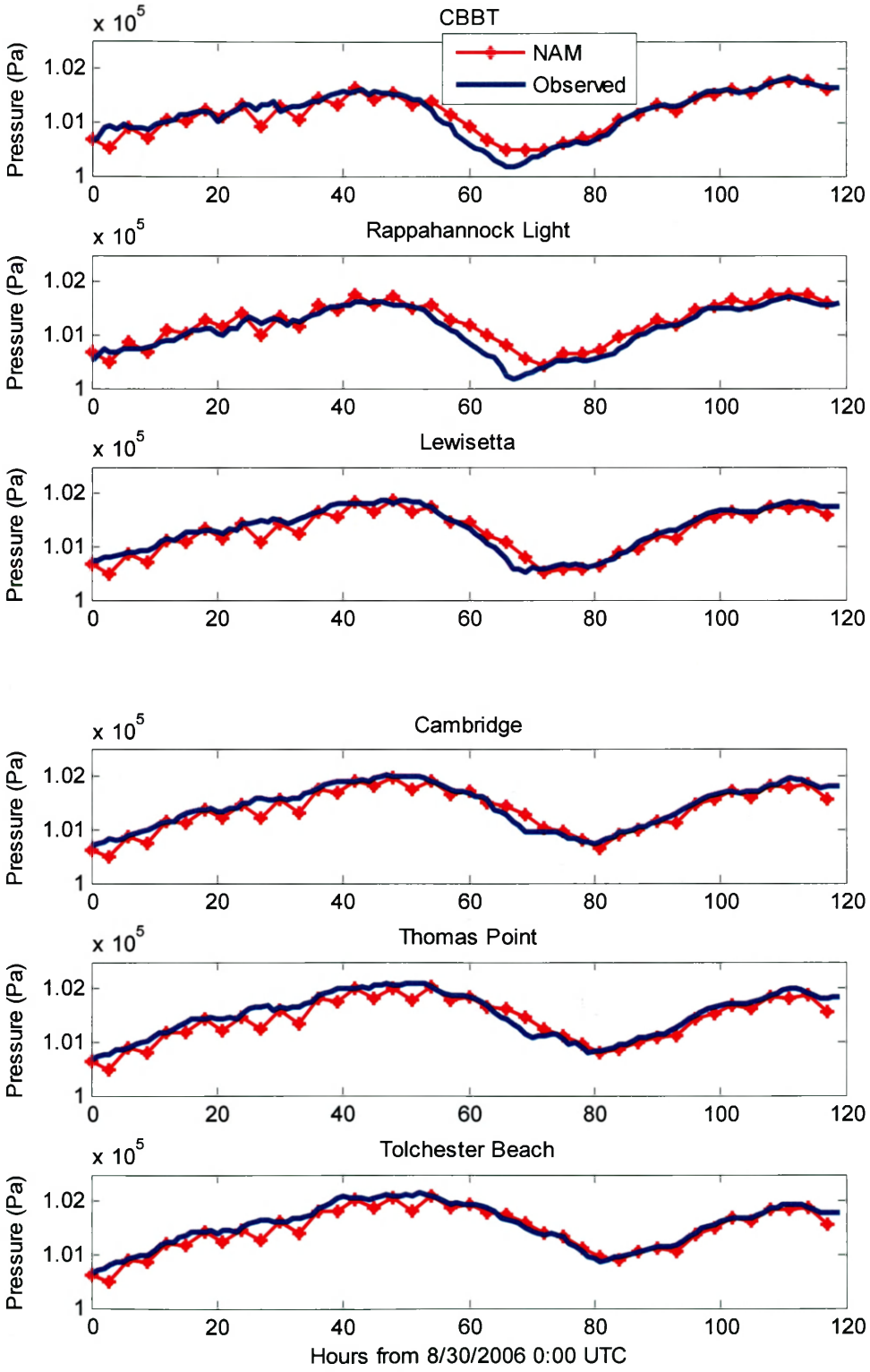

Figure 3.55 Comparison of pressures between NAM modeled pressure and observation in the Bay

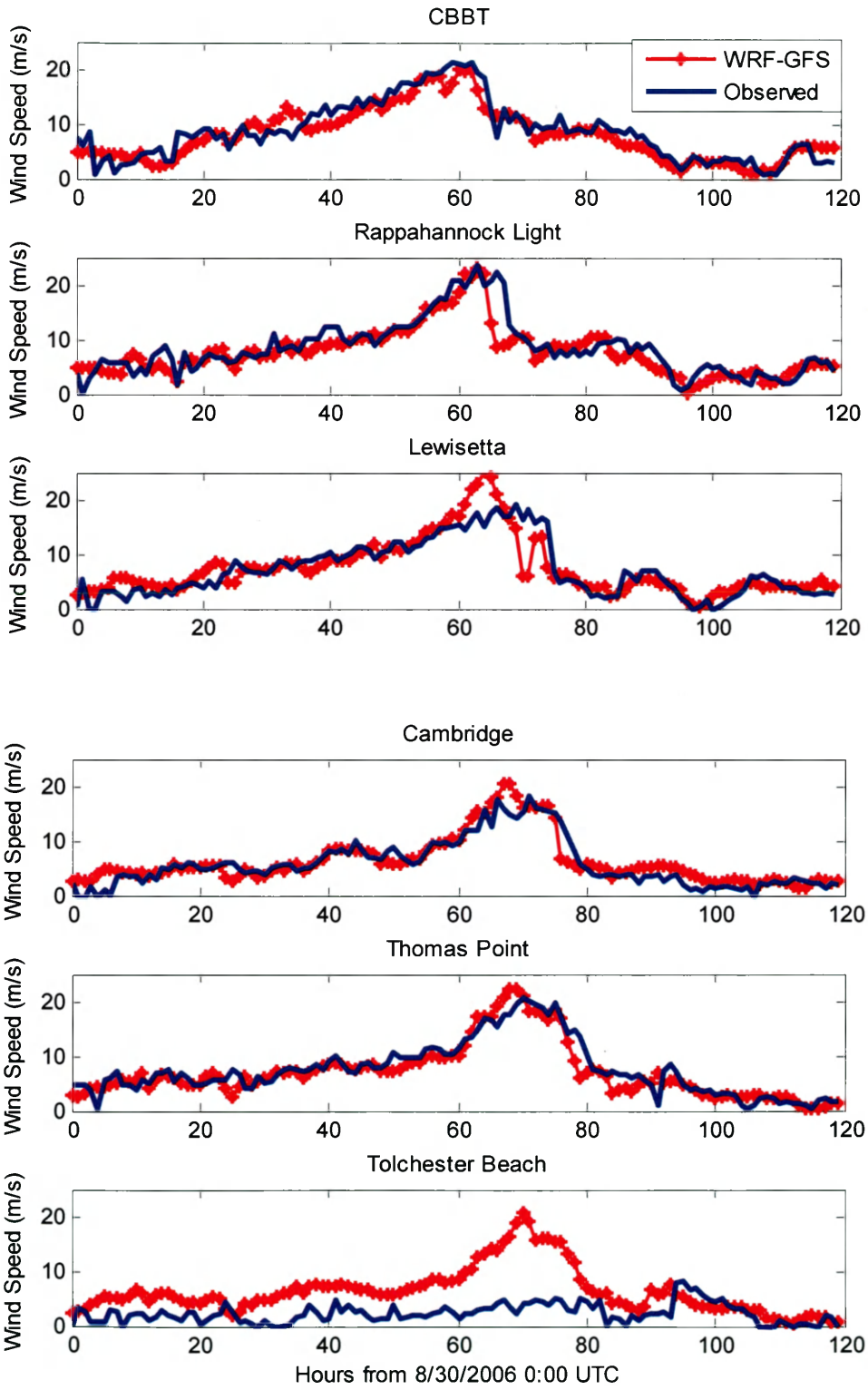

Figure 3.56 Comparison of wind speeds between WRF-GFS modeled wind and observation in the Bay

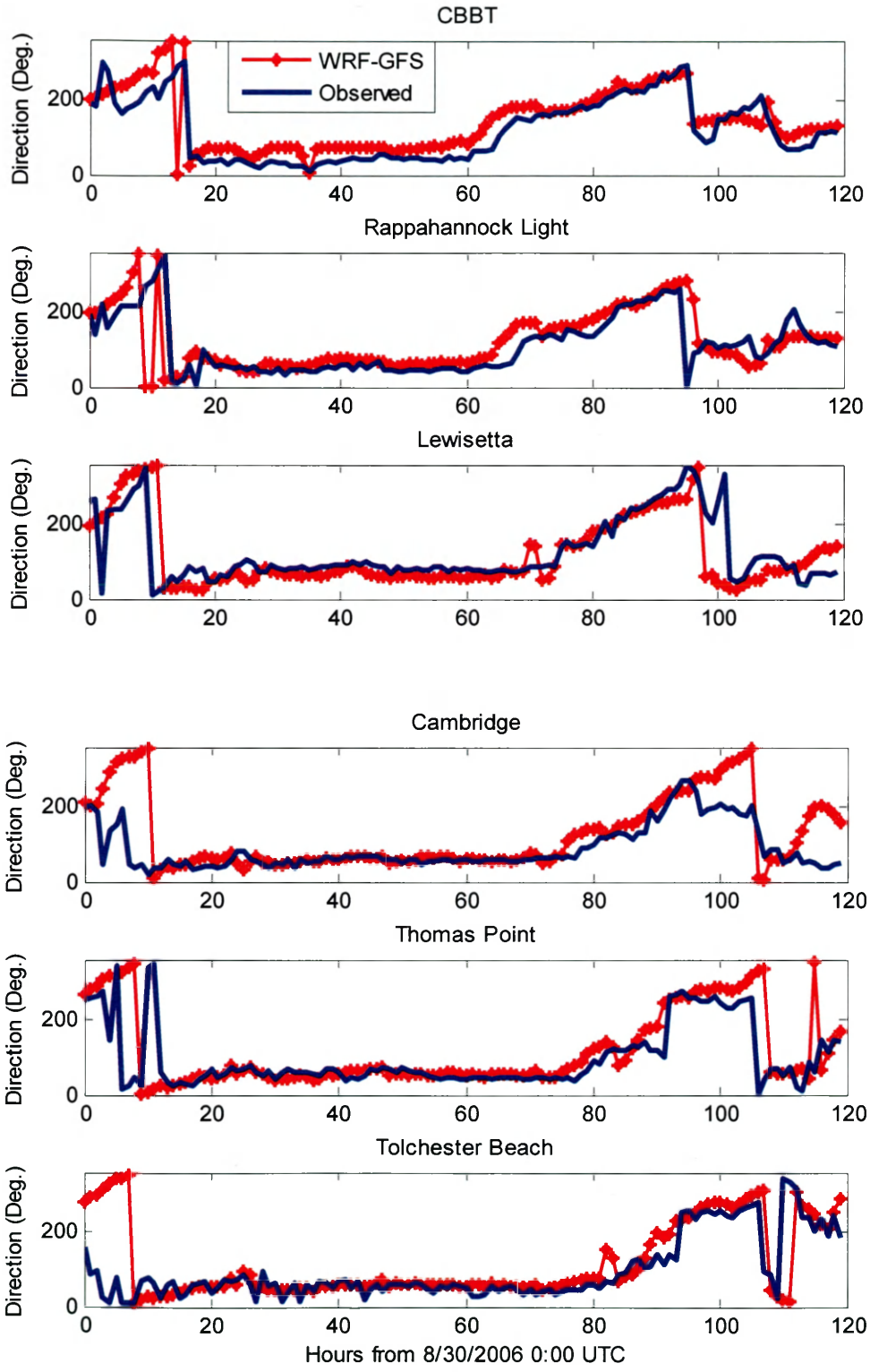

Figure 3.57 Comparison of wind directions between WRF-GFS modeled wind and observation in the Bay

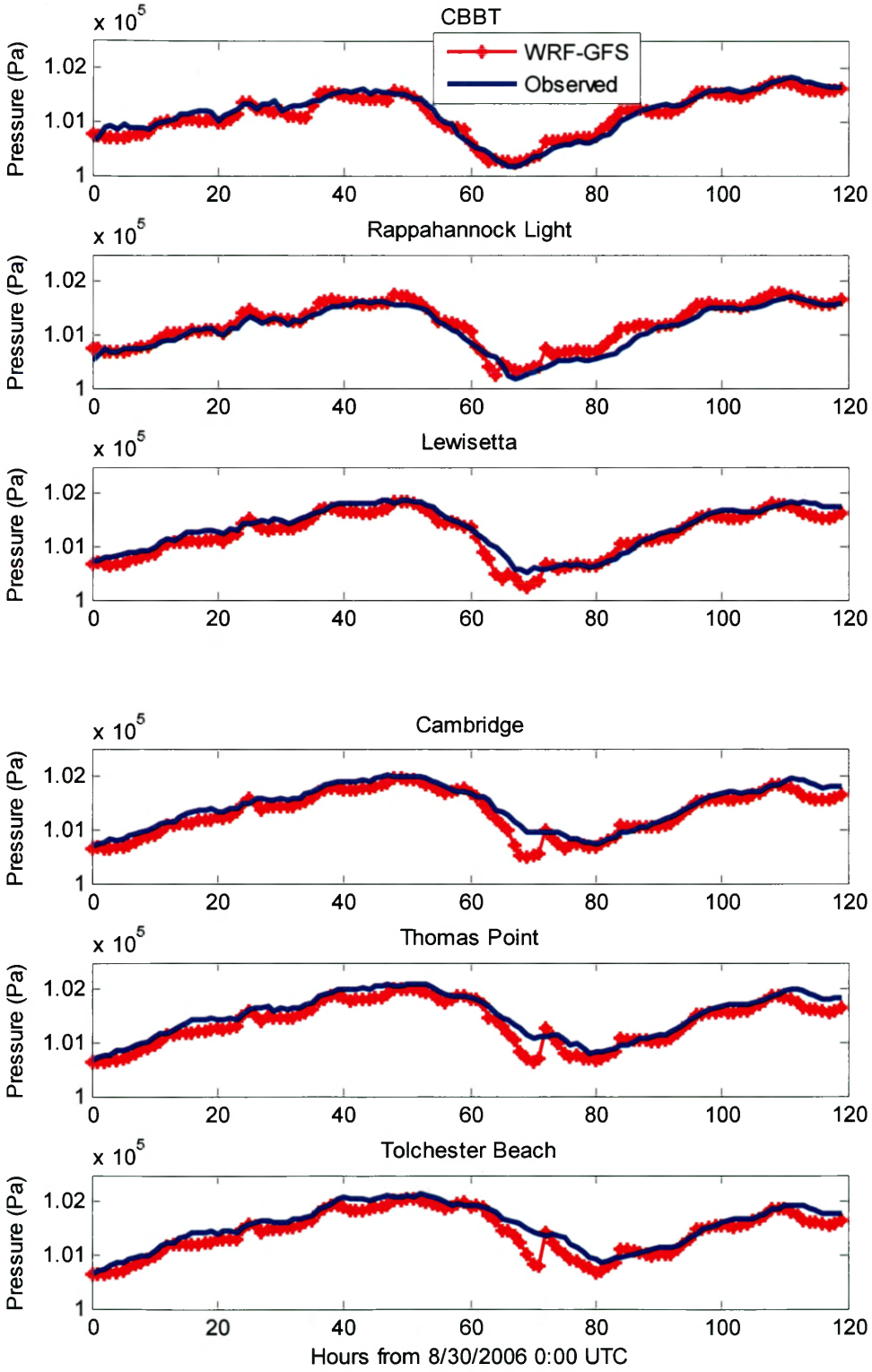

Figure 3.58 Comparison of pressures between WRF-GFS modeled pressure and observation in the Bay

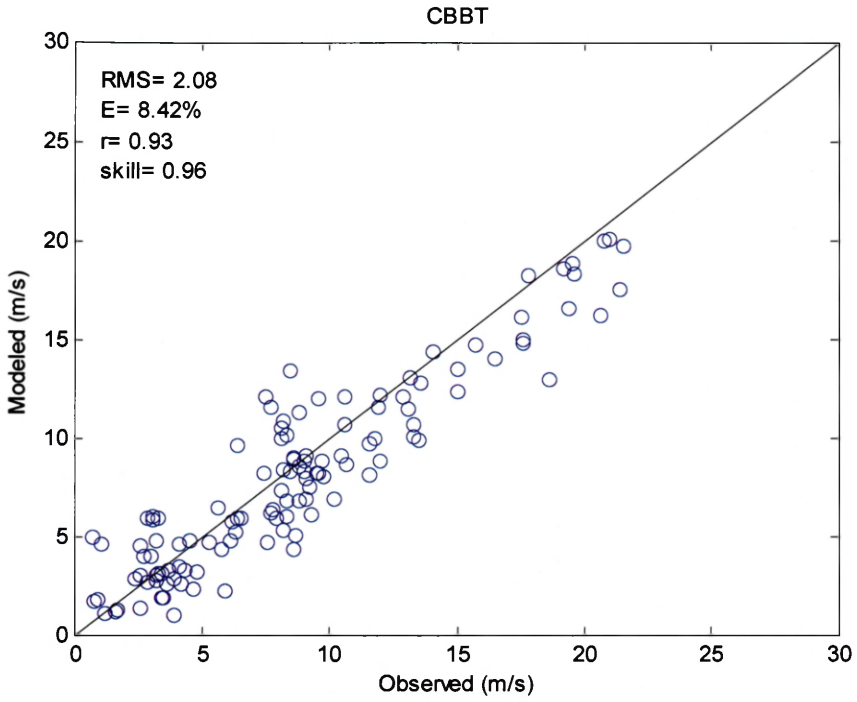

Figure 3.59 WRF-GFS modeled wind speed against observed wind speed at CBBT

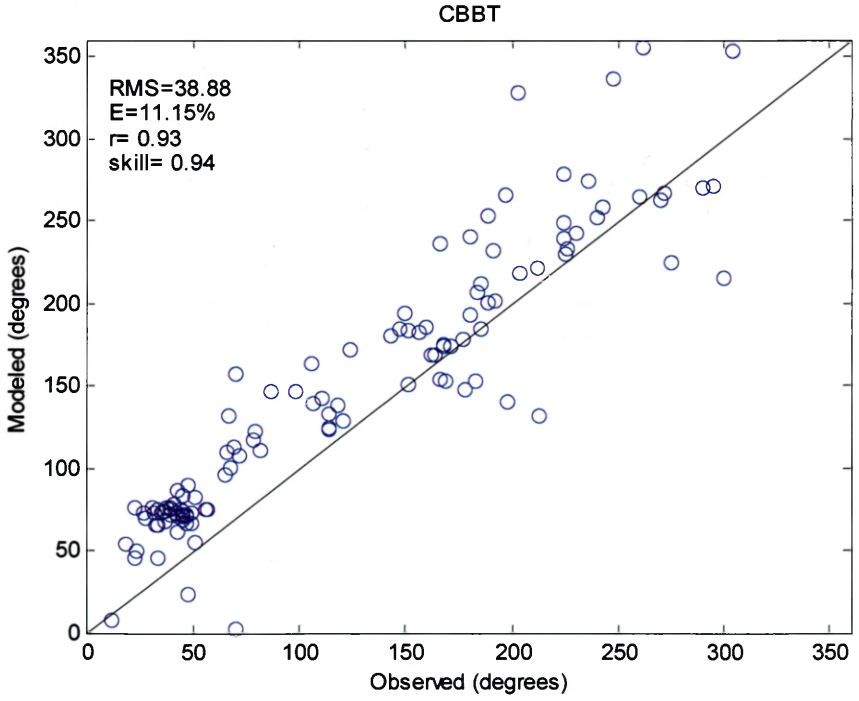

Figure 3.60 WRF-GFS modeled wind direction against observed wind direction at CBBT

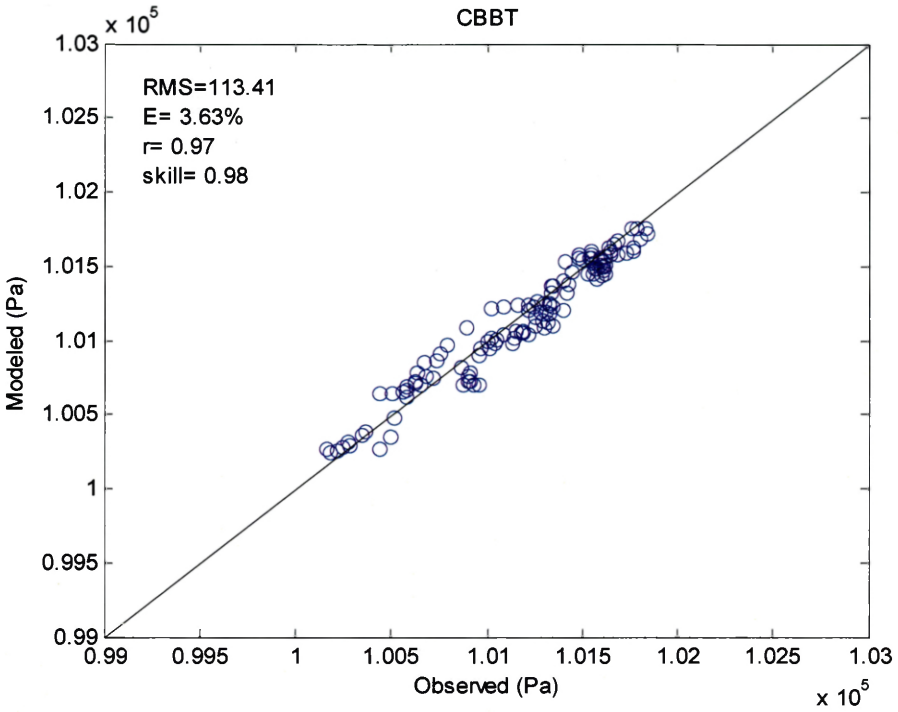

Figure 3.61 WRF-GFS modeled pressure against observed pressure at CBBT

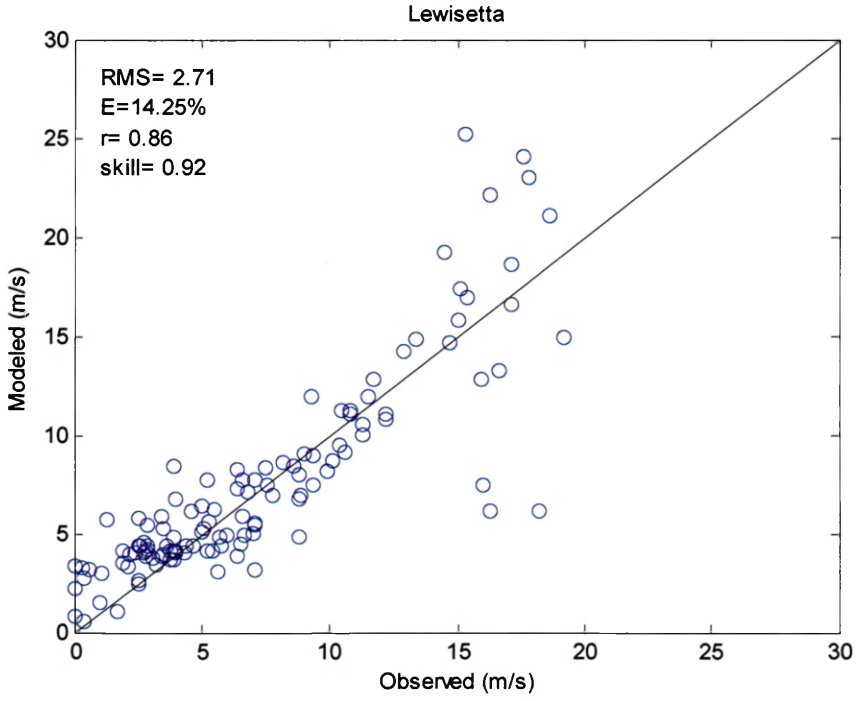

Figure 3.62 WRF-GFS modeled wind speed against observed wind speed at Lewisetta

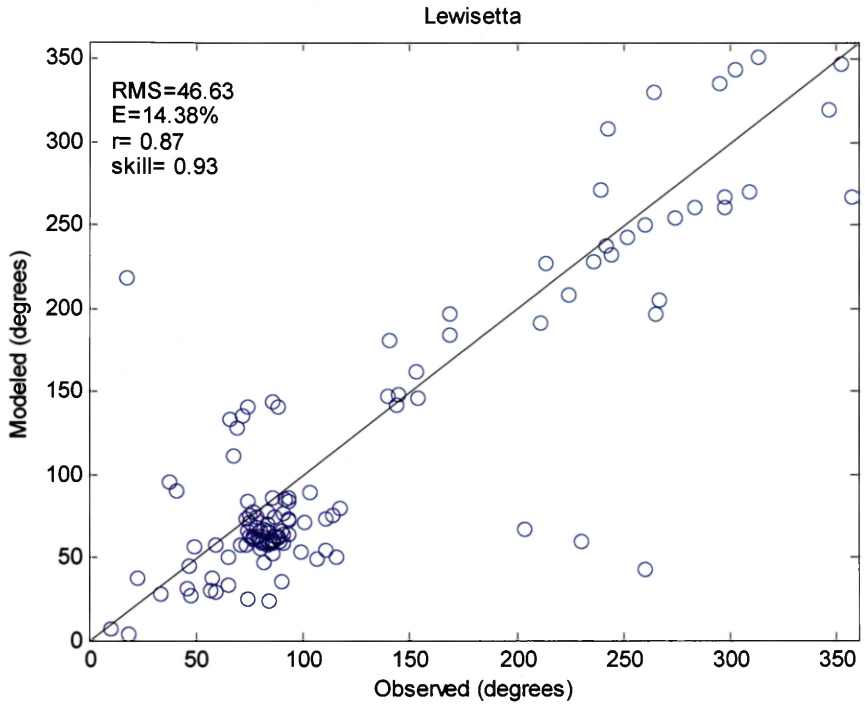

Figure 3.63 WRF-GFS modeled wind direction against observed wind direction at Lewisetta

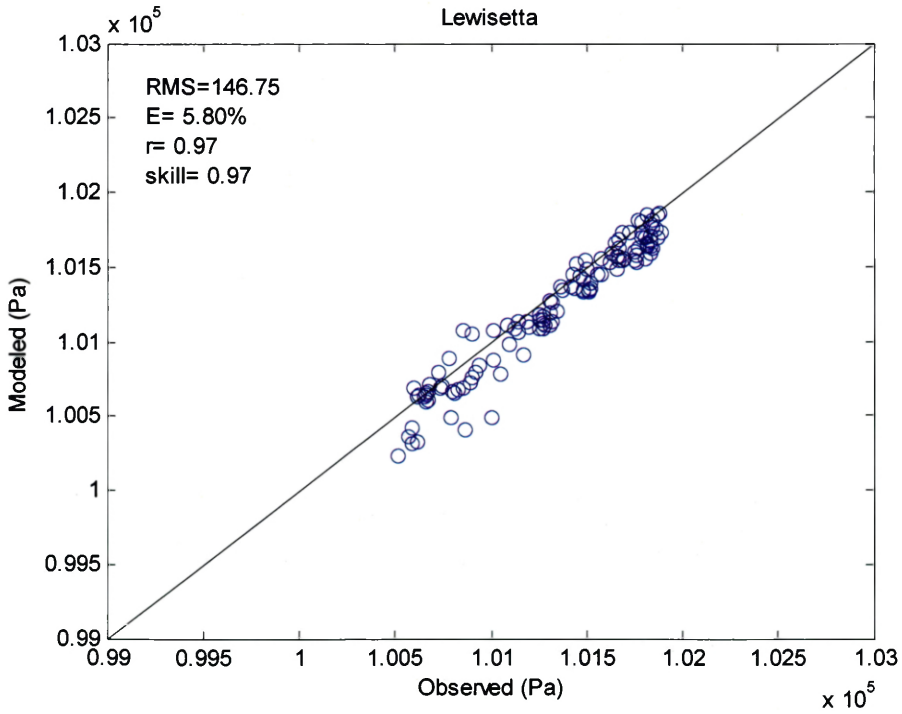

Figure 3.64 WRF-GFS modeled pressure against observed pressure at Lewisetta

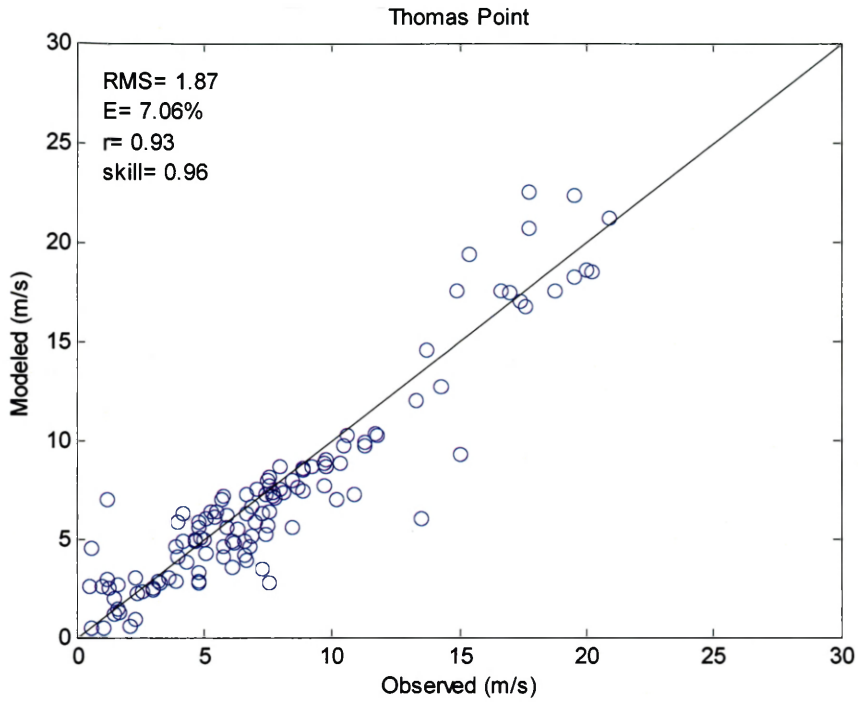

Figure 3.65 WRF-GFS modeled wind speed against observed wind speed at Thomas Point

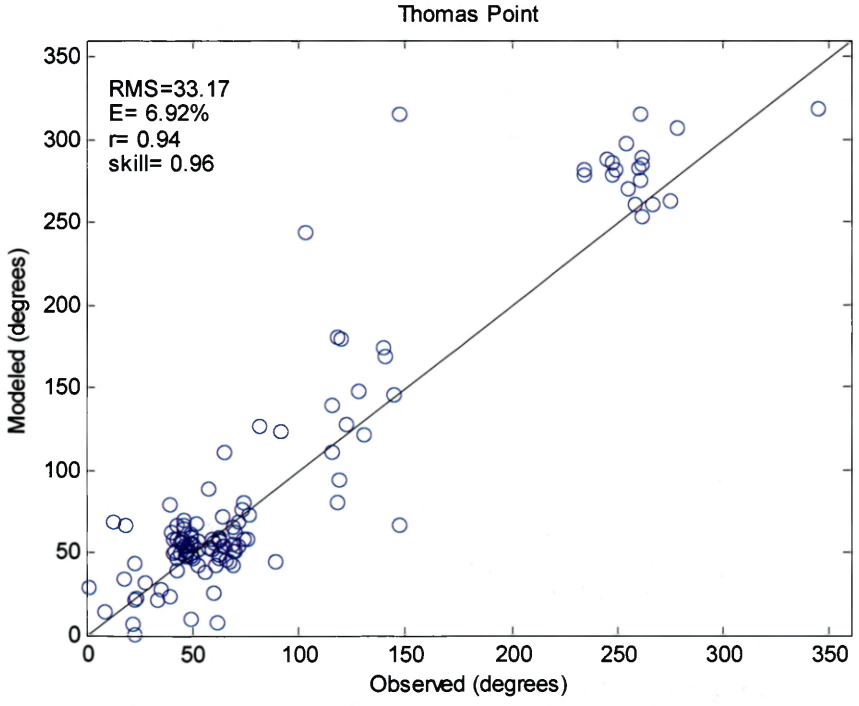

Figure 3.66 WRF-GFS modeled wind direction against observed wind direction at Thomas Point

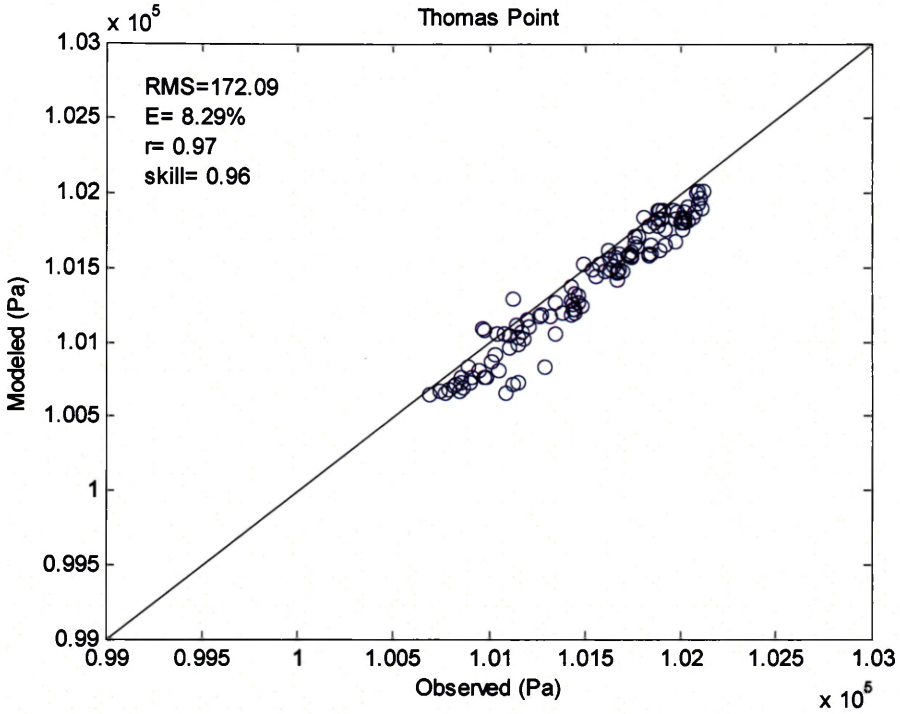

Figure 3.67 WRF-GFS modeled pressure against observed pressure at Thomas Point

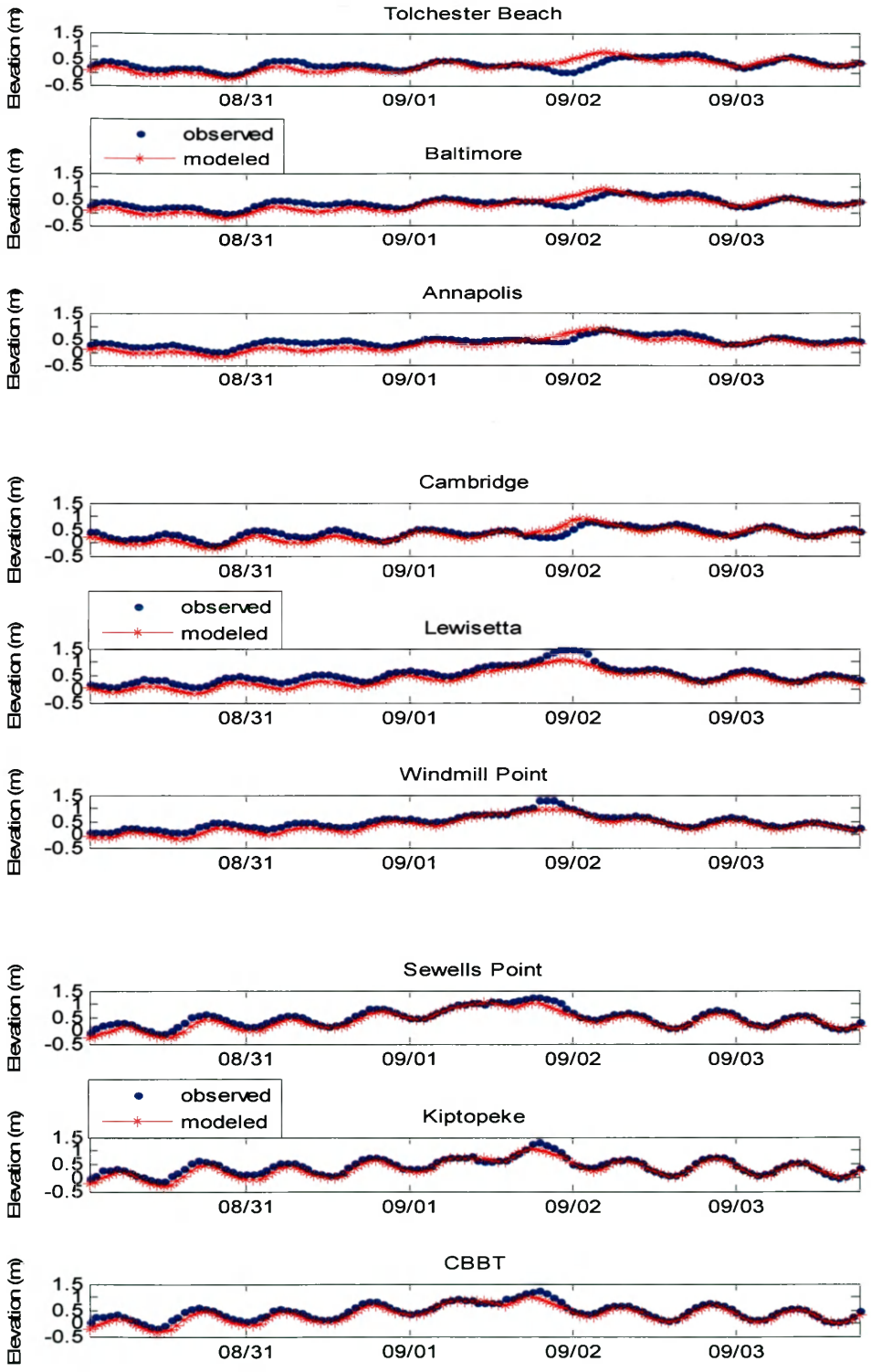

Figure 3.68 Comparison between modeled surface elevation using GFS wind and observation

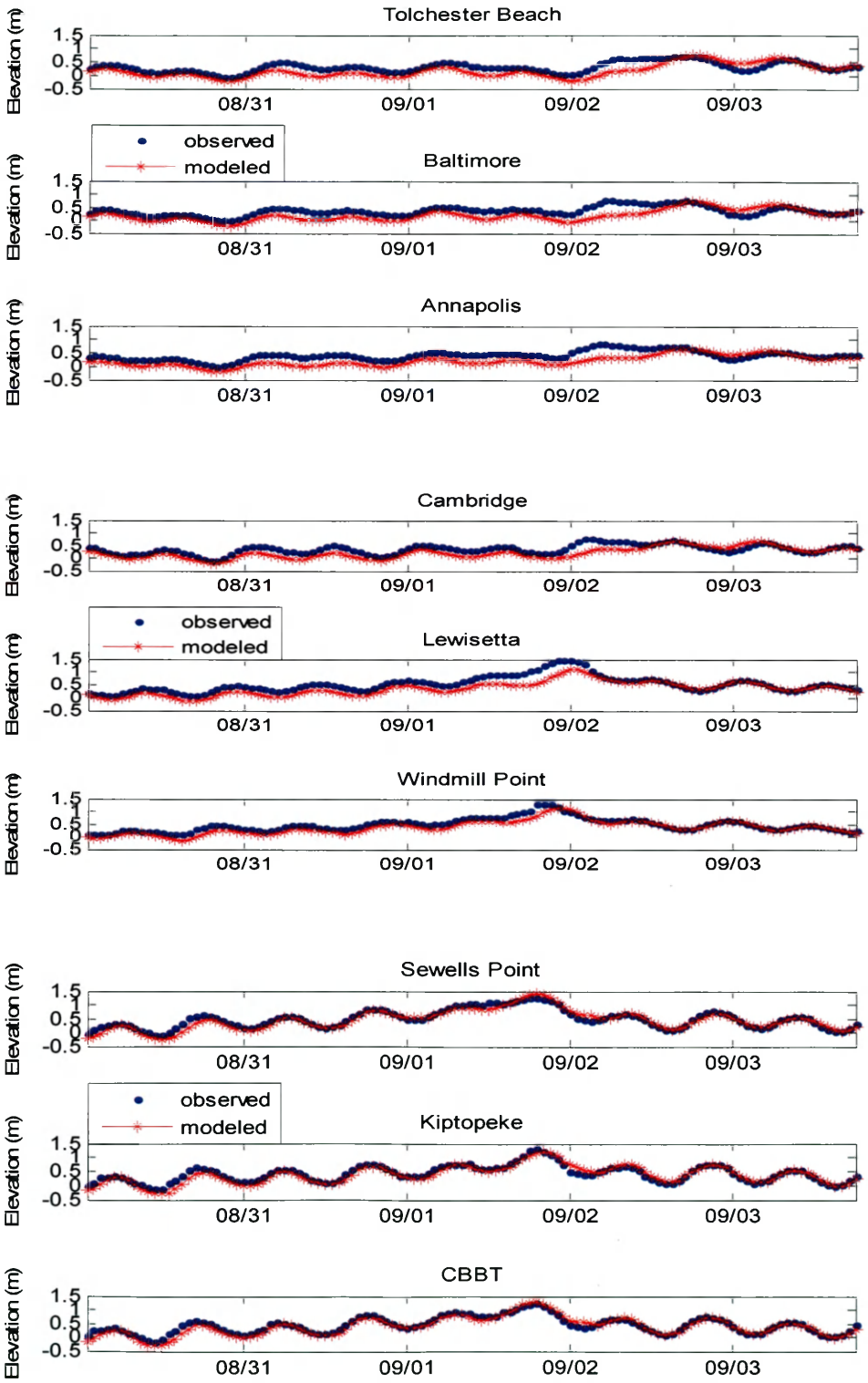

Figure 3.69 Comparison between modeled surface elevation using NAM wind and observation

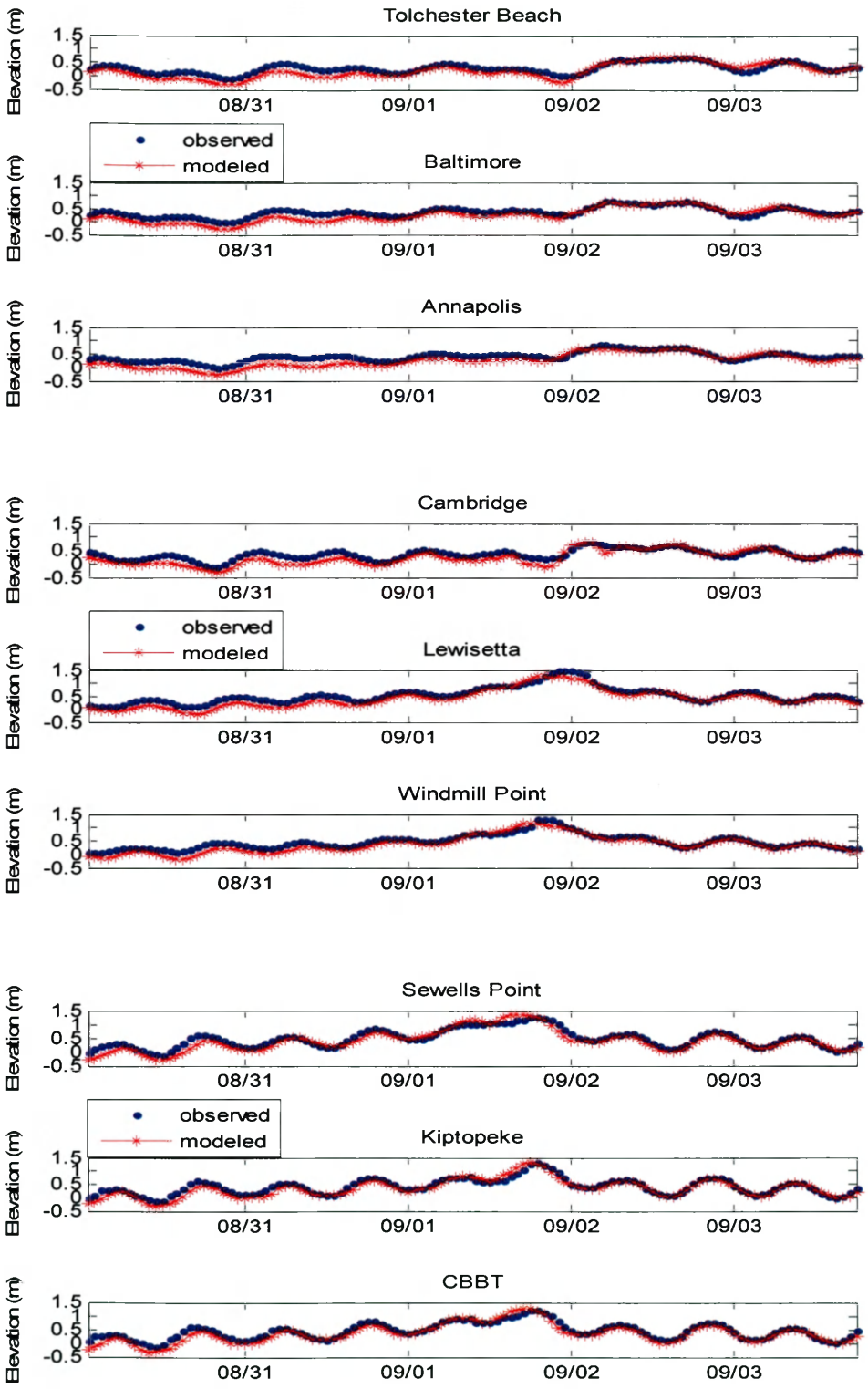

Figure 3.70 Comparison between modeled surface elevation using WRF-GFS wind and observation

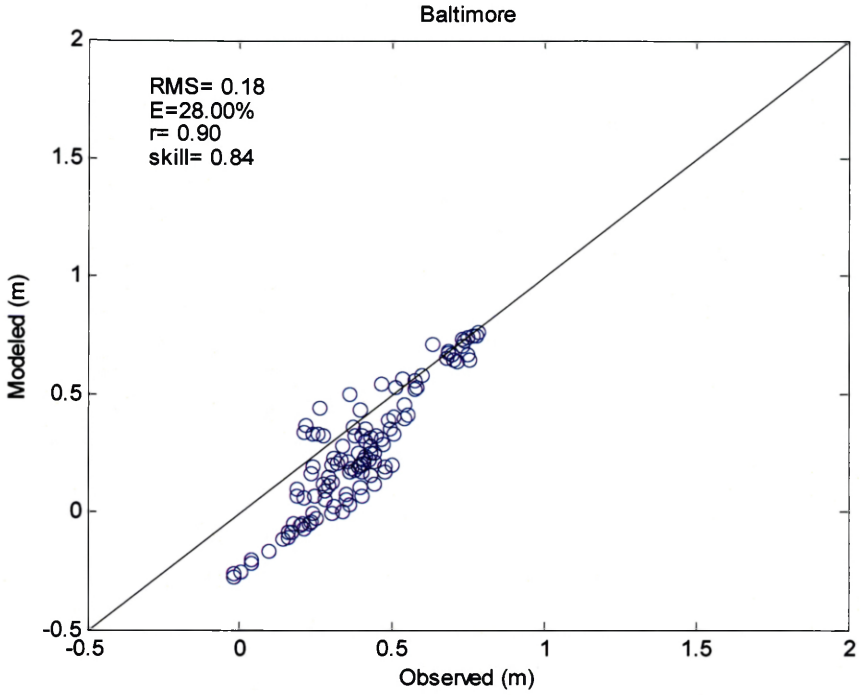

Figure 3.71 Modeled surface elevation against observed storm surge at Baltimore

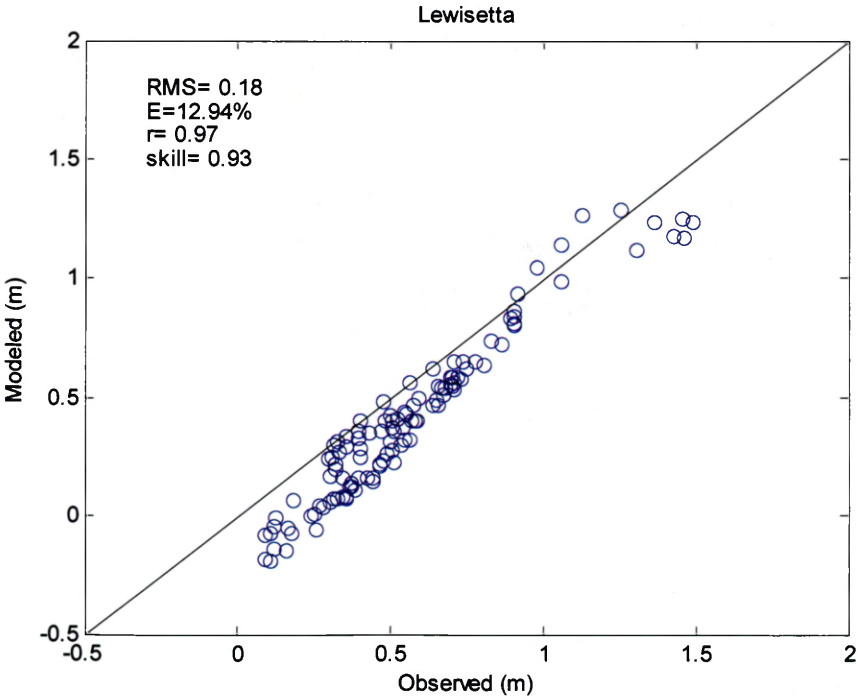

Figure 3.72 Modeled surface elevation against observed storm surge at Lewisetta

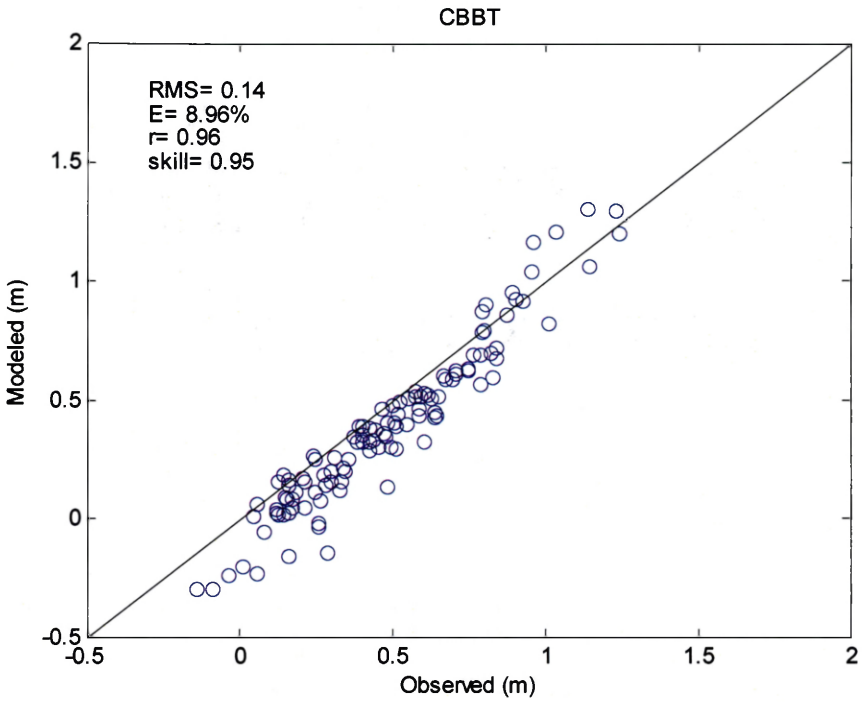

Figure 3.73 Modeled surface elevation against observed storm surge at CBBT

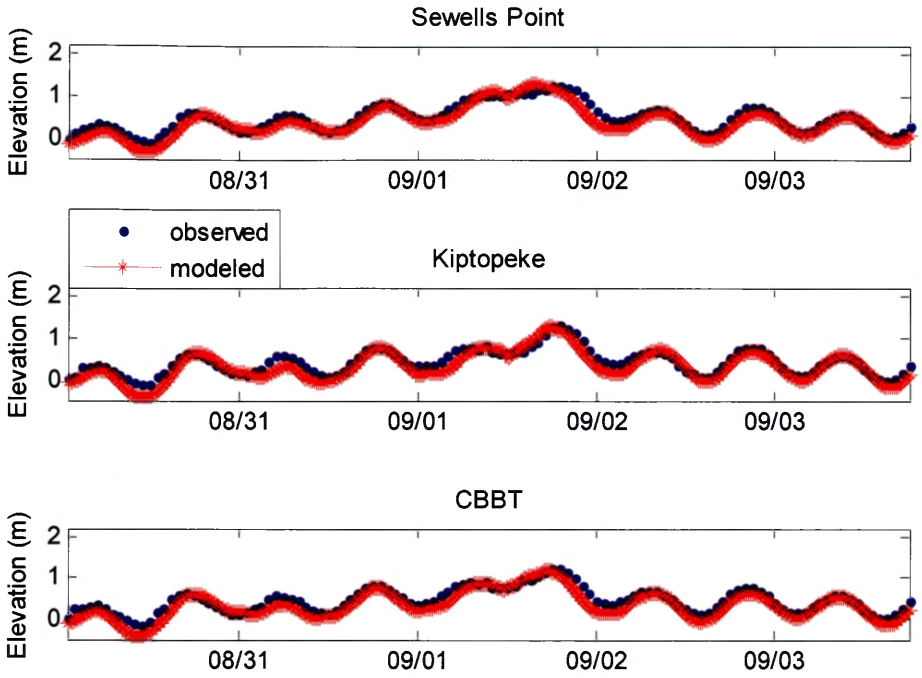

Figure 3.74 Comparison between modeled water elevation and observation during TS Ernesto using small domain grid

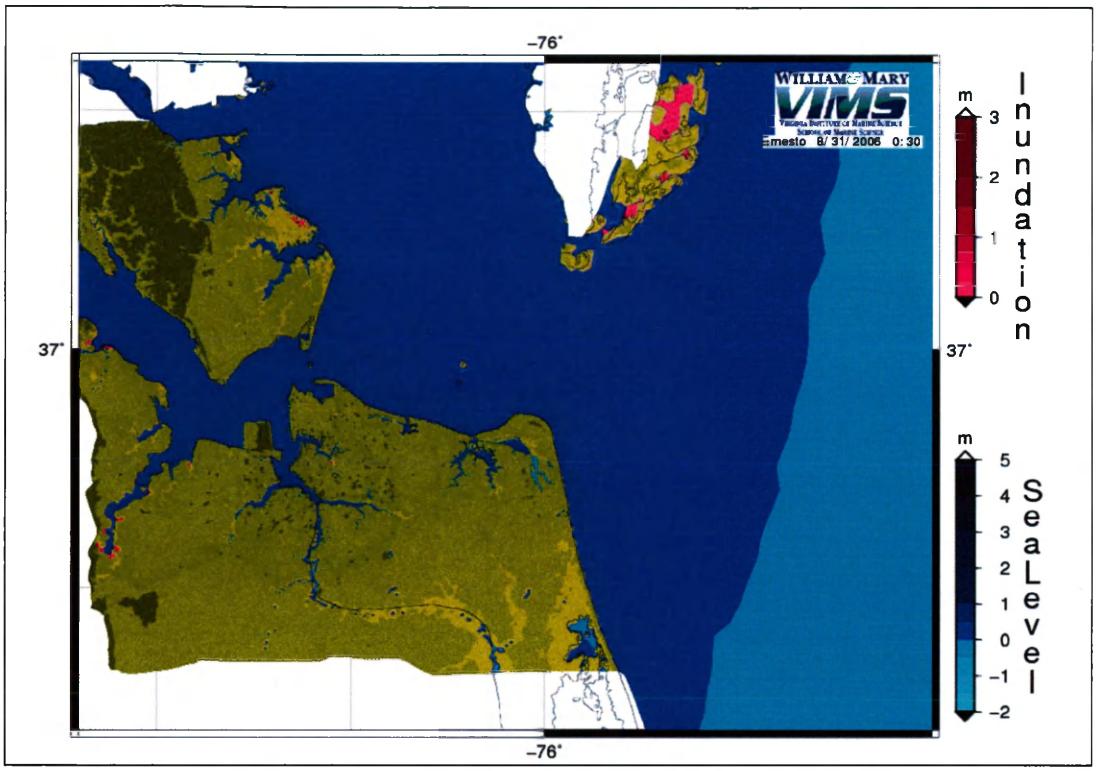

Figure 3.75 Modeled Inundation Map at 0:30 UTC 8/31/2006

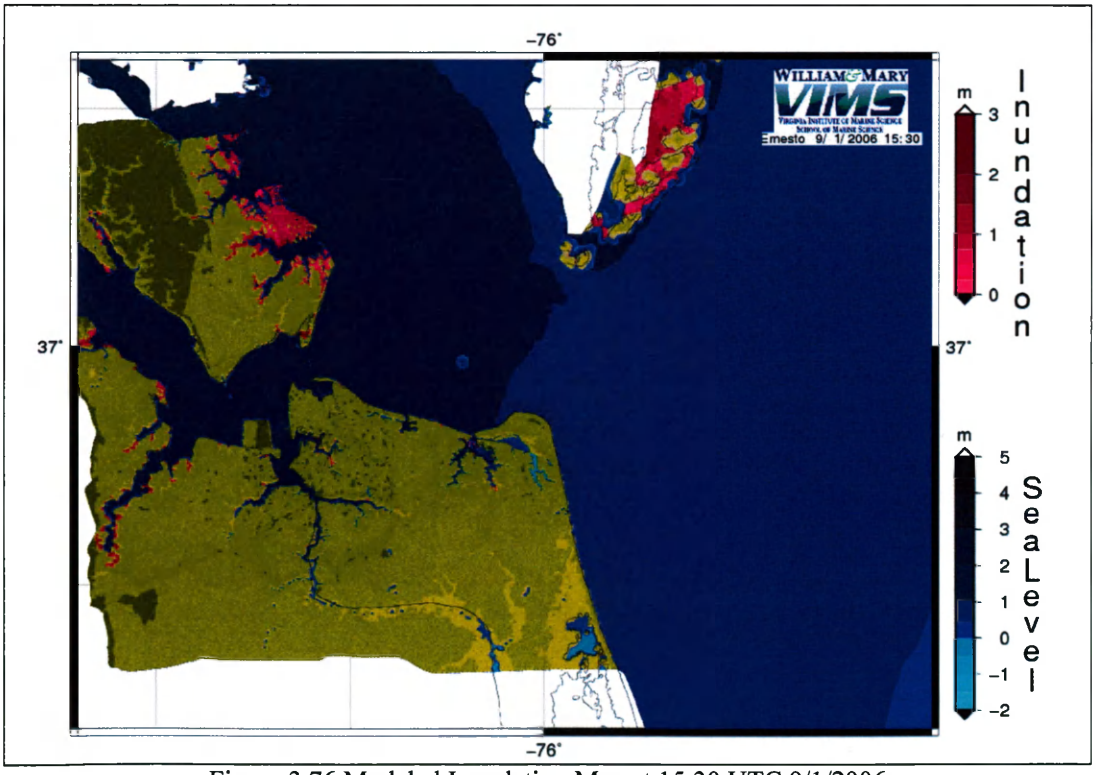

Figure 3.76 Modeled Inundation Map at 15:30 UTC 9/1/2006

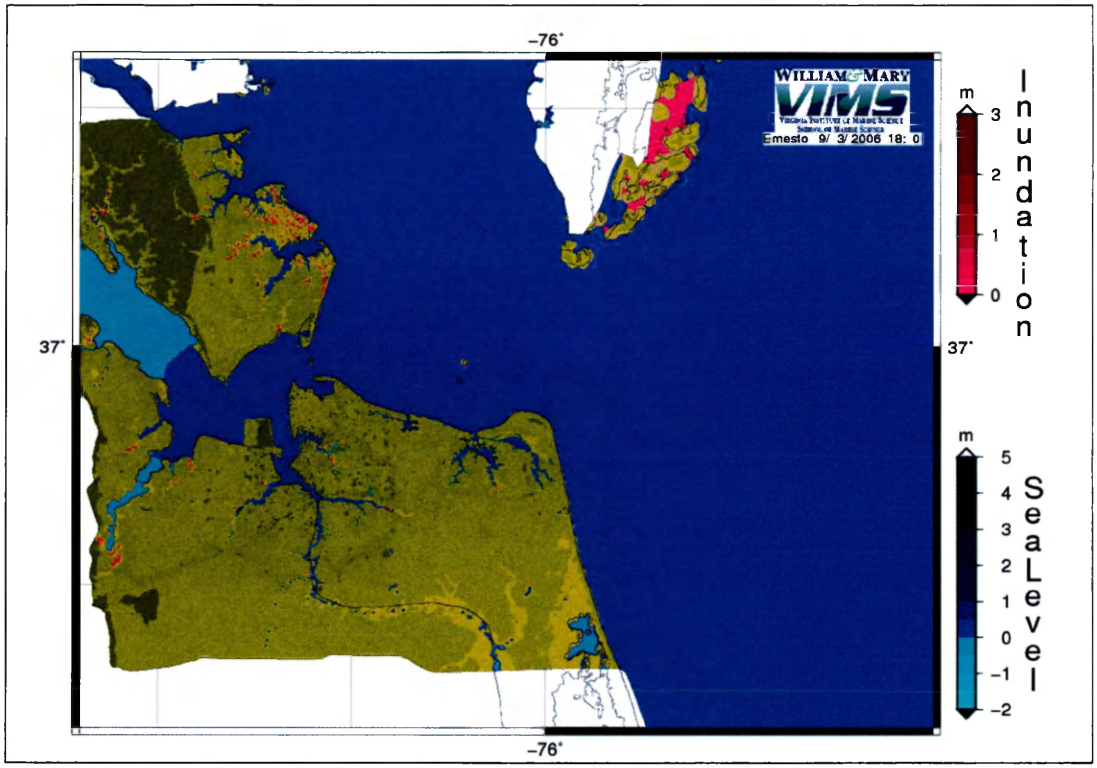

Figure 3.77 Modeled Inundation Map at 18:00 UTC 9/3/2006

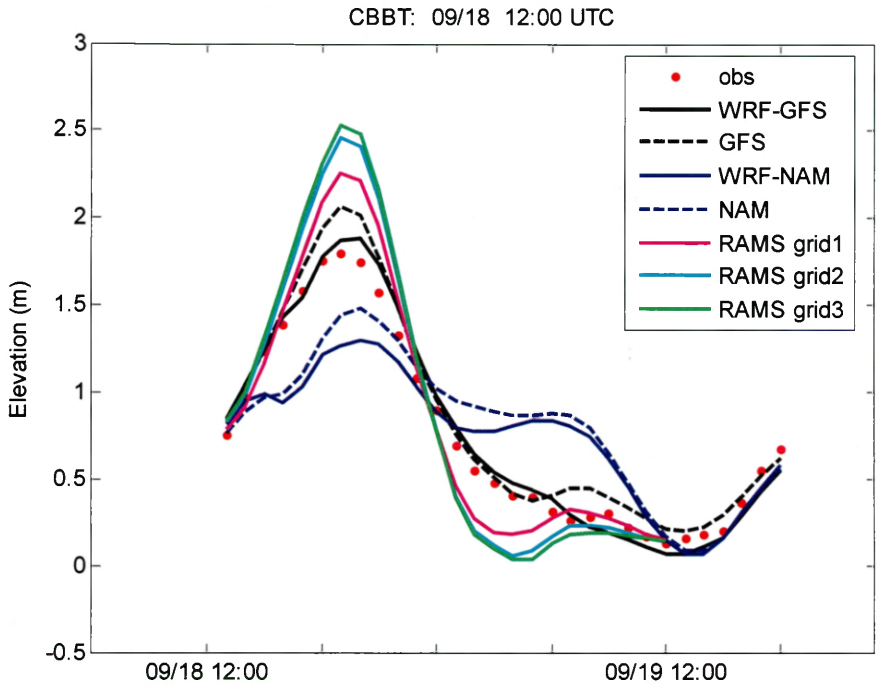

Figure 4.1 Ensemble Forecasting of Storm Tide for Hurricane Isabel at CBBT

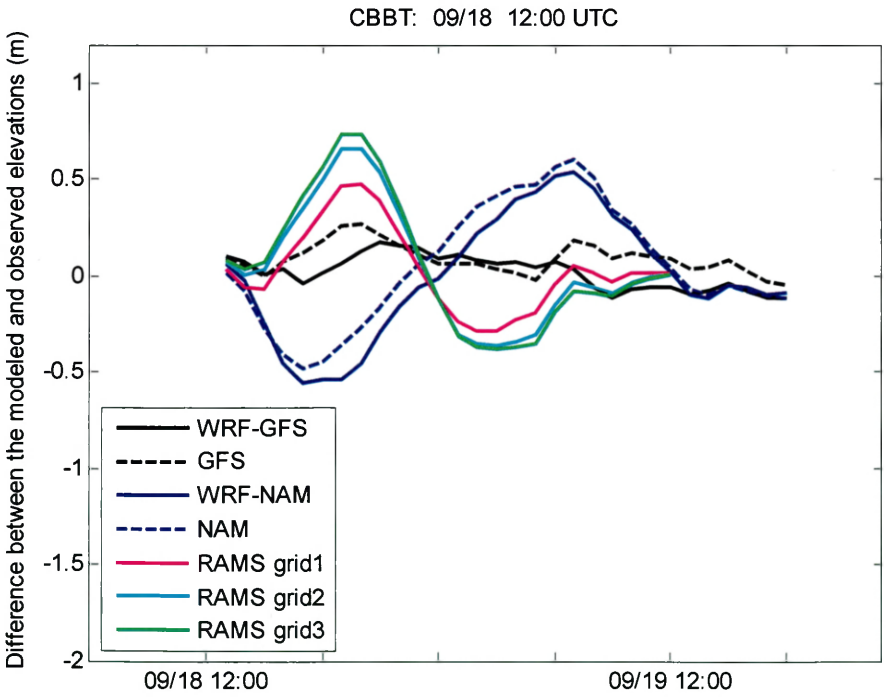

Figure 4.2 Errors of the modeled surface elevations with different winds at CBBT

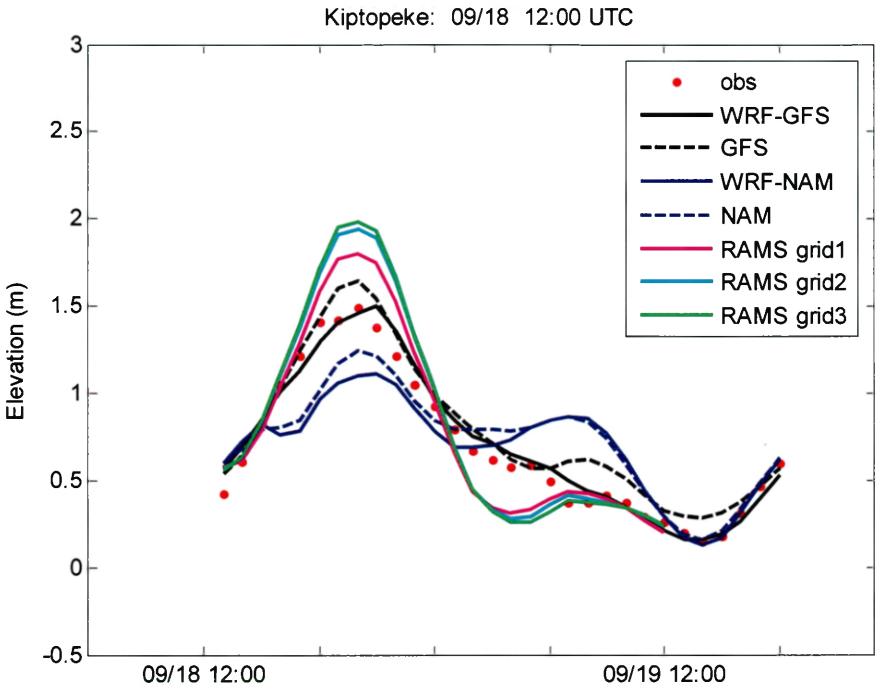

Figure 4.3 Ensemble Forecasting of Storm Tide for Hurricane Isabel at Kiptopeke

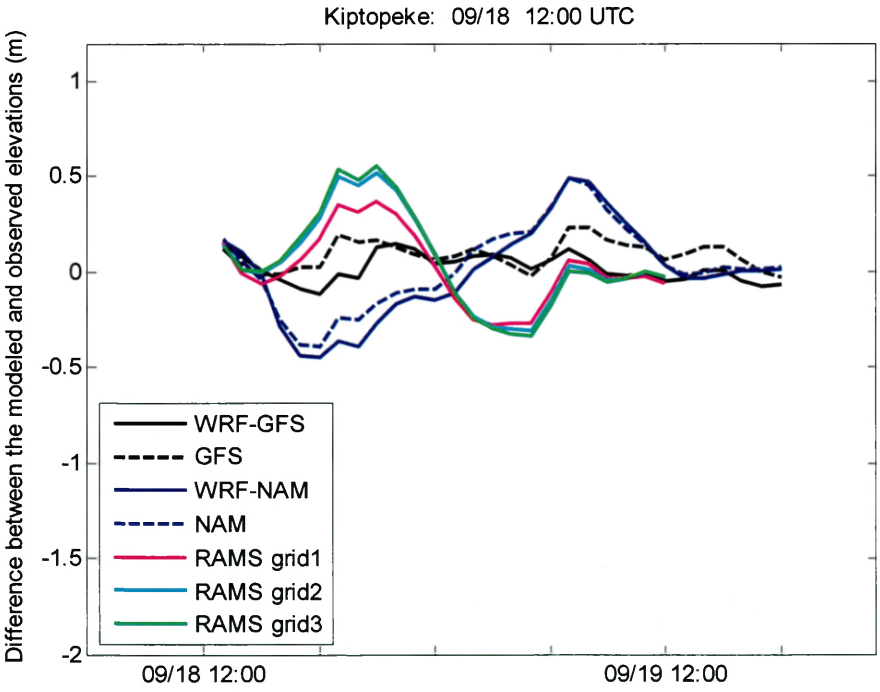

Figure 4.4 Errors of the modeled surface elevations with different winds at Kiptopeke

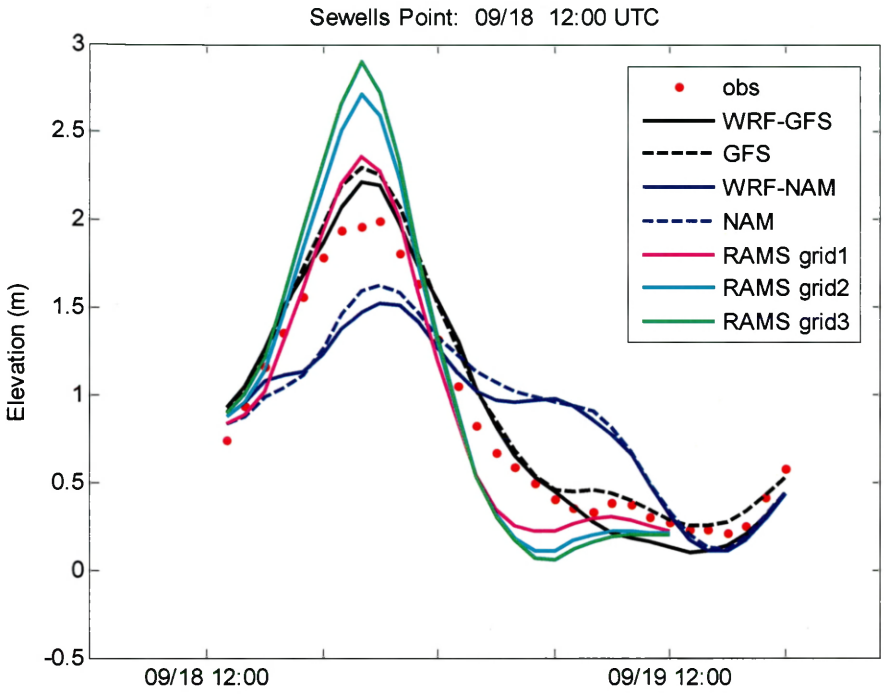

Figure 4.5 Ensemble Forecasting of Storm Tide for Hurricane Isabel at Sewells Point

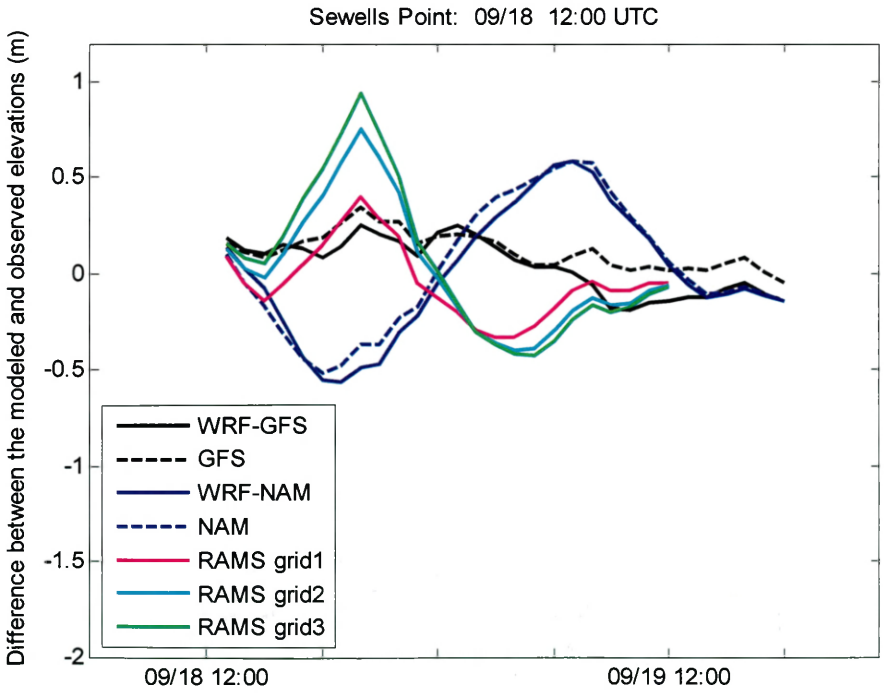

Figure 4.6 Errors of the modeled surface elevations with different winds at Sewells Point

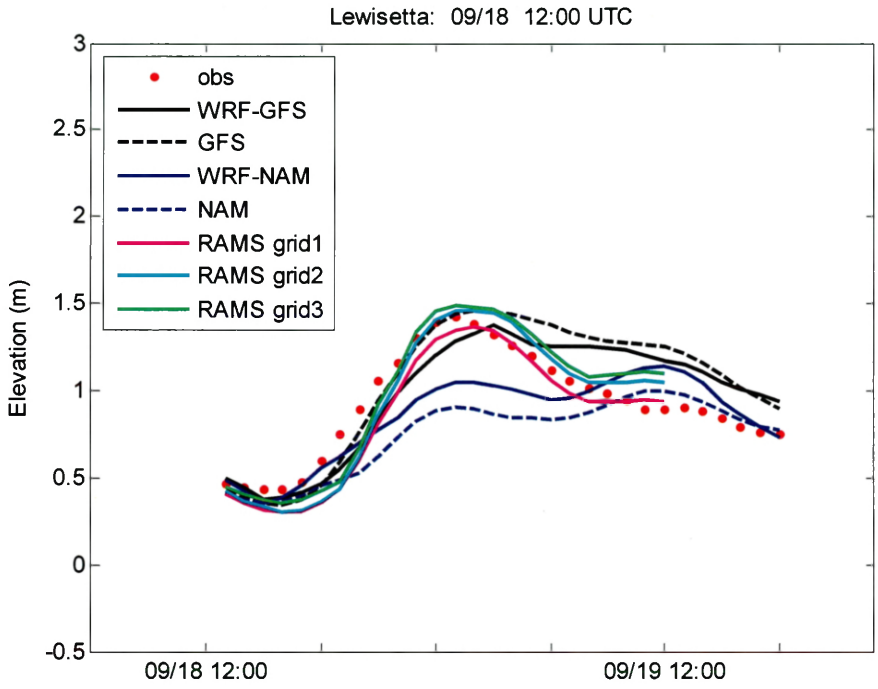

Figure 4.7 Ensemble Forecasting of Storm Tide for Hurricane Isabel at Lewiseatta

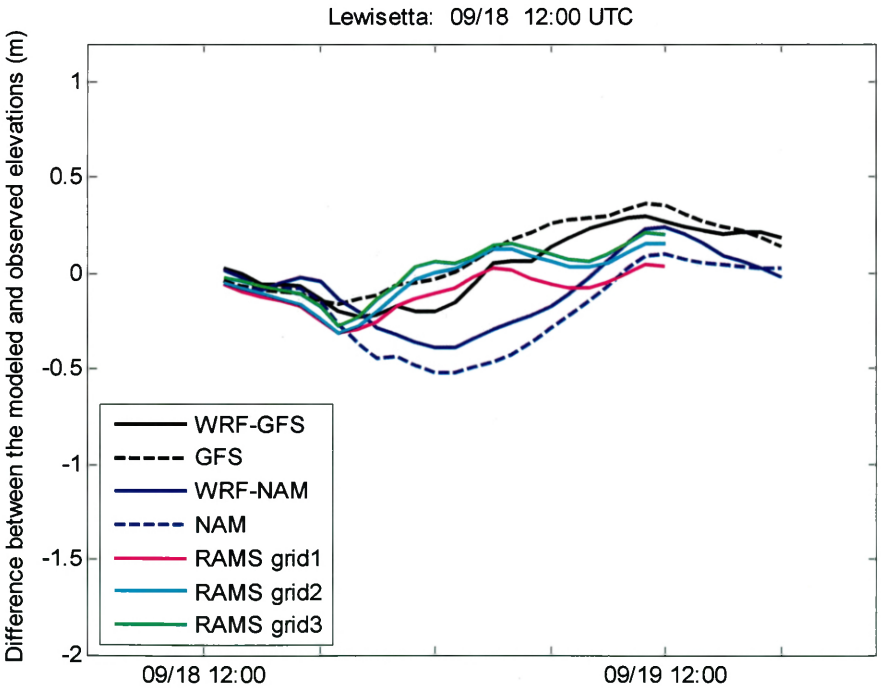

Figure 4.8 Errors of the modeled surface elevations with different winds at Lewisetta

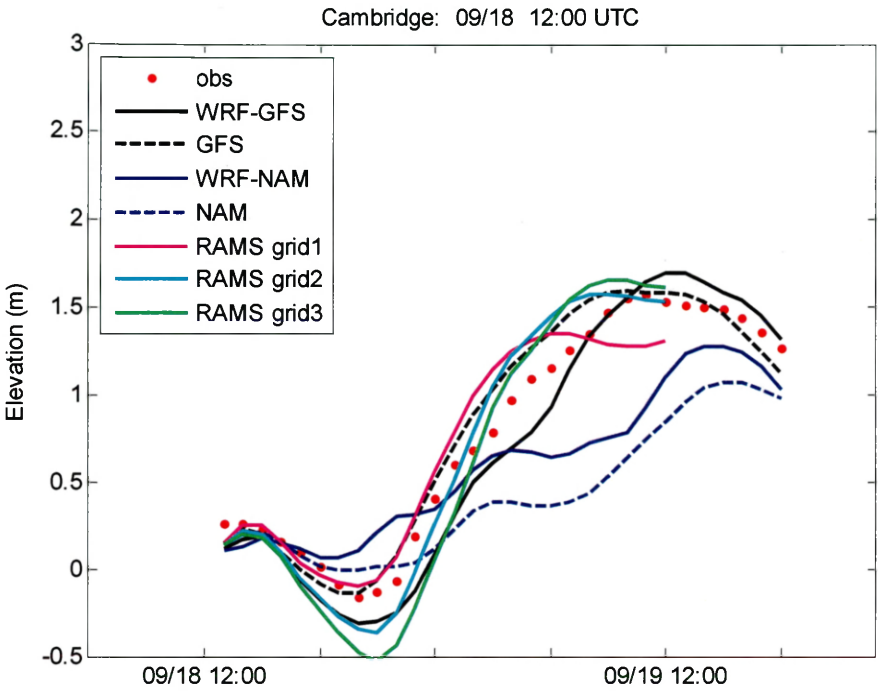

Figure 4.9 Ensemble Forecasting of Storm Tide for Hurricane Isabel at Cambridge

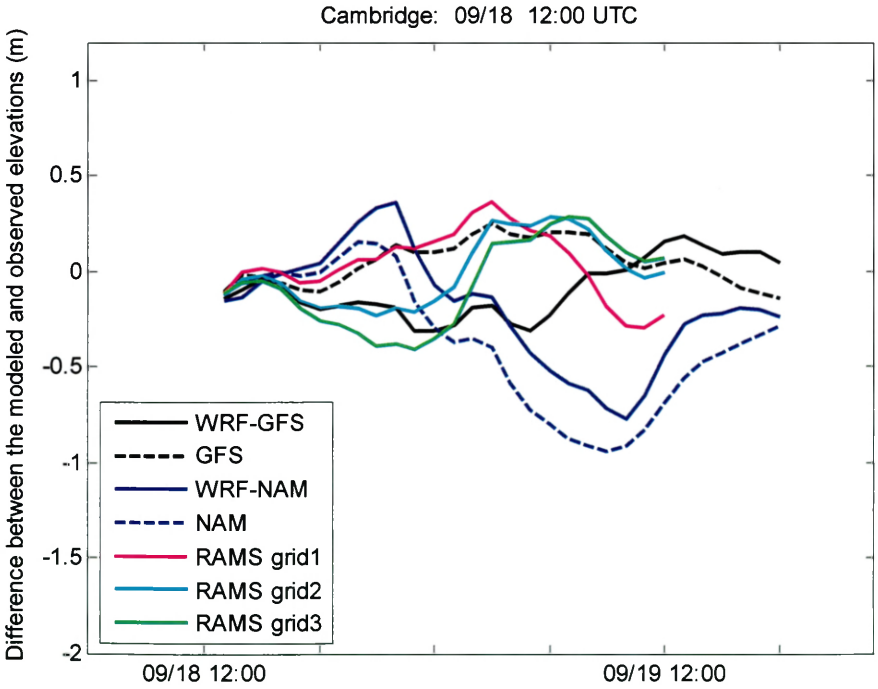

Figure 4.10 Errors of the modeled surface elevations with different winds at Cambridge

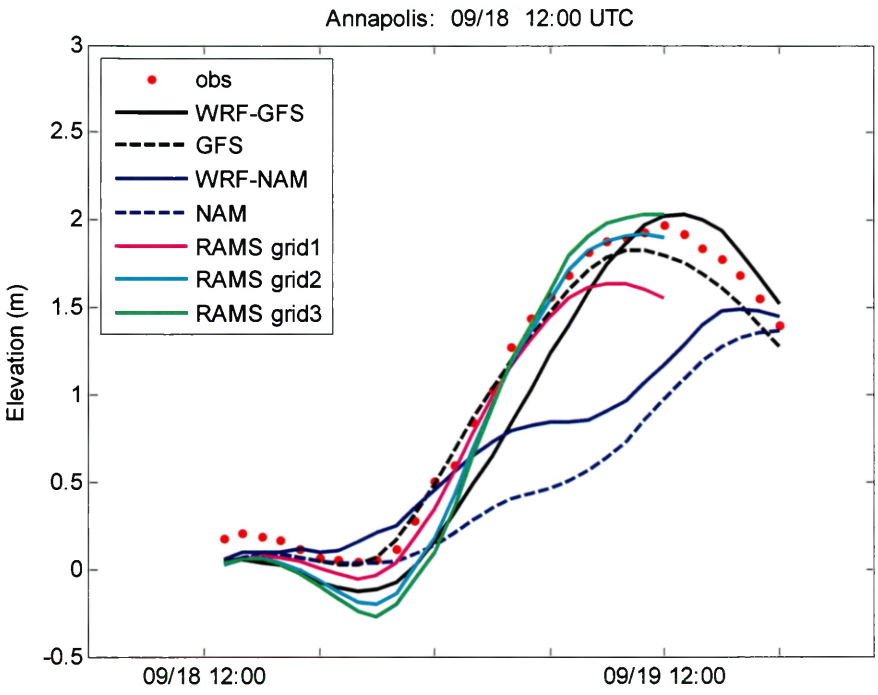

Figure 4.11 Ensemble Forecasting of Storm Tide for Hurricane Isabel at Annapolis

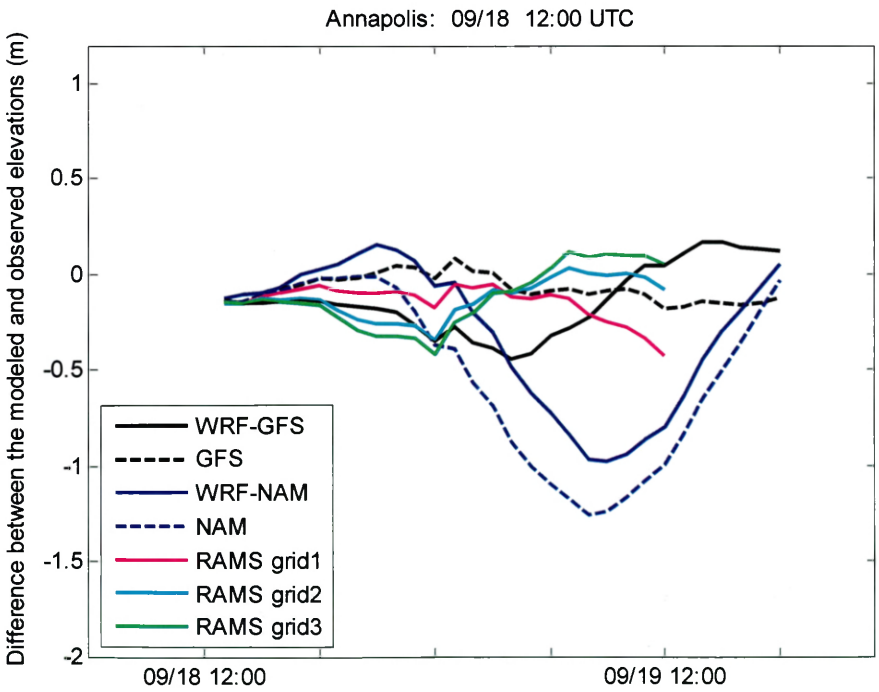

Figure 4.12 Errors of the modeled surface elevations with different winds at Annapolis

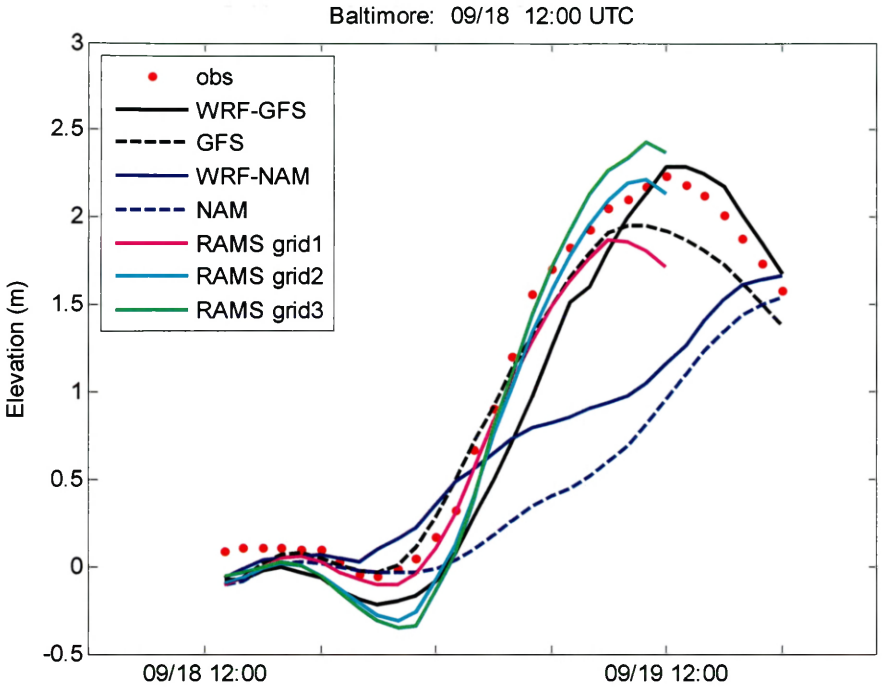

Figure 4.13 Ensemble Forecasting of Storm Tide for Hurricane Isabel at Baltimore

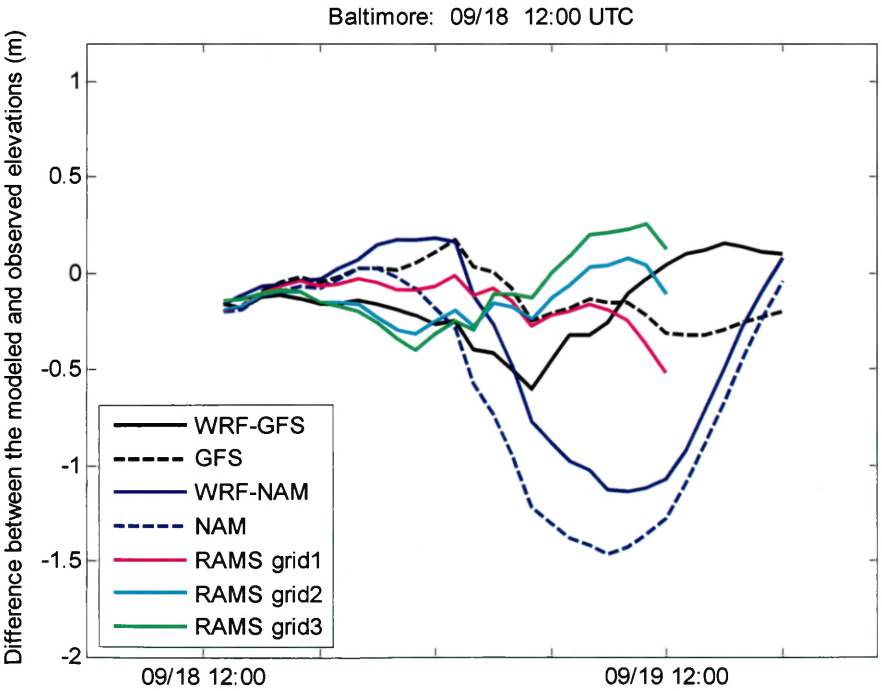

Figure 4.14 Errors of the modeled surface elevations with different winds at Baltimore

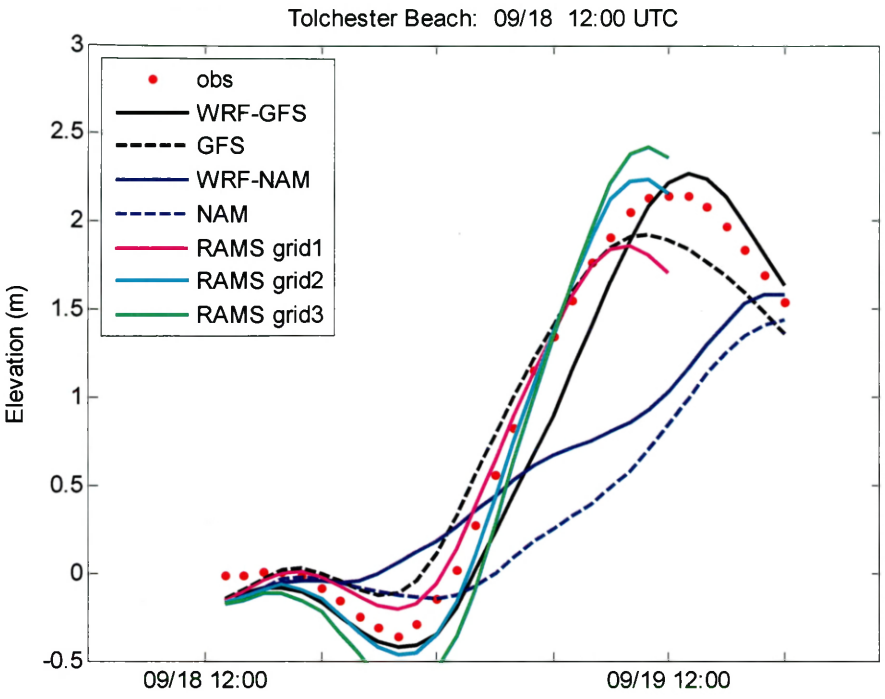

Figure 4.15 Ensemble Forecasting of Storm Tide for Hurricane Isabel at Tolchester Beach

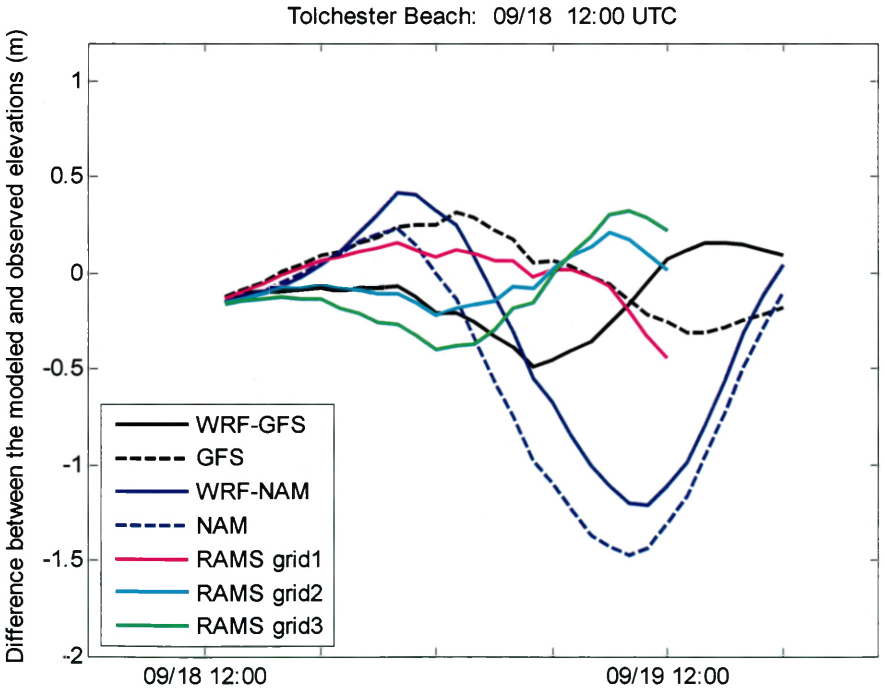

Figure 4.16 Errors of the modeled surface elevations with different winds at Tolchester Beach

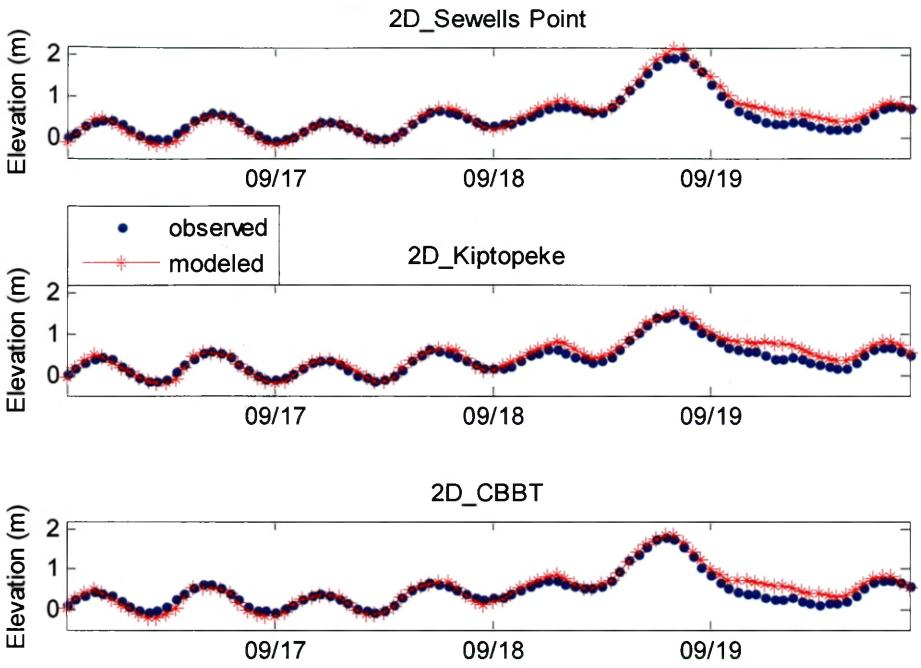

Figure 4.17 Modeled storm tide with 2D mode during Hurricane Isabel

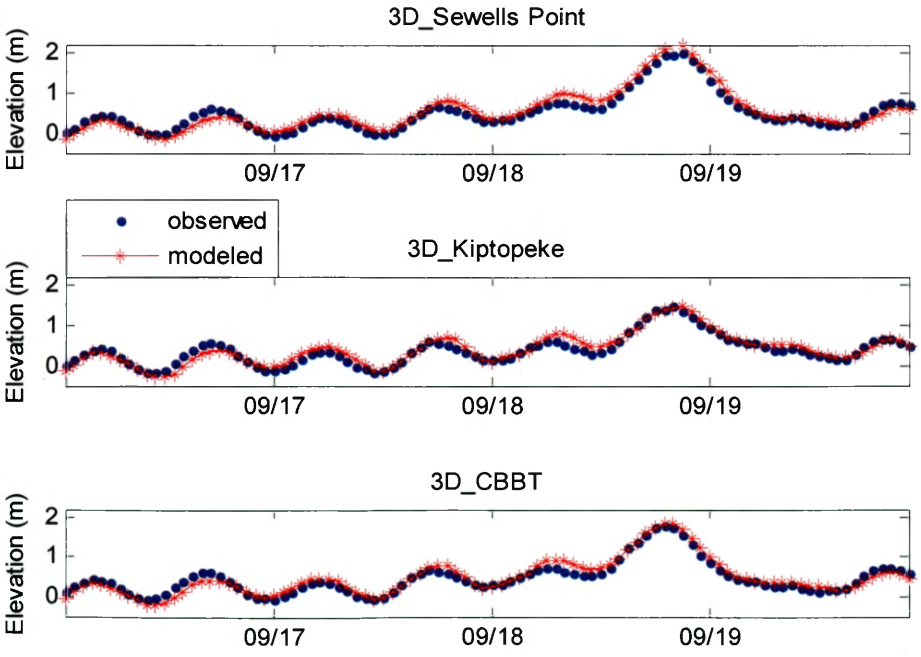

Figure 4.18 Modeled storm tide with 3D mode during Hurricane Isabel

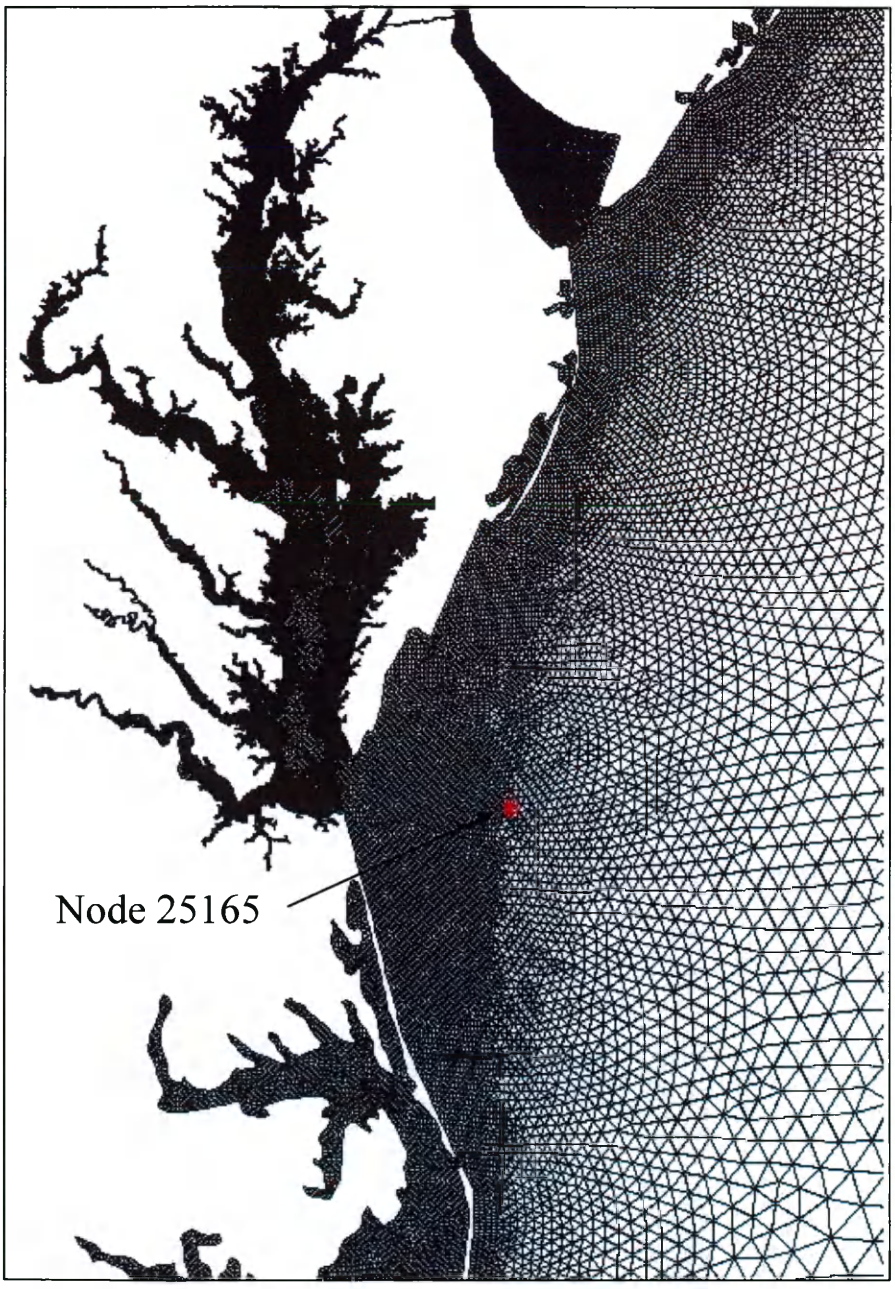

Figure 4.19 Node in the continental shelf selected for plotting the current profiles

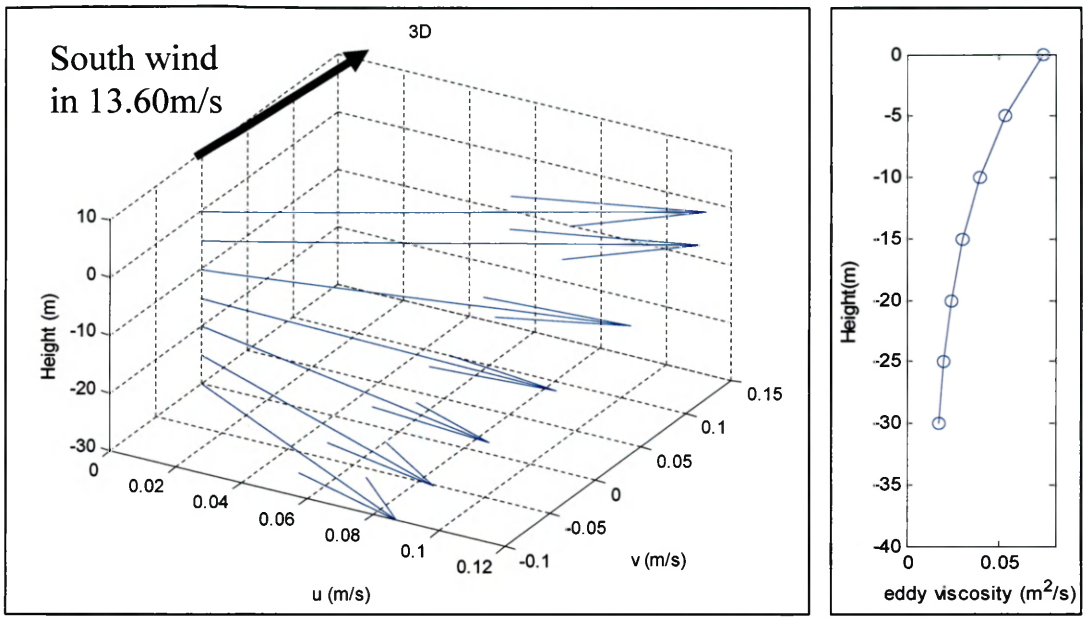

Figure 4.20 Current and eddy viscosity profiles from the results of 3D model during south wind

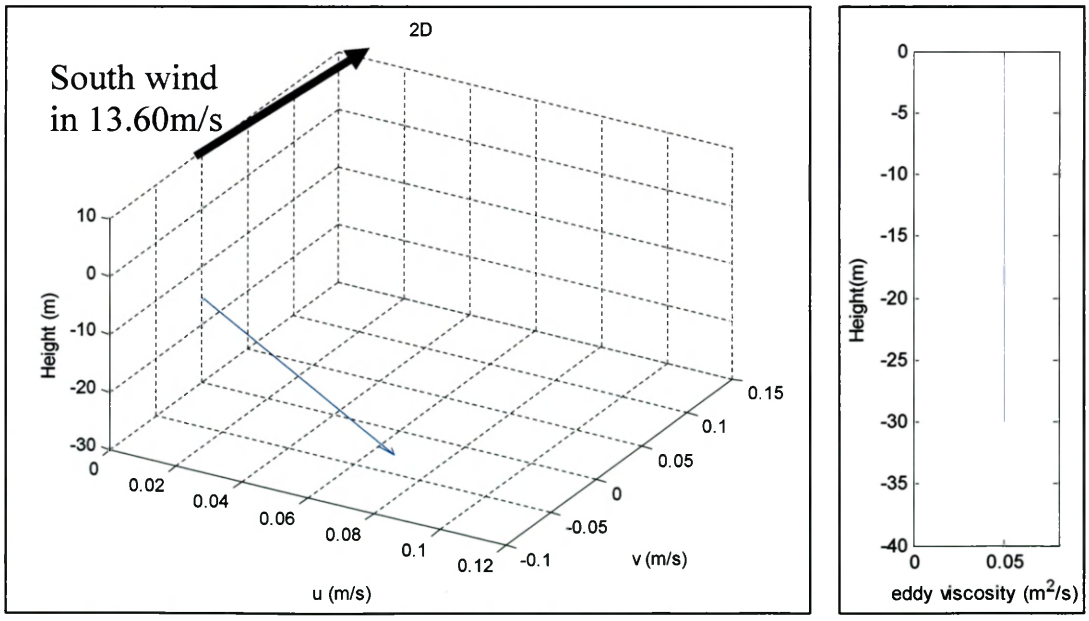

Figure 4.21 Current and eddy viscosity profiles from the results of 2D model during south wind

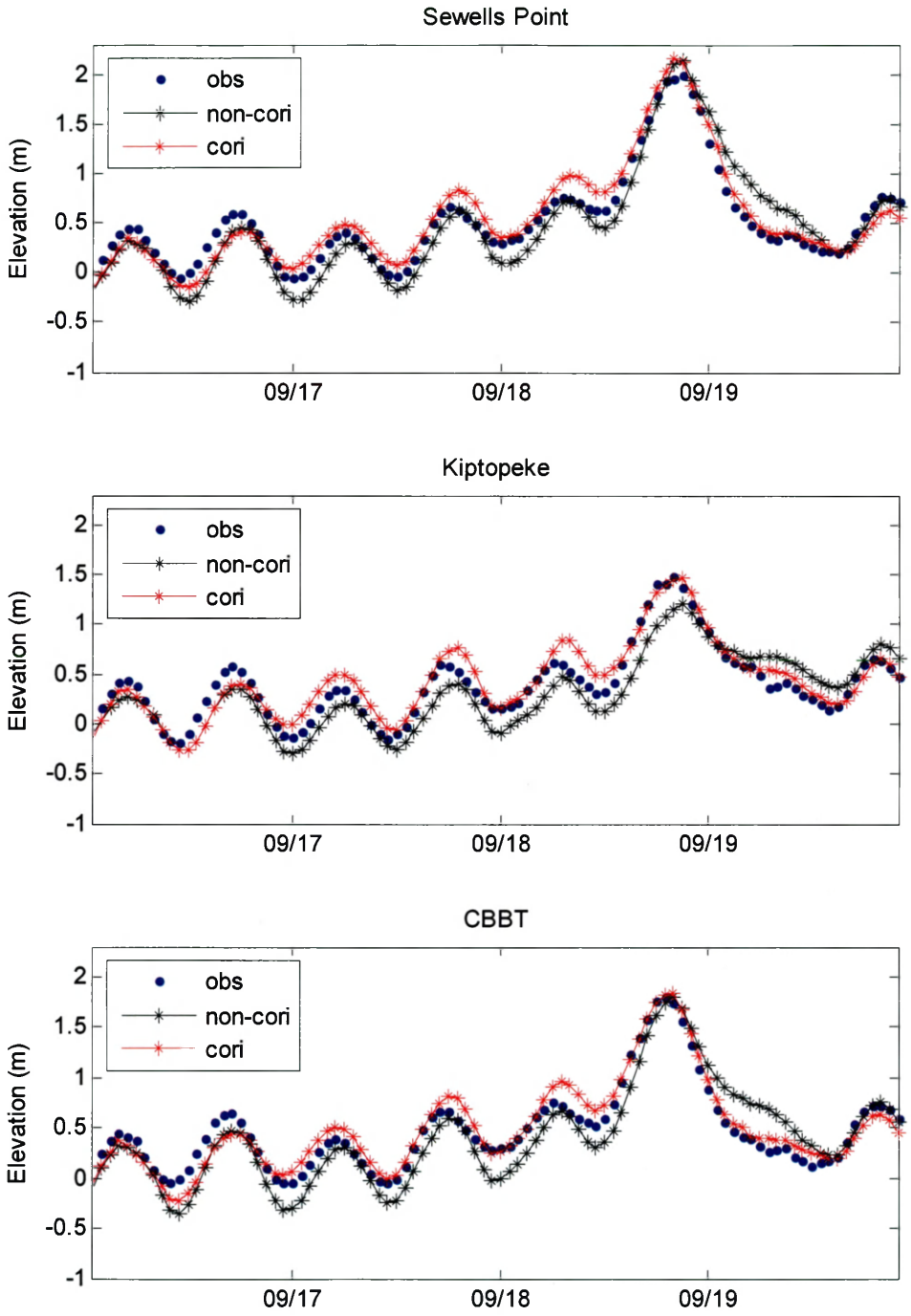

Figure 4.22 Comparison of water elevations simulated with and without Coriolis force

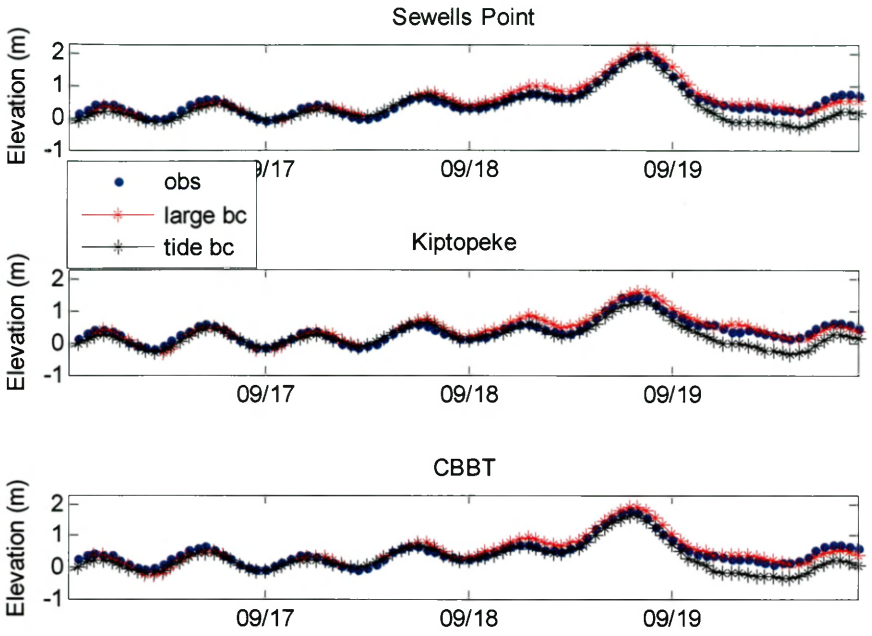

Figure 4.23 Storm tide results simulated with different open boundary condition in the lower Bay

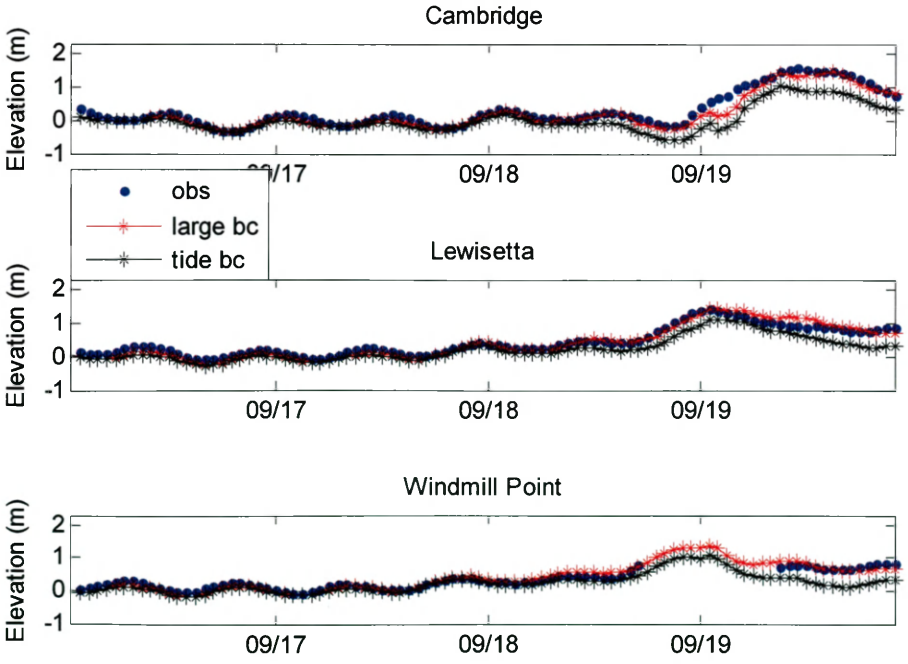

Figure 4.24 Storm tide results simulated with different open boundary condition in the middle Bay

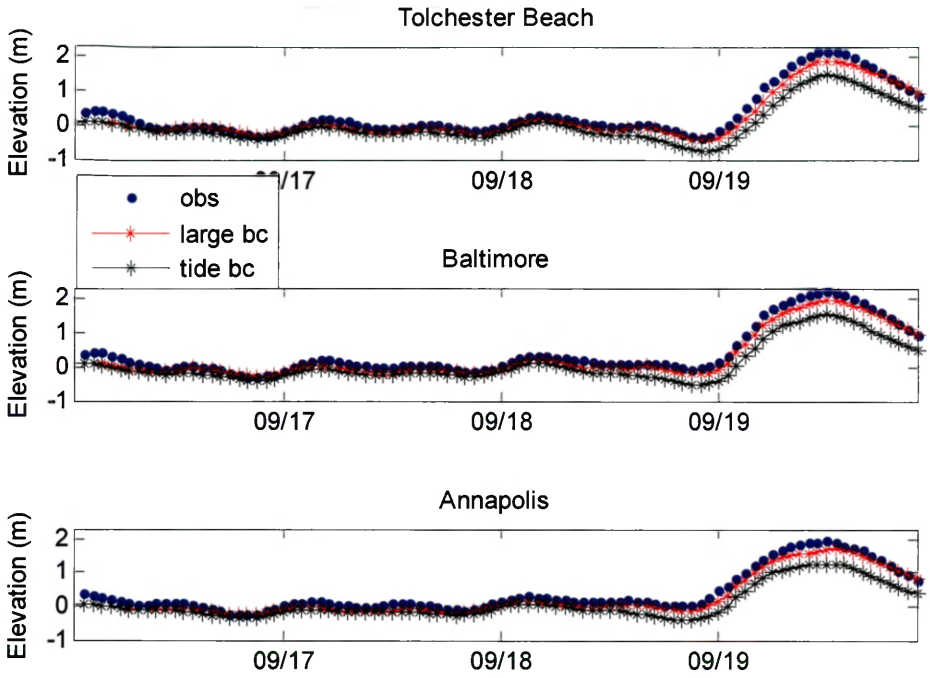

Figure 4.25 Storm tide results simulated with different open boundary conditions in the upper Bay

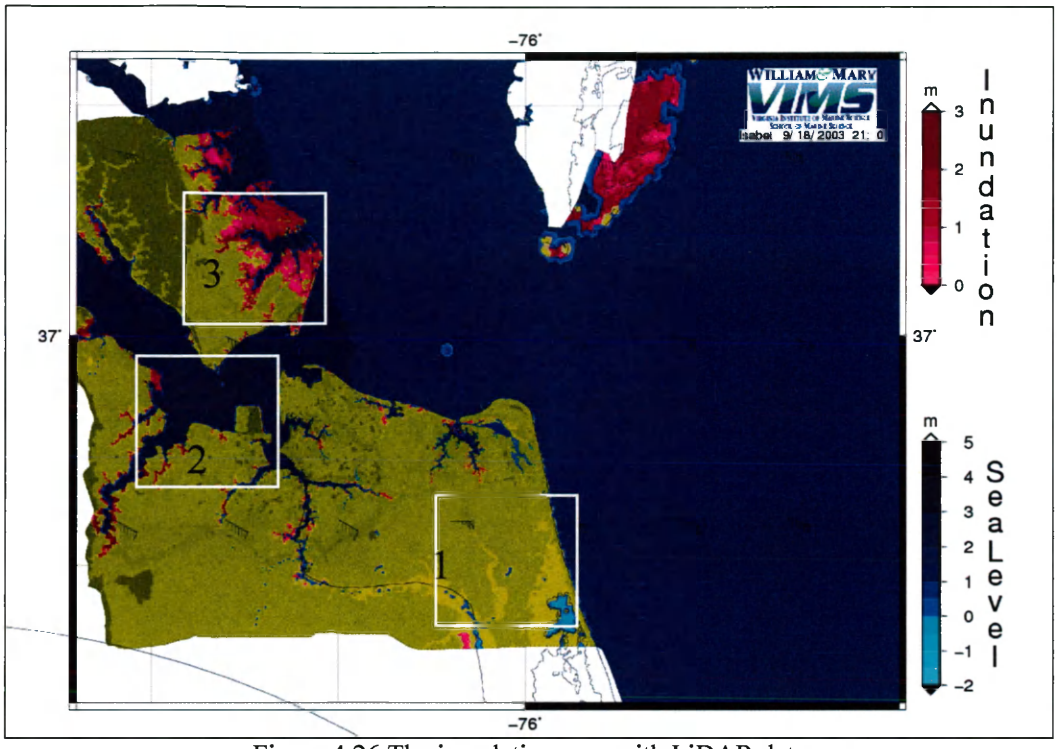

Figure 4.26 The inundation map with LiDAR data

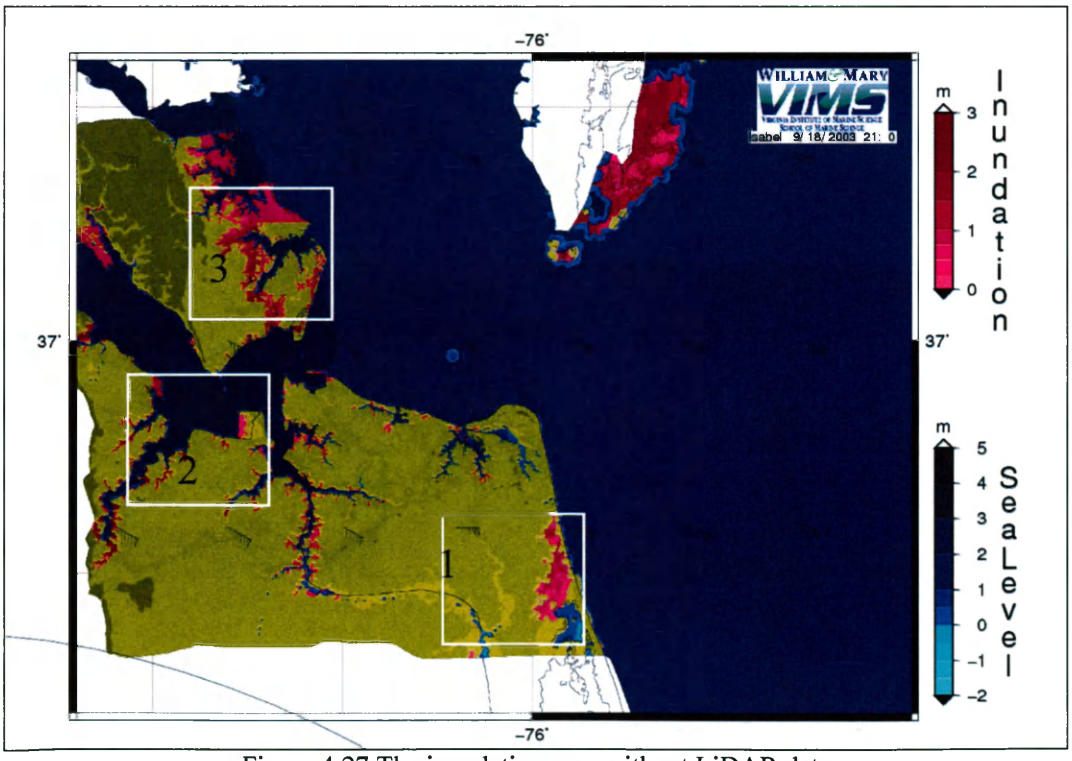

Figure 4.27 The inundation map without LiDAR data

VITA

Tao Shen

Born April 4th, 1983 in Jincheng, Shanxi Province in People's Republic of China. Earned B.S. in Geography from Nanjing University in 2006. Entered masters program in the College of William and Mary in 2006.